



**Universidade de Évora**

**Departamento de Física**

**Aerosol and cloud satellite remote sensing: monitoring and  
modelling using passive radiometers**

**Maria João Tavares da Costa**

**Supervisor: Professor Doctor Ana Maria Guedes de Almeida e Silva**

**Co - Supervisor: Doctor Vincenzo Levizzani**

A dissertation submitted to the University of Évora to  
obtain the Degree of Doctor of Philosophy in Physics

This thesis does not include the critics and suggestions made by the jury

**Évora**

**2004**



**Universidade de Évora**

**Departamento de Física**

**Aerosol and cloud satellite remote sensing: monitoring and  
modelling using passive radiometers**

**Maria João Tavares da Costa**

**Supervisor: Professor Doctor Ana Maria Guedes de Almeida e Silva**

**Co - Supervisor: Doctor Vincenzo Levizzani**



169 085

A dissertation submitted to the University of Évora to  
obtain the Degree of Doctor of Philosophy in Physics

This thesis does not include the critics and suggestions made by the jury

**Évora**

**2004**

# Acknowledgements

The work contained in this thesis has been carried out at the Institute of Atmospheric Sciences and Climate (ISAC) of the Italian Research Council (CNR) in Bologna and at the University of Évora. It has granted me very pleasant stays in Bologna from which I have greatly benefited as a research scientist.

Although a Ph.D. thesis is the work of one person, it is frontline research work and would never come true without the contributions from many people. I would like to thank here all those who helped to make this research possible.

My sincere gratitude goes first to Prof. Ana Maria Silva, my supervisor and friend, for her guidance, valuable advice, and continuous support. I have gained much experience through collaborating with her and would like to testify my admiration for her energy and dedication to work, which has been and is an inspiration to me. I thank her for believing in my capabilities since the beginning of my graduate studies and for entrusting me a fascinating research subject such as satellite remote sensing is.

I also want to show my deepest appreciation to Doctor Vincenzo Levizzani, Head of the Satellite Meteorology Group at ISAC and co-supervisor of this thesis, for hosting me in his research group, offering me an excellent working environment, and making me feel completely integrated since the first day. I'm grateful for his guidance, encouragement, availability, and friendship during the periods at the ISAC institute and all of the Ph.D. study, even through difficult times. I have learned much with him and I'm sure the last few years only represent the beginning of a long-lasting close cooperation and solid friendship.

I'm grateful to Dr. Elsa Cattani and Dr. Francesca Torricella for sharing their scientific skills and radiative transfer knowledge from which I gained much experience. I also thank them and Dr. Samantha Melani for the stimulating discussions, in particular with Dr. Elsa Cattani with whom I worked closely on the later stage of this research work. I am also grateful to all the people in the Satellite Meteorology Group for the countless good moments we shared in Bologna.

I'm also thankful to Prof. Byung-Ju Sohn from the Seoul National University for helpful discussions and the fruitful collaboration that originated the original work on the dust transport over the Korean area.

I wish to thank Dr. Marco Cervino for helpful suggestions and discussions in the beginning of this thesis.

I'm also grateful to Prof. José Borges and Dr. Paulo Canhoto for solidarily substituting me in the lecturing task in a crucial moment of the development of this thesis.

ISAC-CNR has hosted me and offered the possibility of using the available facilities. The Department of Physics and the Geophysics Centre of Évora (CGE) has made available continuous help and facilities that made this thesis possible.

All my friends in Évora and in Bologna that have constantly accompanied, encouraged, and supported me through this crucial period of my life.

My gratitude and affection go to my mother and father for having always supported and greatly stimulated my studies since the early years, and to my sister for being an everyday companion.

I'm grateful and I want to express all my affection to Dr. Daniele Bortoli, who became my dear husband during the PhD work, for his unconditional care, support, friendship, help, and above all for his enduring patience with me. I'm also deeply indebted with him for having introduced me to the Satellite Meteorology Group in the first place to Doctor Vincenzo Levizzani, making possible the development of the major part of this thesis at ISAC.

Finally, a special thought to the one that gave me the final incentive to finish this thesis, I dedicate it to him / her.

I also wish to thank all those people and institutions that have contributed to this thesis by providing computer codes, data and financial support:

- The authors of the Second Simulation of the Satellite Signal in the Solar Spectrum (6S) code (Vermote et al. 1997a), for generously providing it.
- The OpenCLASTR project (<http://www.ccsr.u-tokyo.ac.jp/~clastr/>) for making available the RSTAR (system for transfer of atmospheric radiation) and CAPCOM (Comprehensive Analysis Program for Cloud Optical Measurement) packages.
- The NOAA Air Resources Laboratory (ARL) for the provision of the HYSPLIT transport and dispersion model and/or READY website (<http://www.arl.noaa.gov/ready.html>).
- EUMETSAT for kindly making available the Meteosat imagery used. The Korean Meteorological Administration is also acknowledged for generously providing GMS imagery.
- MODIS data are courtesy of NASA Earth Science Enterprise and the official algorithms were developed by the MODIS Science Teams. They were processed by the MODIS Adaptive Processing System (MODAPS) and Goddard Distributed Active Archive Center (DAAC), the latter being in charge of archiving and distribution.
- POLDER aerosol parameters are products derived from data of the CNES POLDER instrument onboard NASDA's ADEOS.
- CERES data were provided by the Atmospheric Sciences Data Center at NASA Langley Research Center.
- AERONET data are available at <http://aeronet.gsfc.nasa.gov/> thanks to NASA, CNES and CNRS. AERONET investigators and their staff deserve special thanks for establishing and maintaining the sites where the data used in this investigation come from. Their availability to discuss aspects of the data and help through solving specific problems is to be acknowledged.
- Aircraft cloud effective radius measurements of the UK Met Office C-130 aircraft are available for download at [ftp://daac.ornl.gov/data/safari2k/atmospheric/uk\\_met\\_c-130/](ftp://daac.ornl.gov/data/safari2k/atmospheric/uk_met_c-130/) from the Oak

Ridge National Laboratory (ORNL) Distributed Active Archive Center (DAAC), Oak Ridge, Tennessee, USA.

- Data of the ER-2 Cloud Physics Lidar (CPL) are available online at [http://virl.gsfc.nasa.gov/cpl/safari2000\\_pass.html](http://virl.gsfc.nasa.gov/cpl/safari2000_pass.html) from the NASA Goddard Space Flight Center, Greenbelt, Maryland, USA.

This thesis was financially supported by the “ Fundação para a Ciência e a Tecnologia (FCT) e Fundo Social Europeu (FSE) no âmbito do III Quadro Comunitário de Apoio”.

---

# Table of Contents

Table of contents	i
Resumo	vii
Abstract	xi
List of Acronyms	xv
List of Symbols	xix
<b>1. Introduction</b>	<b>1</b>
1.1 Nature of the problem	1
1.2 Research objectives	6
1.3 Structure of the thesis	7
<b>2. Radiative transfer in the atmosphere</b>	<b>11</b>
2.1 Introduction	11
2.2 The radiative transfer equation: approximation for plane-parallel atmospheres with no polarization effects	12
2.3 The radiative transfer equation for the diffuse solar radiation	18
2.3.1 Computational methods in solar radiative transfer	25
2.4 The radiative transfer equation: thermal infrared radiation	28
2.5 Radiative forcing	31
2.6 Applications of radiative transfer to atmospheric remote sensing	34
2.6.1 Remote sensing of tropospheric aerosols	35
<b>3. Satellite passive sensors for aerosol and cloud remote sensing</b>	<b>39</b>
3.1 Introduction	39
3.2 Present and future satellite missions	44
3.3 Satellite instruments used in the present work	54
3.3.1 GEO instruments	54
3.3.1.1 Meteosat	54
3.3.1.2 GMS	59





---

3.3.1.3 MSG	62
3.3.2 LEO instruments	64
3.3.2.1 GOME	64
3.3.2.2 MODIS	66
3.3.2.3 Envisat	69
<b>4. Computer codes used</b>	<b>75</b>
4.1 Introduction	75
4.2 The radiative transfer code 6S	76
4.3 The radiative transfer code RSTAR	83
4.4 A code for the retrieval of cloud properties – CAPCOM	87
<b>5. Methods used for aerosol and cloud characterization</b>	<b>93</b>
5.1 Introduction	93
5.2 Aerosol characterization and direct radiative forcing assessment	94
5.2.1 Automated GOME spectral measurement selection	95
5.2.2 Sensitivity analysis and aerosol quantities retrieval from GOME	100
5.2.3 Aerosol optical thickness retrieval from coupling GOME retrievals with GEO satellite measurements	111
5.2.4 Direct SW aerosol radiative forcing assessment from GEO satellite measurements	112
5.2.5 Validation of the aerosol methodology	114
5.2.5.1 Case studies	115
5.2.5.2 Data	119
5.3 Cloud characterization	124
5.3.1 Cloud properties retrieval	126
5.3.2 Validation of the cloud methodology	134
5.3.2.1 Case studies	135
5.3.2.2 Data	136
<b>6. Results and discussion</b>	<b>143</b>



---

6.1 Introduction	143
6.2 Aerosols	143
6.2.1 Sensitivity analysis	144
6.2.2 Aerosol quantities derived from GOME	158
6.2.2.1 Single scattering albedo	160
6.2.2.2 Phase function	165
6.2.2.3 Ångström exponent	167
6.2.3 Aerosol optical thickness derived from GEO satellite measurements	169
6.2.3.1 Saharan dust over the Atlantic Ocean	169
6.2.3.2 Asian dust over the Yellow Sea	175
6.2.3.3 Dust over the Arabian Sea	177
6.2.3.4 Biomass burning over the southern Atlantic Ocean	179
6.2.3.5 Discussion	180
6.2.4 DSWARF assessment from GEO satellite measurements	181
6.3 Clouds	190
6.3.1 Results	190
6.3.2 Comparisons with MODIS cloud products and in situ measurements	200
<b>7. Conclusions and final remarks</b>	<b>209</b>
7.1 First objective	209
7.2 Second objective	212
7.3 Future work	214
<b>References</b>	<b>217</b>
<b>Appendix A</b> Block diagram of the aerosol method	<b>231</b>
<b>Appendix B</b> Block diagram of the cloud method	<b>233</b>

---



## Resumo

O objectivo do presente trabalho é a caracterização das propriedades dos aerossóis e das nuvens usando medidas combinadas de radiómetros passivos multi-espectrais que se encontram instalados a bordo de satélites. A determinação das propriedades dos aerossóis tem como objectivo a sua subsequente utilização para estimar o forçamento radiativo directo provocado pelos aerossóis na região espectral dos pequenos comprimentos de onda. Por sua vez a determinação das propriedades das nuvens tem como objectivo o estudo das possíveis modificações que as nuvens podem sofrer devido à interacção com os aerossóis presentes na atmosfera, já que isto pode levar a alterações significativas do clima. A investigação está centrada no estudo de episódios intensos e elevada variabilidade temporal de aerossóis sobre o oceano, os quais são caracterizados por grandes quantidades deste tipo de partículas em suspensão na atmosfera em datas e locais específicos, podendo modificar significativamente a composição da atmosfera e afectar o ciclo hidrológico. Esta investigação tem como ponto de partida o facto de que as medidas de satélite em diferentes regiões espectrais são úteis para extrair informações sobre os constituintes atmosféricos (aerossóis e nuvens) e que a combinação de sensores a bordo de satélites em órbitas diferentes, aqui proposta, contribui para melhorar o conhecimento dos aerossóis atmosféricos, fornecendo um instrumento de monitorização efectiva durante a ocorrência de episódios de aerossóis sobre o oceano, dificilmente conseguida apenas com um satélite.

As propriedades ópticas dos aerossóis representativas das condições atmosféricas são obtidas através da inversão de medidas obtidas do instrumento Global Ozone Monitoring Experiment (GOME), as quais apresentam alta resolução espectral. As propriedades ópticas dos aerossóis obtidas desta inversão, são utilizadas em cálculos de transferência radiativa para a determinação da espessura óptica dos aerossóis usando agora medidas de satélite em órbita geoestacionária (Meteosat e GMS), com uma resolução espacial e temporal superior à do sensor GOME e portanto mais adequados à caracterização de eventos de aerossóis. Esta combinação de sensores para a caracterização de aerossóis intensos e de relativa curta duração, substitui com enorme vantagem o uso dos modelos fixos de aerossóis disponíveis na literatura. As propriedades ópticas dos aerossóis obtidas representam uma componente essencial para a determinação do forçamento radiativo dos aerossóis à escala regional. O método desenvolvido para a caracterização das

nuvens é baseado em medidas de satélite multi-espectrais, usadas em combinação com cálculos de transferência radiativa para determinar as propriedades microfísicas das nuvens (espessura óptica da nuvem, raio eficaz das gotas e temperatura do topo da nuvem) e as suas modificações devido à interação com aerossóis.

Para avaliar a qualidade dos métodos utilizados, as propriedades ópticas dos aerossóis obtidas por inversão das imagens de satélite são comparadas com medidas à superfície da Aerosol Robotic NETwork (AERONET) (Holben et al. 1998). Para situações particulares também se recorre a medidas de radiação feitas à superfície durante uma campanha intensiva que decorreu na Coreia do Sul (Kim et al., 2004), ou com produtos oficiais dos instrumentos POLarization and Directionality of Earth Reflectances (POLDER) e MODerate Resolution Imaging Spectroradiometer (MODIS). Os valores do albedo de difusão simples (um dos parâmetros climatologicamente mais relevantes para o estudo do forçamento radiativo dos aerossóis à escala regional e global) obtidos da AERONET estão sempre dentro das barras dos erros apresentadas para os resultados obtidos do GOME, sendo as diferenças inferiores a 0.04. Uma primeira estimativa da precisão dos valores da espessura óptica (outra quantidade climatologicamente relevante para o estudo do forçamento radiativo dos aerossóis) baseada na comparação com medidas da AERONET, conduz a  $\Delta\tau^a = \pm 0.02 \pm 0.22\tau^a$  quando todos os valores da espessura óptica são considerados ou a  $\Delta\tau^a = \pm 0.02 \pm 0.16\tau^a$  para os episódios de aerossóis ( $\tau^a > 0.4$ ). Ambos os valores são comparáveis com os obtidos por outros autores. O fluxo ascendente no topo da atmosfera (TOA) obtido através de cálculos de transferência radiativa e usado para estimar o forçamento radiativo dos aerossóis à escala regional, é comparado com as medidas do instrumento Clouds and the Earth's Radiant Energy System (CERES). Esta comparação mostra que mais de 90% dos valores calculados diferem dos fluxos medidos pelo CERES menos de  $\pm 15\%$ .

No que respeita às propriedades das nuvens que foram aqui obtidas são comparadas com resultados do produto oficial MODIS nuvens (King et al. 1998), e com medidas in situ feitas de aviões durante a campanha de medidas Southern African Fire-Atmosphere Research Initiative 2000 (SAFARI 2000) (Swap et al. 2003). Os resultados mostram que as diferenças relativas com os produtos oficiais MODIS sobre as nuvens estão confinadas ao intervalo de confiança de  $\pm 25\%$  referido para o produto MODIS nuvens (King et al. 1998). A interpretação das comparações dos resultados para as propriedades das nuvens com os

dados do SAFARI 2000 revela-se mais complicada. A presença de uma camada absorvente de aerossóis acima da nuvem afecta a determinação dos parâmetros do topo da nuvem através da metodologia proposta baseada exclusivamente em medidas de satélite, sendo necessário proceder a alterações da metodologia agora utilizada, objecto de trabalho em curso.

Exceptuando-se a situação anteriormente referida, poderá considerar-se que tanto a metodologia adoptada para caracterizar episódios de aerossóis como a utilizada para caracterizar as propriedades microfísicas das nuvens na presença de episódios de aerossóis, se revelaram muito valiosas, tendo produzido resultados que concordam com observações e outros métodos independentes. Os resultados obtidos na determinação do forçamento radiativo directo pelos aerossóis concordam igualmente com os obtidos por outros métodos e autores.





## Abstract

The goal of the present work is the characterization of aerosol and cloud properties using combined measurements of multi-wavelength passive radiometers onboard satellites. The determination of the aerosol properties is aimed at their subsequent use to estimate the direct aerosol radiative forcing in the short wave (SW) spectral region. The determination of cloud properties is aimed at providing information on the possible modification of clouds through the interaction with atmospheric aerosol particles, as this may lead to significant changes of the Earth's climate. The research is focused on the study of aerosol events over the ocean, characterized by "heavy" particle loads in the atmosphere in specific dates and geographical locations, which may strongly modify the atmospheric composition and affect the hydrological cycle. The starting point of the investigation is that satellite measurements in different spectral regions are suitable for retrieving information on the atmospheric constituents (clouds and aerosols). In addition, that the combination of satellite sensors in different orbits proposed here, contributes to improve the knowledge of atmospheric aerosol particles, providing an effective aerosol monitoring tool during the occurrence of strong aerosol events over the ocean.

Aerosol optical properties representative of the atmospheric conditions are obtained from the inversion of high spectral resolution measurements from the Global Ozone Monitoring Experiment (GOME) instrument. The derived aerosol optical properties are input in radiative transfer calculations for the retrieval of the aerosol optical thickness using now geostationary visible broadband measurements (Meteosat and GMS), with a better spatial and temporal resolution with respect to GOME and therefore more adequate for the characterization of aerosol events. This combination of sensors for the characterization of intense and short-term aerosol episodes, replaces with great advantage the use of fixed aerosol models available in literature. The retrieved effective aerosol optical properties represent an essential component for the regional aerosol radiative forcing assessment. The method developed for cloud characterization is based on satellite multi-spectral measurements used in combination with radiative transfer calculations to retrieve the cloud microphysical properties (cloud optical thickness, droplet effective radius and cloud top temperature) and the cloud modifications due to the interaction with aerosol particles.

In order to evaluate the quality of the methods, the retrievals of the aerosol optical quantities obtained by inversion of the satellite measurements are checked against results from Sun and sky radiance measurements from the ground based AEROSOL ROBOTIC NETWORK (AERONET) (Holben et al. 1998). For particular situations, radiation ground-based measurements taken in South Korea (Kim et al. 2004) are also used, or satellite aerosol official products of the POLARIZATION and DIRECTIONALITY OF EARTH REFLECTANCES (POLDER) and the MODERATE RESOLUTION IMAGING SPECTRORADIOMETER (MODIS). The single scattering albedo values (one of the climate-relevant aerosol parameters for aerosol radiative forcing studies at the regional and global scale) from AERONET are always within the errors bars of the GOME retrievals, resulting in differences lower than 0.04. A first estimate of the optical thickness (another climate-relevant quantity for aerosol radiative forcing studies) accuracy derived from comparisons with AERONET data, leads to  $\Delta\tau^a = \pm 0.02 \pm 0.22\tau^a$  when all optical thickness values are retained or to  $\Delta\tau^a = \pm 0.02 \pm 0.16\tau^a$  for aerosol transport events ( $\tau^a > 0.4$ ). Both values are comparable with the ones by other authors. The upwelling flux at the top of the atmosphere (TOA) computed via radiative transfer calculations and used to estimate the regional aerosol radiative forcing, are compared with space-time co-located measurements from the Clouds and the Earth's Radiant Energy System (CERES) TOA flux product. It is found that more than 90% of the values differ from CERES fluxes for less than  $\pm 15\%$ .

As for the cloud properties retrieved with the present method, they are checked against results from the MODIS official product (King et al. 1998), and aircraft in situ measurements taken during the Southern African Fire-Atmosphere Research Initiative 2000 (SAFARI 2000) field campaign (Swap et al. 2003). Results show that the relative differences with the MODIS official cloud product are confined between the  $\pm 25\%$  error reported for the MODIS cloud product (King et al. 1998). The interpretation of the comparisons of the present cloud retrievals with the SAFARI 2000 data revealed to be more complicated. The presence of an absorbing aerosol layer above cloud top affects the quality of the cloud top parameter retrieval from satellite sensors with the present methodology. Changes to the methodology are needed and this represents ongoing work.

Except for the SAFARI 2000 situation, it can be stated that both the methodology for the characterization of aerosol events and the methodology for the cloud properties characterization in the presence of aerosol events revealed valuable tools, producing results

that are in agreement with observations and independent methods. The results obtained for the direct aerosol radiative forcing are equally in agreement with the ones obtained from other methods and authors.



## List of Acronyms

- AATSR** - Advanced Along Track Scanning Radiometer
- ADEOS** - Advanced Earth Observing Satellite (of NASDA, Japan)
- AERONET** - AErosol RObotic NETwork
- AFGL** – Air Force Geophysics Laboratory
- AOT** – Aerosol Optical Thickness
- ARL** - Air Resources Laboratory
- ATLID** – ATmospheric LIDar
- ATN** - Advanced TIROS-N satellite series
- ATS** - Applications Technology Satellite
- ATSR** - Along Track Scanning Radiometer
- AVHRR** - Advanced Very High Resolution Radiometer
- AVNIR** - Advanced Visible and Near Infrared Radiometer
- BBR** - Broad-Band Radiometer
- BRDF** - Bi-directional Reflectance Distribution Function
- CALIOP** - Cloud-Aerosol Lidar with Orthogonal Polarization
- CALIPSO** - Cloud-Aerosol Lidar and Infrared Pathfinder Satellite Observations
- CAPCOM** - Comprehensive Analysis Program for Cloud Optical Measurement
- CCD** - Charge-Coupled Device
- CCSR** - Center for Climate System Research
- CERES** - Clouds and the Earth’s Radiant Energy System
- CPL** - Cloud Physics Lidar
- CPR** - Cloud Profiling Radar
- CZCS** - Coastal Zone Colour Scanner
- DAAC** – Distributed Active Archive Center
- DSWAF** - Direct Short Wave Aerosol Radiative Forcing
- EarthCARE** - Earth, Clouds, Aerosol and Radiation Explorer
- EGPM** – European contribution to the Global Precipitation Measurement mission
- Envisat** - ENVironmental SATellite
- EOS** - Earth Observing System
- EPS** - EUMETSAT Polar System

**ERS** - European Remote-Sensing satellite  
**ESA** - European Space Agency  
**EUMETSAT** - European Organisation for the Exploitation of Meteorological Satellites  
**FGGE** - First Global GARP Experiment  
**FTS** - Fourier Transform Spectrometer  
**GARP** - Global Atmospheric Research Programme  
**GEO** - Geostationary Earth Orbit  
**GERB** - Geostationary Earth Radiation Budget  
**GMS** - Geostationary Meteorological Satellite (of Japan)  
**GOES** - Geostationary Operational Environmental Satellite (of the USA)  
**GOME** - Global Ozone Monitoring Experiment  
**GOMS** - Geostationary Operational Meteorological Satellite (of Russia)  
**GPM** - Global Precipitation Measurement mission  
**HIRDLS** - High Resolution Dynamics Limb Sounder  
**HRV** - High Resolution Visible  
**HYSPLIT** - HYbrid Single-Particle Lagrangian Integrated Trajectory Model  
**IIR** - Imaging Infrared Radiometer  
**ILAS** - Improved Limb Atmospheric Spectrometer  
**IMG** - Interferometric Monitor for Greenhouse Gases  
**INDOEX** - Indian Ocean Experiment  
**IODC** - Indian Ocean Data Coverage  
**IPCC** - Intergovernmental Panel on Climate Change  
**IR** - Infrared  
**ISCCP** - International Satellite Cloud Climatology Project  
**ITOS** - Improved TIROS Observational System  
**IWC** - Ice Water Content  
**IWP** - Ice Water Path  
**LEO** - Low Earth Orbit  
**LIDAR** - LIght Detection And Ranging  
**LUT** - Look-Up Table  
**LW** - Long Wave  
**LWC** - Liquid Water Content

**LWP** - Liquid Water Path

**MADRAS** - Microwave Analysis and Detection of Rain and Atmospheric Structures

**MAP** - Mesoscale Alpine Programme

**MERIS** - Medium Resolution Imaging Spectrometer

**Meteor** - Polar Meteorological satellite series of Russia

**Meteosat** - Geostationary meteorological satellites of EUMETSAT

**Metop** - Meteorological Operational polar satellites of EUMETSAT

**MLS** - Microwave Limb Sounder

**MODIS** - MODerate resolution Imaging Spectroradiometer

**MSG** - Meteosat Second Generation

**MSI** - Multi-Spectral Imager

**MVIRI** - Meteosat Visible and Infrared Imager

**NASA** - National Aeronautics and Space Administration (of the USA)

**NASDA** - National Space Development Agency (of Japan)

**NCEP GDAS** - National Centers for Environmental Prediction Global Data Assimilation System

**NIR** - Near-Infrared

**NIST** - National Institute of Standard and Technology

**NOAA** - National Oceanic and Atmospheric Administration (of the USA) (and its polar satellite series)

**NSCAT** - NASA Scatterometer

**OCTS** - Ocean Colour and Temperature Scanner

**OMI** - Ozone Monitoring Experiment

**PARASOL** - Polarisation et Anisotropie des Réflectances au sommet de l'Atmosphère, couplées avec un Satellite d'Observation emportant un Lidar

**pixel** - picture element

**PMD** - polarization monitoring device

**POLDER** - POLarization and Directionality of Earth Reflectances

**PR** - Precipitation Radar

**RADAR** - RADio Detection And Ranging

**RIS** - Retroreflector in Space

**RSS** - Rapid Scanning Service

- RSTAR** - System for Transfer of Atmospheric Radiation
- RTC** – Radiative Transfer Code
- SAFARI 2000** - Southern African Fire-Atmosphere Research Initiative 2000
- SAPHIR** - Sondeur Atmospherique du Profil d’Humidite Intertropicale par Radiometrie
- ScaRab** – Scanner for RAdiation Budget
- SCIAMACHY** - SCanning Imaging Absorption spectroMeter for Atmospheric ChartographY
- SeaWiFS** - Sea-viewing Wide Field-of-view Sensor
- SEVIRI** - Spinning Enhanced Visible and Infrared Imager
- SMS** - Synchronous Meteorological Satellite
- SOS** - Successive Orders of Scattering
- SST** - Sea Surface Temperature
- SW** - Short wave
- TES** - Tropospheric Emission Spectrometer
- TIROS** - Television Infrared Observation Satellite
- TOA** - Top Of the Atmosphere
- TOMS-EP** - Total Ozone Mapping Spectrometer onboard the Earth Probe
- TRMM** - Tropical Rainfall Measuring Mission
- UTC** - Universal Time Coordinated
- UV** - Ultraviolet
- VIRS** - Visible Infrared Radiometer
- VIS** - Visible
- VISSR** - Visible and Infrared Spin Scan Radiometer
- WFC** - Wide-Field Camera
- WV** - Water Vapour
- 6S** - Second Simulation of the Satellite Signal in the Solar Spectrum



## List of Symbols

$B_\lambda$ (T) – Planck function	$(W.m^{-2}.sr^{-1}.\mu m^{-1})$
C - measured digital count	Count
$C_0$ – Offset	Count
c - Velocity of light in vacuum	$(2.9979 \times 10^8 m.s^{-1})$
D - Cloud geometrical thickness	-
dA - Element of area	$(m^2)$
d $\omega$ - Element of solid angle	$(sr)$
ew - Equivalent water vapour amount	$(kg.m^{-2})$
$F_0$ - Total solar flux density	$(W.m^{-2})$
$F_{0_\lambda}$ - Monochromatic solar flux density	$(W.m^{-2})$
$F^+$ - Upward total flux density	$(W.m^{-2})$
$F^-$ - Downward total flux density	$(W.m^{-2})$
$F_\lambda^{dir}$ - Direct solar flux	$(W.m^{-2})$
$F^{net}$ - Net radiation	$(W.m^{-2})$
$f_\lambda$ - Spectral response function of a sensor	-
$g_\lambda$ - asymmetry parameter	-
h - Planck constant	$(6.6262 \times 10^{-34} J.s)$
$I_\lambda$ – Monochromatic radiance	$(W.m^{-2}.sr^{-1}.\mu m^{-1})$
$I_\lambda^{dir}$ - Direct solar monochromatic radiance	$(W.m^{-2}.sr^{-1}.\mu m^{-1})$
$I_{0_\lambda}$ - TOA incident solar monochromatic radiance	$(W.m^{-2}.sr^{-1}.\mu m^{-1})$
$J_\lambda$ – Monochromatic source function	$(W.m^{-2}.sr^{-1}.\mu m^{-1})$
k - Boltzmann constant	$(1.3806 \times 10^{-23} J.K^{-1})$
$k_\lambda^e$ - Mass extinction cross section	$(m^2.kg^{-1})$
$k_\lambda^s$ - Mass scattering cross section	$(m^2.kg^{-1})$
$k_\lambda^a$ - Mass absorption cross section	$(m^2.kg^{-1})$

$m$ - Mass	(kg)
$m_\lambda$ - Refractive index	-
$m_{r_\lambda}$ - Real part of the refractive index	-
$m_{i_\lambda}$ - Imaginary part of the refractive index	-
$n(r)$ - Particle size distribution	$\mu\text{m}^{-1}\text{cm}^{-3}$
$n(L)$ - Ice crystal size distribution being $L$ the major dimension	$\mu\text{m}^{-1}\text{cm}^{-3}$
$P_\lambda(\Theta)$ - Scattering phase function	-
$P^c$ - Cloud top pressure	(hPa)
$P(z)$ - Vertical profile of the pressure	(hPa)
$Pd_F$ - Fine mode percentage particle density	-
$Pd_C$ - Coarse mode percentage particle density	-
$Q_\lambda^e$ - Mie extinction efficiency	-
$Q_\lambda^s$ - Mie scattering efficiency	-
$Q_\lambda^a$ - Mie absorption efficiency	-
$r$ - particle radius	( $\mu\text{m}$ )
$r_M$ - mode radius	( $\mu\text{m}$ )
$r_F$ - Fine mode modal radius of the log-normal size distribution	( $\mu\text{m}$ )
$r_C$ - Coarse mode modal radius of the log-normal size distribution	( $\mu\text{m}$ )
$r_{eff}$ - effective radius	( $\mu\text{m}$ )
$S_\lambda$ - Spherical or global albedo	-
T - Absolute temperature	(K)
$T^c$ - Cloud top absolute temperature	(K)
$T^{surf}$ - Surface absolute temperature	(K)
$T(z)$ - Vertical profile of the absolute temperature	(K)
$t^{gas}$ - Gaseous transmission	-
$t_\lambda$ - Total atmospheric transmission	-
$\mathfrak{T}_\lambda$ - Monochromatic transmittance	-

---

$V$ - Volume	$(m^3)$
$W$ - Liquid water path	$(kg.m^{-2})$
$wv(z)$ - Vertical profile of the water vapour amount	$(kg.m^{-3})$
$w$ - Liquid water content	$(kg.m^{-3})$
$Z^c$ - Cloud top height	$(km)$
$z$ - Height	$(km)$
$\alpha$ - Ångström exponent	-
$\alpha_{calib}$ - calibration coefficient	$(W.m^{-2}.sr^{-1}.count^{-1})$
$\beta$ - Ångström turbidity coefficient	-
$\beta_\lambda^e$ - Volume extinction coefficient	$(m^{-1})$
$\beta_\lambda^s$ - Volume scattering coefficient	$(m^{-1})$
$\beta_\lambda^a$ - Volume absorption coefficient	$(m^{-1})$
$\Delta F$ - Total radiative forcing	$(W.m^{-2})$
$\Delta\tau^a$ - Aerosol optical thickness accuracy	-
$\delta(\mu - \mu_0)$ - Dirac's $\delta$ function	-
$\varepsilon_\lambda$ - Monochromatic emissivity of the atmosphere	-
$\Theta$ - Scattering angle	$(^\circ)$
$\theta$ - Zenith angle	$(^\circ)$
$\theta_0$ - Solar zenith angle	$(^\circ)$
$\lambda$ - Wavelength	$(\mu m)$
$\mu$ - Cosine of the zenith angle	-
$\mu_0$ - Cosine of the solar zenith angle	-
$\rho$ - Density	$(kg.m^{-3})$
$\rho_i$ - Ice density	$(kg.m^{-3})$
$\rho_\lambda$ - Spectral reflectance	-
$\sigma_\lambda^e$ - Extinction cross section	$(m^2)$
$\sigma_\lambda^s$ - Scattering cross section	$(m^2)$

---

$\sigma_{\lambda}^a$ - Absorption cross section	$(m^2)$
$\sigma_F$ - Fine mode standard deviation of the log-normal size distribution	$(\mu m)$
$\sigma_C$ - Coarse mode standard deviation of the log-normal size distribution	$(\mu m)$
$\tau_{\lambda}$ - Optical thickness	-
$\tau^a$ - Aerosol optical thickness	-
$\tau_{\lambda=0.55\mu m}^{aerosol}$ - Aerosol optical thickness at the reference wavelength of 550nm	-
$\tau^c$ - Cloud optical thickness	-
$\nu_{eff}$ - Effective variance	-
$\phi$ - Azimuth angle	$(^{\circ})$
$\phi_0$ - Solar azimuth angle	$(^{\circ})$
$\phi - \phi_0$ - Relative azimuth angle	$(^{\circ})$
$\chi$ - Mie size parameter	-
$\chi^2$ - Chi-square function	-
$\varpi$ - Single scattering albedo	-

# Chapter 1

## Introduction

### 1.1 Nature of the problem

The need for a thorough monitoring and modelling that lead to an increased understanding of the climate system has been increasingly recognized in the past years, not only for societal objectives related to business activities and the protection of life and property, but also to support climate change scenarios taking into account both anthropogenic influences and human impacts (Goody et al. 2002). The two main factors that regulate the climate system are the planetary albedo and the greenhouse effect. The planetary albedo is strongly dependent upon the cloud cover fraction, the atmospheric aerosols, and the surface reflectance.

The radiation budget in clear sky conditions depends mainly on the surface properties and vertical distributions and amounts of aerosols, water vapour and ozone. The growing consciousness of the strong influence of atmospheric aerosols on atmospheric processes (e.g. IPCC 2001) and consequently on climate, prompts for local and global studies aimed to quantify the aerosol load in the atmosphere (aerosol optical thickness), as well as aerosol optical properties. Aerosol particles play a twofold role in the atmosphere: on one hand they directly scatter and absorb solar radiation, and secondly they may enter cloud microphysical processes as cloud condensation nuclei. Moreover, the importance of strong aerosol mobilization and transport episodes is becoming increasingly clear to scientists since these events are usually connected with higher aerosol concentrations in the atmosphere, thus altering the atmospheric composition and entering delicate mechanisms such as the water cycle (Haywood and Boucher 2000; Ramanathan et al. 2001; Kaufman et al. 2002). This may cause an enhancement/suppression of many related atmospheric processes affecting not only the local and regional, but also the global climate (Karyampudi et al. 1999). It is therefore of extreme importance that such aerosol events be accurately detected, characterized, and monitored. The primary natural source of aerosol particles on a global scale is sea salt, followed by soil dust, which is a major contributor especially in sub-tropical and tropical regions (IPCC 2001). Another substantial natural

source of aerosols on a global scale is biomass burning in Africa, Asia, Siberia, and South America, particularly in the Amazon. For example, smoke from forest fires is a source of strong absorbing aerosols, which in certain circumstances may reduce the amount of sunlight scattered back to space and lead to absorption of solar radiation within the atmospheric column (Kaufman et al. 2002; Ramanathan et al. 2001).

A great number of studies were conducted on the possible modification of cloud properties through the interaction with atmospheric aerosol particles, as this may lead to important changes of the Earth's climate. On one hand, aerosol particles acting as cloud condensation nuclei may be responsible for direct modifications of the cloud properties (Albrecht 1989; Bréon et al. 2002; Kawamoto and Nakajima 2003) - first indirect effect. It consists of a decrease of droplet size due to an increase in droplet concentration (assuming a constant liquid water content), when a cloud is polluted with anthropogenic aerosol particles serving as additional cloud condensation nuclei (Twomey 1974). On the other hand, due to the decrease of cloud particle size, aerosol particles may indirectly interfere with cloud lifetime and precipitation efficiency, originating the second indirect effect, which is characterized by the diminution of the efficiency of precipitation forming processes, tending to increase the liquid water content, cloud lifetime and thickness (Rosenfeld 1999, 2000). Therefore, both effects may interfere with the planetary albedo. The biomass burning aerosol is considered one of the main responsible of this kind of cloud properties modification. In addition, this type of aerosols contains organic compounds and black carbon, the latter being a strong absorber of solar radiation that can greatly impact cloud formation and evaporation (Ackerman et al. 2000). Aerosol particles mobilized in great quantities from desert areas, the "desert dust", represent another main natural sources of atmospheric aerosol. Dust aerosol layers are capable of travelling thousands of kilometres at high altitudes, depending on the meteorological conditions. Apart from the possible consequences of cloud-aerosol interactions, desert dust particles apparently have a strong ability to act as ice nuclei. This statement is supported by observations of the conversion of supercooled water clouds to ice clouds at temperatures about 20°C higher than those that are expected for homogeneous nucleation of cloud droplets in the middle and upper troposphere. This can lead to the formation of cirrus clouds at much higher temperatures than normally thought (Sassen 2002; Sassen et al. 2003; DeMott et al. 2003). For all these reasons the monitoring of the optical properties of

atmospheric aerosol is crucial for a quantification of the radiative forcing at the local, regional and global scales given the key role played by aerosols both in cloud-free and cloudy conditions.

Satellite measurements provide indispensable data for effective global observations of cloud and aerosol properties. This is the reason why the interest in aerosol observations from satellite passive radiometers is steadily increasing, and the application of cloud and aerosol retrieval algorithms to satellite radiances strongly recommended (Nakajima and King 1990; Levizzani and Setvák 1996; Rossow and Schiffer 1999; NASA GISS 1997; King et al. 1999; IPCC 2001). However, the assessment of the reliability of the retrievals depends on the comparison with independent measurements that allow for the error estimation, constituting the quality control of global satellite products.

The accurate retrieval of the aerosol optical properties and their monitoring from satellite, however, require sensors with high spectral resolution and span that avoid as much as possible gas absorption regions and have adequate spatial and temporal resolution. Further requirements are on data from the ultraviolet spectral range and/or multi-angle geometry measurements since it is necessary a quantification of the aerosol absorbing potential or the aerosol vertical distribution. Note that such an “ideal” sensor encompassing all the above characteristics is by no means presently available on board current satellites (Kaufman et al. 1997). Although geostationary Earth orbiting (GEO) satellite sensors ensure the adequate temporal and spatial resolution for monitoring the aerosol optical thickness at the global scale (Griggs 1979; Dulac et al. 1992; Moulin et al. 1997a; Moulin et al. 1997b), they generally lack the necessary spectral resolution, thus preventing a characterization of the aerosol properties. Therefore, the available aerosol retrieval techniques are constrained to use fixed aerosol models available from the literature. This fact alone can introduce considerable errors on the aerosol optical thickness retrievals, particularly in the presence of heavy aerosol events, due to the high spatial variability and short residence time of the aerosols. In consequence, significant uncertainties affect the direct shortwave aerosol radiative forcing (DSWARF) estimates. Literature models are in fact based on average or standard atmospheric conditions that may not adequately represent the atmospheric state at the time of the satellite overpass.

On the other hand, sensors on board low Earth orbit (LEO) satellites do not lend themselves to monitoring atmospheric aerosol concentrations due to their poor temporal

resolution, which can result in a smoothing of retrieved fields and/or a loss of important features in aerosol optical thickness global maps or regional transport events. Note that, however, the most recent LEO instruments are very valuable tools for aerosol quantitative analysis (King et al. 1999). Their unique multi-spectral, multi-angular, and polarization capabilities prompt for improved techniques to retrieve the aerosol optical thickness and the aerosol optical properties in general. Tanré et al. (1997) used spectral measurements from the MODerate resolution Imaging Spectroradiometer (MODIS) for a study on the retrieval of the aerosol optical thickness and asymmetry parameter, the relative dominant role of the accumulation or coarse modes, and to a lesser extent the ratio between the modes and the size of the main mode. Veefkind and de Leeuw (1998) developed an algorithm to derive the spectral optical thickness over the ocean from dual view measurements taken by the Along Track Scanning Radiometer 2 (ATSR-2). Polarization measurements taken by the short-lived POLarization and Directionality of Earth Reflectances (POLDER) instrument have been used to derive the aerosol optical thickness, the Ångström exponent, and the refractive index (Leroy et al. 1997; Goloub et al. 1999). In spite of its coarse spatial resolution, the Global Ozone Monitoring Experiment (GOME) spectrometer (Burrows et al. 1999) on board the LEO European Remote-Sensing satellite (ERS-2) has been successfully used to retrieve aerosol properties over the ocean. Torricella et al. (1999) presented a method devised not only to detect strong aerosol events, determine the aerosol type, and retrieve high aerosol optical thickness values, but also to correctly detect aerosol load and type over oceanic areas (optical thickness of the order of 0.1). Ramon et al. (1999) describe an algorithm based on GOME spectral reflectances to derive aerosol optical thickness, aerosol type, and surface type, applicable over ocean and over land surfaces. Bartoloni et al. (2000) developed an operational processing system to derive the aerosol type and optical thickness from GOME spectra. All these techniques take advantage of the high spectral resolution of the instrument trying to avoid gas absorption as much as possible.

As already mentioned, clouds are a major driving force of the climate system, controlling the planetary albedo. They strongly modulate the energy balance of the Earth through absorption and scattering of solar radiation and absorption and emission of terrestrial radiation (Liou 1976; Ramanathan 1987; Cess et al. 1989), and they regulate, together with precipitation, the hydrological cycle. Although the importance of clouds is



widely recognised, their impact is associated with great uncertainties due to the complexity and space-time variation of cloud phenomena. Early investigations have focused on the importance of total cloud cover, neglecting the effect of cloud type variation. Nevertheless, it is now clear that both can equally contribute to determine the cloud radiative effects and influence the Earth radiation budget (Chen et al. 2000; Alados et al. 2000; Bergman and Hendon 2000; Bortoli et al. 2002), justifying radiative studies of different cloud types. Melani et al. (2003) for example, simulate the radiative effects of cirrus clouds on top of deep convective storms. Therefore, the global monitoring of the cloud optical and microphysical properties becomes a main task/necessity.

Remote sensing of cloud properties such as cloud optical thickness and / or droplet effective radius using multi-wavelength radiometers flying on aircrafts began in the early 1970s (Hansen and Pollack 1970; Twomey and Cocks 1982; King 1987). These kinds of studies were then extended to satellite measurements (Curran and Wu 1982; Arking and Childs 1985; Rossow and Schiffer 1991; Nakajima and King 1990; Nakajima and Nakajima 1995), aiming at providing global coverage of cloud properties. However, the accuracy introduced by the multi-wavelength information obtained from the LEO satellites is offset by the fact that these satellites do not ensure adequate space-time coverage of the globe, which is undoubtedly provided by GEO satellites, whose radiometers, however, are restricted to broadbands in the visible and infrared spectral regions (Porcú and Levizzani 1992). The development of the present methodology to derive cloud properties is encouraged by the existence of a new generation of GEO satellite measurements such as those of the Spinning Enhanced Visible and Infrared Imager (SEVIRI) flying on Meteosat Second Generation (MSG) (Schmetz et al. 2002). This innovative sensor opens new perspectives with respect to past and present GEO systems since it provides the necessary additional spectral measurements, supplied until now exclusively by LEO satellite sensors. The doubled sampling frequency and improved spatial resolution prompts for global monitoring of cloud properties and eventually advances in cloud-aerosol interaction studies, facilitating the task of comparing the derived cloud properties with in situ measurements as well. Data from MSG-1 SEVIRI was not yet distributed on a regular basis at the moment the present study was carried out and therefore measurements from the MODerate resolution Imaging Spectroradiometer (MODIS) (Barnes et al. 1998) onboard Terra and Aqua LEO satellites were used, which present

comparable spectral channels in the visible (VIS), thermal infrared (IR), and near IR (NIR).

The awareness of the importance of the problematic described in the above paragraphs, namely of the important role that aerosols and cloud play on the climate system, constitute the main motivation of the present work. In addition, the new generation satellite sensors already in orbit, as well the planned satellite missions, that present improved capabilities concerning the spectral, spatial and temporal resolution open new horizons in aerosol and cloud remote sensing, which undoubtedly deserve to be studied. This constitutes a further incentive to carry on the research work presented hereafter.

## 1.2 Research objectives

The general goal of the present research is to provide information on aerosol and cloud properties from satellite remote sensing. The determination of the aerosol properties is aimed to a subsequent use to estimate the radiative forcing induced by the aerosol direct effect, which still remains highly uncertain depending on the aerosol type (IPCC 2001). The research further aims to retrieve cloud properties with the purpose of providing information on the possible modification of cloud properties through the interaction with atmospheric aerosol particles, as this may lead to significant changes of the Earth's climate (Twomey 1974; Albrecht 1989; Bréon et al. 2002; Kawamoto and Nakajima 2003). Moreover, this investigation was focused on the study of aerosol events, characterized by “heavy” particle loads in the atmosphere in specific dates and geographical locations, corresponding to situations when the study of the direct aerosol radiative forcing, as well as of the aerosol indirect effect on cloud properties have paramount importance. This is the reason why the geographical area selected for the study does not always coincide with the Portuguese region, rather it varies according to the availability of strong aerosol events characterized by different particle types.

The hypothesis that serves as a starting point to this investigation is that passive radiation instruments onboard satellites measuring in different spectral regions are suitable for retrieving information on the atmospheric constituents (clouds and aerosols). The original contribution that this work brings forward to the scientific community is

represented by the combined use of different satellite sensors to characterize aerosols. The combination of measurements from satellites in different orbits (LEO and GEO) having different spectral, spatial, and temporal resolutions, with the intention of developing an effective aerosol monitoring tool during strong aerosol events over the ocean (Costa et al. 2002) is a novelty introduced here with respect to other satellite-based algorithms already in use. Until now, satellite-based methods were directed either to aerosol monitoring (Dulac et al. 1992; Moulin et al. 1997a) or to a more accurate aerosol characterization (Tanré et al. 1997; Deuzé et al. 2000), falling short of providing both aspects, which are equally important for climate studies. The method developed and presented here is not subject to this shortcoming, presenting as key features the improved accuracy of the aerosol characterization with respect to the methods based on GEO measurements and the stretching of the spatial and temporal coverage of the LEO retrievals to the GEO spatial-temporal scale. The results indicate the potential of this method to be extended over land improving therefore quite significantly the present retrievals.

### **1.3 Structure of the thesis**

This thesis is divided into seven major chapters. Chapters 5 and 6 represent the bulk of the present work since they contain the developed methodologies and the results obtained. This justifies the larger summary dedicated here to these chapters.

The first chapter introduces the thesis, presenting a review of the related work, emphasizing the central role that satellite remote sensing plays on aerosol and cloud studies.

Chapter 2 deals with the propagation of electromagnetic radiation in the atmosphere and its interaction with the Earth's surface and atmospheric constituents, which are responsible for the absorption, emission and scattering of radiation in the atmosphere, presenting the radiative transfer equation limited to the complexity required by the present work.

Chapter 3 aims to illustrate the past, present and future satellite passive sensors useful for aerosol and cloud remote sensing.

In Chapter 4 the computer codes used are described, namely the Second Simulation of the Satellite Signal in the Solar Spectrum (6S; Vermote et al. 1997a), the System for Transfer of Atmospheric Radiation (RSTAR), and the Comprehensive Analysis Program for Cloud Optical Measurement (CAPCOM) packages available from the OpenCLASTR (Center for Climate System Research - CCSR – University of Tokyo).

Chapter 5 consists of two main parts. In the first part the method developed for the aerosol characterization is presented whereas the method for cloud characterization is presented in the second part. The aerosol characterization is derived from the comparison between GOME spectral reflectance measurements with the corresponding simulated spectral reflectances contained in Look-Up Tables (LUTs). LUTs are derived for different aerosol climatological models (Dubovik et al. 2002a), and refined through the variation of some of the size distribution parameters (fine mode modal radius and fine mode percentage density of particles), the imaginary part of the refractive index in two spectral regions and the aerosol optical thickness. The aerosol characterization that best fits the measurements is considered the derived aerosol model. The aerosol optical quantities (single scattering albedo, phase function and extinction coefficient) are obtained from Mie calculations considering spherical aerosol shapes. These quantities are used to derive the aerosol optical thickness from GEO satellite measurements avoiding the use of literature aerosol models. Finally, the optical thickness at the GEO spatial-temporal scale together with the aerosol optical quantities characterizing a certain aerosol event are applied to estimate the direct SW aerosol radiative forcing at the Top Of the Atmosphere (TOA), surface, and of the entire atmosphere. In addition, the physical assumptions made in the radiative transfer calculations, as well as the methodology, are tested via a sensitivity analysis, considering also instrumental errors in order to identify significant parameters that most affect the quantities to be derived. The second part of Chapter 5 presents the method developed for cloud characterization, which is based on satellite multi-spectral measurements used in combination with radiative transfer calculations to retrieve the cloud optical thickness, droplet effective radius and cloud top temperature. The retrieval procedure is applied to strong aerosol events from intense biomass burning aerosol transports that occurred in Southern Africa and Portugal in summer 2000 and 2003, respectively, in order to investigate possible alterations of the cloud properties.

Chapter 6 is devoted to the presentation of the results obtained from the application of the methodologies developed, and comparisons with independent results. In the first part of the chapter, the retrievals of the aerosol optical quantities are checked against retrievals from Sun and sky radiance measurements from the ground based AEROSOL ROBOTIC NETWORK (AERONET) (Holben et al. 1998) and from an intensive field measurement campaign (Kim et al. 2004). One of the most important climate-relevant aerosol quantities, the single scattering albedo, derived from the GOME-based method presents uncertainties lower than 0.04. All the corresponding single scattering albedo values obtained from AERONET are within this error. Furthermore, the retrieved aerosol optical thickness values (another climate-relevant aerosol quantity) are compared with the independent space-time co-located measurements from the AERONET, as well as to the satellite aerosol official products of POLDER and MODIS. A first estimate of the aerosol optical thickness accuracy ( $\Delta\tau^a$ ) derived from comparisons with AERONET data leads to  $\Delta\tau^a = \pm 0.02 \pm 0.22\tau^a$  when all optical thickness values are retained or to  $\Delta\tau^a = \pm 0.02 \pm 0.16\tau^a$  for aerosol transport events ( $\tau^a > 0.4$ ). The upwelling flux at the TOA was computed via radiative transfer calculations and used to estimate the TOA DSWARF; a comparison with space-time co-located measurements from the Clouds and the Earth's Radiant Energy System (CERES) TOA flux product was also done. It was found that more than 90% of the calculated values differ from CERES fluxes for less than  $\pm 15\%$ . The second part of Chapter 6 presents the retrievals of the cloud properties, as well as the comparisons with independent results. The comparisons between the retrieved cloud parameters (droplet effective radius, cloud optical thickness and top temperature) and MODIS cloud products have been carried out and shown that the agreement is generally better than  $\pm 25\%$  (error reported for the MODIS cloud product by King et al. 1998). Moreover, comparisons with in situ measurements of the droplet effective radius, liquid water content, and cloud top height, obtained from the Southern African Fire-Atmosphere Research Initiative 2000 (SAFARI 2000) (<http://mercury.ornl.gov/safari2k/>) field campaign are presented, in the attempt to improve the understanding of the interactions between clouds and aerosol.

Finally, chapter 7 presents the conclusions arising from this work, as well as a brief discussion on the possible work to be developed in future investigations.



## Chapter 2

# Radiative transfer in the atmosphere

### 2.1 Introduction

This chapter deals with the propagation of electromagnetic radiation in the atmosphere and its interaction with the Earth's surface and atmospheric constituents, which are responsible for the absorption, emission and scattering of radiation in the atmosphere. The radiative transfer equation presented is limited to the complexity required by the present work, considering that the maximum generality possible in the mathematical formalism would be out of the scope here.

An electromagnetic radiation wave is characterized by electric and magnetic vectors that form an orthogonal set with the direction of propagation of the wave. A light beam consists of many electromagnetic waves propagating. For natural or unpolarized light, as it is the light emitted from the sun, there is no preferred direction and the waves propagate randomly, therefore there is no change in the beam intensity. However, after entering the atmosphere and interacting with molecules and particles through the scattering process, generally the electric field starts oscillating as it propagates in some preferred direction that defines the direction of polarization and sunlight becomes then partially polarized. However the state of polarization of the radiation is not considered in the radiative transfer equation used in the present work, since no polarization measurements are used.

The plane-parallel approximation is adopted, which considers an atmosphere stratified in infinite parallel planes where the physical properties remain invariant over a plane. This constitutes a good approximation in the case of an atmosphere where the vertical variations of the physical properties are much more rapid than the horizontal variations. It is applied in the present study since the satellite measurements used are characterized only by nadir viewing geometry. The approximation, for example, would be unfeasible in the case of limb observations since the plane-parallel approximation neglects the Earth's sphericity.

The present chapter includes also a description of the simplifications that the radiative transfer equation may suffer due to the spectral region considered. In addition, the physical properties of aerosols and clouds, relevant in the radiative processes, are described. Finally, also some of the applications of radiative transfer to remote sensing of the atmosphere are discussed.

## 2.2 The radiative transfer equation: approximation for plane-parallel atmospheres with no polarization effects

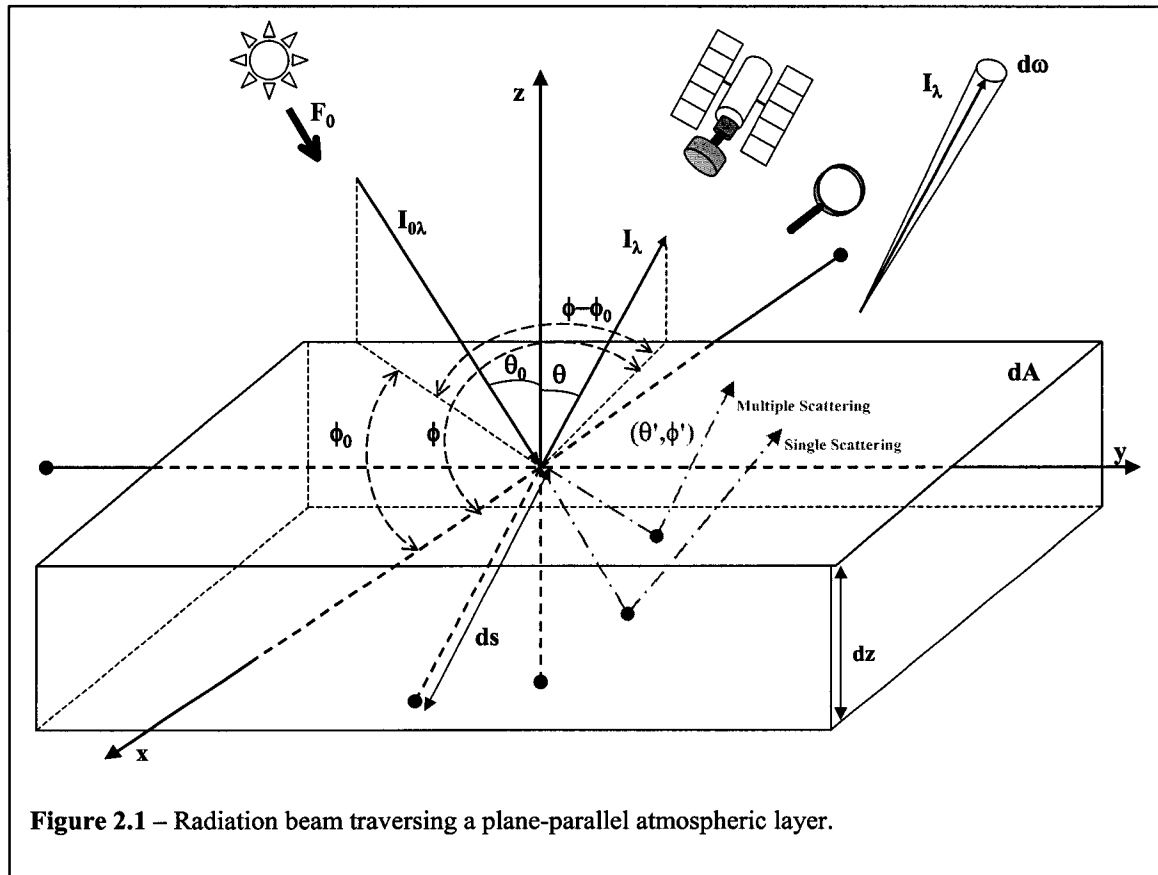


Figure 2.1 – Radiation beam traversing a plane-parallel atmospheric layer.

Let  $F_0$  be the solar flux density at the top of the atmosphere (TOA) incident on a plane perpendicular to the solar beam.  $I_{0\lambda}$  is the TOA incident solar monochromatic radiance at the wavelength  $\lambda$  that is transported across the element of area  $dA$ , traveling



through a thickness  $ds$ , and in directions confined to an element of solid angle  $d\omega$ .  $\theta_0$  is the angle that the incident radiation beam  $I_{0,\lambda}$  forms with the outward normal to  $dA$  (solar zenith angle) and  $\phi_0$  the angle between the horizontal direction of the incident radiation beam and the reference direction considered in Figure 2.1 as being the south (solar azimuth angle).  $\theta$  is the angle that the emerging radiation beam ( $I_\lambda$ ) forms with the outward normal to  $dA$  and  $\phi$  the angle between the horizontal direction of the emerging radiation beam and the reference direction south. If the emerging radiation beam is the one sensed by the satellite, the angles can be called respectively satellite zenith and satellite azimuth angles. The difference between both azimuth angles ( $\phi - \phi_0$ ) is commonly referred to as the relative azimuth angle, defined as the angle between the horizontal directions of the incident and emergent radiation beams.

The difference  $dI$  between the incident and emerging radiance is due to the interactions with the medium (atmosphere). On one hand there is a reduction in the radiance due to absorption and single scattering of radiation by atmospheric constituents as aerosols, clouds and gases, but on the other hand the radiance is increased due to the contributions from emission and radiation redirected from all other directions by the scattering process (multiple scattering) into the emerging radiation beam. Since the differential solid angle  $d\omega$  relates with the zenithal ( $\theta$ ) and azimuthal angles ( $\phi$ ) as follows (Figure 2.1):

$$d\omega = \sin \theta \cdot d\theta \cdot d\phi \quad (2.1)$$

the change in the radiance beam upon passing through the infinitesimal layer  $ds$  may be written as:

$$dI_\lambda(s; \theta, \phi) = -k_\lambda^e \cdot \rho \cdot I_\lambda(s; \theta, \phi) \cdot ds + J_\lambda(s; \theta, \phi) \cdot k_\lambda^e \cdot \rho \cdot ds \quad (2.2)$$

where  $k_\lambda^e$  is the mass extinction cross section of the atmospheric layer at the wavelength  $\lambda$  in units of area per unit mass and  $\rho$  is the density of the atmospheric layer in units of mass per unit volume.  $J_\lambda$  is the source function at the wavelength  $\lambda$ , which represents the

contributions of emission, single scattering and multiple scattering to the increase of the emergent radiance beam, in units of energy per unit time, solid angle and wavelength. Dividing all members of equation (2.2) by the mass extinction cross section and rearranging it yields:

$$\frac{dI_{\lambda}(s;\theta,\phi)}{k_{\lambda}^e \cdot \rho \cdot ds} = -I_{\lambda}(s;\theta,\phi) + J_{\lambda}(s;\theta,\phi) \quad (2.3)$$

The term  $-I_{\lambda}$  is a sink function and represents the attenuated radiance caused by the absorption and single scattering processes.

Since a plane-parallel atmosphere is assumed, it is convenient to rewrite equation 2.3 in terms of the altitude variable  $z$  normal to the plane of stratification, instead of the slant path  $s$ , where  $dz = ds \cdot \cos\theta$  and  $\cos\theta$  is represented by  $\mu$ :

$$\mu \frac{dI_{\lambda}(z;\mu,\phi)}{k_{\lambda}^e(z) \cdot \rho \cdot dz} = -I_{\lambda}(z;\mu,\phi) + J_{\lambda}(z;\mu,\phi) \quad (2.4)$$

The normal optical thickness of the atmosphere, measured from the TOA ( $z=0$ ) downward, is defined as:

$$\tau_{\lambda} = \int_{z=0}^{\infty} k_{\lambda}^e(z) \cdot \rho \cdot dz \quad (2.5)$$

or

$$\tau_{\lambda} = \int_{z=0}^{\infty} \beta_{\lambda}^e(z) \cdot dz \quad (2.6)$$

$\beta_{\lambda}^e$  is the volume extinction coefficient expressed in units of per length. Introducing the normal optical thickness definition into equation 2.4 it becomes:

$$\mu \frac{dI_{\lambda}(\tau;\mu,\phi)}{d\tau} = I_{\lambda}(\tau;\mu,\phi) - J_{\lambda}(\tau;\mu,\phi) \quad (2.7)$$

which constitutes the basic equation for the radiative transfer in plane-parallel atmospheres. Considering that the atmosphere is bounded at the bottom with  $\tau = \tau_1$  and at the top with  $\tau = 0$ , and that the downward direction is negative ( $\mu < 0$ ), it follows that the formal solution of equation 2.7 is:

$$I_\lambda(\tau; -\mu, \phi) = I_\lambda(0; -\mu, \phi) e^{-\frac{\tau}{\mu}} + \int_0^\tau J_\lambda(\tau'; -\mu, \phi) e^{-\frac{(\tau-\tau')}{\mu}} \frac{d\tau'}{\mu} \quad 1 \geq \mu > 0 \quad (2.8)$$

and

$$I_\lambda(\tau; +\mu, \phi) = I_\lambda(\tau_1; +\mu, \phi) e^{-\frac{(\tau_1-\tau)}{\mu}} + \int_\tau^{\tau_1} J_\lambda(\tau'; +\mu, \phi) e^{-\frac{(\tau'-\tau)}{\mu}} \frac{d\tau'}{\mu} \quad 1 \geq \mu > 0 \quad (2.9)$$

representing respectively the downward and upward monochromatic diffuse intensities at the atmospheric layer  $\tau$ . To obtain both intensities at the bottom and top of the atmosphere, the normal optical thickness  $\tau$  is substituted respectively by  $\tau = \tau_1$  and  $\tau = 0$ . If it is assumed that there is no diffuse / emitted downward radiation at the TOA ( $I_\lambda(0; -\mu, \phi) = 0$ ), the monochromatic diffuse intensity is at the bottom:

$$I_\lambda(\tau_1; -\mu, \phi) = \int_0^{\tau_1} J_\lambda(\tau'; -\mu, \phi) e^{-\frac{(\tau_1-\tau')}{\mu}} \frac{d\tau'}{\mu} \quad (2.10)$$

and at the TOA

$$I_\lambda(0; +\mu, \phi) = I_\lambda(\tau_1; +\mu, \phi) e^{-\frac{\tau_1}{\mu}} + \int_0^{\tau_1} J_\lambda(\tau'; +\mu, \phi) e^{-\frac{\tau'}{\mu}} \frac{d\tau'}{\mu} \quad (2.11)$$

where the first term of equation 2.11 represents the upward radiation at the surface (i.e. reflection / emission from the surface) attenuated by the atmosphere and the integral term represents, in both equations, the internal atmospheric contributions.

Equation 2.10 does not account for the direct solar radiation  $I_{\lambda}^{dir}$ , which must be added separately. The downward direct solar radiance reaching the surface obeys the Beer-Bouguer-Lambert law, which states that there is an exponential dependence between the radiation transmitted through a homogeneous medium and the optical thickness of the medium ( $\tau = \tau_1$ ), and is given by:

$$I_{\lambda}^{dir}(\tau_1; -\mu, \phi) = I_{0\lambda} \cdot e^{-\frac{\tau_1}{\mu_0}} \quad (2.12a)$$

or

$$I_{\lambda}^{dir}(\tau_1; -\mu, \phi) = F_{0\lambda} \cdot e^{-\frac{\tau_1}{\mu_0}} \cdot \delta(\mu - \mu_0) \cdot \delta(\phi - \phi_0) \quad (2.12b)$$

where  $F_{0\lambda}$  is the incident monochromatic solar flux density on a plane perpendicular to the incident beam at the TOA,  $\mu_0$  the cosine of the solar zenith angle and  $\delta(\mu - \mu_0)$  represents the Dirac's  $\delta$  function ( $\delta(\mu - \mu_0) = 1$  if  $\mu = \mu_0$  else  $\delta(\mu - \mu_0) = 0$ ). Equation 2.12b implies that the incident solar radiance on the top of the scattering layer (for example at the TOA where  $\tau = 0$ ) can be approximated as monodirectional in the form  $I_{0\lambda} = F_{0\lambda} \cdot \delta(\mu - \mu_0) \cdot \delta(\phi - \phi_0)$ . If the direct solar radiance is considered at the level  $\tau = \tau_1$ , the exponential attenuation ( $e^{-\frac{\tau_1}{\mu_0}}$ ) has to be considered.

The total downward monochromatic intensity that gets to the surface is then given by the sum of equations 2.10 and 2.12b:

$$I_{\lambda}(\tau_1; -\mu, \phi) = F_{0\lambda} \cdot e^{-\frac{\tau_1}{\mu_0}} \cdot \delta(\mu - \mu_0) \cdot \delta(\phi - \phi_0) + \int_0^{\tau_1} J_{\lambda}(\tau'; -\mu, \phi) \cdot e^{-\frac{(\tau_1 - \tau')}{\mu}} \frac{d\tau'}{\mu} \quad (2.13)$$

The source function  $J_{\lambda}$  that accounts for the emission and scattering physical processes, is given by:

$$\begin{aligned}
J_\lambda(\tau; \mu, \phi) = & (1 - \varpi_\lambda) B_\lambda(T) + \frac{\varpi_\lambda}{4\pi} F_{0\lambda} P_\lambda(\mu, \phi; -\mu_0, \phi_0) e^{-\frac{\tau}{\mu_0}} \\
& + \frac{\varpi_\lambda}{4\pi} \int_0^1 \int_{-1}^{2\pi} I_\lambda(\tau; \mu', \phi') P_\lambda(\mu, \phi; \mu', \phi') d\mu' d\phi'
\end{aligned} \tag{2.14}$$

where  $B_\lambda(T)$  is the Planck function that relates the emitted monochromatic intensity with the wavelength and the absolute temperature of the emitting substance (Earth's surface or atmosphere). The second term represents the diffuse intensity scattered out of the incident direct solar flux density ( $F_{0\lambda}$ ) coming from the  $(-\mu_0, \phi_0)$  direction into the emerging direction  $(-\mu, \phi)$ , due to single scattering. The third term respects the multiple scattering processes constituted by the diffuse intensity that suffered the scattering process more than once, coming from the  $(\mu', \phi')$  direction into the emerging direction  $(\mu, \phi)$  (see Figure 2.1).  $P_\lambda(\mu, \phi; \mu', \phi')$  is the non-dimensional scattering phase function and represents the appropriate radiation stream coming from the direction  $(\mu', \phi')$  into the direction  $(\mu, \phi)$ , thus integrating over the entire solid angle  $(d\mu' d\phi')$ , gives all possible multiple scattered radiant energy contributions from  $d\mu' d\phi'$  to  $d\mu d\phi$ .  $\varpi_\lambda$  is the single scattering albedo that represents the fraction of radiation scattered with respect to extinction (further detail on these two radiative properties can be found in the next section).

The solar and terrestrial radiation spectra are generally considered separated at the wavelength of 4.0  $\mu\text{m}$ , with a small overlapping in the surrounding spectral regions. This separation gives the possibility of treating the radiative transfer of solar radiation independently of terrestrial (thermal IR) radiation since the dominant physical processes resulting from the interaction with the atmospheric constituents (gases and aerosols) differ in the two spectral regions. The 3.7  $\mu\text{m}$  window used here for cloud study purposes is one exception since it is located in the overlapping spectral region. In this case, both contributions from solar and terrestrial radiation must be accounted for during daytime.

The next two sections deal with the transfer of solar and thermal IR radiation in the atmosphere, respectively, illustrating the possible simplifications that the radiative transfer equation may suffer in each of the cases.

## 2.3 The radiative transfer equation for the diffuse solar radiation

In the solar spectral region (wavelengths lower than 3.5  $\mu\text{m}$ ) the emission of radiation  $B_\lambda(T)$  can be in good approximation neglected, being the scattering of radiation (in the source function defined in equation 2.14) the dominant physical process. In this case, the source function becomes:

$$J_\lambda(\tau; \mu, \phi) = \frac{\varpi_\lambda}{4\pi} \cdot F_{0\lambda} \cdot P_\lambda(\mu, \phi; -\mu_0, \phi_0) \cdot e^{-\frac{\tau}{\mu_0}} + \frac{\varpi_\lambda}{4\pi} \int_0^1 \int_{-1}^1 I_\lambda(\tau; \mu', \phi') \cdot P_\lambda(\mu, \phi; \mu', \phi') \cdot d\mu' \cdot d\phi' \quad (2.15)$$

The source function written in this way accounts for the single and multiple scattering of the solar radiation. The single scattering albedo can be defined as the ratio of the volume scattering coefficient to the volume extinction coefficient (scattering plus absorption), providing the percentage of radiation that is scattered in a single scattering event:

$$\varpi_\lambda = \frac{\beta_\lambda^s}{\beta_\lambda^e} \quad (2.16)$$

where the volume extinction coefficient is given by the sum of the volume scattering and absorption coefficients:

$$\beta_\lambda^e = \beta_\lambda^s + \beta_\lambda^a \quad (2.17)$$

The single scattering albedo is thus related to the fraction of radiation that is absorbed by the atmospheric constituents, and it ranges from zero (nonscattering atmosphere where  $\beta_\lambda^s = 0$ ) to one (pure scattering atmosphere where  $\beta_\lambda^e = \beta_\lambda^s$ ), also called the conservative case when no absorption would occur. However, these extreme cases are never reached in the atmosphere but simply used sometimes as an approximation. This parameter is one of the most important climate-relevant aerosol quantities.

The scattering phase function or simply phase function  $P_\lambda(\mu, \phi; \mu', \phi')$  that represents the angular distribution of the scattered radiation depends on the properties of the scattering particles but not on their number. The simplest case is to consider isotropic scattering,  $P_\lambda(\mu, \phi; \mu', \phi') = 1$ , which is however a very rough approximation not suitable for aerosol and cloudy atmospheres. In the case of molecular scattering (Rayleigh scattering), the phase function is given by:

$$P_\lambda(\Theta) = \frac{3}{4}(1 + \cos^2 \Theta) \quad (2.18)$$

where  $\Theta$  is the angle between the directions of the incident and scattered radiation, known as the scattering angle. The phase function can also be experimentally obtained measuring over a wide range of angles the scattered radiation by a small volume element (to avoid multiple scattering). These measurements are then fitted using a mathematical function.

For aerosols and clouds, the non-dimensional scattering phase function  $P_\lambda(\Theta)$  as well as the volume extinction and scattering coefficients  $(\beta_\lambda^e, \beta_\lambda^s)$ , can be obtained from Mie theory if the physical and chemical characteristics of the scattering particles as size, shape and composition are known. In many applications, Mie theory is used considering homogeneous spherical particles, as in the present case. The aerosol scattering phase function  $P_\lambda(\Theta)$  is another climate-relevant quantity, together with the single scattering albedo  $\omega_\lambda$ . The refractive index  $m_\lambda$  is a key property, which is related to the chemical composition of the scattering particles. If these particles also absorb radiation, the imaginary part of the refractive index is non zero ( $m_{i\lambda} \neq 0$ ),  $m_{r\lambda}$  is the real part and the refractive index is given by:

$$m_\lambda = m_{r\lambda} - im_{i\lambda} \quad (2.19)$$

The imaginary part of the refractive index  $m_{i\lambda}$  relates with the volume absorption coefficient in the following way:

$$m_{i\lambda} = \frac{\lambda \cdot \beta_{\lambda}^a}{4\pi} \quad (2.20)$$

A description of Mie theory is out of the scope here and a detailed discussion may be found for example in Liou (1980). Therefore, only the equations describing the resulting physical properties of a homogeneous spherical particle, relevant for aerosol and cloud radiative studies, are presented. The extinction cross section ( $\sigma_{\lambda}^e$ ), expressed in units of area, is given by:

$$\sigma_{\lambda}^e(r, m) = \pi \cdot r^2 \cdot Q_{\lambda}^e(r, m) \quad (2.21)$$

where  $r$  is the radius of the sphere and  $Q_{\lambda}^e$  the Mie extinction efficiency defined as:

$$Q_{\lambda}^e(r, m) = \frac{2}{\chi^2} \sum_{n=1}^{\infty} (2n+1) \text{Re}(a_n + b_n) \quad (2.22)$$

with  $\text{Re}$  meaning the real part and  $a_n$  and  $b_n$  being the Mie coefficients corresponding respectively to magnetic and electric oscillations, respectively. They depend on the refractive index, derived from the boundary conditions at the particle surface.  $\chi$  is the Mie size parameter, given by:

$$\chi = \frac{2 \cdot \pi \cdot r}{\lambda} \quad (2.23)$$

Similarly, the scattering cross section can be defined as:

$$\sigma_{\lambda}^s(r, m) = \pi \cdot r^2 \cdot Q_{\lambda}^s(r, m) \quad (2.24)$$

with the Mie scattering efficiency given by:



$$Q_{\lambda}^s(r, m) = \frac{2}{\chi^2} \sum_{n=1}^{\infty} (2n+1) (|a_n|^2 + |b_n|^2) \quad (2.25)$$

Note that  $\sigma_{\lambda}^{s/e}(r, m) = k_{\lambda}^{s/e} \times m$ , where  $m$  is the aerosol mass content and  $k_{\lambda}^{s/e}$  the scattering / extinction cross section at the wavelength  $\lambda$ . The absorption cross section and the Mie absorption efficiency can then be obtained from the following relations:

$$\sigma_{\lambda}^a(r, m) = \sigma_{\lambda}^e(r, m) - \sigma_{\lambda}^s(r, m) \quad (2.26)$$

$$Q_{\lambda}^a(r, m) = Q_{\lambda}^e(r, m) - Q_{\lambda}^s(r, m) \quad (2.27)$$

The phase function  $P_{\lambda}(r, m, \Theta)$  is obtained from Mie theory as being:

$$P_{\lambda}(r, m, \Theta) = \frac{2\pi.r^2}{\chi^2.\sigma_{\lambda}^s(r, m)} (|S_1|^2 + |S_2|^2) \quad (2.28)$$

$S_1(\chi, m, \Theta)$  and  $S_2(\chi, m, \Theta)$  are complex functions defined from the Maxwell's equations, related to the amplitude of the scattered radiation perpendicular and parallel to the scattering plane, respectively.  $\chi$  is the Mie size parameter and  $\sigma_{\lambda}^s(r, m)$  the scattering cross section, defined in equations 2.23 and 2.24, respectively.

The phase function  $P_{\lambda}(r, m, \Theta)$  is usually normalized, obeying the following condition:

$$\int_0^{2\pi} \int_0^{\pi} P_{\lambda}(r, m, \Theta) \sin \Theta . d\Theta . d\phi = 4\pi \quad (2.29)$$

From spherical geometry, the cosine of the scattering angle can be expressed in terms of the incident and emergent directions:

$$\cos \Theta = \cos \theta . \cos \theta' + \sin \theta . \sin \theta' \cos(\phi' - \phi) \quad (2.30)$$

All the results from Mie theory presented so far refer to a single homogeneous sphere. Results are now extended to a sample of particles that can be aerosols or clouds, in order to derive equations that have practical application in atmospheric studies. Assuming that the scattering particles are sufficiently far from each other compared to the wavelength of the incident radiation it is possible to study the scattering process of one particle without referring to the others and consequently it is possible to sum the scattered intensities of the individual particles. This assumption is known as independent scattering and in the context the radiative properties can be now derived for a sample of homogenous spherical particles with radii between  $R_{\min}$  and  $R_{\max}$ , using the size distribution concept. Consider a sample of particles whose size is described by the particle size distribution function  $n(r).dr$  that represents the number of particles per unit volume with radii between  $r$  and  $r + dr$ , expressed in particles per unit volume. One common way of representing the size distribution of aerosol and cloud particles is using a log-normal distribution function:

$$n(r) = \frac{N}{\sqrt{2\pi.r.\log\sigma}} \exp\left[-\frac{1}{2}\left(\frac{\log r - \log r_M}{\log\sigma}\right)^2\right] \quad (2.31)$$

The adjustable parameters of the distribution function are the mode radius  $r_M$  and the geometric standard deviation  $\sigma$ . When the size of particles ranges from  $R_{\min}$  to  $R_{\max}$ ,  $N$  is

given by  $\int_{R_{\min}}^{R_{\max}} n(r).dr$  and denotes the total number concentration expressed in particles per

unit volume. The log-normal size distribution is widely used in atmospheric aerosol studies, because it often provides a good fit, approximating well the ambient aerosol size distributions. Besides, the physical interpretability of its parameters is a strong advantage of this function. In addition, the logarithmic representation and the possibility of associating several log-normal functions to build multimodal size distributions are very convenient characteristics of this distribution type to deal with the wide atmospheric aerosol size range (distributed from about 1 nm to 100  $\mu\text{m}$ , including nonprecipitating clouds).

It is useful sometimes to use the effective radius  $r_{eff}$ , the ratio of the total volume to the total surface area of the particles, and its associated effective variance  $\nu_{eff}$ , which can be expressed in terms of the size distribution parameters, respectively as:

$$r_{eff} = \frac{\int_0^{\infty} r^3 \cdot n(r) \cdot dr}{\int_0^{\infty} r^2 \cdot n(r) \cdot dr} \quad (2.32)$$

and

$$\nu_{eff} = \frac{\int_0^{\infty} (r - r_{eff})^2 \cdot r^2 \cdot n(r) \cdot dr}{r_{eff}^2 \cdot \int_0^{\infty} r^2 \cdot n(r) \cdot dr} \quad (2.33)$$

For the particular case of water clouds, the liquid water path (LWP) can be obtained from the definition of vertically integrated liquid water content (LWC), for spherical particles, as:

$$LWP = \int_{z_1}^{z_2} LWC \cdot dz \quad (2.34)$$

and

$$LWC = \frac{4\pi}{3} \rho_l \int_0^{\infty} r^3 \cdot n(r) \cdot dr \quad (2.35)$$

In addition, the effective radius can be related with the  $LWP$  as:

$$LWP = \frac{2}{3} \cdot \tau_{\lambda} \cdot r_{eff} \quad (2.36)$$

For the particular case of clouds formed by ice crystals, the ice water content is given by:

$$IWC = \int_0^{\infty} V \cdot \rho_i \cdot n(L) \cdot dL \quad (2.37)$$

where  $V$  is the volume of an ice crystal,  $\rho_i$  is the ice density and  $n(L)$  the ice crystal size distribution being  $L$  the major dimension. The ice water path ( $IWP$ ) is then obtained, similarly to the  $LWP$ , from  $\int_{z_1}^{z_2} IWC \cdot dz$ .

As to the optical properties of a sample of particles, the volume extinction and scattering coefficients are given by:

$$\beta_{\lambda}^e(m) = \int_{R_{\min}}^{R_{\max}} \pi \cdot r^2 \cdot Q_{\lambda}^e(r, m) \cdot n(r) \cdot dr = \int_{R_{\min}}^{R_{\max}} \sigma_{\lambda}^e(r, m) \cdot n(r) \cdot dr \quad (2.38)$$

$$\beta_{\lambda}^s(m) = \int_{R_{\min}}^{R_{\max}} \pi \cdot r^2 \cdot Q_{\lambda}^s(r, m) \cdot n(r) \cdot dr = \int_{R_{\min}}^{R_{\max}} \sigma_{\lambda}^s(r, m) \cdot n(r) \cdot dr \quad (2.39)$$

and analogously the volume absorption coefficient:

$$\beta_{\lambda}^a(m) = \int_{R_{\min}}^{R_{\max}} \pi \cdot r^2 \cdot Q_{\lambda}^a(r, m) \cdot n(r) \cdot dr = \int_{R_{\min}}^{R_{\max}} \sigma_{\lambda}^a(r, m) \cdot n(r) \cdot dr \quad (2.40)$$

Finally, the phase function of the sample of particles described by the particle size distribution function  $n(r)$ , may be expressed by:

$$P_{\lambda}(m, \Theta) = \int_{R_{\min}}^{R_{\max}} \frac{\lambda^2}{2\pi \cdot \sigma_{\lambda}^s(r, m)} \cdot (|S_1|^2 + |S_2|^2) \cdot n(r) \cdot dr \quad (2.41)$$

Another radiative parameter sometimes used to characterize the scattering properties of particles is the asymmetry parameter ( $g_\lambda$ ) of the phase function, an average cosine of the scattering angle weighted by the phase function, defined in the following equation:

$$g_\lambda = \frac{\int_{-1}^1 \cos \Theta \cdot P_\lambda(m, \Theta) \cdot d \cos \Theta}{\int_{-1}^1 P_\lambda(m, \Theta) \cdot d \cos \Theta} \quad (2.42)$$

The spectral variation of the aerosol optical thickness (equation 2.6) is sometimes approximated by the Ångström power law:

$$\tau_\lambda = \beta \cdot \lambda^{-\alpha} \quad (2.43)$$

Where  $\beta$  is the Ångström turbidity coefficient and  $\alpha$  the Ångström exponent, related to the particle size ( $\alpha$  decreases when the particle size increases). The Ångström exponent can be obtained from the aerosol optical thickness values at two different wavelengths ( $\lambda_1$  and  $\lambda_2$ ):

$$\alpha = \frac{\log\left(\frac{\tau_1}{\tau_2}\right)}{\log\left(\frac{\lambda_1}{\lambda_2}\right)} \quad (2.44)$$

### 2.3.1 Computational methods in solar radiative transfer

One of the computational methods for the numerical solution of the radiative transfer equation for downward (equation 2.8) and upward radiation (equation 2.9), when the source function is given by equation 2.15, is the Successive Orders of Scattering (SOS). First of all the boundary conditions are fixed, considering that there is no diffuse downward and upward radiation at the top and bottom of the finite atmosphere:



$$I_{\lambda}(0; -\mu, \phi) = 0 \quad (2.45)$$

$$I_{\lambda}(\tau_1; +\mu, \phi) = 0 \quad (2.46)$$

Considering only the primary scattering, i.e. radiation scattered only once, the source function given by equation 2.15 becomes:

$$J_{\lambda}(\tau; \mu, \phi) = \frac{\varpi_{\lambda}}{4\pi} \cdot F_{0\lambda} \cdot P_{\lambda}(\mu, \phi; -\mu_0, \phi_0) \cdot e^{-\frac{\tau}{\mu_0}} \quad (2.47)$$

It follows that the downward (equation 2.8) and upward (equation 2.9) intensities, respectively at the bottom and top of a finite atmospheric layer  $\tau$  are:

$$I_{\lambda}^1(\tau; -\mu, \phi) = \frac{1}{\mu} \int_0^{\tau_1} \frac{\varpi_{\lambda}}{4\pi} \cdot F_{0\lambda} \cdot P_{\lambda}(-\mu, \phi; -\mu_0, \phi_0) \cdot e^{-\frac{\tau'}{\mu_0}} \cdot e^{-\frac{(\tau-\tau')}{\mu}} \cdot d\tau' \quad (2.48)$$

$$I_{\lambda}^1(\tau; +\mu, \phi) = \frac{1}{\mu} \int_0^{\tau_1} \frac{\varpi_{\lambda}}{4\pi} \cdot F_{0\lambda} \cdot P_{\lambda}(+\mu, \phi; -\mu_0, \phi_0) \cdot e^{-\frac{\tau'}{\mu_0}} \cdot e^{-\frac{(\tau'-\tau)}{\mu}} \cdot d\tau' \quad (2.49)$$

The superscript 1 in  $I_{\lambda}^1$  denotes the first order of scattering (radiation scattered only once). Assuming an homogeneous atmospheric layer,  $\varpi_{\lambda}$  and  $P_{\lambda}$  do not depend on  $\tau_{\lambda}$  and the integral in the last two equations can be analytically solved yielding the transmitted and reflected intensities for the finite atmospheric layer bounded at the bottom by  $\tau = \tau_1$  and at the top by  $\tau = 0$ :

$$I_{\lambda}^1(\tau_1; -\mu, \phi) = \begin{cases} \frac{\varpi_{\lambda} \mu_0 F_{0_{\lambda}}}{4(\mu - \mu_0)} P(-\mu, \phi; -\mu_0, \phi_0) \times \begin{pmatrix} -\frac{\tau_1}{\mu} & -\frac{\tau_1}{\mu_0} \\ e & -e \end{pmatrix} & \mu \neq \mu_0 \\ \frac{\varpi_{\lambda} \tau_1 F_{0_{\lambda}}}{4 \cdot \mu_0} P(-\mu, \phi; -\mu_0, \phi_0) \times e^{-\frac{\tau_1}{\mu_0}} & \mu = \mu_0 \end{cases} \quad (2.50)$$

$$I_{\lambda}^1(0; +\mu, \phi) = \frac{\varpi \mu_0 F_{0_{\lambda}}}{4(\mu + \mu_0)} P(+\mu, \phi; -\mu_0, \phi_0) \cdot \left[ 1 - e^{-\tau_1 \left( \frac{1}{\mu} + \frac{1}{\mu_0} \right)} \right] \quad (2.51)$$

The higher orders of scattering are computed individually and then summed up to obtain the total intensity. The source function and the intensities for higher orders of scattering are expressed by:

$$J_{\lambda}^n(\tau; \mu, \phi) = \frac{\varpi_{\lambda}}{4\pi} \int_0^{\tau} \int_{-1}^{+1} I_{\lambda}^{n-1}(\tau'; \mu', \phi') P_{\lambda}(\mu, \phi; \mu', \phi') d\mu' d\phi' \quad n \geq 1 \quad (2.52)$$

$$I_{\lambda}^n(\tau; -\mu, \phi) = \int_0^{\tau} J_{\lambda}^n(\tau'; -\mu, \phi) e^{-\frac{(\tau-\tau')}{\mu}} \frac{d\tau'}{\mu} \quad n \geq 1 \quad (2.53)$$

$$I_{\lambda}^n(\tau; +\mu, \phi) = \int_{\tau}^{\tau_1} J_{\lambda}^n(\tau'; +\mu, \phi) e^{-\frac{(\tau'-\tau)}{\mu}} \frac{d\tau'}{\mu} \quad n \geq 1 \quad (2.54)$$

The zero-order intensity is given by:

$$I_{\lambda}^0(\tau; \mu', \phi') = F_{0_{\lambda}} e^{-\frac{\tau}{\mu_0}} \cdot \delta(\mu - \mu_0) \cdot \delta(\phi - \phi_0) \quad (2.55)$$

where  $\delta(\mu - \mu_0)$  represents the Dirac's  $\delta$  function as already mentioned

One of the advantages of using the successive orders of scattering is given by the fact that there is a good physical understanding of the problem because the scattering process is constantly followed.

Another widely used way of solving the radiative transfer equation is the discrete-ordinates method. It was developed by Chandrasekhar (1950) for radiative transfer in planetary atmospheres and its usefulness for applications in aerosol loaded- and cloudy atmospheres is well documented by several authors (Liou 1980; Liou 1992; Lenoble 1985). The method involves the discretization of the basic radiative transfer equation presented in equation 2.7 and the expansion of the phase function in a series of Legendre polynomials, providing analytical solutions of the diffuse intensity for any optical thickness. Useful approximations can also be developed from this method for flux calculations.

## 2.4 The radiative transfer equation: thermal infrared radiation

In the infrared spectral region ( $\lambda > 4 \mu\text{m}$ ), the scattering of radiation can be in good approximation neglected, being the absorption / emission of radiation the dominant physical process. The Planck function  $B_\lambda(T)$  gives the emitted monochromatic radiance from a blackbody as a function of the wavelength and of the temperature of the emitting material considered to behave as a blackbody. In the following formulation, the monochromatic radiance has units of energy per unit time, area, solid angle and wavelength:

$$B_\lambda(T) = \frac{2hc^2}{\lambda^5 (e^{\frac{hc}{k\lambda T}} - 1)} \quad (2.56)$$

where  $h$  is the Planck constant ( $h = 6.6262 \times 10^{-34} \text{ Js}$ ),  $c$  is the velocity of light in vacuum ( $c = 2.9979 \times 10^8 \text{ ms}^{-1}$ ) and  $k$  is the Boltzmann constant ( $k = 1.3806 \times 10^{-23} \text{ JK}^{-1}$ ).

Considering a nonscattering ( $\varpi = 0_\lambda$ ) absorbing and emitting atmosphere in local thermodynamic equilibrium, the source function defined in equation 2.14 reduces to the Planck function multiplied by the monochromatic emissivity of the atmosphere ( $\varepsilon_\lambda$ )



whenever an emitting material does not behave as a blackbody. The assumption of a plane-parallel atmosphere (only the vertical variations of the physical properties are considered) implies the symmetry of absorption and emission processes with respect to the azimuth angle, therefore the source function depends only on the height coordinate and on the zenith angle (Liou 1992).

$$J_{\lambda}(\tau; \mu) = \varepsilon_{\lambda} B_{\lambda}(T) \quad (2.57)$$

Assuming that the Earth's surface and atmosphere may be considered as blackbodies in the infrared spectral region ( $\varepsilon_{\lambda} = 1$ ), the radiative transfer equation in plane-parallel atmospheres (equation 2.7) for a nonscattering medium, may then be written as:

$$\mu \frac{dI_{\lambda}(\tau; \mu)}{d\tau} = I_{\lambda}(\tau; \mu) - B_{\lambda}(T) \quad (2.58)$$

This equation is known as the equation of Schwarzschild.

The general solution of the radiative transfer equation presented in equations 2.8 and 2.9, describing the downward and upward monochromatic radiances, for an atmosphere bounded at the bottom with  $\tau = \tau_1$  and at the top with  $\tau = 0$  and considering that there is no emission at the TOA ( $B_{\lambda}(T_{(0)}) = 0$  so  $B_{\lambda}(T_{(0)})e^{-\frac{\tau}{\mu}} = 0$ ), becomes in this case:

$$I_{\lambda}(\tau; -\mu) = \int_0^{\tau} B_{\lambda}(T_{(\tau')}) e^{-\frac{(\tau-\tau')}{\mu}} \frac{d\tau'}{\mu} \quad (2.59)$$

and for the upward radiance:

$$I_{\lambda}(\tau; +\mu) = B_{\lambda}(T_{(\tau_1)}) e^{-\frac{(\tau_1-\tau)}{\mu}} + \int_{\tau}^{\tau_1} B_{\lambda}(T_{(\tau')}) e^{-\frac{(\tau'-\tau)}{\mu}} \frac{d\tau'}{\mu} \quad (2.60)$$

The first term on the right hand side of equation 2.60 represents the emission contribution of the Earth's surface attenuated by the atmosphere and the integral, in both equations (2.59 and 2.60), states the emission contributions of each of the atmospheric layers.

The monochromatic transmittance can be defined as:

$$\mathfrak{T}_\lambda(\tau/\mu) = e^{-\frac{\tau}{\mu}} \quad (2.61)$$

and

$$\frac{d\mathfrak{T}_\lambda(\tau/\mu)}{d\tau} = -\frac{1}{\mu} e^{-\frac{\tau}{\mu}} \quad (2.62)$$

Substituting the monochromatic transmittance definition into the formal solutions of the Schwarzschild's equation, the downward and upward monochromatic intensities become:

$$I_\lambda(\tau; -\mu) = \int_0^\tau B_\lambda(T_{(\tau')}) \frac{d\mathfrak{T}_\lambda[(\tau - \tau')/\mu]}{d\tau'} d\tau' \quad (2.63)$$

and

$$I_\lambda(\tau; +\mu) = B_\lambda(T_{(\tau_1)}) \mathfrak{T}_\lambda[(\tau_1 - \tau)/\mu] - \int_\tau^{\tau_1} B_\lambda(T_{(\tau')}) \frac{d\mathfrak{T}_\lambda[(\tau' - \tau)/\mu]}{d\tau'} d\tau' \quad (2.64)$$

Equation 2.64 constitutes an important equation for applications to satellite remote sensing in the infrared spectral region, such as surface temperature estimation, cloud top properties determination and atmospheric temperature and gaseous species soundings, depending on the selected spectral region. Introducing the definition of normal optical thickness (equation 2.5) into the monochromatic transmittance (equation 2.61), the transmittance can now be written as:

$$\mathfrak{T}_\lambda(z) = \exp \left[ -\frac{\int_0^\infty k_\lambda^e(z') \cdot \rho \cdot dz'}{\mu} \right] \quad (2.65)$$

The transmittance at a given height  $z$  is expressed in reference to the TOA. At the TOA  $z = \infty$ ,  $\tau = 0$  and at the surface  $z = 0$ ,  $\tau = \tau_1$ . The upwelling radiance at the top of the atmosphere in  $z$  coordinates can be written in the form:

$$I_{\lambda}(\infty; +\mu) = B_{\lambda}(T_{(0)})\mathfrak{T}_{\lambda}(0) + \int_{z=0}^{z=\infty} B_{\lambda}(T_{(z)}) \frac{\partial \mathfrak{T}_{\lambda}(z)}{\partial z} dz \quad (2.66)$$

The first term, which represents the spectral radiance emitted by the surface attenuated by the atmosphere is often called the boundary term; whereas the second term is the spectral radiance emitted to space by the atmosphere.  $T_{(0)}$  and  $T_{(z)}$  are the absolute temperatures at the surface ( $z = 0$ ) and at a given height ( $z$ ), respectively, and  $\frac{\partial \mathfrak{T}_{\lambda}(z)}{\partial z}$  is called the weighting function that multiplied by the Planck function yields the upwelling radiance from the height  $z$ . This equation is the basis for atmospheric vertical soundings. However, the information content of the temperature is under the integral operator, which leads to an ill-conditioned mathematical problem. Nevertheless, if the atmosphere is sensed at several wavelengths whose weighting functions  $\frac{\partial \mathfrak{T}_{\lambda}(z)}{\partial z}$  are known, as well as the surface absolute temperature  $T_{(0)}$  and the monochromatic transmittance  $\mathfrak{T}_{\lambda}(0)$ , there are a number of methods that allow for the retrieval of the Planck function values  $B_{\lambda}(T_{(z)})$  and consequently the vertical profile of the temperature (see Liou 1980 for details).

## 2.5 Radiative forcing

The circulation of the Earth-atmosphere system can be thought of as being powered by a heat engine. The solar radiation provides the fuel supply while the infrared radiation heat loss to space from the entire system is the exhaust. The distribution of sunlight with latitude, together with the conservation of angular momentum of both the atmosphere and the Earth and each of the subsystems of the climate system are responsible for the major climatic zones (Tropical, Temperate and Polar). The composition of the atmosphere and

the radiometric characteristics of the Earth's surface also play an important role in the climate of local regions such as deserts.

Globally the Earth-atmosphere system is in radiative equilibrium (the reflected and emitted radiation compensate the incoming absorbed solar radiation). Small changes in the solar or terrestrial radiation due to natural or man induced changes in the atmosphere and in the surface properties (compositions) might lead to variations in the global climate. Assuming a perturbation in the atmospheric composition or surface cover, there results a disturbance in the Earth-atmosphere net radiation balance usually referred to as radiative forcing. A positive radiative forcing for example at the TOA would imply a warming at the surface of the Earth, while a negative radiative forcing at the TOA would imply a cooling at the surface.

In radiation balance studies, it is necessary to define the total flux density ( $F^\pm$ ) in the upward or downward direction, expressed in units of energy per unit time and area:

$$F^\pm = \int_0^\infty F_\lambda^\pm d\lambda \quad (2.67)$$

The monochromatic flux density  $F_\lambda^\pm$  is obtained by integrating the monochromatic radiance  $I_\lambda$  in the zenith and azimuth directions. Since the radiative transfer equation discussed in section 2.3 only includes the diffuse radiation, the direct solar flux reaching the surface ( $F_\lambda^{dir} = \mu_0 \cdot F_{0\lambda} \cdot e^{-\frac{\tau_1}{\mu_0}}$ ) must be added to the downward diffuse solar flux, yielding at the surface:

$$F_\lambda^- = \int_0^{2\pi} \int_0^+ I_\lambda(-\mu, \phi) \cdot \mu \cdot d\mu \cdot d\phi + \mu_0 \cdot F_{0\lambda} \cdot e^{-\frac{\tau_1}{\mu_0}} \quad (2.68)$$

and the upwelling diffuse solar flux at the TOA:

$$F_\lambda^+ = \int_0^{2\pi} \int_0^+ I_\lambda(+\mu, \phi) \cdot \mu \cdot d\mu \cdot d\phi \quad (2.69)$$

The monochromatic total atmospheric transmission ( $t_\lambda$ ) and reflectance ( $\rho_\lambda$ ) (also called local or planetary albedo) are nondimensional parameters that can be obtained from the total (diffuse + direct) downward and diffuse upward monochromatic flux density definitions  $F_\lambda^-$  and  $F_\lambda^+$ , respectively, as:

$$t_\lambda(\mu_0) = \frac{F_\lambda^-}{\mu_0 \cdot F_{0\lambda}} \quad (2.70)$$

$$\rho_\lambda(\mu_0) = \frac{F_\lambda^+}{\mu_0 \cdot F_{0\lambda}} \quad (2.71)$$

Similarly, the monochromatic reflectance at the surface can be written as  $\rho_\lambda(\mu_0) = \frac{F_\lambda^{+surf}}{F_\lambda^{-surf}}$ .

The spherical or global albedo ( $S_\lambda$ ) that represents the ratio of the planetary reflected radiation to the incident radiation on the entire planet is then given by:

$$S_\lambda = 2 \int_0^1 r_\lambda(\mu_0) \cdot \mu_0 \cdot d\mu_0 \quad (2.72)$$

The radiation balance at a given level is denoted by the net radiation and can be written:

$$F^{net} = F^- - F^+ \quad (2.73)$$

The positive sign denotes once more the upward direction and the negative sign the downward direction.

It is sometimes convenient to introduce the separation between the short wave (SW) and long wave (LW) radiation:

$$F^\pm = F_{SW}^\pm + F_{LW}^\pm \quad (2.74)$$

And consequently:

$$F^{net} = F_{SW}^- - F_{SW}^+ + F_{LW}^- - F_{LW}^+ \quad (2.75)$$

Or separating also the net radiation into the SW and LW components:

$$F_{SW}^{net} = F_{SW}^- - F_{SW}^+ \quad (2.76)$$

$$F_{LW}^{net} = F_{LW}^- - F_{LW}^+ \quad (2.77)$$

The total radiative forcing ( $\Delta F$ ) at a given level, expressed in units of energy per unit time and area, is defined as:

$$\Delta F = F_{perturb}^{net} - F_{NOperturb}^{net} \quad (2.78)$$

The first term corresponds to the total net flux at a certain level of the atmosphere that suffered an external perturbation and the second term to the total atmospheric net flux at the same level that did not suffer the perturbation. For aerosol study purposes the SW radiative forcing  $\Delta F_{SW}$  is adequate since the direct effects of these particles on the radiation field are connected to their interaction with sunlight mainly through the scattering and sometimes absorption processes. Hence, the short wave radiative forcing due to an increase of the aerosol load in the atmosphere can be determined by:

$$\Delta F_{SW} = F_{SW_{perturb}}^{net} - F_{SW_{NOperturb}}^{net} \quad (2.79)$$

## 2.6 Applications of radiative transfer to atmospheric remote sensing

Radiative transfer serves as a mechanism for exchanging energy between the atmosphere and the underlying surface and between different layers of the atmosphere. The

radiation reflected/backscattered or emitted from the Earth-atmosphere system and sensed by satellite sensors is the basis for satellite remote sensing of the atmosphere.

The remote sensing methods to retrieve aerosol and cloud properties can be divided in two major steps: the detection of aerosol particles or clouds in the field of view under study; once the presence of aerosols or clouds is certain the associated physical properties can be retrieved, often making use of radiative transfer techniques. The next section give examples on the aerosol properties retrieval from satellite radiation measurements.

### 2.6.1 Remote sensing of tropospheric aerosols

Satellite remote sensing of the properties that characterize the aerosol particles present in the lower part of the atmosphere – troposphere mostly relies on observations of the scattered radiation that is sensed by the instrument onboard the satellite. The monochromatic radiance arriving to the satellite in clear-sky conditions (absence of clouds) in the visible and near infrared spectral regions, is described by equation 2.11 and the source function  $J_\lambda(\tau', \mu, \phi)$  can be written:

$$J_\lambda = J_\lambda^{aerosol} + J_\lambda^{Rayleigh} + J_\lambda^{gases} \quad (2.80)$$

The first term corresponds to the aerosol contribution, the second term to the Rayleigh scattering, and the third term to gaseous contribution. As already pointed out, the first term in equation 2.11 represents the surface contribution arriving to the satellite level. The satellite measurements must then be corrected for the surface reflection, Rayleigh scattering  $J_\lambda^{Rayleigh}$  and gaseous absorption  $J_\lambda^{gases}$  (if there is any in the spectral region considered) in order to get the aerosol radiation term  $J_\lambda^{aerosol}$ .

To estimate the surface contribution term it is necessary to have knowledge of the spectral reflectance ( $\rho_\lambda$ ) of the surface, which can be problematic over land regions especially if not homogenous, therefore land surfaces are often avoided. Many aerosol studies are confined to regions over the ocean where there is less uncertainty on the spectral reflectance values since in the visible its values are lower than 5% and in the near

infrared drop down to near zero. However, there are few situations when the ocean surface should be avoided in aerosol studies because there is an abrupt increase of the surface reflectance values, namely in Sun glint regions, observed in the point of the Sun's specular reflection and sometimes in a wider area due to the ocean surface roughness (therefore related to the wind speed) and in oceanic regions with suspended particles (for example plankton) that may alter the surface reflectance values.

The Rayleigh scattering corresponds to the contribution of the monochromatic radiance scattered by molecules and can be assessed as described by several authors (Liou 1980; Lenoble 1993). The gaseous correction (ozone, water vapour and other gases) can be simply based on climatological values or on measurements from other satellite sensors. Assuming that the satellite measurements are corrected for the surface, Rayleigh scattering and gas absorption terms, the monochromatic radiance received by the satellite due to the aerosol contribution (equation 2.11) can be written:

$$I_{\lambda}^{sat}(0;+\mu,\phi) = \int_0^{\tau_1} J_{\lambda}^{aerosol}(\tau';+\mu,\phi) e^{-\frac{\tau'}{\mu}} \frac{d\tau'}{\mu} \quad (2.81)$$

And the source function considering single and multiple scattering is given by:

$$J_{\lambda}^{aerosol}(\tau;\mu,\phi) = \frac{\omega_{\lambda}^{aerosol}}{4\pi} \cdot F_{0\lambda} \cdot P_{\lambda}^{aerosol}(\mu,\phi;-\mu_0,\phi_0) \cdot e^{-\frac{\tau^{aerosol}}{\mu_0}} + \frac{\omega_{\lambda}^{aerosol}}{4\pi} \int_0^{\tau} \int_{-1}^1 I_{\lambda}^{aerosol}(\tau';\mu',\phi') \cdot P_{\lambda}^{aerosol}(\mu,\phi;\mu',\phi') \cdot d\mu' \cdot d\phi' \quad (2.82)$$

The SOS method presented in section 2.3.1 can be applied to numerically solve equation 2.81 together with equation 2.82 and the satellite-measured radiance may be given by:

$$I_{\lambda}^{sat}(0;+\mu,\phi) = \sum_{n=1}^{\infty} I_{\lambda}^{n,aerosol}(0;+\mu,\phi) \quad (2.83)$$

The different orders of scattering ( $n$ ) are individually calculated and then summed up to obtain the total monochromatic radiance at the satellite level, due to aerosols.



Many techniques rely on the comparison between the radiance value obtained in this way and the satellite measurements (with a pre defined error interval), to retrieve aerosol properties such as the aerosol single scattering albedo  $\varpi_{\lambda}^{aerosol}$ , aerosol phase function  $P_{\lambda}^{aerosol}(\mu, \phi; -\mu_0, \phi_0)$  and aerosol optical thickness  $\tau_{\lambda}^{aerosol}$ . These are the aerosol properties relevant to climate studies. The spectral characteristics of the measurements determine the number and type of parameters that can possibly be retrieved, i.e., measurements in a single visible band may allow for the retrieval of the aerosol optical thickness, assuming that the other aerosol properties are known, whereas measurements in several narrow spectral bands (multi-spectral) distributed in the SW spectral range provide important information to retrieve also the other aerosol properties.



## Chapter 3

# Satellite passive sensors for aerosol and cloud remote sensing

### 3.1 Introduction

Remote Sensing is a compact way of defining the detection and measurement of radiation of different wavelengths emanating from distant “objects” of whatever size and composition. The material these objects are made of possesses unique radiation properties or signatures by which it can be identified and categorized by class/type, substance, and spatial distribution. In Earth and atmospheric studies, the targets are located at the Earth's surface or in the atmosphere. Properties of primary interest for Earth remote sensing are the absorption/emission spectra of atmospheric constituents and surface features. Examples of atmospheric constituents are clouds, aerosols, and gases like water vapour and ozone. Examples of surface features are vegetation, water, snow and ice, soils, and rocks. The instruments used for remote sensing may be divided in two different types - passive and active.

Passive instruments detect only radiation, which is reflected or emitted from the observed scene. Reflected sunlight is the most common external source of radiation sensed by passive instruments. Examples of passive instruments are the radiometers and spectrometers. The radiometer is an instrument that quantitatively measures the intensity of electromagnetic radiation at a certain wavelength band of the electromagnetic spectrum. Usually a radiometer is further identified by the portion of the spectrum it covers, for example, visible, infrared, or microwave. The imaging radiometer has the additional scanning capability, providing a two-dimensional array of pixels from which an image may be produced. The spectroradiometer is a type of radiometer with the capability for measuring radiation in many wavelength bands (i.e., multispectral), often bands of relatively high spectral resolution designed for the remote sensing of specific atmospheric and surface parameters. The spectrometer is an instrument that allows for the detection,

measurement and analysis of the incident electromagnetic radiation spectral content. Conventional imaging spectrometers use gratings and/or prisms to disperse the radiation for spectral discrimination.

A remote sensing instrument that transmits its own electromagnetic radiation to detect an object or to scan an area for observation and receives the reflected or backscattered radiation is called an active instrument. Examples of these are the radars (RAdio Detection And Ranging), scatterometers and lidars (LIght Detection And Ranging). A radar uses a transmitter operating at either radio or microwave frequencies to emit electromagnetic radiation and a directional antenna or receiver to measure the reflection or backscattering of radiation from distant objects. Distance to the object can be determined since electromagnetic radiation propagates at the speed of light. A scatterometer is a radar that measures the backscattering coefficient of the surface of the viewed object. Over ocean surfaces, measurements of backscattering coefficient in the microwave spectral region can be used to derive maps of surface wind speed and direction. A lidar uses a laser to transmit a light pulse and a receiver with sensitive detectors to measure the backscattered or reflected light. Distance to the object is determined by recording the time between the transmitted and backscattered pulses and using the speed of light to calculate the travelled distance. Lidars can determine the profile of aerosols, clouds, and other constituents in the atmosphere.

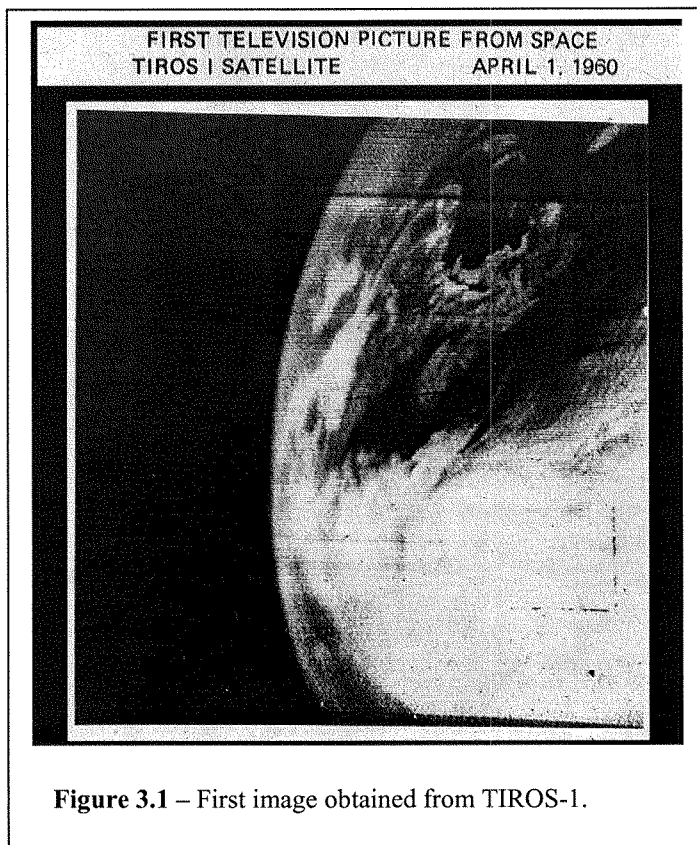
Both types of remote sensing instruments can be installed onboard satellite platforms, flying in different orbit types. The present work deals exclusively with data from passive remote sensing instruments, placed mainly into two different orbits described in the next paragraph.

The Geostationary Earth Orbit (GEO) satellites are positioned in the Earth's equatorial plane and fly at about 36000 km completing a circular orbit of the Earth every 24 hours, thus matching the Earth's rotation speed and remaining practically stationary over one point on the equator. An instrument on a geostationary satellite does not view the entire Earth and has a poor view of the Polar Regions. However, a satellite in a geostationary orbit can obtain frequent images and other data of nearly a quarter of the Earth's surface (mid-latitude and tropical regions), which constitutes an advantage for weather studies and environmental monitoring for these regions. While GEO satellites provide a continuous view of the earth disc from an apparently stationary position in space,

the instruments on Low Earth Orbit (LEO) satellites, flying at a much lower altitude (less than 2000 km above the surface of the Earth in an orbit with a period that varies between ninety minutes and two hours), provide more precise detailed measurements, although with a less frequent global coverage. Most of the LEO systems employ polar, or near-polar, orbits in order to fill the lack of observational coverage in these parts of the globe, (Polar Regions). Most satellites used for meteorological and environmental studies are placed in one of these two orbit types.

The idea of sending a satellite into space was thought of in 1687 by Sir Isaac Newton, but the actual launch took some time. The first views of the Earth from space were not obtained from satellites but from converted military rockets carrying cameras, in the early 1950s. Satellites made it into space with the launch of Sputnik-1 (LEO system) by the USSR on 4 October 1957. Sputnik-1 emitted a radio beep, but this was enough to qualify it as an orbiting satellite, and the first one in space.

The world's first satellite completely dedicated to meteorology (22nd successfully



launched satellite), a polar-orbiting satellite, was launched by the USA from Cape Canaveral on 1 April 1960. Named TIROS for Television InfraRed Observation Satellite, it demonstrated the advantage of mapping the Earth's cloud cover from satellite altitudes. It carried two television cameras, one low-resolution and one high-resolution and was in a circular polar orbit. A magnetic tape recorder for each camera was supplied for storing photographs while the satellite was out of range of the ground station network. The

video systems relayed thousands of pictures containing cloud-cover views of the Earth. Early photographs provided information concerning the structure of large-scale cloud

regimes. TIROS showed clouds banded and clustered in unexpected ways. Sightings from the surface had not prepared meteorologists for the interpretation of the cloud patterns that the view from an orbiting satellite would show (see Figure 3.1). In five years ten TIROS satellites were launched, ensuring continuity of data throughout the early years. This satellite was such an effective proof of concept giving new insights into the meteorology of the planet, observing the weather and the Earth's environment that by 1966 the USA had launched the first of a long line of operational polar weather satellites (ESSA-1). The Nimbus was another USA program with the aim of developing observation systems meeting the research and development requirements of atmospheric and Earth scientists. The Nimbus satellites, first launched in 1964, carried a number of instruments: microwave radiometers, atmospheric sounders, ozone mappers, the Coastal Zone Color Scanner (CZCS), infrared radiometers, etc. Nimbus-7, the last in the series, provided significant global data on sea-ice coverage, atmospheric temperature, atmospheric chemistry (i.e. ozone distribution), the Earth's radiation budget, and sea-surface temperature. The TOMS instrument aboard the NIMBUS-7 satellite was able to map the real extent of the phenomenon known as the Ozone hole.

In 1966 the USA launched the Applications Technology Satellite (ATS-1), the first meteorological satellite in geostationary orbit, which was in fact the next major step forward. It demonstrated the advantage of a fixed observation point relative to the Earth, enabling frequent images to be taken and used to generate moving pictures of the world's weather. This satellite series consisted of a set of six NASA multi-purpose spacecrafts launched from December 1966 to May 1974, created to explore and flight-test new technologies and techniques for communications, meteorological and navigation satellites, from GEO orbit. The major objective of the early ATS satellites was to test whether gravity would anchor the satellite in a synchronous orbit (14 000 km above the Earth), allowing it to move at the same rate the Earth is turning, thus seeming to remain stationary. Although the ATS satellites were intended mainly as test beds, they also collected and transmitted meteorological data and functioned at times as communications satellites. ATS provided the first colour images from space as well as regular cloud cover images for meteorological studies.

In 1969 the USSR launched the first of a long series of polar orbiting meteorological satellites (Meteor-I-n1). In January 1970, the first of the Improved TIROS

Operational Satellites (ITOS-1) was launched. Between December 1970 and July 1976 five ITOS satellites designated NOAA-1 through 5 were launched. NOAA-2 demonstrated the possibility of measuring the temperature of the atmosphere from space. In 1972, the effectiveness of weather satellite observations had been proven, but the study of land features was untried. The Landsat Program (originally Earth Resources Technology Satellite) was the first successful step, opening an entire new field for scientific study and practical applications: remote sensing.

In 1974 the Synchronous Meteorological Satellite (SMS-1) and one year later the Geostationary Operational Environmental Satellite (GOES-1) of the USA became the first operational geostationary satellites; in 1977 also Japan launches and operates a geostationary meteorological satellite (GMS-1). In the same year the European Space Agency (ESA) also initiated its geostationary satellite series launching Meteosat-1, with an imager that introduced the capability of observing the atmospheric water vapour. Through special efforts a complete satellite constellation of five geostationary satellites and two polar orbiters was put in place in 1978 for the First Global GARP Experiment (FGGE), GARP being the Global Atmospheric Research Programme. Thus, within 18 years of the first practical demonstration by TIROS-1, a fully operational meteorological satellite system was in place, giving routine data coverage of most of the planet. This rapid evolution of a very expensive new system was unprecedented and indicates the enormous value of these satellites to meteorology and society.

From 1978 to 1981, satellites of the TIROS-N series were launched. The N represented the next generation of operational satellites. NOAA-6 and NOAA-7 were launched during this time frame. Flight of the AVHRR (Advanced Very High Resolution Radiometer) and TIROS Operational Vertical Sounder (TOVS) started on TIROS-N, enabling atmospheric soundings of temperature and humidity globally on a routine operational basis. The first of the Advanced TIROS-N (ATN) satellites designated NOAA-8 was launched in 1983. These satellites are physically larger and have more power than their predecessors to accommodate more equipment. NOAA continues to operate the ATN series of satellites and since 1998 from NOAA-K, a new system of improved instruments was initiated. Also the geostationary systems have evolved during the years: with the launch of the Geostationary Operational Environmental Satellite (GOES-8) in 1994, the USA demonstrated a new generation of geostationary satellites capable of frequent

imagery and simultaneous atmospheric soundings. In the same year Russia launched its first Geostationary Operational Meteorological Satellite (GOMS-1). In 1997 EUMETSAT launched Meteosat-7, the last of the first Meteosat series planned to be in operation until at least the end of 2003. A new series of Meteosat satellites with improved capabilities started on 28 August 2002, when the first Meteosat Second Generation (MSG-1) was successfully launched. EUMETSAT is currently preparing the European component of a polar satellite system (EUMETSAT Polar System - EPS) of a joint European / USA program. EUMETSAT plans to assume responsibility for the "morning" (local time) orbit and the USA will continue with the "afternoon" coverage (NOAA satellites). It is planned to carry EUMETSAT instruments on the Meteorological Operational polar satellites of EUMETSAT (METOP), developed in cooperation with ESA. METOP-1 will be Europe's first polar-orbiting satellite of a series of at least three to be launched sequentially over 14 years, starting in 2005, dedicated to operational meteorology. It represents the European contribution to a new cooperative venture with the United States providing data that will be used to improve weather forecasting and monitor our climate.

In early years weather forecasting was deemed the most promising application of space-based observations, however in the last few years the concept of weather satellites have evolved to environmental satellites, providing not only essential data for weather forecasting to national weather services across the globe, but also dedicating to understanding the total Earth system and the effects of natural and human-induced changes on the global environment. New instruments on research satellites have also provided insights into future satellite systems, such that more than four decades after the first Earth images, new systems are still being designed and implemented, illustrating the continued and dynamic interest in this unique source of environmental data. The next section describes the most important present and future satellite missions for gases, aerosol and cloud studies.

### **3.2 Present and future satellite missions**

Since 40 years meteorological satellites monitor the Earth and its atmosphere from a variety of heights and perspectives. The beginning of the new millennium marks a crucial



step between the past of simple visual monitoring of weather systems and the future when new instruments will continuously gather information on the physics of the atmosphere at smaller and smaller scales. Cloud structure, precipitation, gases, aerosols are key topics together with applications such as flood monitoring, disaster management, space communication technology and much more (Levizzani 2004a, b). Table 3.1 shows the launch schedules of several satellite missions dedicated to these applications.

The ESA mission ERS-2 (Second European Remote Sensing Satellite) was launched in 1995 and it is still operating (see online at <http://earth.esa.int/ers/>). It carries onboard several instruments and among them the Global Ozone Monitoring Experiment (GOME), a nadir-scanning ultraviolet and visible spectrometer for ozone monitoring (Burrows et al. 1999). A key feature of GOME is its ability to detect chemically active atmospheric trace-gases as well as aerosol distribution. Another instrument onboard the ERS-2 satellite is the Along Track Scanning Radiometer (ATSR-2). The first ATSR instrument, ATSR-1, was launched on board the ESA mission ERS-1, in July 1991, as part of the Earth Observation Programme. The ATSR-2 provides images of the Earth in four spectral bands (1.6, 3.7, 11.0 and 12.0  $\mu\text{m}$ ) with a spatial resolution of 1.0 km. The data from these instruments is useful for scientific studies of the land surface, atmosphere, clouds, oceans, and the cryosphere.

Jan	Feb	Mar	Apr	May	Jun	Jul	Aug	Sep	Oct	Nov	Dec	Year	
ERS-2												1995	
TOMS-EP						ADEOS-1						1996	
										TRMM		1997	
												1998	
											Terra	1999	
GOES-L						NOAA-L						2000	
GOES-M												2001	
Envisat-1				Aqua		NOAA-M		MSG-1		ADEOS-2			2002
												2003	
										Aura		2004	
CloudSat		CALIPSO		PARASOL		METOP-1						2005	
Megha-Tropiques												2006	
										GPM		2007	
												2008	
EarthCARE						EGPM						2009	
												2010	

Table 3.1 – Launch schedule of several relevant satellite missions for atmospheric studies.

A mission primarily devoted to ozone studies is the Earth Probe Total Ozone Mapping Spectrometer (TOMS-EP), which provides global measurements of total column ozone on a daily basis (see online at <http://toms.gsfc.nasa.gov/>). The data from TOMS have also been increasingly used to understand the behaviour of aerosol particles within the atmosphere. TOMS is the first instrument that allows for observation of aerosols as the particles cross the land/sea boundary while discriminating between different aerosol particle types based on their size (dust tends to have larger particles than smoke) and absorbing properties in the UV (Torres et al. 1998; Hsu et al. 1999; Torres et al. 2002). The use of these data gives the possibility of observing a wide range of phenomena such as desert dust storms, forest fires and biomass burning.

The ADvanced Earth Observing Satellite 1 (ADEOS-1), launched in August 1996, was the first in a series of two scheduled joint international cooperative programs to contribute to global environmental monitoring. The objectives of ADEOS-1 were to acquire data on worldwide environmental changes such as the greenhouse effect, ozone layer depletion, tropical rain deforestation, and abnormal climatic conditions. ADEOS-1 stopped functioning after less than one year, end of June 1997. It carried eight instruments onboard: the Ocean Color and Temperature Scanner (OCTS), the Advanced Visible and Near Infrared Radiometer (AVNIR), the NASA Scatterometer (NSCAT), the Total Ozone Mapping Spectrometer (TOMS), the Improved Limb Atmospheric Spectrometer (ILAS), the Retroreflector in Space (RIS), the Interferometric Monitor for Greenhouse Gases (IMG) and the Polarization and Directionality of the Earth's Reflectance (POLDER) (Deschamps et al. 1994).

The Tropical Rainfall Measuring Mission (TRMM) launched in late 1997, is a joint mission between NASA and the National Space Development Agency (NASDA) of Japan. It was designed to monitor and study tropical rainfall and the associated release of energy that helps powering the global atmospheric circulation shaping both weather and climate around the globe (see online at <http://trmm.gsfc.nasa.gov/>). It carries several instruments, among which a Precipitation Radar (PR), the first space borne instrument designed to provide three-dimensional maps of storm structures, providing invaluable information on the rain intensity and distribution, on the rain type, on the storm depth and on the height at which the snow melts into rain. It also carries the Visible Infrared Radiometer (VIRS) and

the Clouds and the Earth's Radiant Energy System (CERES), a broadband scanning radiometer used to study the energy exchanged between the Sun, the Earth's atmosphere, surface and clouds and space (Wielicki et al. 1996).

At the end of 1999 the Terra (formerly EOS AM-1) satellite was launched into a LEO. Terra is the first EOS (Earth Observing System) platform, and carries a payload of five state-of-the-art sensors measuring global data on the state of the atmosphere, land, and oceans, as well as their interactions with solar radiation and with one another (see online at <http://terra.nasa.gov>). Particularly the MODerate-resolution Imaging Spectroradiometer (MODIS - <http://modis.gsfc.nasa.gov>) provides global coverage of the Earth's surface / atmosphere every one to two days in 36 discrete spectral bands between 0.4 and 14.4  $\mu\text{m}$ , and it acquires data at three spatial resolutions - 250, 500, and 1000m. The Terra spacecraft also carries two identical CERES instruments (Wielicki et al. 1996) that measure the Earth's total radiation budget and provide cloud property estimates. One CERES instrument operates in a cross-track scan mode and the other in a biaxial scan mode. The cross-track mode essentially continues the measurements of the CERES - TRMM, while the biaxial scan mode provides new angular flux information that will improve the accuracy of angular models used to derive the Earth's radiation balance.

A new series of GEO systems initiated with the launch of GOES-L in 2000 and GOES-M in 2001 (once in orbit denominated GOES-11 and 12), with the aim of obtaining higher spatial and temporal resolution weather imagery and full-time operational soundings (vertical temperature and moisture profiles of the atmosphere), used to support weather forecasting, severe storm tracking, and meteorological research. These satellites are being stored in orbit as a fully functioning replacement for GOES-8 (or GOES-East, positioned at 75 W longitude and the equator) and GOES-10 (or GOES-West, positioned at 135 W longitude and the equator) on failure.

Late in 2000 the NOAA-L (improved polar-orbiting meteorological satellites that began with NOAA-K in 1998) was launched into a LEO (once in orbit NOAA-16), providing global coverage of numerous atmospheric and surface parameters for weather forecasting and meteorological research, as well as space environmental monitoring. In 2002 the polar orbiting NOAA-M was also successfully launched therefore denominated NOAA-17.

In March 2002, ESA launched the ENVironmental SATellite (Envisat), an advanced polar-orbiting Earth observation satellite that provides measurements of the atmosphere, ocean, land, and ice. The Envisat satellite has an ambitious and innovative payload that will ensure the continuity of the data measurements of the ESA ERS satellites (see online at <http://envisat.esa.int>). Envisat data supports Earth science research and allows monitoring of the evolution of environmental and climatic changes. Later in the same year ESA and EUMETSAT coordinated efforts resulted in the launch of MSG-1 (Schmetz et al. 2002; EUMETSAT 2001), a significantly enhanced follow-on GEO system to the current generation of Meteosat. It has been designed in response to user requirements and will serve the needs of nowcasting applications and numerical weather prediction in addition to provision of important data for climate monitoring and research. The MSG system consists of a space segment and a ground segment. It is designed to provide data, products and services over a system lifetime of, at least, 12 years, based on a series of three satellites MSG-1 through 3. The MSG system will perform regular operations with one satellite at the nominal location of 0° longitude over the equator, and foresees a stand-by satellite that would be used in case of emergencies or during major configuration changes. MSG carries a new radiometer, the Spinning Enhanced Visible and Infrared Imager (SEVIRI) (see online at <http://esapub.esrin.esa.it/bulletin/bullet111/MSG15-17.pdf>) that provides images every 15 minutes in twelve discrete spectral bands between 635 nm and 1340 nm, with a spatial resolution of 1 km at nadir; it also carries aboard the Geostationary Earth Radiation Budget (GERB) instrument (see online at <http://www.sp.ph.ic.ac.uk/gerb/>), which provides valuable data on reflected solar radiation and thermal radiation emitted by the Earth and atmosphere every 15 minutes. In addition to these two instruments, MSG carries a comprehensive communications payload serving the needs of satellite operation, data communication and user data dissemination.

The second Advanced Earth Observing Satellite (ADEOS-2) mission was launched at the end of 2002 prepared to work operationally for at least three years. The three scientific goals were: to regularly monitor the water and energy cycle as a part of the global climate system; to quantitatively estimate the biomass and fundamental productivity as part of the carbon cycle, which plays an important role for global warming; to detect the signal of long term climate change as a result of continuous observations succeeded from ADEOS-

1. It carried a payload of five instruments, among them the Polarization and Directionality of the Earth's Reflectances (POLDER) described by Deschamps et al. (1994), a wide field of view imaging radiometer that provides global, systematic measurements of spectral directional and polarized characteristics of the solar radiation reflected by the Earth and atmosphere. Unfortunately, due to a solar panel failure, contacts with the satellite were lost on October 25, 2003.

The Aqua mission (formerly EOS PM, signifying its afternoon equatorial crossing time) was launched in mid 2002 as part of the international EOS (see online at <http://aqua.nasa.gov>). Aqua carries six state-of-the-art instruments in a near-polar LEO, among them the MODIS and CERES sensors, similar to those flying on Terra spacecraft. This mission focuses on the multi-disciplinary study of Earth's interrelated processes (atmosphere, oceans, and land surface) and their relationship to changes in the Earth system. The global change research emphasized with the Aqua instrument data sets includes atmospheric temperature and humidity profiles, clouds, precipitation and radiative balance; terrestrial snow and sea ice; sea surface temperature and ocean productivity; soil moisture; and the improvement of numerical weather prediction. Aqua will fly in orbital

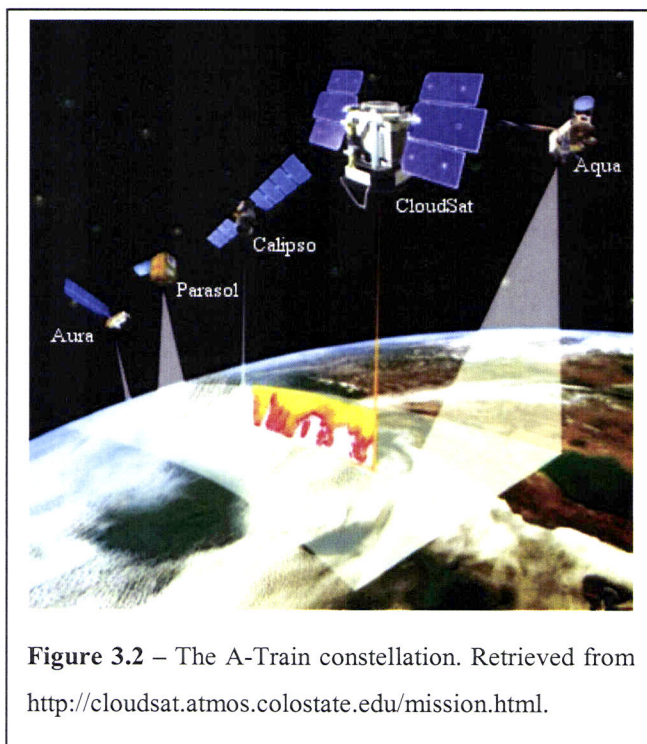


**Figure 3.2** – The A-Train constellation. Retrieved from <http://cloudsat.atmos.colostate.edu/mission.html>.

formation with other four satellites forming a constellation of five satellites referred to as the A-Train (Stephens et al. 2002). The other four missions – CloudSat, CALIPSO, PARASOL and Aura - are scheduled for launch during late 2004 and early 2005 (see Table 3.1). Figure 3.2 represents the concept of the A-Train.

CloudSat is an experimental satellite mission planned to be launched in early 2005 that will fly the first space borne millimetre wavelength radar to measure jointly

most of the cloud condensate and precipitation within its nadir field of view and the vertical structure of these properties with a vertical resolution of 500 m (Stephens et al.

2002). Current satellites can only image the uppermost layers of clouds, CloudSat will be one of the first satellites to study clouds on a global basis, providing the first vertical cloud profiling from space, improving weather forecasts and advancing our understanding of key climatic processes. The Cloud-Aerosol Lidar and Infrared Pathfinder Satellite Observations (CALIPSO - <http://www-calipso.larc.nasa.gov>) is another mission taking part of this constellation, carrying three instruments to provide key measurements of aerosol and cloud properties needed to improve climate predictions and address their role in the Earth's radiation budget: the Cloud-Aerosol Lidar with Orthogonal Polarization (CALIOP), the Imaging Infrared Radiometer (IIR) and the Wide-Field Camera (WFC). CALIOP is a two-wavelength (532 and 1064 nm) polarization-sensitive lidar that provides high-resolution vertical profiles of aerosols and clouds; it has three receiver channels: one measuring the 1064 nm backscattered intensity, and two channels measuring orthogonally polarized components (parallel and perpendicular to the polarization plane of the transmitted beam) of the 532 nm backscattered signal. The IIR is a nadir-viewing, non-scanning imager having a  $64 \times 64 \text{ km}^2$  swath with a pixel size of 1 km, providing measurements at three channels in the thermal infrared window region at 8.7, 10.5 and 12.0  $\mu\text{m}$ . These wavelengths were selected to optimise joint CALIOP/IIR retrievals of cirrus cloud emissivity and particle size. The CALIOP beam is nominally aligned with the centre of the IIR image. The WFC is a fixed, nadir-viewing imager with a single spectral channel covering the 620-670 nm region, selected to match band 1 of the MODIS instrument on Aqua. The WFC is operated in a push-broom mode, collecting images with 125 m spatial resolution over a 61 km cross-track swath centred on the CALIOP footprint. The PARASOL (Polarisation et Anisotropie des Réflectances au sommet de l'Atmosphère, couplées avec un Satellite d'Observation emportant un Lidar) is a microsatellite project constituted mainly by the POLDER instrument (Deschamps et al. 1994) (see online at <http://smc.cnes.fr/PARASOL/index.htm>). Its main purpose is to perform measurements of the polarized and multi-directional reflectances, on areas observed by CALIOP as a priority, improving the characterization of the clouds and aerosols microphysical and radiative properties, needed to understand and model the radiative impact of clouds and aerosols using as best as possible the data complementarity from the different sensors on board the Aqua platform, and those from the CALIPSO and CLOUDSAT missions. Finally, the EOS Aura mission (see online at <http://eos-chem.gsfc.nasa.gov>) at one end of

the A-Train constellation is designed exclusively to conduct research on the composition, chemistry and dynamics of the Earth's upper and lower atmosphere employing multiple instruments. Aura carries onboard the High Resolution Dynamics Limb Sounder (HIRDLS), the Microwave Limb Sounder (MLS), the Ozone Monitoring Experiment (OMI) to ensure continuity of TOMS measurements, and the Tropospheric Emission Spectrometer (TES). The nominal time separation between Aqua and Aura will be about 15 min. Aura's limb viewing instruments will measure the same portion of the Earth as Aqua's nadir viewing instruments to within eight minutes. The time separation between Cloudsat and CALIPSO is only about 15 s and they are both about two minutes behind Aqua. PARASOL follows CALIPSO with a delay of about two minutes. The unique data set of aerosol and cloud optical and physical properties and aerosol-cloud interactions obtained from the instruments on the satellites forming the A-Train constellation will substantially increase our understanding of the atmospheric physical processes within the climate system and the potential for climate change, providing observationally based estimates of the clouds and aerosols direct and indirect radiative forcing, improved evaluation of the Earth's radiative budget and quantifying its response to anthropogenic modifications and its evolution in time.

METOP-1, the first European operational polar-orbiting weather satellite, is planned to be ready for launch by mid 2005, replacing one of two satellite services operated by NOAA. METOP will carry a payload of eight instruments for observing the planet, providing high-resolution images, detailed vertical temperature and humidity profiles, temperatures of the land and ocean surface on a global basis, monitoring of ozone levels and other gases in the atmosphere and wind flow over the oceans (see online at <http://www.esa.int/export/esaME/index.html>). The Advanced Very High Resolution Radiometer (AVHRR/3) is one of the NOAA's 'heritage' instruments present on METOP payload: it scans the Earth surface in six spectral bands in the range of 580 - 125 nm providing day-night imaging of land, water and clouds, measures of the sea surface temperature, ice, snow and vegetation cover. The Global Ozone Monitoring Experiment - 2 (GOME-2) on METOP is an enhanced successor to GOME-1 spectrometer (Burrows et al. 1999), launched on ESA's ERS-2 in 1995. The spectra will be used to derive a detailed picture of the atmospheric content and profile of ozone, nitrogen dioxide, water vapour, oxygen / oxygen dimmer, bromine oxide and other gases.

The Megha-Tropiques mission scheduled for launch in 2006, was studied in the context of TRMM follow up, with the following objectives: improve the knowledge of the water cycle in the intertropical region, to evaluate its consequences on the energy budget; study the life cycle of tropical convective systems over ocean and continents, the environmental conditions for their appearance and evolution, their water budget, and the associated transports of water vapour; provide data about the dramatic weather events affecting the Tropical countries, as hurricanes and systems producing heavy rainfalls. Megha-Tropiques is a mini-satellite with a payload of three instruments: a multi-frequency microwave scanning radiometer (MADRAS) aimed mainly to study precipitation and cloud properties, including ice at the top of clouds; a multi-channel microwave sounding instrument (SAPHIR) providing humidity profile of the atmosphere; and a multi-channel radiometer (ScaRaB), measuring the radiances in two wide channels, a solar channel (0.2 - 4  $\mu\text{m}$ ) and a total channel (0.2 - 200  $\mu\text{m}$ ), providing data on the Earth's radiation budget. The key of this mission is the repetitivity of the measurement in the Tropics (coverage from 23°N to 23°S), obtaining measurements from 3 to 6 times per day. The MEGHA-TROPIQUES mission is an experimental mission with an estimated duration of three years, without plan for operational follow-up, however it could be useful to use in synergy with GEO systems, especially MSG that carries not only SEVIRI but also GERB.

The Global Precipitation Measurement (GPM) mission is part of the EOS program, with launch scheduled for Fall 2007 (see online at <http://gpm.gsfc.nasa.gov>). Building upon the success of TRMM, it will initiate the measurement of global precipitation, a key climate factor. Its science objectives are: to improve ongoing efforts to predict climate by providing near-global measurement of precipitation, its distribution, and physical processes; to improve the accuracy of weather and precipitation forecasts through more accurate measurement of rain rates and latent heating; and to provide more frequent and complete sampling of the Earth's precipitation. GPM is envisioned to consist of a primary spacecraft to measure precipitation structure and to provide a calibration standard for the constellation spacecraft, an international constellation of spacecrafts to provide frequent precipitation measurements on a global basis using passive microwave radiometers, calibration/validation sites distributed globally with a broad array of precipitation-measuring instrumentation, and a global precipitation data system to produce and distribute global rain maps and climate research products.



The Earth Explorer is part of ESA's Living Planet programme (see online at <http://www.esa.int/export/esaLP/>), addressing the interests of the growing community of users in the public and private sectors. Earth Explorer missions fall into two categories - Core and Opportunity missions. Core Explorers are ESA-led, dedicated to a long-term research objective. Opportunity Explorers are smaller, low-cost satellites, and are less complex and quicker to implement. They respond to evolving situations or areas of immediate environmental concern projects, not necessarily led by ESA.

The Earth, Clouds, Aerosol and Radiation Explorer (EarthCARE) mission is a possible Future Core Mission currently undergoing feasibility study (Phase A). If it is selected to go forward to Phase B (design and development), the mission will be eventually launched in the period 2007-2010. EarthCARE addresses the need for a better understanding of the interactions between cloud, radiative and aerosol processes that play a role in climate regulation (see online at <http://www.esa.int/export/esaLP/earthcare.html>). It has been specifically defined with the scientific objectives of determining the global distribution of vertical profiles of cloud and aerosol field characteristics to provide basic essential input data for numerical modelling and global studies of: divergence of radiative energy, aerosol-cloud-radiation interaction, vertical distribution of water and ice and their transport by clouds, and the vertical cloud field overlap and cloud-precipitation interactions. The payload consists of a Backscatter Lidar (ATLID), a Cloud Profiling Radar (CPR), a Fourier Transform Spectrometer (FTS), a Multi-Spectral Imager (MSI) and a Broad-Band Radiometer (BBR).

As part of the Earth Explorers Opportunity Missions, EGPM - the European contribution to the international Global Precipitation Measurement mission (GPM), was selected to undergo feasibility study (Phase A) and, if selected for implementation its launch is envisaged for 2008 or later. The aim of EGPM is to provide one element in a constellation of satellites (GPM), which will ensure the delivery of global precipitation fields every 3 hours (see online at <http://www.esa.int/export/esaLP/egpm.html>). The basic EGPM mission would consist of a satellite with a five-channel microwave radiometer, for measurements of liquid water, water vapour, ice, snow and discrimination between liquid water and ice. To meet the accuracy levels for precipitation required by the European user community, tentatively a satellite carrying two instruments would be required, namely a microwave radiometer and a precipitation radar.

This is the general scenario with respect to the most important present and future satellite missions dedicated to atmospheric studies, particularly to aerosols and clouds and their important role in the Earth's climate. In the next section an intensive description of the instruments used to obtain the measurements used in the present work is given.

## **3.3 Satellite instruments used in the present work**

### **3.3.1 GEO instruments**

#### **3.3.1.1 Meteosat**

The Meteosat satellite system was firstly designed in the early 1970s and the first spacecraft launched in 1977. Meteosat-7 with the very same original design is still in orbit at the present time, together with Meteosat 5 and 6. The expected 26 years of operational service amply justifies the initial development effort.

The overall size of the satellite is 2.1 m in diameter and 3.195 m length. Its initial mass in orbit is 322 kg. Additional to this dry mass is the hydrazine propellant used for station keeping, amounting to approximately a further 39 kg at the beginning of life. In orbit, the satellite spins at 100 rpm around its main axis, which is aligned nearly parallel to the Earth's north-south axis (EUMETSAT, 2000).

The operational Meteosat is located at 0° longitude, while the spare satellite may be located at 10° E or W, from which positions it can be used occasionally for test purposes or special services. At present the operational and spare satellites are respectively Meteosat-7 (launched in 1997) and Meteosat-6 (launched in 1993). EUMETSAT supported the international Mesoscale Alpine Programme (MAP) experiment (see online at <http://www.map.ethz.ch>) by performing special limited scans of the Alpine region in autumn 1999. Since the scan lines are fewer, the image is completed in less time than a full Earth disk scan, providing imagery with a higher temporal resolution than that of the normal half-hourly full Earth disk. This mode of scanning is often referred to as rapid scanning. Following the success of the rapid scanning support provided to MAP, a new operational Rapid Scanning Service (RSS) was started in September 2001 and it continues

to be provided by Meteosat-6 as long as it is the in-orbit spare spacecraft. The RSS is available for the region that covers a latitude range from approximately 10°N to 70°N, or for a subset of this region that covers all Europe.

During the period from January until May 1998, the old Meteosat-5 (launched in 1991) was slowly moved from 10° W to 63° E in preparation for the support to the Indian Ocean Experiment (INDOEX), an international atmospheric field experiment started in February 1998 with an intensive field phase taking place between January and April 1999 (see online at <http://www-indoex.ucsd.edu>). The operational service from this position started on July 1998. After the end of INDOEX in 1999, EUMETSAT agreed to further extend the operational coverage of the Indian Ocean area until the end of the year 2003. The service is referred to as the Indian Ocean Data Coverage (IODC).

The positions of the operational (0°), spare (10° E or W) and IODC (63° E) Meteosat spacecrafts are nominal locations but, because of the uneven shape of the Earth and the gravitational influence of the moon and sun, the satellite does not stay precisely at the nominal location. The satellite is normally maintained within a defined box around its nominal location. When it reaches the eastern extremity of the permitted box, the thrusters are activated and the satellite is moved back to the western extremity of the box, where the process starts again. This cycle repeats every few months (depending on the current size of the permitted box), but is not expensive in fuel utilization.

The Meteosat Visible and InfraRed Imager (MVIRI) is a radiometer that constitutes the main payload of Meteosat. The instrument allows continuous imaging of the Earth, measuring the reflected and emitted radiation in three spectral regions (visible – VIS, water vapour – WV and infrared – IR; these channels are broadband), using a total of eight detectors, two redundant pairs in the VIS, two redundant pairs in the WV and two redundant pairs in the IR. The spinning motion of Meteosat and consequently of MVIRI allow for the scan of the Earth scene from east-to-west and the stepping motion of the telescope provides south-to-north scanning. Images are acquired simultaneously in the three spectral bands during a 25-minute period, followed by a five-minute retrace and stabilization interval, so that one complete set of full earth disk images is available every half-hour. The Meteosat images are usually referred to as slots, distinguished by a progressive number (from 1 to 48) that indicates the time of the scan, for example the image scanned between 0000 and 0030 UTC corresponds to slot 1.

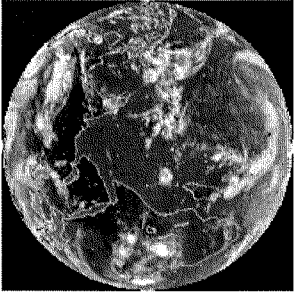
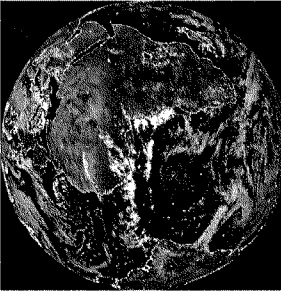
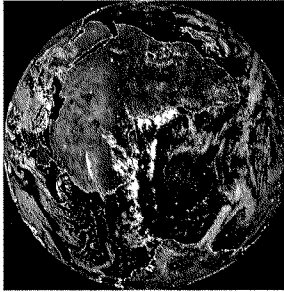
The IR and WV images consist of 2500 lines  $\times$  2500 elements per line, whereas the VIS image comprises a total of 5000 lines  $\times$  5000 elements since there are two visible detectors in operation. This results in a pixel resolution of  $2.5 \times 2.5 \text{ km}^2$  in the VIS and  $5.0 \times 5.0 \text{ km}^2$  in the WV and IR at the subsatellite point. Table 3.2 summarizes the main characteristics of the Meteosat satellites used in the present work.

Quantitative application of satellite measurements requires the absolute calibration of the observed raw radiance data. Calibration techniques of the satellite spectral channels rely on onboard calibration employing a blackbody for the IR channels and on vicarious techniques for the VIS channel. All techniques associate the raw measured units, expressed as counts, with calculated radiances, in order to retrieve a one to one relation between them. The present work implicates the calibration of Meteosat VIS spectral channel and the measured radiance is retrieved using the following equation:

$$I = \alpha_{calib} \times (C - C_0) \quad (3.1)$$

where  $I$  is the radiance expressed in  $\text{W.m}^{-2}.\text{sr}^{-1}$ ,  $\alpha_{calib}$  the calibration coefficient expressed in  $\text{W.m}^{-2}.\text{sr}^{-1}/\text{count}$ ,  $C$  the measured digital count and  $C_0$  the offset (zero intercept). The radiance in the spectral band between the wavelengths  $\lambda_{min}$  and  $\lambda_{max}$  is related to the monochromatic radiance by:

$$I = \int_{\lambda_{min}}^{\lambda_{max}} I_{\lambda} d\lambda \quad (3.2)$$

Meteosat	Launch Date	Present Nominal Position	Instrument	Image Frequency	Disk Image Coverage (copyright 2003 EUMETSAT)	Nominal Spectral Channels ( $\mu\text{m}$ )	Spectral resolution	Number of detectors (+ redundant)	Nadir Pixel Size ( $\text{km}^2$ )	
5	2 March 1991	63° E	MVIRI	30 minutes		VIS	Broadband	2 (+2)	2.5 x 2.5	
						WV			5.40 – 7.40	5.0 x 5.0
						IR			10.0 – 13.10	5.0 x 5.0
6*	20 Nov. 1993	10° E*	MVIRI	30 minutes		VIS	Broadband	2 (+2)	2.5 x 2.5	
						WV			5.40 – 7.35	5.0 x 5.0
						IR			10.0 – 13.10	5.0 x 5.0
7	2 Sept 1997	0°	MVIRI	30 minutes		VIS	Broadband	2 (+2)	2.5 x 2.5	
						WV			5.40 – 7.50	5.0 x 5.0
						IR			10.0 – 13.10	5.0 x 5.0

\* Data from Meteosat-6 was used in this work when the satellite was located at 0° (operational satellite).

Table 3.2 – Summary of the main characteristics of Meteosat satellites used in the present work.

The calibration coefficients for Meteosat-5, -6 and -7 VIS channels are obtained from the vicarious calibration that relies on the SEVIRI solar channel calibration algorithm, which was specifically developed for the operational calibration of the solar channels of SEVIRI (Govaerts et al. 2001). This algorithm is based upon radiative transfer simulation over bright desert and sea targets. To reduce and estimate the calibration error, a large number of images, typically corresponding to 10 days of daylight data acquired under different illumination conditions, are processed. The calibration coefficients used depend on the spacecraft and date and are available at <http://www.eumetsat.de/en/dps/mpef/calibration.html>

The radiance measured by any broadband sensor is given by:

$$I = \frac{\int_{\lambda_{\min}}^{\lambda_{\max}} f_{\lambda} \cdot I_{\lambda} \cdot d\lambda}{\int_{\lambda_{\min}}^{\lambda_{\max}} f_{\lambda} \cdot d\lambda} \quad (3.3)$$

$f_{\lambda}$  is the spectral response function of the sensor, determined by the instrument optics and sensor. Since MVIRI has broadband channels, the corresponding simulated radiances have to be weighted by the instrument spectral response, using equation 3.3. The resulting weighted radiance can then be compared with the satellite radiance measurements.

Due to problems in the pre-launch phase to measure the sensor spectral responses of Meteosat-5 and 6, the curves obtained for Meteosat-7 are much more reliable. Since all these spacecrafts are very similar and it is demonstrated that the use of Meteosat-7 spectral response data for Meteosat-5 and 6 gives more consistent results, the VIS channel spectral response of these two spacecrafts is replaced with that of Meteosat-7 (Govaerts 1999). The spectral response functions for

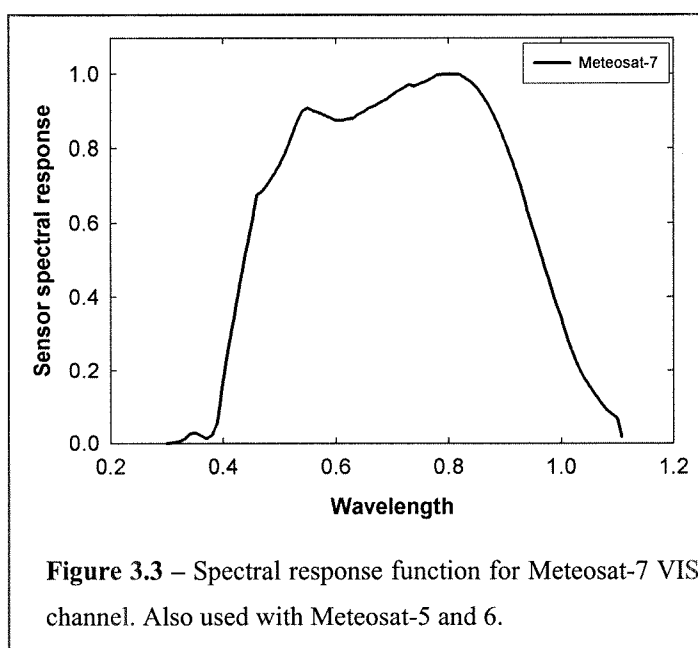


**Figure 3.3** – Spectral response function for Meteosat-7 VIS channel. Also used with Meteosat-5 and 6.

each Meteosat spacecraft and each channel are available online at <http://www.eumetsat.de>. Figure 3.3 shows the spectral response function graph corresponding to Meteosat-7 VIS channel, also used for Meteosat-5 and 6.

### 3.3.1.2 GMS

The GMS series are the GEO meteorological spin-stabilized satellites operated by the Japan Meteorological Agency. The spacecraft height is 3.54 m and its diameter 2.15 m. Its weight is approximately 344 kg at the beginning of life. The satellites consist of a despun earth-oriented antenna assembly and a spinning section rotating at 100 rpm (GMS user's guide 1997). The current operational satellite is GMS-5 and it was launched in March 1995. Its nominal position is at 140° E longitude.

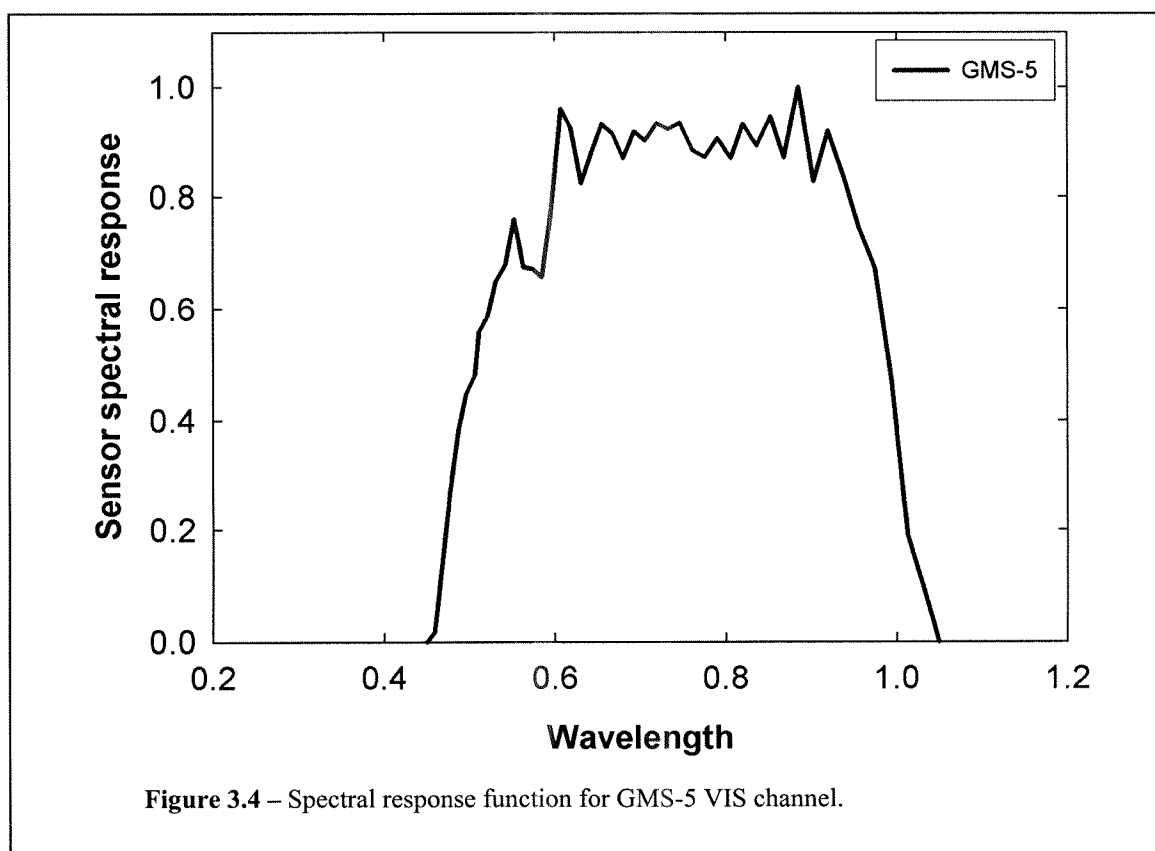
The Visible and Infrared Spin Scan Radiometer (VISSR) constitutes the main payload of GMS. It allows continuous imaging of the Earth, measuring the reflected and emitted radiation in four spectral intervals (one in the VIS and three in the IR that include one in the WV absorption region), using a total of fourteen detectors, four redundant pairs in the VIS and three redundant pairs in the IR. VISSR optical axis is in line with the spacecraft mechanical center axis and its spinning motion orients the line of sight to the earth scene west-to-east and the stepping motion of the scan mirror reflection angle provides north-to-south scanning. Images are acquired simultaneously in the four spectral bands during a 25-minute period, followed by a five-minute retrace and stabilization interval, so that the full earth disk imagery is available every half-hour. The IR and WV images consist of 2500 lines  $\times$  2500 elements per line, whereas the VIS image comprises a total of 10000 lines  $\times$  10000 elements since there are four visible detectors in operation. This results in a pixel resolution of 1.25  $\times$  1.25 km<sup>2</sup> in the VIS and 5.0  $\times$  5.0 km<sup>2</sup> in the WV and IR at the subsatellite point. Table 3.3 summarizes the main characteristics of the GMS-5 satellite used in the present work.

The GMS-5 calibration for the IR channels relies on onboard calibration techniques employing a blackbody. In VIS channel, the onboard calibration is not performed due to the unreliability of the VISSR calibration target therefore only results of the pre-flight test have been used to generate the fixed calibration table (Tokuno 1997). The conversion of the measured counts into reflectance (VIS) values is achieved applying the appropriate calibration table published in the GMS user's guide (1997).

Simulated VISSR reflectance values obtained from measurements in the VIS spectral channel are weighted by the sensor spectral response, as it is done for the radiances (see previous section – equation 3.3). The corresponding broadband reflectance ( $\rho$ ) is obtained in a similar way, weighting the monochromatic reflectance ( $\rho_\lambda$ ) by the instrument spectral response ( $f_\lambda$ ):

$$A = \frac{\int_{\lambda_{\min}}^{\lambda_{\max}} f_{\lambda} \cdot A_{\lambda} \cdot d\lambda}{\int_{\lambda_{\min}}^{\lambda_{\max}} f_{\lambda} \cdot d\lambda} \quad (3.4)$$

The spectral response functions for each GMS-5 channel are available online at <http://mscweb.kishou.go.jp/>. Figure 3.4 presents the spectral response function graph corresponding to the GMS-5 VIS channel.





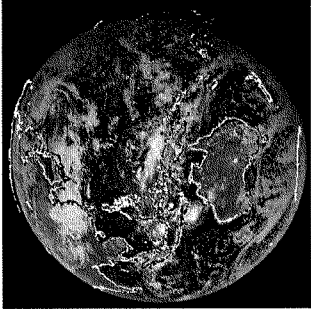
GMS	Launch Date	Present Nominal Position	Instrument	Image Frequency	Disk Image Coverage Source: Japan Meteorological Agency GMS-5 via Bureau of Meteorology, Australia	Nominal Spectral Channels ( $\mu\text{m}$ )	Spectral resolution	Number of detectors (+ Redundant)	Nadir Pixel Size ( $\text{km}^2$ )
5	18 March 1995	140° E	VISSR	30 minutes		VIS	Broadband	4 (+4)	1.25 × 1.25
						WV		1 (+1)	5.0 × 5.0
						IR1		1 (+1)	5.0 × 5.0
						IR2		1 (+1)	5.0 × 5.0

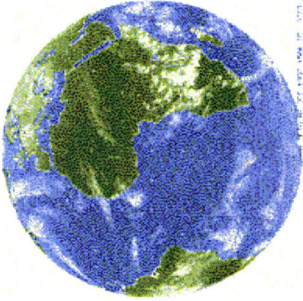
Table 3.3 – Summary of the main characteristics of GMS-5 satellite used in the present work.

### 3.3.1.3 MSG

MSG-1 SEVIRI data is not used in the present work since its data is not yet available to the users. It is now ongoing the commissioning phase to make the necessary verifications on the satellite and prepare it to routine operations and it is expected to continue at least until the end of 2003. Nevertheless a short description of the system including the SEVIRI instrument are deemed relevant in the context since the future use of SEVIRI data instead of MVIRI (aerosol studies) and MODIS (cloud studies) is of great interest for the present work.

MSG-1 satellite is basically cylindrical with an overall size of 3.7 m in diameter and 2.4 m in height. The satellite spins at 100 rpm in a counter-clockwise direction around its main axis, which is aligned nearly parallel to the Earth's north-south axis as in Meteosat. The spin is required to both stabilize the satellite and to assist in the scanning of the Earth by the SEVIRI radiometer. Once MSG-1 enters the operational phase it will substitute the current Meteosat-7 at the nominal location of  $0^\circ$  longitude over the equator (EUMETSAT 2001).

The SEVIRI instrument provides the basic data of the MSG-1 system, namely 12 spectral channels spanning the VIS and IR parts of the electromagnetic spectrum, using 42 detectors. Each channel has an array of three detector elements, with the exception of the High Resolution Visible (HRV) channel, imaging in the VIS spectral region, which has 9 detectors. A series of mirrors within the radiometer direct the radiation originating from the Earth surface, its atmosphere and cloud systems, received via an opening in the side of the satellite, onto the array of detectors. Readings are taken from the detectors as the satellite spins, so that the spin is used to scan the Earth in the east-west direction. After every scan line a mirror is stepped in the south-north direction in order to acquire subsequent scan lines. The nominal repeat cycle for a complete scan of the full Earth disk is 15 minutes, this includes measurement of onboard calibration sources and scan mirror retrace. The satellite can obtain shorter repeat cycles if a reduced area of the Earth is imaged. The nominal image size for all channels except for the HRV is 3712 lines  $\times$  3712 elements per line, reflecting in a pixel resolution of  $3.0 \times 3.0 \text{ km}^2$  at the sub-satellite point. The image size for the HRV channel is of 11136 lines  $\times$  5568 elements (N-S by E-W) with a sampling distance of  $1.0 \times 1.0 \text{ km}^2$  at the sub-satellite point. Table 3.4 summarizes the main characteristics of the SEVIRI instrument onboard MSG-1 satellite.

MSG	Launch Date	Nominal Position	Instrument	Image Frequency	Disk Image Coverage <small>(copyright 2003 EUMETSAT)</small>	Nominal Spectral Channels ( $\mu\text{m}$ )	Spectral resolution	Number of detectors	Nadir Pixel Size ( $\text{km}^2$ )
1	28 August 2002	0° *	SEVIRI	15 minutes		VIS 0.6	Broadband	3	3.0 x 3.0
						VIS 0.8		3	3.0 x 3.0
						IR 1.6		3	3.0 x 3.0
						IR 3.9		3	3.0 x 3.0
						IR 8.7		3	3.0 x 3.0
						WV 6.2		3	3.0 x 3.0
						WV 7.3		3	3.0 x 3.0
						IR 9.7		3	3.0 x 3.0
						IR 10.8		3	3.0 x 3.0
						IR 12.0		3	3.0 x 3.0
						IR 13.4		3	3.0 x 3.0
						HRV		9	1.0 x 1.0
						0.5 - 0.9			

\*When it becomes EUMETSAT's operational satellite.

Table 3.4 – Summary of the main characteristics of the SEVIRI instrument onboard MSG-1.

The SEVIRI solar channels (HRV, VIS0.6, VIS0.8, IR1.6 – see Table 3.4) are operationally calibrated using a vicarious technique, as in the case of Meteosat VIS channel, based on calculated radiances over special selected ground targets (Govaerts et al. 2001). The operational calibration of the “cold” channels (IR3.9, WV 6.2, WV7.3, IR8.7, IR9.7, IR10.8, IR12.0, IR13.4 – see Table 3.4) is performed several times a day. An onboard black body source is placed in the optical path of the instrument, at two different known temperatures. The response of the instrument at these two temperatures is then fed into a mathematical model, representing the instrument optics, which gives the required calibration coefficient and offset needed to be applied to the instrument output in order to determine the corresponding radiance for any output.

### **3.3.2 LEO instruments**

#### **3.3.2.1 GOME**

GOME is a spectrometer measuring in the ultraviolet (UV) and VIS spectral regions (240 to 790 nm) primarily dedicated to global monitoring of atmospheric ozone (Burrows et al. 1999). A key feature of GOME is its ability to detect several chemically active atmospheric trace-gases as well as aerosol distribution. It flies onboard ERS-2, launched in April 1995, in a near polar orbit at a height of about 795 km crossing the equator at 10:30 am local time.

The GOME instrument is a double monochromator that combines a predisperser prism and four diffraction gratings as dispersing elements. The light arriving from the sun-illuminated atmosphere is reflected off the scan mirror and focussed by a telescope to match the entrance slit of the spectrometer. It is then split into four separate spectral regions (four channels). In each of these regions the light is dispersed by the diffraction gratings and then sensed by four individual linear detector arrays each with 1024 detector pixels. The spectral resolution is high and varies between 0.2 nm (UV) and 0.4 nm (VIS) – see Table 3.5. Part of the light reaching the predisperser prism is branched out and recorded with three broadband polarization monitoring devices (PMD), which approximately cover three spectral ranges (295 - 397 nm; 397 - 580 nm; 580 - 745 nm). The PMDs measure the amount of light at an instrument defined polarization angle.

ERS	Launch Date	Instrument	Nominal Spectral Channels (nm)		Spectral resolution (nm)	Nadir Pixel Size (Km <sup>2</sup> )
			Ch	Wavelength Range (nm)		
2	21 April 1995	GOME	Ch 1A	237 - 307	0.20	40 x 320
			Ch 1B	307 - 315	0.20	40 x 320
			Ch 2	312 - 406	0.17	40 x 320
			Ch 3	397 - 609	0.29	40 x 320
			Ch 4	576 - 794	0.33	40 x 320
			PMD1	295 - 397	Broadband	40 x 20
			PMD2	397 - 580	Broadband	40 x 20
			PMD3	580 - 745	Broadband	40 x 20

Table 3.5 – Summary of the main characteristics of the GOME instrument onboard ERS-2.

The various pointing geometries of the GOME scan mirror permit in addition to Earth and solar nadir viewing (scan mirror angle of  $\pm 32^\circ$ ), polar viewing (during polar summer; scan mirror angle of  $47^\circ$ ), and lunar observations (about six times per year; scan mirror angle of about  $80^\circ$ ). The solar irradiance measurements are carried out once a day (every fourteenth orbit), when the ERS-2 satellite crosses the terminator in the North Polar Region coming from the night side.

In the nadir viewing geometry GOME scans the Earth from east ( $-32^\circ$ ) to west ( $+32^\circ$ ) and back (maximum scan width of 960 km) resulting in four ground pixel types called East, Nadir, West, and Backscan. The forward scan consists of the first three pixels, each presenting a ground size of  $40 \times 320 \text{ km}^2$ ; the Backscan pixel size is  $40 \times 960 \text{ km}^2$ . It is possible to vary the forward scan ground pixel size of the GOME instrument between  $40 \times 40 \text{ km}^2$  and  $40 \times 320 \text{ km}^2$ , nevertheless the largest of these sizes is provided most of the times since it favours global coverage that is then achieved with the minimum number of orbits (43 orbits achieved within three days).

Prior to launch, the spectral irradiance of the GOME flight model was calibrated using a 1000 Watt FEL lamp, which in turn was referenced to an absolute standard at the National Institute of Standard and Technology (NIST). The absolute accuracy of the NIST standard is quoted to be 1 to 3% in the range 250-340 nm. Spectral radiance of GOME was calibrated by placing a Spectralon diffuser plate between the FEL lamp and the nadir scan mirror. The Spectralon diffuser plate was compared with the NASA integrating sphere, which served as radiance standard to calibrate the NASA instruments onboard the Solar Backscatter UV (SBUV). The agreement between the two standards is within 1%. The radiance response was determined as a function of the scan mirror

angle. GOME absolute radiometric calibration consists of converting the raw data measurements in absolute radiance and solar irradiance values, after correcting the measured signal for the polarization effects taking into account the sensitivity of the instrument, known from pre-flight calibration measurements, and the PMD data. Once a month, the internal calibration lamp that emits at least six lines in each of the GOME's spectral channels, is switched on over an entire orbit. During this sequence a series of lamp measurements with and without a solar diffuser permit the investigation of long term degradation of the diffuser and an update in the wavelength calibration of the detector arrays, respectively.

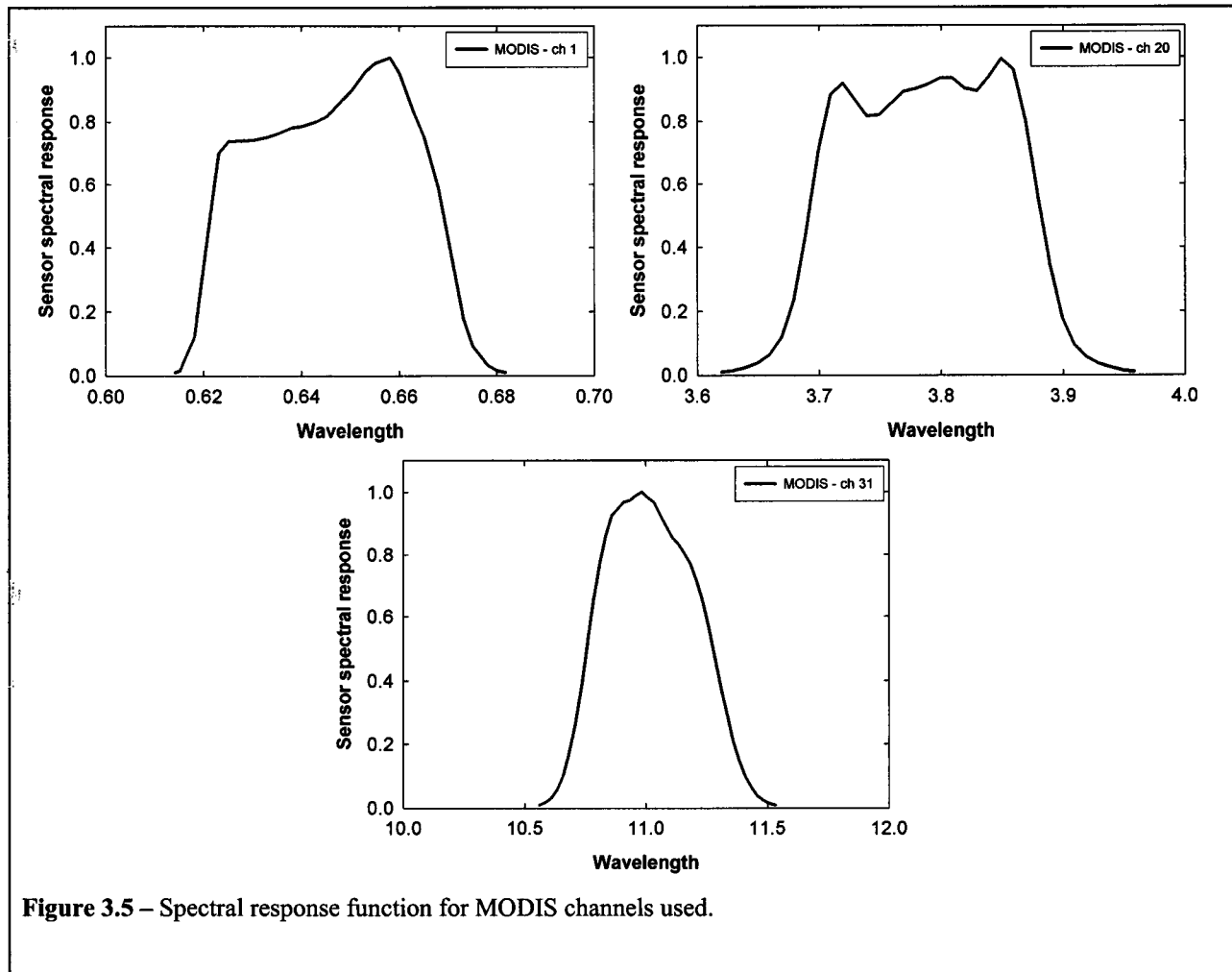
#### 3.3.2.2 MODIS

MODIS is a key instrument aboard the Terra (EOS AM) and Aqua (EOS PM) satellites (see previous section). Terra's orbit around the Earth is timed so that it passes from north to south across the equator in the morning, while Aqua passes south to north over the equator in the afternoon. Terra MODIS and Aqua MODIS are viewing the entire Earth's surface, acquiring data in 36 spectral bands. These data will improve our understanding of global dynamics and processes occurring over land, in the oceans, and in the lower atmosphere. MODIS is playing a vital role in the development of validated, global, interactive Earth system models able to predict global change (see online at <http://modis.gsfc.nasa.gov>).

The MODIS instrument provides high radiometric sensitivity in 36 spectral bands ranging in wavelength from approximately 0.4 to 14.4  $\mu\text{m}$  (see Table 3.6). Two bands are imaged at a nominal resolution of 250 m at nadir, five bands at 500 m and the remaining 29 bands at 1000 m. A  $\pm 55^\circ$  scanning pattern at the EOS orbit of 705 km achieves a 2330 km swath and provides global coverage every one to two days.

MODIS has a full complement of onboard calibrators to provide radiometric, spectral and spatial calibration of the instrument (see online at <http://www.mcst.ssai.biz/mcstweb/index.html>). A blackbody is the prime calibration source for the thermal bands located from 3.5 to 14.4  $\mu\text{m}$ , while a solar diffuser provides a diffuse, solar-illuminated calibration source for the VIS, near IR, and short-wave IR bands (wavelengths between 0.4 and 2.2  $\mu\text{m}$ ). A solar diffuser stability monitor tracks changes in the reflectance of the solar diffuser via reference to the sun so that potential instrument changes are not incorrectly attributed to changes in this calibration source. Another calibration source is the spectroradiometric calibration assembly, a very complex, multifunction calibration instrument that provides in-flight spectral, radiometric and spatial calibration.

In addition, MODIS uses two other calibration techniques that consist of views of the moon and deep space. The advantage of "looking" at the moon is that it enables MODIS to view an object that has roughly the same brightness as the Earth. The Sun illuminates the moon as well as the onboard solar diffuser. However, unlike the solar diffuser, the moon is not expected to change over the lifetime of the MODIS mission. "Looking" at the moon provides a second method for tracking degradation of the solar diffuser. "Looking" at deep space provides a photon input signal of zero, which will be used as an additional point of reference for calibration.



Along with the data from other instruments on board the Terra and Aqua spacecrafts, MODIS data are transferred to ground stations. The data are processed to produce Level1A (raw data), Level1B (calibrated data: radiances/ reflectances), and geolocated products. There are also higher-level products produced on a regular basis dedicated to land (<http://modis-land.gsfc.nasa.gov>), ocean (<http://modis-ocean.gsfc.nasa.gov>) and atmospheric (<http://modis-atmos.gsfc.nasa.gov>) studies. All level products are available online at <http://daac.gsfc.nasa.gov>.

The spectral response functions for each of the three MODIS spectral channels used hereafter are presented in the graphs of Figure 3.5.

MODIS Spectral Bands			
Spectral Resolution: Broadband			
Reflected Radiation		Emitted Radiation	
Pixel: 250 x 250 m <sup>2</sup>	Pixel: 500 x 500 m <sup>2</sup>	Pixel: 1 x 1 km <sup>2</sup>	Pixel: 1 x 1 km <sup>2</sup>
1 (620-670 nm)	3 (459-479 nm)	8 (405-420 nm)	20 (3.660-3.840 μm)
2 (841-876 nm)	4 (545-565 nm)	9 (438-448 nm)	21 (3.929-3.989 μm)
	5 (1230-1250 nm)	10 (483-493 nm)	22 (3.939-3.989 μm)
	6 (1628-1652 nm)	11 (526-536 nm)	23 (4.020-4.080 μm)
	7 (2105-2155 nm)	12 (546-556 nm)	24 (4.433-4.498 μm)
		13 (662-672 nm)	25 (4.482-4.549 μm)
		14 (673-683 nm)	27 (6.535-6.895 μm)
		15 (743-753 nm)	28 (7.175-7.475 μm)
		16 (862-877 nm)	29 (8.400-8.700 μm)
		17 (890-920 nm)	30 (9.580-9.880 μm)
		18 (931-941 nm)	31 (10.780-11.280 μm)
		19 (915-965 nm)	32 (11.770-12.270 μm)
		26 (1.360-1.390 μm)	33 (13.185-13.485 μm)
			34 (13.485-13.785 μm)
			35 (13.785-14.085 μm)
			36 (14.085-14.385 μm)

Table 3.6 – MODIS spectral bands.



### 3.3.2.3 Envisat

Envisat data is not used in the present work. However a short description of three of the onboard instruments (SCIAMACHY, MERIS and AATSR) is deemed relevant for similar reasons to those indicated in the MSG section. In this case it would be of great interest for the present work to substitute GOME with data from these instruments since the spectral coverage would be enlarged and the spatial resolution improved.

The SCanning Imaging Absorption spectroMeter for Atmospheric Chartography (SCIAMACHY) is the follow-on of the GOME spectrometer (see online at <http://envisat.esa.int/instruments/sciamachy>). The primary mission objective of SCIAMACHY is to perform global measurements of trace gases in the troposphere and in the stratosphere. SCIAMACHY adds limb and solar occultation measurements, to the GOME capability of nadir viewing geometry, and extends the wavelength coverage to 2.4  $\mu\text{m}$  (Bovensmann et al. 1999). In limb mode the instrument scans the atmosphere tangentially to the Earth's surface at different tangent heights (about 3 km vertical resolution) over a range of up to 960 km in horizontal direction. Occultation measurements are performed using the same geometry as in limb mode, but with the Sun or the moon in SCIAMACHY's field of view. Atmospheric densities are obtained by comparing measurements of the transmitted solar or lunar radiation with the source that do not suffer attenuation.

Solar occultation measurements are performed regularly during sunrise (latitude range: 90° N - 65° N). Lunar occultation measurements are possible during moonrise for about one week per month (between 30°S - 90°S). One of the most important features of SCIAMACHY is the possibility to observe the same atmospheric volume first in limb and then after about 7 minutes in nadir geometry. The use of the Limb/Nadir matching allows for obtaining three-dimensional improved information about the atmosphere.

In the nadir viewing mode SCIAMACHY has a nominal footprint of 30 km along-track and a maximum scan width of 960 km (across-track) subdivided into smaller pixels whose size varies along the orbit between 20  $\times$  30 km<sup>2</sup> and 30  $\times$  240 km<sup>2</sup>, according to the spectral region and geographic location. A typical spatial resolution is 30 km (along track)  $\times$  60 km (across track). Global coverage is achieved in three days.

Envisat	Launch Date	Instrument	Nominal Spectral Channels (nm)		Spectral resolution (nm)	Nadir Pixel Size (km <sup>2</sup> )
			Ch	Wavelength Range		
1	1 March 2002	SCIAMACHY	Ch 1	240 - 314	0.24	30 x (30-240)
			Ch 2	309 - 405	0.26	30 x (30-240)
			Ch 3	394 - 620	0.44	30 x (30-240)
			Ch 4	604 - 805	0.48	30 x (30-240)
			Ch 5	785 - 1050	0.54	30 x (30-240)
			Ch 6	1000-1750	1.48	30 x (30-240)
			Ch 7	1940-2040	0.22	30 x (30-240)
			Ch 8	2265-2380	0.26	30 x (30-240)
			PMD1	310 - 377	Broadband	30 x 15
			PMD2	450 - 525	Broadband	30 x 15
			PMD3	617 - 705	Broadband	30 x 15
			PMD4	805 - 900	Broadband	30 x 15
			PMD5	1508-1645	Broadband	30 x 15
			PMD6	2265-2380	Broadband	30 x 15
			PMD7 (45°)	802 - 905	Broadband	30 x 15

Table 3.7 – Summary of the main characteristics of SCIAMACHY instruments onboard Envisat-1.

The core element of SCIAMACHY is a high resolution grating spectrometer, operating in eight overlapping channels over the spectral range 0.24 - 2.38  $\mu\text{m}$  (see Table 3.7). Observed spectra are corrected for polarization effects using data from the PMDs as in GOME. SCIAMACHY measures the polarization of the incoming light perpendicular to its optical plane in six different spectral bands indicated in Table 3.7. In addition, a seventh PMD sensor measures the polarization component at 45°, useful in the limb mode case. SCIAMACHY is also equipped with a calibration unit that provides in-flight spectral and radiometric calibration capability. It contains two calibration lamps: a spectral line source that provides fine spectral lines with well-known and stable wavelengths over the entire SCIAMACHY wavelength range; a "white light source" that provides a rather uniform illumination ( $\sim$  blackbody) over the entire SCIAMACHY wavelength range.

The Medium Resolution Imaging Spectrometer (MERIS) is a push broom imaging spectrometer onboard Envisat-1, which measures the solar reflected radiation from the Earth from 0.4 to 1.05  $\mu\text{m}$ , with programmable spectral band position and width between 2.5 and 20 nm (see online at <http://envisat.esa.int/instruments/meris>). In accordance with the mission goals and priorities of MERIS instrument, the 15 spectral bands indicated in Table 3.8 have been derived for oceanographic and interdisciplinary applications.

A wide swath of 1150 km is observed thus achieving global coverage within three days. Because of the dependence on the visible to near-IR spectral range, MERIS observations can only be performed with sufficient sun illumination (a sub-satellite sun elevation greater than  $10^\circ$  is required, obtained 43.5 min per orbit). The 1150-km-wide swath is divided into five segments covered by five identical cameras having corresponding fields of view with a slight overlap between adjacent cameras. Each camera images an across-track stripe of the Earth's surface onto the entrance slit of an imaging optical grating spectrometer. This entrance slit is imaged through the spectrometer onto a two-dimensional CCD array, thus providing spatial and spectral information simultaneously. Full spatial resolution data is 300 m at nadir and reduced spatial resolution data is achieved by on board combination of  $4 \times 4$  adjacent pixels across-track and along-track resulting in a resolution of approximately 1200 m at nadir.

The spatial, spectral and radiometric programmability of MERIS is justified by the different scales of the various targets to be observed and the diversity of their spectral and radiometric properties respectively. The advantage of the programmability is not only to select width and position of a respective spectral band, but also to be able to tune the dynamic range thus make it adaptable to different target observation, which may have become of a (higher) priority during the MERIS mission.

MERIS calibration is performed at the orbital South Pole, when a reference diffuser is illuminated by the Sun. During calibration, the Earth-view port is closed and the sun-view port opened to provide, in the case of radiometric calibration, a uniform radiance source, and in the case of spectrometric calibration, a radiance source with a spectral signature. The reference for the absolute calibration is based on an assumed solar irradiance at the time of the calibration. The radiance is adjusted from this reference by applying appropriate seasonal scaling.

Envisat	Launch Date	Instrument	Nominal Spectral Channels (nm)		Spectral resolution (nm)	Nadir Pixel Size (m <sup>2</sup> )
			Ch	Wavelength Range (nm)		
1	1 March 2002	MERIS	Ch 1	407 – 417	Broadband	300 x 300 (1200 x 1200)
			Ch 2	437 – 447		
			Ch 3	485 – 495		
			Ch 4	505 – 515		
			Ch 5	555 – 565		
			Ch 6	615 – 625		
			Ch 7	660 – 670		
			Ch 8	678 – 685		
			Ch 9	704 – 714		
			Ch 10	750 – 758		
			Ch 11	759 - 763		
			Ch12	771 - 786		
			Ch13	855 - 875		
			Ch 14	880 - 890		
			Ch 15	895 - 905		

Table 3.8 – Summary of the main characteristics of MERIS instruments onboard Envisat-1.

The Advanced Along Track Scanning Radiometer (AATSR) onboard Envisat-1 is the third in the ATSR series, with the prime objective of measuring the global Sea Surface Temperature (SST) at high levels of accuracy (0.3 K or better), ensuring continuity of the ATSR-1 and ATSR-2 data sets and providing a unique 10 year near-continuous data set required for climate research and modelling.

The AATSR instrument provides observations of the same surface scene at two different angles through the intervening atmosphere. A single scan sweeps around from the nadir position to a point about 900 km along the satellite's track. A few minutes after acquiring a forward view of the scene, the satellite is directly above it and the nadir view is acquired. As the two views of the same scene are taken through different atmospheric path lengths, it is possible to calculate a correction for the effect of atmospheric absorption, which makes AATSR also very suitable for land surface

studies, particularly vegetation. In the nadir-viewing mode the spatial resolution is  $1.0 \times 1.0 \text{ km}^2$ . At the centre of the forward view the pixel size results in 2.0 km length along track and 1.5 km across track. The AATSR has seven spectral channels in the VIS, near IR and thermal IR (see Table 3.9).

The instrument carries on-board calibration systems: for the IR channels it uses two black bodies, viewed every scan; for the VIS channels a sample of solar radiation scattered from a diffuser plate is viewed once per orbit.

Envisat	Launch Date	Instrument	Nominal Spectral Channels (nm)		Spectral resolution (nm)	Pixel Size ( $\text{Km}^2$ )
1	1 March 2002	AATSR	Ch1	530 - 580	Broadband	1.0 x 1.0 (Nadir view)
			Ch2	634 - 684		
			Ch3	840 - 890		2.0 x 1.5 (Forward view)
			Ch4	1520 - 1700		
			Ch5	3400 - 4120		
			Ch6	9800 - 11900		
			Ch7	10900 - 13100		

Table 3.9 – Summary of the main characteristics of AATSR instrument onboard Envisat-1.



## Chapter 4

# Computer codes used

### 4.1 Introduction

The instruments onboard satellites measure radiation, therefore the interpretation of their data requires the study of radiative transfer in the atmosphere. Since the transfer of solar and terrestrial radiation represents the prime physical process that drives the circulation of the atmosphere and the ocean, an understanding of climate and the mechanisms of climatic changes also requires detailed understanding of radiative processes and the radiative energy balance in the earth-atmosphere system.

The radiative transfer codes are computer-based programs that allow for modelling the radiation transfer processes occurring in the atmosphere and the interactions with the surface. The utilization of the radiative transfer codes stems from two key foundations: i) the atmosphere is an obscurant to be mathematically eliminated from the field of view; ii) the atmosphere is the holder of the desired signature, providing unique information of its instantaneous state. The first point of view requires the separation between the target (surface) and the atmospheric effects and is usually referred to as atmospheric correction. The latter is the one adopted in the present work, since the aim is the characterization of the atmospheric aerosol and cloud properties, using the spectroscopic signature of the atmosphere.

The radiative processes are addressed in these codes by suitable physical and mathematical models/algorithms. The modelling has sometimes to be simplified due to physical limitations imposed by the computing facilities (computer time is a concern) while keeping acceptable levels of accuracy.

The most important features of the radiative transfer codes used in the present work are described in the next sections. The method developed for the determination of aerosol properties makes use of the Second Simulation of the Satellite Signal in the Solar Spectrum (6S) code, described by Vermote et al. (1997a). The methodology for the cloud properties estimates presented uses instead the System for Transfer of Atmospheric Radiation

(RSTAR) and the Comprehensive Analysis Program for Cloud Optical Measurement (CAPCOM) packages available from the OpenCLASTR (Center for Climate System Research - CCSR – University of Tokyo).

## 4.2 The radiative transfer code 6S

The 6S is a radiative transfer code that permits the simulation of satellite, airborne or ground-based radiation measurements (reflectance or radiance) in cloudless atmospheres, between 0.25 and 4.0  $\mu\text{m}$ , for a wide range of atmospheric and surface conditions, fully described by Vermote et al. (1997b).

Assuming that the surface presents a uniform Lambertian reflectance and that the atmosphere is plane-parallel (see Chapter 2), where the radiance  $I_\lambda$  emerging from the surface of the Earth is independent of the direction, the monochromatic reflectance ( $\rho_\lambda$ ) can be written as:

$$\rho_\lambda = \frac{\pi I_\lambda}{\mu_0 \cdot F_{0\lambda}} \quad (4.1)$$

where  $I_\lambda$  is the monochromatic radiance,  $\mu_0$  the cosine of the solar zenith angle and  $F_{0\lambda}$  the monochromatic incident solar flux density perpendicular to the incident beam at the TOA. The reflectance obtained at the TOA is calculated in 6S using the following equation (the subscript  $\lambda$  is omitted for simplicity):

$$\begin{aligned} \rho^{TOA}(\mu_0, \mu, \phi - \phi_0) &= t^{gas}(\mu_0, \mu, U^{gas}) \\ &\times \left\{ \rho^{Ray}(\mu_0, \mu, \phi - \phi_0) + \left[ \rho^{Ray+Aer}(\mu_0, \mu, \phi - \phi_0) - \rho^{Ray}(\mu_0, \mu, \phi - \phi_0) \right] \right. \\ &\left. \times t^{H_2O}(\mu_0, \mu, \frac{1}{2} U_{H_2O}) + t(\mu_0) \times t(\mu) \times \frac{\rho^{surf}}{1 - S\rho^{surf}} \times t^{H_2O}(\mu_0, \mu, U_{H_2O}) \right\} \end{aligned} \quad (4.2)$$

where  $\mu$  is the cosine of the observation (satellite) zenith angle,  $\phi - \phi_0$  the relative azimuth angle,  $t^{gas}$  the gaseous transmission due to six different atmospheric gases ( $O_2, O_3, CO_2, CH_4, N_2O, CO$ ),  $t^{H_2O}$  the water vapour transmission,  $\rho^{Ray}$  the molecular



scattering reflectance (Rayleigh contribution),  $\rho^{Ray+Aer}$  the atmospheric reflectance (Rayleigh and aerosol contributions),  $t(\mu_0)$  and  $t(\mu)$  are the transmission in the incident and observation (satellite) directions, respectively,  $\rho^{surf}$  the surface reflectance, and  $S$  the spherical albedo that accounts for successive reflections and scattering between the surface and the atmosphere.

The gaseous transmission is calculated for the incident, observing and total paths, considering seven different atmospheric gases ( $O_2, O_3, CO_2, CH_4, N_2O, CO, H_2O$ ), using two random exponential band models: the Goody model for water vapour (Goody 1964) and the Malkmus (1967) model for the other gaseous species are adopted. The spectroscopic data used in the model are taken from the AFGL atmospheric absorption line parameters compilation (1991 edition) described by Rothman et al. (1983). The transmission of each gas is calculated between 0.25 and 4.0  $\mu\text{m}$  with a spectral resolution of  $10 \text{ cm}^{-1}$  and the transmission due to all considered gases, except water vapour, is put as the product of each single transmission:

$$t^{gas}(\mu_0, \mu, U^{gas}) = \prod_{i=1}^6 t^i(\mu_0, \mu, U^i) \quad i = O_2, O_3, CO_2, CH_4, N_2O, CO \quad (4.3)$$

where  $U^i$  is represents the absorber amount.

The interaction between water vapour absorption and aerosol scattering is taken into account in an approximate way, considering an average case where half of the atmospheric water vapour absorbs the aerosol path radiance.  $\rho^{Ray+Aer}(\mu_0, \mu, \phi - \phi_0) - \rho^{Ray}(\mu_0, \mu, \phi - \phi_0)$  in equation 4.2, represents an estimate of the aerosol intrinsic reflectance.

The molecular scattering reflectance is calculated using an approximation that saves computer resources but maintains a good accuracy (Vermote and Tanré 1992):

$$\rho^{Ray}(\mu_0, \mu, \phi - \phi_0) = \rho^{Ray^1}(\mu_0, \mu, \phi - \phi_0) + (1 - e^{-\tau/\mu_0})(1 - e^{-\tau/\mu})\Delta\tau \quad (4.4)$$

The first term represents the single scattering contribution and the second gives a rough estimate of the higher orders of scattering.

The atmospheric reflectance (mixed Rayleigh-aerosol atmosphere) represented in equation 4.2 by  $\rho^{Ray+Aer}(\mu_0, \mu, \phi - \phi_0)$ , as well as the transmissions ( $t(\mu_0)$  and  $t(\mu)$ ) and the spherical albedo  $S$  are calculated using the Successive Orders of Scattering (SOS) method described in section 2.3.1.

The atmospheric scattering functions (atmospheric reflectance, total transmission and spherical albedo) are calculated at ten discrete reference wavelengths well distributed over the solar spectrum (0.400, 0.488, 0.515, 0.550, 0.633, 0.694, 0.860, 1.536, 2.250 and 3.750  $\mu\text{m}$ ), corresponding to atmospheric windows used in remote sensing. These atmospheric functions can be obtained at any wavelength value, interpolating between 0.4 and 3.75  $\mu\text{m}$  and extrapolating for the two extreme intervals 0.25 – 0.4  $\mu\text{m}$  and 3.75 – 4.0  $\mu\text{m}$ . The spectral integration over a certain spectral band is done with a spectral resolution of 2.5 nm. The code contains the extraterrestrial solar irradiance values between 0.25 and 4.0  $\mu\text{m}$ , with a spectral resolution of 2.5 nm, taken from Neckel and Labs (1984). The variability of the solar constant during the year is taken into account applying a multiplicative correcting factor to the mean solar irradiance values (Paltridge and Platt 1976).

The radiances / reflectances may be computed using 6S for any values of the zenith and azimuth angles that may be given directly as input to the code. Otherwise, there are available routines conceived to calculate the solar geometry and the observation geometries of several satellite sensors such as the Meteosat, GOES, NOAA-AVHRR

The 6S radiance / reflectance calculations may be referred to a single wavelength (monochromatic) or to a spectral interval of any length. In the last case, if the calculations correspond to the simulation of instrumental measurements, it is possible to specify its spectral response function, in order to weight the simulated values and make them comparable to the actual measurements (see equation 3.3, section 3.3.1.1). The code also foresees the possibility to simulate several widely used satellite sensor observations, containing in the database their spectral band ranges and the respective spectral response functions. Among the considered satellite sensors are the visible Meteosat and GOES bands, the visible (VIS) and near infrared (NIR) AVHRR bands for NOAA-6 through 11 and MODIS bands 1 to 7 (see table 3.6).

The 6S radiative transfer code not only handles homogeneous lambertian surfaces, but is also prepared to deal with the Bi-directional Reflectance Distribution Function -

BRDF - (defined in section 2.6.2) of several surface types. If the lambertian surface approximation is adopted, the user may directly supply the surface spectral reflectance values or select a typical surface type from the code database, which contains the mean spectral reflectance values correspondent to: clear water (Viollier 1980), sand (Staetter and Schroeder 1978), vegetation (Manual of Remote Sensing, 1983) and lake water (Kondratyev 1969). When the BRDF is considered in the 6S calculations, the user can enter the directional reflectance values for a defined grid of solar and viewing zenith and azimuth angles. In addition, the spherical albedo of the surface has to be specified, as well as the observed reflectance in the selected geometry. The values of the directional reflectance are assumed spectrally independent, so that the BRDF has to be specified at the wavelength for monochromatic conditions or as a mean value over a spectral band. If these values are not available, the user may select from a variety of BRDF models available in 6S (eight for land surfaces and one for ocean surface), and enter the respective necessary parameters (Vermote et al. 1997b). The ocean BRDF model defined by Morel (1988) is used in the present work; the input parameters are the wind speed, the wind direction, the salt concentration and the pigment concentration. The model takes into account the effects of foam and ocean roughness, both for isotropic and directional wind.

The vertical profile of the atmospheric gaseous compounds (water vapour and ozone) is taken into account in 6S considering 34 atmospheric levels distributed from the ground to an altitude of 100 km, considered here the TOA (from 0 to 25 km step of 1 km; from 25 to 50 km step of 5 km; two values at 70 and 100 km). The 6S database includes six atmospheric models, consisting of pressure, temperature, water vapour and ozone vertical profiles at the 34 atmospheric levels, representative of the following standard atmospheres: tropical, mid-latitude summer, mid-latitude winter, sub-arctic summer, sub-arctic winter and US standard 62, all taken from McClatchey et al. (1971). In addition, it is possible to define the atmospheric model entering the altitude, pressure, temperature, water vapour and ozone on 34 levels, or simply to provide the water vapour and ozone total column contents (the profile is automatically taken from the US standard 62). Finally it is also possible to turn off the gaseous absorption.

The 6S offers a wide range of possibilities with respect to aerosol characterization, enabling the use of either standard models available from the database or user-defined microphysical / optical properties. Three of the standard models - Continental, Maritime

and Urban - correspond to a mixture of the four basic components of the *International Radiation Commission* (1983): dust-like, oceanic, water-soluble and soot components. The optical properties correspondent to these standard tropospheric models are calculated considering an external mixing of the basic components, thus making a weighted average of the components optical properties, using the percentage density values ( $Pd_j$ , where  $j$  refers to each component), i.e. the aerosol fraction by density of the component  $j$ , indicated in Table 4.1. The user may also define other aerosol models specifying the new percentage densities of the basic components.

	Dust-like	Water-soluble	Oceanic	Soot
<b>Continental</b>	$2.26490 \times 10^{-6}$	0.938299		0.0616987
<b>Maritime</b>		0.999579	$4.20823 \times 10^{-4}$	
<b>Urban</b>	$1.65125 \times 10^{-7}$	0.592507		0.407492

Table 4.1 – Percentage density of particles from each of the four basic components that define the following standard tropospheric aerosol models: Continental, Maritime and Urban.

The extinction, scattering and absorption coefficients of the resultant model are then given by:

$$\beta_{\lambda}^e = \sum_{j=1}^4 Pd_j \cdot \beta_{\lambda_j}^e \quad (4.6)$$

$$\beta_{\lambda}^s = \sum_{j=1}^4 Pd_j \cdot \beta_{\lambda_j}^s \quad (4.7)$$

$$\beta_{\lambda}^a = \sum_{j=1}^4 Pd_j \cdot \beta_{\lambda_j}^a \quad (4.8)$$

where  $\beta_{\lambda_j}^e$ ,  $\beta_{\lambda_j}^s$  and  $\beta_{\lambda_j}^a$  values are contained in the 6S database, obtained from the *International Radiation Commission* (1983).

Analogously, the asymmetry parameter ( $g_\lambda$ ) and phase function ( $P_\lambda(m, \Theta)$ ) can be written as:

$$g_\lambda = \frac{1}{\beta_\lambda^s} \sum_{j=1}^4 Pd_j \cdot g_{\lambda_j} \cdot \beta_{\lambda_j}^s \quad (4.9)$$

$$P_\lambda(m, \Theta) = \frac{1}{\beta_\lambda^s} \sum_{j=1}^4 Pd_j \cdot P_\lambda(m, \Theta)_j \cdot \beta_{\lambda_j}^s \quad (4.10)$$

where  $g_{\lambda_j}$  and  $P_\lambda(m, \Theta)_j$  values are once again archived in the 6S database, obtained from the *International Radiation Commission* (1983). The single scattering albedo is obtained applying directly equation 2.16.

The 6S database contains also pre-computed optical properties of a desert aerosol model described in Shettle (1984), a stratospheric aerosol model obtained from measurements at Mauna Loa (Hawaii) during the El Chichon eruption in Mexico and described by King et al. (1984), and a biomass burning aerosol model defined from ground-based sun-photometer measurements taken in Amazonia (Remer et al. 1996).

The user-defined aerosol options allow for directly supplying the spectral (at the ten wavelengths indicated before) aerosol optical properties - extinction and scattering coefficients, phase function, asymmetry parameter and single scattering albedo.

It is also possible to provide the code with sun-photometer measurements of the radius and volume size distribution or with the aerosol microphysical properties using afterwards one of three size distribution functions available in 6S. In any of these cases the spectral complex refractive index at the ten reference wavelengths has to be supplied. One of the particle size distribution functions available is the Junge power-law (Junge 1952):

$$n(r) = cr_0^\alpha \left( \frac{1}{r} \right)^\alpha \quad (4.11)$$

where the constant  $c$  is fixed by the total number of particles with radius  $r_0$ , being  $r_0$  an arbitrary radius, and  $\alpha$  is the Junge distribution parameter that varies between 3 and 5. If this function is selected, the size distribution parameter ( $\alpha$ ) has to be specified.

Another function available to describe the particle size distribution is the modified gamma distribution first used by Deirmendjian (1964) to calculate the scattering and polarization properties of water clouds and haze:

$$n(r) = A \left( \frac{r}{r_0} \right)^\alpha \exp \left[ -b \left( \frac{r}{r_0} \right)^\gamma \right] \quad r_0 = 1 \mu m \quad (4.12)$$

where  $A$  is related to the total number of particles with radius  $r_0$  and the constants  $b$ ,  $\alpha$  and  $\gamma$  are the modified gamma distribution adjustable parameters that need to be given as input to the code.

Finally the third particle size distribution function available is a log-normal distribution function, already presented (equation 2.31) and discussed in chapter 2. This size distribution is multimodal, allowing up to four modes. For each of the modes the percentage density of particles ( $Pd_j$ ), the standard deviation ( $\sigma_j$ ) and the mode radius ( $r_{Mj}$ ) are required.

The spectral complex refractive index ( $m_\lambda$ ) and the minimum and maximum radii of the aerosol particles ( $R_{\min}$ ,  $R_{\max}$ ) have to be specified for any of the adopted size distribution functions since  $m_\lambda$  is required for the Mie calculations (spherical particles are assumed; see chapter 2) whereas  $R_{\min}$  and  $R_{\max}$  allow for the integration of the aerosol optical properties under the assumption of independent scattering (see section 2.3) defined by equations 2.38 through 2.41. Computationally, the aerosol properties are integrated as follows and the volume extinction ( $\beta_\lambda^e$ ), scattering ( $\beta_\lambda^s$ ) and absorption ( $\beta_\lambda^a$ ) coefficients and the phase function ( $P_\lambda(m, \Theta)$ ) become:

$$\beta_\lambda^e(m) = \sum_{R_{\min}}^{R_{\max}} \pi \cdot r^2 \cdot Q_\lambda^e(r, m) \cdot n(r) \cdot \Delta r \quad (4.13)$$

$$\beta_{\lambda}^s(m) = \sum_{R_{\min}}^{R_{\max}} \pi \cdot r^2 \cdot Q_{\lambda}^s(r, m) \cdot n(r) \cdot \Delta r \quad (4.14)$$

$$\beta_{\lambda}^a(m) = \sum_{R_{\min}}^{R_{\max}} \pi \cdot r^2 \cdot Q_{\lambda}^a(r, m) \cdot n(r) \cdot \Delta r \quad (4.15)$$

$$P_{\lambda}(m, \Theta) = \sum_{R_{\min}}^{R_{\max}} \frac{\lambda^2}{2\pi \cdot \sigma_{\lambda}^s(r, m)} \cdot (|S_1|^2 + |S_2|^2) \cdot n(r) \cdot \Delta r \quad (4.16)$$

where  $\Delta r$  is defined as follows:

$$\log\left(\frac{r + \Delta r}{r}\right) = 0.03 \quad (4.17)$$

When the log-normal size distribution is considered with more than one mode (mixture of particles from different origins) the aerosol optical properties are calculated considering that there is external mixing, as for the standard aerosol models obtained from the basic components (see Table 4.1), and thus equations 4.6 through 4.10 are used as well.

The extinction, scattering and absorption coefficients calculated from equations 4.6 through 4.8 or from equations 4.13 through 4.15, are normalized in the code to the extinction coefficient at  $0.55 \mu\text{m}$  ( $\beta_{\lambda \text{ norm}}^{e,s,a} = \frac{\beta_{\lambda}^{e,s,a}}{\beta_{0.55\mu\text{m}}^e}$ ), in such a way that the value of the normalized extinction coefficient at  $0.55 \mu\text{m}$  is one.

### 4.3 The radiative transfer code RSTAR

A brief description of this code is given since it does not constitute the main radiative transfer engine used to carry on this work, but simply represents a tool utilized to

set up Look-Up Tables (LUTs) of radiative quantities, necessary to apply the CAPCOM code, described in the next section, to the retrieval of cloud properties.

A look-up table is a sort of dataset that contains in the present case tabulated results of radiative transfer calculations and can then be used to retrieve radiative properties saving computational time and maintaining the accuracy of the radiative transfer code.

The RSTAR radiative transfer code allows for the simulation of radiation fields in the atmosphere-surface system (surface or satellite levels) in the presence of clouds and / or aerosols, at wavelengths between 0.2 and 200  $\mu\text{m}$ , assuming similarly to 6S that the atmosphere is plane-parallel (see chapter 2), divided into several homogeneous sub layers. The code solves the radiative transfer equation (equations 2.8 and 2.9) to calculate radiances with a combined discrete-ordinate-matrix-operator method (Nakajima and Tanaka 1986, 1988) and the gaseous absorption is obtained by a three-term correlated k distribution method (Kneisys et al. 1988). Twenty-eight different gaseous species are taken into account, namely:  $\text{H}_2\text{O}$ ,  $\text{CO}_2$ ,  $\text{O}_3$ ,  $\text{N}_2\text{O}$ ,  $\text{CO}$ ,  $\text{CH}_4$ ,  $\text{O}_2$ ,  $\text{NO}$ ,  $\text{SO}_2$ ,  $\text{NO}_2$ ,  $\text{NH}_3$ ,  $\text{HNO}_3$ ,  $\text{OH}$ ,  $\text{HF}$ ,  $\text{HCl}$ ,  $\text{HBr}$ ,  $\text{HI}$ ,  $\text{ClO}$ ,  $\text{OCS}$ ,  $\text{H}_2\text{CO}$ ,  $\text{HOCl}$ ,  $\text{N}_2$ ,  $\text{HCN}$ ,  $\text{CH}_3\text{Cl}$ ,  $\text{H}_2\text{O}_2$ ,  $\text{C}_2\text{H}_2$ ,  $\text{C}_2\text{H}_6$  and  $\text{PH}_3$ . The code also estimates the downward and upward fluxes, integrating the radiance values as shown in equations 2.68 and 2.69. In addition, the reflectance and transmission values associated with the reflected (upward) diffuse flux density and transmitted total (diffuse + direct) downward flux density, respectively, can be estimated from the downward and upward fluxes (equations 2.70 and 2.71).

The radiance and flux calculations are either monochromatic or integrated in spectral bands, whose width and spectral resolution are defined by the user. It is also possible to specify the spectral response function of an instrument to simulate satellite measurements (section 3.3.1.1). The spectral solar irradiance values used are taken from LOWTRAN7 code (Kneisys et al. 1988).

The geometry is defined by the user and consists of the solar zenith angle, observation (satellite) zenith angle and corresponding relative azimuth angles (see section 2.2 – Figure 2.1).

The surface of the Earth is considered Lambertian and its reflectance has to be specified. In addition, there is a model for the ocean surface that considers the wind speed (Nakajima and Tanaka 1983). As for the atmospheric vertical characterization, the RSTAR code considers 50 default levels, distributed from the ground to an altitude of 120 km



considered as the TOA (from 0 to 25 km step of 1 km; from 25 to 50 km step of 2.5 km; from 50 to 120 km step of 5 km). The code database includes six atmospheric profiles (tropical, mid-latitude summer, mid-latitude winter, high-latitude summer, high-latitude winter and US standard) taken, similarly to 6S, from McClatchey et al. (1971), comprising height, pressure, temperature and concentration of the twenty-eight gaseous species stated before. A different number of atmospheric layers can also be used, specifying the respective levels.

As for the particle characterization (clouds and / or aerosols), the RSTAR code allows for simulating the presence of clouds, aerosols or both simultaneously as a mixture of particle polydispersions. The code contains a dataset of eleven particle volume concentration profiles and corresponding spectral complex refractive index values taken from d'Almeida et al. (1991), typical of water, ice, dust-like, soot, volcanic-ash, 75% H<sub>2</sub>SO<sub>4</sub>, rural, sea spray, urban, generic tropospheric aerosol and yellow sand. All particle types are considered spherical, including ice particles, therefore Mie theory is used at all times. The results from Mie theory are tabulated inside the code and hence the particle optical properties such as the volume extinction ( $\beta_{\lambda}^e$ ), scattering ( $\beta_{\lambda}^s$ ) and absorption ( $\beta_{\lambda}^a$ ) coefficients, phase function ( $P_{\lambda}(m, \Theta)$ ), single scattering albedo ( $\varpi_{\lambda}$ ) and asymmetry parameter ( $g_{\lambda}$ ) can be calculated from equations 2.38, 2.39, 2.40, 2.41, 2.16 and 2.42, respectively.

The particle size distribution may be described by the same functions available in 6S: Junge power-law, modified gamma or log-normal distribution functions given respectively by equations 4.11, 4.12 and 2.31, providing the corresponding size distribution parameters (see previous section). Any of these size distributions may be combined to get a multimodal function, allowing up to four modes, considering an external mixing and thus equations 4.6 through 4.10 can be used to calculate the optical properties of the particles.

The scattering phase function of optically thick media, like clouds and high aerosol loads, is strongly peaked in the forward direction. The discrete-ordinates method, used in the RSTAR code, requires the phase function obtained from Mie theory represented as an expansion of Legendre polynomials (see end of section 2.3.1), which in these cases has to be of high-order to succeed in reproducing the asymmetrical features of the phase function (Levoni et al. 2001). However, the use of high-order polynomials is many times difficult due to the computer resources available. Consequently approximations have to be taken

into consideration as the delta-M approximation, used in RSTAR, that consists of expressing the phase function as a sum of a Dirac  $\delta$  function (see section 2.2) representing the sharp forward scattering peak and a truncated series expansion corresponding to the phase function without the peak (Wiscombe 1977; Nakajima and Tanaka 1988). The phase function expressed in terms of the cosine of the scattering angle (equation 2.30)  $P(\cos\Theta)$  can be thus approximated as:

$$P(\cos\Theta) \approx 2f\delta(1-\cos\Theta) + (1-f)P^*(\cos\Theta) \quad (4.18)$$

The factor 2 arises from the phase function normalization (equation 2.29),  $f$  is the truncation fraction and  $P^*(\cos\Theta)$  the truncated function that represents only the “smoother” part of the phase function ( $P(\cos\Theta)$ ) requiring for that reason a smaller number of Legendre polynomials to be described. This approximation of the phase function allows for solving the radiative transfer equation (equations 2.10 and 2.11 with the source function given by equation 2.15) using  $P^*(\cos\Theta)$ , which greatly diminishes the computational time since it is well represented by a few polynomial terms. The approximation originates fluctuations in the phase function that hardly affect the multiple scattering since the intensity field becomes smoother and more isotropic when the scattering orders increase, masking the details of the phase function. However, it is not suitable for the singly scattered radiation (first term of equation 2.15) that relies on the realistic features of the phase function to be accurately estimated. The method used in RSTAR to overcome this fact consists of subtracting the singly scattered radiation obtained with the phase function approximation from the total scattered radiation (all orders of scattering) and then adding the exact singly scattered radiation calculated using the original phase function ( $P(\cos\Theta)$ ) obtained from Mie theory.

#### 4.4. A code for the retrieval of cloud properties - CAPCOM

The CAPCOM is a widely known code (Nakajima and King 1990; Nakajima and Nakajima 1995; Kawamoto et al. 2001) for the simultaneous retrieval of cloud optical thickness, effective particle radius and cloud top temperature from satellite radiance measurements in three spectral intervals (one in the VIS, one in the NIR and one in thermal infrared), corresponding to atmospheric windows (avoiding as much as possible gas absorption bands).

The physical basis of this algorithm arises from the fact that the cloud reflected solar radiance in the VIS spectral region depends mainly on the cloud optical thickness but is almost independent of the droplet size: due to the fact that the imaginary part of the liquid water / ice refractive index is extremely small at these wavelengths ( $m_{i\lambda} \approx 10^{-9}$ ), there is practically no cloud absorption (see equation 2.20) and the radiation can penetrate deeply into the cloud allowing for the determination of large optical thickness values. In contrast, the cloud reflected radiation at NIR wavelengths is quite sensitive to droplet size since the imaginary part of the liquid water / ice refractive index is much higher ( $m_{i\lambda} \approx 10^{-3}$ ), therefore constituting an appropriate spectral region for the effective particle radius retrieval (equation 2.32). The thermal infrared spectral region (hereinafter IR) is instead indicated for the cloud top temperature determination (see section 2.4).

The method relies on the comparison between the modelled cloud radiances in the three spectral bands and the corresponding satellite radiance measurements corrected to yield the cloud signal. The spectral response functions of the satellite sensor, corresponding to the selected spectral channels, are taken into account as described in section 3.3.1.1 (equation 3.3). The radiance reaching a satellite ( $I_{\lambda_1}^{sat}$ ), in the VIS spectral band (here denoted by  $\lambda_1$ ), from a plane-parallel cloudy atmosphere (monolayer) with an underlying lambertian surface can be modelled as:

$$I_{\lambda_1}^{sat}(\tau, r_{eff}, Z^c, D; \mu_0, \mu, \phi - \phi_0) \cong I_{\lambda_1}^c(\tau^c, r_{eff}^c, Z^c, D; \mu_0, \mu, \phi - \phi_0) + t_{\lambda_1}^{tot}(\tau, r_{eff}; \mu_0) \cdot t_{\lambda_1}^{tot}(\tau, r_{eff}; \mu) \frac{\rho_{\lambda_1}^{surf}}{1 - S_{\lambda_1}^c(\tau^c, r_{eff}^c, Z^c, D) \rho_{\lambda_1}^{surf}} \frac{\mu_0 \cdot F_{0\lambda_1}}{\pi} \quad (4.19)$$

where  $I_{\lambda}^c$  is the radiance reflected by the cloud layer,  $t_{\lambda}^{tot}$  the total atmospheric transmission (from the TOA to the surface),  $\rho_{\lambda}^{surf}$  the surface reflectance,  $S_{\lambda}^c$  the cloud spherical albedo,  $F_{0\lambda}$  the TOA solar flux density in the spectral band considered,  $\tau$  and  $\tau^c$  the optical thicknesses of the atmosphere and cloud layer, respectively,  $r_{eff}$  the effective radius,  $Z^c$  the cloud top height,  $D$  the cloud geometrical thickness,  $\mu_0$  and  $\mu$  are the cosines of the solar and satellite zenith angles, and  $\phi - \phi_0$  is the relative azimuth angle, as already mentioned before. The second term of equation 4.19 thus represents the surface reflected solar radiance attenuated by the atmosphere and transmitted through the cloud in the sun-surface-satellite path.

In the NIR spectral region ( $\lambda_2$ ) the satellite modelled radiance ( $I_{\lambda_2}^{sat}$ ) is roughly given by (see end of section 2.2):

$$\begin{aligned}
I_{\lambda_2}^{sat}(\tau, r_{eff}, ew, Z^c, D; \mu_0, \mu, \phi - \phi_0) &\cong t_{\lambda_2}^a(ew^a; \mu_0) t_{\lambda_2}^a(ew^a; \mu) I_{\lambda_2}^c(\tau^c, r_{eff}, Z^c, D; \mu_0, \mu, \phi - \phi_0) \\
&+ t_{\lambda_2}^a(ew^a; \mu) \cdot [1 - t_{\lambda_2}^c(\tau^c, r_{eff}, Z^c, D; \mu) - \rho_{\lambda_2}^c(\tau^c, r_{eff}, Z^c, D; \mu)] B_{\lambda_2}(T^c) \\
&+ t_{\lambda_2}^{tot}(\tau, r_{eff}, ew, Z^c, D; \mu) \frac{1 - \rho_{\lambda_2}^{surf}}{1 - S_{\lambda_2}^c(\tau^c, r_{eff}, Z^c, D) \rho_{\lambda_2}^{surf}} \cdot B_{\lambda_2}(T^{surf}) \\
&+ t_{\lambda_2}^{tot}(\tau, r_{eff}, ew, Z^c, D; \mu_0) t_{\lambda_2}^{tot}(\tau, r_{eff}, ew, Z^c, D; \mu) \frac{\rho_{\lambda_2}^{surf}}{1 - S_{\lambda_2}^c(\tau^c, r_{eff}, Z^c, D) \rho_{\lambda_2}^{surf}} \frac{\mu_0 \cdot F_{0\lambda_2}}{\pi} \\
&+ I_{\lambda_2}^{atm a}(ew^a, B_{\lambda_2}(T(z)); \mu) \\
&+ t_{\lambda_2}^a(ew^a; \mu) t_{\lambda_2}^c(\tau^c, r_{eff}, Z^c, D; \mu) \cdot I_{\lambda_2}^{atm b}(ew^b, B_{\lambda_2}(T(z)); \mu)
\end{aligned} \tag{4.20}$$

where  $I_{\lambda_2}^c$  is the radiance reflected by the cloud layer in the spectral band represented by  $\lambda_2$ ,  $t$  and  $\rho$  the transmission and reflectance, respectively, the superscripts  $a$  and  $b$  refer to the layers above ( $a$ ) and below ( $b$ ) the cloud and  $c$  the cloud layer itself,  $B_{\lambda_2}$  the Planck function (equation 2.56),  $T^c$  and  $T^{surf}$  the cloud top and surface absolute temperatures,

$I_{\lambda_2}^{atm\ a}$  the atmospheric emission from the layers above the cloud, and  $I_{\lambda_2}^{atm\ b}$  the atmospheric emission from the layers below the cloud, being both function of the atmospheric vertical temperature profile ( $T(z)$ ).  $ew$  is the equivalent water vapour amount, defined as:

$$ew = \int_{z=0}^{\infty} wv(z) \left[ \frac{P(z)}{P^{surf}} \right]^{0.9} \left[ \frac{T^{surf}}{T(z)} \right]^{0.5} dz \quad (4.21)$$

where  $P(z)$ ,  $T(z)$  and  $wv(z)$  are the atmospheric vertical profiles of pressure, temperature and water vapour amount as a function of the altitude ( $z$ ), being  $P^{surf}$  and  $T^{surf}$  the pressure and temperature at the surface level. The atmospheric vertical profiles are the same used in the RSTAR code, specified at identical atmospheric levels.

The second and third terms in equation 4.20 represent the cloud-emitted radiation attenuated by the atmosphere above the cloud and the surface emitted radiation attenuated by the atmosphere (from the surface to the satellite), respectively. The fourth term is the surface reflected solar radiance attenuated by the atmosphere in the sun-surface-satellite path and the last two terms correspond to the atmospheric emission above and below the cloud, being the latter attenuated by the cloud and atmosphere above it.

In the IR spectral region ( $\lambda_3$ ) the satellite modelled radiance ( $I_{\lambda_3}^{sat}$ ) can be approximated as the sum of the cloud top emitted radiation attenuated by the atmospheric layer above the cloud, the surface emitted radiation attenuated by the atmosphere (between the surface and the satellite), and the atmospheric emitted radiation from the layers above and below the cloud, being the last one attenuated by the cloud and atmosphere above it. The respective equation may then be written as:

$$\begin{aligned}
 I_{\lambda_3}^{sat}(\tau, r_{eff}, ew, Z^c, D; \mu) &\cong t_{\lambda_3}^a(ew^a; \mu) \cdot [1 - t_{\lambda_3}^c(\tau^c, r_{eff}, Z^c, D; \mu)] \cdot B_{\lambda_3}(T^c) \\
 &+ t_{\lambda_3}^{tot}(\tau, r_{eff}, ew, Z^c, D; \mu) \cdot (1 - \rho_{\lambda_3}^{surf}) \cdot B_{\lambda_3}(T^{surf}) \\
 &+ I_{\lambda_3}^{atm\ a}(ew^a, B_{\lambda_3}(T(z)); \mu) \\
 &+ t_{\lambda_3}^a(ew^a; \mu) \cdot I_{\lambda_3}^c(\tau^c, r_{eff}, Z^c, D; \mu) \cdot I_{\lambda_3}^{atm\ b}(ew^b, B_{\lambda_3}(T(z)); \mu)
 \end{aligned} \tag{4.22}$$

The code makes use of several LUTs that allow for saving computational time maintaining the accuracy on the retrievals, calculated using the radiative transfer code RSTAR described in the previous section. The LUTs contain the modelled values of the cloud reflected radiances, transmission, reflectance and cloud spherical albedo in the VIS and NIR selected bands, the atmospheric emitted radiation in the NIR and IR and the transmission values in the IR spectral band. These radiative quantities are determined for a grid of selected values of the cloud optical thickness ( $\tau^c$ ), cloud particle effective radius ( $r_{eff}$ ), cloud top temperature ( $T^c$ ), equivalent water vapour above the cloud ( $ew^a$ ) and equivalent water vapour of the cloud layer ( $ew^c$ ), solar zenith ( $\theta_0$ ), satellite zenith ( $\theta$ ), and relative azimuth ( $\phi - \phi_0$ ) angles.

The algorithm that uses the Newton-Raphson iterative method is started using first-guess values of the physical properties to retrieve - cloud optical thickness, effective radius and top temperature - taken from the LUT grid. The user must specify for each satellite pixel, the satellite-measured radiances in the VIS, NIR and IR spectral bands, as well as the latitude, longitude, solar zenith, satellite zenith and relative azimuth angles. In addition, the cloud type in accordance with the classification used by Liou (1976), or the cloud geometrical thickness has to be defined.

If the cloud geometrical thickness is user-defined, the cloud type is established from the current retrieval variables ( $\tau^c$ ,  $r_{eff}$  and  $T^c$ ) values according to the classification proposed by the International Satellite Cloud Climatology Project (ISCCP) (Rossow and Schiffer 1991; Rossow and Schiffer 1999) based on cloud optical thickness and top pressure thresholds. On the other hand, if the cloud type is the parameter used initially to

characterize the cloud, its geometrical thickness ( $D$ ) is estimated from the ratio of the liquid water path ( $W = \frac{2}{3} \tau^c \cdot r_{eff} \cdot \rho$ ) to the liquid water content ( $w$ ) as follows:

$$D = \frac{2}{3} \frac{\tau^c \cdot r_{eff}}{w} \rho \quad (4.23)$$

where  $\rho$  is the liquid water /ice density. The liquid water content ( $w$ ) values used here are tabulated in the code for each cloud type, as proposed by Liou (1976).

The cloud top height ( $Z^c$ ) and pressure ( $P^c$ ) are directly obtained from the cloud top temperature value ( $T^c$ ), interpolating linearly the atmospheric vertical profiles. The equivalent water vapour amount values can then be calculated from the pressure, temperature and water vapour profiles (equation 4.21), for the cloud layer ( $ew^c$ ) and for the layers above and below the cloud ( $ew^a$ ,  $ew^b$ ), since the vertical position of the cloud atmospheric layer is now defined by the physical properties of its top ( $T^c$ ,  $Z^c$  and  $P^c$ ) and by the cloud geometrical thickness ( $D$ ).

The modelled values of the cloud reflected radiances in the VIS, NIR and IR spectral bands ( $I_{\lambda_1}^{c \text{ model}}$ ,  $I_{\lambda_2}^{c \text{ model}}$  and  $I_{\lambda_3}^{c \text{ model}}$ ) are obtained from the LUTs, making use of the values of  $\tau^c$ ,  $r_{eff}$ ,  $T^c$ ,  $ew^a$ ,  $ew^c$ ,  $\theta_0$ ,  $\theta$  and  $\phi - \phi_0$ . On the other hand, the satellite-measured radiances in the same three spectral bands are corrected according to equations 4.19, 4.20 and 4.22 to get the radiance reflected by the cloud ( $I_{\lambda_1}^c$ ,  $I_{\lambda_2}^c$  and  $I_{\lambda_3}^c \equiv B_{\lambda_3}(T^c)$ ), subtracting the undesirable contribution terms. The physical properties necessary for these corrections (transmission, reflectance, spherical albedo and atmospheric emission) are obtained from linear interpolation of the LUTs, using the values of  $\tau^c$ ,  $r_{eff}$ ,  $T^c$ ,  $ew^a$ ,  $ew^c$ ,  $\theta_0$ ,  $\theta$  and  $\phi - \phi_0$  as well. The measured and modelled radiances in the three spectral channels are then compared, calculating the relative differences:

$$DIFF_{\lambda_i} = \left| \frac{I_{\lambda_i}^c - I_{\lambda_i}^{c \text{ model}}}{I_{\lambda_i}^c} \right| \quad i = 1,2,3 \quad (4.24)$$

The criterion to decide if the cloud optical thickness, cloud particle radius and cloud top temperature are within acceptable error limits is expressed by the condition:

$$\sum_{i=1}^3 DIFF_{\lambda_i} \leq 0.005 \quad (4.25)$$

If the convergence test is fulfilled then  $\tau^c$ ,  $r_{eff}$  and  $T^c$  are considered retrieved, otherwise the Newton-Raphson method is used to generate new values of these three cloud properties and the entire process is repeated until the condition in equation 4.25 is satisfied. In case the convergence condition is never fulfilled due for example to the generation of unexpected values of  $\tau^c$ ,  $r_{eff}$  or  $T^c$ , the code exits with a flag indicating that the retrieval was not accomplished.



## Chapter 5

# Methods used for aerosol and cloud characterization

### 5.1 Introduction

The present chapter documents the methodologies developed to characterize the aerosol and cloud properties, based on multi-spectral satellite measurements used in combination with radiative transfer techniques. The chapter is divided into two major sections. The first one describes the retrieval method of the aerosol optical parameters (scattering, extinction and absorption coefficients, single scattering albedo, phase function and asymmetry parameter calculated from the phase function) and aerosol optical thickness. The method relies on the combination of multi-spectral satellite data from different platforms (LEO and GEO) and radiative transfer calculations; the successive application of these quantities to assess the aerosol direct radiative forcing in the SW spectral region is also addressed in this section. The second major section illustrates the methodology for the retrieval of cloud properties (type, optical thickness, effective radius and top temperature), which is based on the use of multi-spectral satellite data and radiative transfer calculations. The majority of the chapter is dedicated to the aerosol thematic since it constitutes the core of the present thesis, being clouds addressed at a somewhat lower level, which serves as a starting point for the future research work.

The data used in both methodologies is described and the validation of the derived aerosol and cloud properties is discussed. The datasets are also presented along with the adopted strategy that relies on the study of several specific test cases.

## 5.2 Aerosol characterization and direct radiative forcing assessment

The method for the atmospheric aerosol characterization is developed having in mind principally strong aerosol outbursts that may often occur in certain regions of the Earth, affecting dramatically the local and regional climate and most likely generating changes in the global equilibrium (Haywood and Boucher 2000; Ramanathan et al. 2001; Kaufman et al. 2002). Focus is on aerosol events of different origin (desert and biomass burning types) that occur over the ocean, with the intention of comparing the resulting properties and their radiative impact on climate.

The method is based on LEO (GOME) and GEO satellite measurements used in combination with radiative transfer calculations with the aim of merging the good spectral resolution from GOME (see Section 3.3.2.1) and the unrivalled spatial and temporal resolution from GEO satellites (Costa et al. 1999), such as Meteosat (see Chapter 3, Section 3.3.1). The variation of aerosol microphysical properties in the GOME spectral reflectance fitting procedure to retrieve an actual effective aerosol class is a novelty introduced by the present algorithm. Torricella et al. (1999) fitted the measured to the correspondent simulated spectra varying the aerosol optical thickness only and selecting among several literature aerosol classes. The radiative transfer calculations are done here using the 6S code (Vermote et al. 1997a), described in Chapter 4 (Section 4.2). The methodology is described in the next sections and its block diagram presented in Appendix A.

The methodology does not take into account the location of the aerosol layer in the atmosphere, although it is also an important factor affecting the radiative quantities for wavelengths below 0.4  $\mu\text{m}$ , especially for absorbing aerosols such as desert dust or biomass burning types. In order to include the aerosol vertical distribution among the variable parameters, LIDAR data (backscattering coefficient) and/or measurements from intensive airborne campaigns would be needed, which are not always available. On the other hand, throughout the present work the aerosol particles are assumed spherical. However, the aerosol particle shape may be an issue, especially for desert dust (Dubovik et al. 2002a) and for marine aerosol in low humidity atmospheric conditions (Silva et al.

2002). The application of non-spherical theories to satellite based retrieval algorithms is still a very difficult task dwelling on current satellite systems (Wang et al. 2003a). On one hand, satellite observations do not allow for an accurate determination of particle shape and on the other hand, even if these shapes were perfectly known, the necessary analytical tools for their description may not be available. The integration of non-spherical theories in the methodology at its present status of development would introduce further assumptions on particle shape and consequently further uncertainties, and therefore the Mie theory is chosen. Nevertheless, planned future developments of the methodology will have to address the aerosol layer height and the particle shape problem, making use of additional satellite and complementary ground-based measurements when necessary.

### 5.2.1 Automated GOME spectral measurement selection

The retrieval of aerosol properties from GOME spectral measurements requires a first step consisting in a spectral and geographical selection where aerosol particles are modelled with fewer uncertainties.

The GOME instrument (Section 3.3.2.1) measures the solar irradiance (in photons  $\text{s}^{-1} \text{cm}^{-2} \text{nm}^{-1}$ , one spectrum per day) and the radiance scattered by the Earth's atmosphere and/or reflected by the surface (in photons  $\text{s}^{-1} \text{cm}^{-2} \text{nm}^{-1} \text{sr}^{-1}$ , one spectrum per pixel), in the spectral range between 0.240 and 0.793  $\mu\text{m}$  with a good spectral resolution that varies between  $0.2 \times 10^{-3}$  and  $0.4 \times 10^{-3}$   $\mu\text{m}$  (Burrows et al. 1999). The spectral reflectance ( $\rho_{\lambda}^{\text{GOME}}$ ), which is the ratio between the upward radiance from the Earth surface and the extraterrestrial solar irradiance, is then calculated from the radiance and irradiance measurements applying equation 4.1. The spectral reflectance is used to avoid instrumental effects that in this manner are cancelled, since the radiance and irradiance are measurements from the same instrument.

The absorption of radiation by atmospheric gases may interfere with the processes of scattering and absorption by aerosols so that the selection of wavelengths poorly or not at all affected by gases is important. Torricella et al. (1999) present such a study, which allows for the selection of four wavelengths from the GOME high-resolution spectra to be used in the present work: 0.361, 0.421, 0.753 and 0.783  $\mu\text{m}$ .

The geographical areas (pixels) selected for the retrieval of the aerosol quantities from the spectral reflectance measurements ( $\rho_{\lambda_i}^{GOME}$ ) should only be cloud free areas over the ocean with low reflectance variability that ensures pixel homogeneity. This poses selection problems due to GOME's low spatial resolution (each GOME pixel is  $320 \times 40 \text{ km}^2$ ) as well as to its lack of spectral information in the infrared, which is most relevant for cloud and aerosol detection, as explained in the next pages. The proposed way of overcoming these limitations involves a combined use of GEO data, so that the GOME geo-location is matched with the nearest in time GEO classified images (clouds, aerosols or clear situation). Note that the GEO sensors have better spatial and temporal resolutions and in addition include IR measurements (see Chapter 3, Section 3.3.1). A crucial requirement is the availability of simultaneous or nearly simultaneous GOME and GEO data over the selected areas. The longer the time lag between the two datasets the higher the risk of erroneous attribution of the pixel category. The maximum time difference between a GOME overpass and the nearest GEO scan is of 15 minutes since GEO satellite imagery has a frequency of at least 30 minutes; often the time difference between GOME and GEO images is better than 15 minutes.

The GEO image pixel pairs are classified using the statistical algorithm of Porcù and Levizzani (1992) originally developed for the Meteosat Visible and InfraRed Imager (MVIRI) visible-infrared (VIS-IR) channels. It has also been applied to validate a GOME-based cloud detection algorithm (Cervino et al. 2000). The technique is used to discriminate between several classes, namely water (background aerosol contamination), land (background aerosol contamination), broken cloud over water, broken cloud over land, cloud or aerosol event (strong aerosol contamination). The different spatial resolutions of the GEO VIS and IR channels (see Chapter 3, Tables 3.2 and 3.3) are taken into account degrading the VIS spatial resolution (arithmetical average of adjacent pixels) to match that of the IR channel. Figure 5.1 shows an example of the bi-spectral classification procedure.

A clustering technique is applied to the bi-dimensional histograms obtained from the GEO VIS and IR sensor measured counts, resulting in the separation of the histogram in several clusters (classes), which allow for obtaining the classified image (see Figure 5.1). The clusters are then analysed in terms of the VIS and IR count values and a classification is attributed to each of the clusters (cloud, water, aerosol, etc), obtaining a

supervised classification of the image. The supervised classification is subsequently filtered with the sea land mask to resolve possible classification mismatches and the final classified image is obtained.

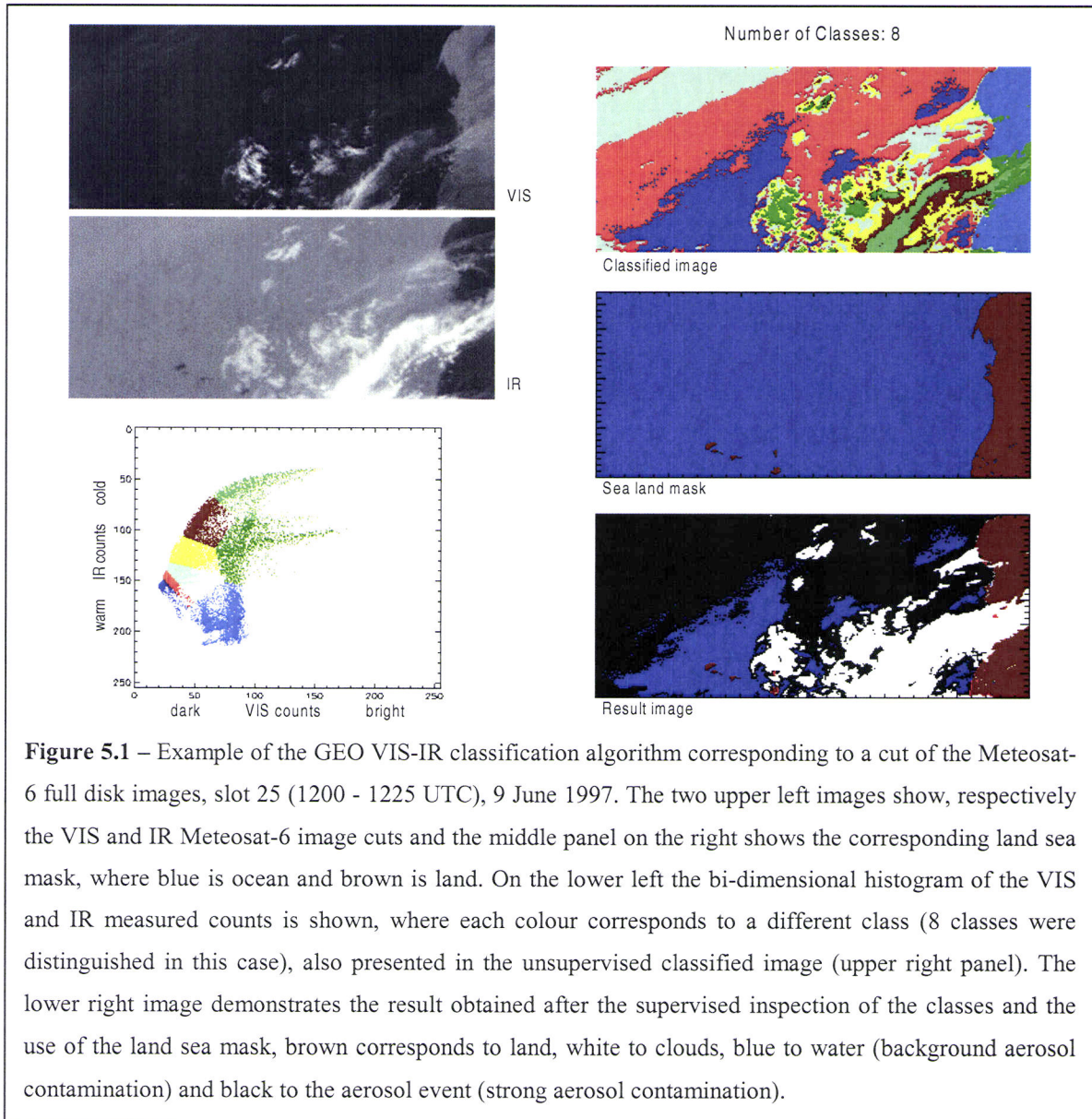


**Figure 5.1** – Example of the GEO VIS-IR classification algorithm corresponding to a cut of the Meteosat-6 full disk images, slot 25 (1200 - 1225 UTC), 9 June 1997. The two upper left images show, respectively the VIS and IR Meteosat-6 image cuts and the middle panel on the right shows the corresponding land sea mask, where blue is ocean and brown is land. On the lower left the bi-dimensional histogram of the VIS and IR measured counts is shown, where each colour corresponds to a different class (8 classes were distinguished in this case), also presented in the unsupervised classified image (upper right panel). The lower right image demonstrates the result obtained after the supervised inspection of the classes and the use of the land sea mask, brown corresponds to land, white to clouds, blue to water (background aerosol contamination) and black to the aerosol event (strong aerosol contamination).

A strong Saharan dust transport off the western African coast on 9 June 1997 is shown in Figure 5.1. The GEO VIS and IR images are cuts from the Meteosat-6 full disk images, slot 25 (1200 - 1225 UTC).

The classified image contains eight different clusters identified out off the bi-spectral classification, which after the supervised inspection are categorized in water, land, aerosol and cloud classes. The resultant image shows a vast area classified as strong aerosol contamination (black colour), some areas classified as water or land, respectively

in blue and brown (background aerosol contamination) and a few areas classified as clouds (white colour).

The classification method required at all times a supervised inspection that attributes a class type to each of the clusters distinguished as potential classes. This was time consuming and prevented an automation of the aerosol retrieval method. Therefore, it

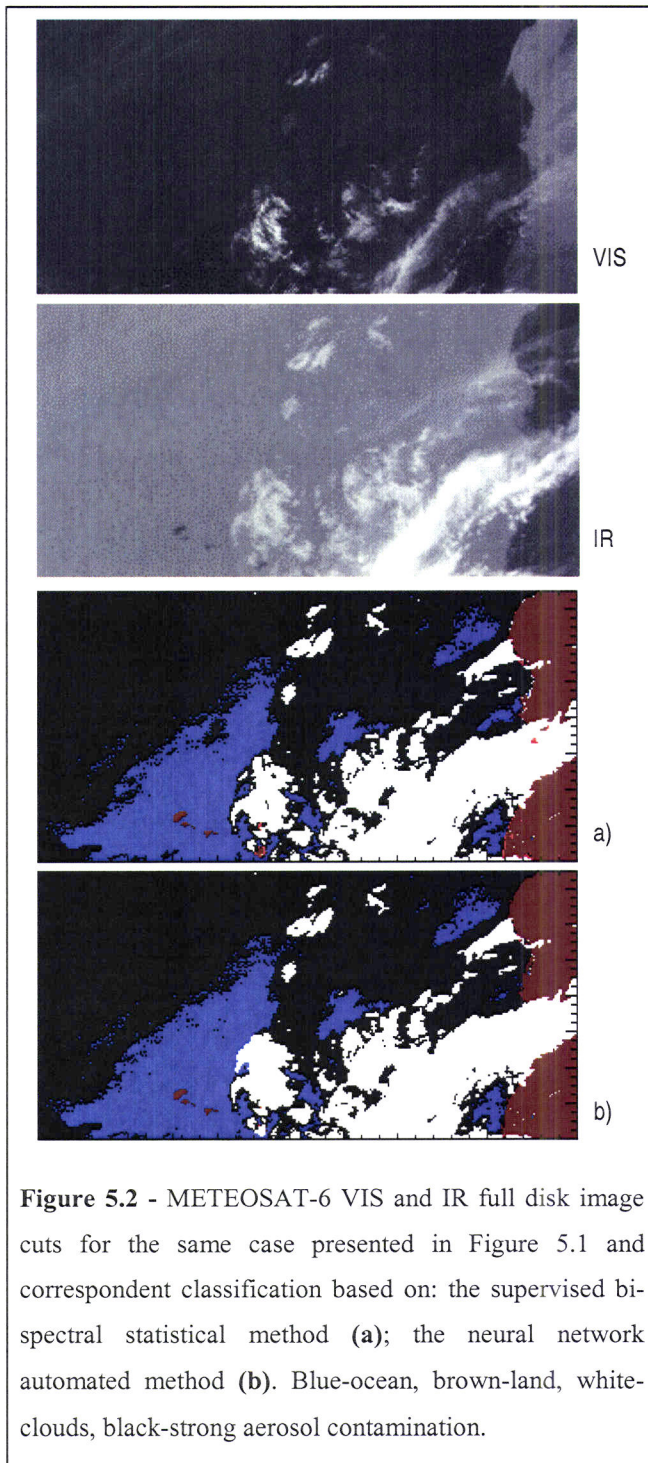


**Figure 5.2** - METEOSAT-6 VIS and IR full disk image cuts for the same case presented in Figure 5.1 and correspondent classification based on: the supervised bi-spectral statistical method (a); the neural network automated method (b). Blue-ocean, brown-land, white-clouds, black-strong aerosol contamination.

was modified to obtain a non-supervised GEO image classification methodology, using a neural network. The neural network used in the present work was the Qnet shareware software (see online at <http://qnetv2k.com/>). A training dataset was prepared using the supervised bi-spectral classification method, consisting of several classified GEO full disk images (at different times and from different days), chosen randomly in order to encompass a complete set of possibilities. After the training process, the neural network classification was applied to more than 50 different cases that were not included in the training dataset and results were compared with those obtained with the supervised bi-spectral method. Both classifications resulted quite similar and the neural network method was adopted since it allowed for a faster and automated image classification.

Figure 5.2 shows the same

case of Figure 5.1 applying both classifications to the Meteosat-6 image cuts – supervised bi-spectral method (a) and neural network automated method (b). The two classifications are almost identical: small differences can be noted in the distinction between ocean, which corresponds to a background aerosol situation (blue) and aerosol contamination (black). This is due to the difficulty of establishing the limit between these two classes.

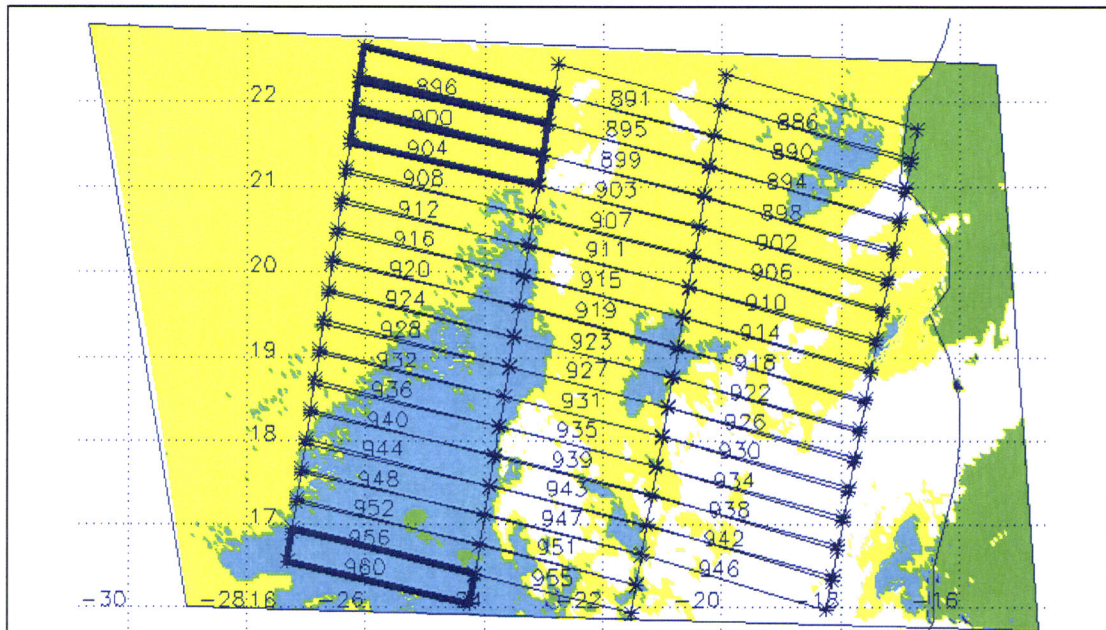


**Figure 5.3** – Example of the GOME homogenous pixel selection for the case in Figure 5.1 and 5.2, by overlapping the GOME geolocation (orbit 115) and the best time coincident Meteosat-6 classified image. Four classes are represented: water (blue), land (green), cloud (grey), and aerosol event over water (yellow). GOME pixels bounded by thick lines delimit the selections.

The different spatial resolution of the GEO and GOME sensors is taken into account when overlapping the respective geo-locations by determining which GEO image pixels are located inside each GOME pixel. The latter is marked and selected for the aerosol quantities retrieval only if the GEO satellite image pixels that fall inside are all classified as water or all classified as aerosol contaminated, thus ensuring spatial homogeneity within the pixel. Figure 5.3 shows the same example of Figures 5.1 and 5.2, for the choice of homogeneous GOME pixels. The pixels bounded with the thicker line survived the selections as described above.

The chance of observing cloud free ground pixels has been estimated for the examined cases (see Section 5.2.5.1), based on the number of pixels selected for the inversion with respect to the number of analysed pixels, and found that between 10% and

13% of the analysed pixels were selected for the inversion. The effect of the GOME pixel dimension, i.e. the assumption that the aerosol distribution is horizontally homogeneous over the pixel and the use of a single Sun/satellite geometry, was also assessed through the examination of the GEO radiance values that fall inside each selected GOME pixel and the subsequent error propagation on the retrievals. Results of this analysis are presented in Section 6.2.1.

The first European Meteorological Operational polar satellite (METOP), planned to be ready for launch by mid 2005 (see Section 3.2), carries the GOME-2 instruments that maintains GOME's spectral characteristics, but greatly increases the spatial resolution to  $40 \times 40 \text{ km}^2$ . The present methodology may well be used with GOME-2 data, surely increasing the number of selectable cloud free homogeneous pixels and improving the confidence on the retrieved mean aerosol model.

### 5.2.2 Sensitivity analysis and aerosol quantities retrieval from GOME

The idea of using the spectral information contained in GOME data to derive the aerosol type information is central to the present methodology. Once GOME spatially homogenous cloud-free pixels have been selected, relevant aerosol microphysical parameters are retrieved from the inversion of the spectral reflectance measurements corresponding to these pixels. In reality, this is a pseudo-inversion since it is based on the comparison between the selected measurements and the corresponding simulated spectral reflectance  $\rho_{\lambda}^{\text{model}}$ , altering the aerosol characterization through the variation of the size distribution, complex refractive index and optical thickness. Therefore, an aerosol characterization is obtained, which is supposedly more realistic than those from the literature. It should be pointed out that the method is developed assuming that the spatial extension of the aerosol plumes under study are sufficiently large to encompass several GOME pixels. The ground spatial resolution of GOME is certainly coarse but it is considered sufficient for the aerosol type retrieval at the local scale since the latter varies considerably less than the aerosol loads over a given area. Aerosols are assumed to be characterized by a bimodal log-normal size distribution (see equation 2.31) with a fine and



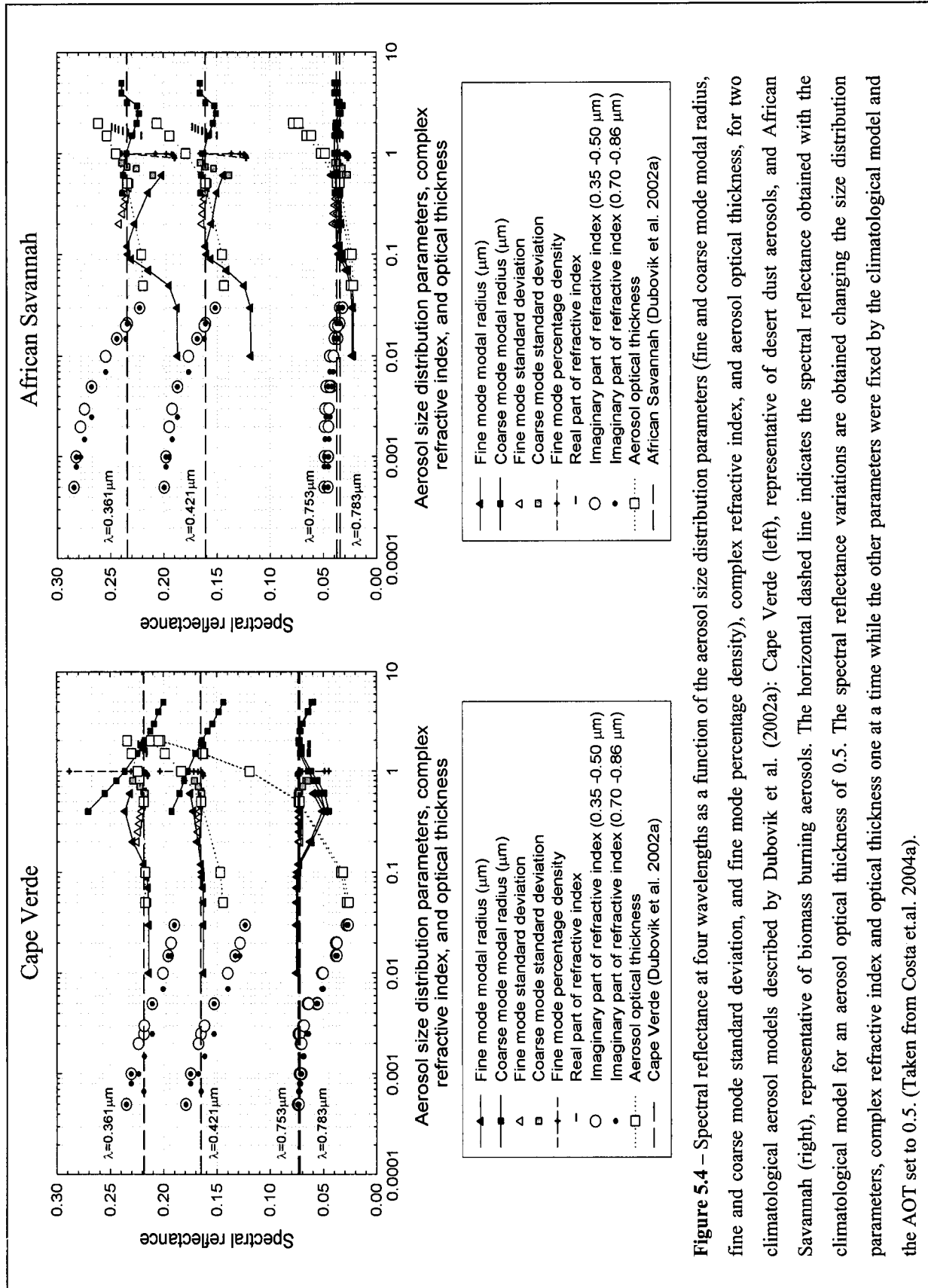
a coarse mode, and a complex refractive index (see equation 2.19) common to both modes, assumed wavelength-independent in the spectral range: 0.35 – 0.86  $\mu\text{m}$ . The size distribution and spectral complex refractive index values are taken from the series of climatological aerosol models of Dubovik et al. (2002a), which are based on the analysis of several years of ground based measurements from the AErosol RObotic NETwork (AERONET) (Holben et al. 1998) relative to diverse aerosol types and geographic locations. In one of the case studies (Asian dust) the values are taken from ground-based measurements (Sohn personal communication). The present GOME spectral reflectance pseudo-inversion conducted over wider geographical areas and shorter periods is then useful to refine these climatological models, which refer to longer periods and point measurements. The refinement is possible through the variation of some of the aerosol properties such as the aerosol size distribution parameters (fine and coarse mode modal radii, fine and coarse mode standard deviations, and fine mode percentage density) and / or spectral complex refractive index. The sensitivity of the TOA spectral reflectance, aerosol optical thickness (AOT), and the direct short wave (SW) aerosol radiative forcing (DSWARF) are investigated with respect to the individual variation of each of the size distribution parameters and complex refractive index in order to assess which of these parameters mostly influence the physical quantities under study. The graphs in Figure 5.4 present the TOA spectral reflectance at four wavelengths as a function of the aerosol size distribution parameters, the complex refractive index (real and imaginary part, the latter in two spectral regions: 0.35-0.50  $\mu\text{m}$  and 0.70-0.86  $\mu\text{m}$ ), and AOT. This is done for two of the climatological aerosol models described by Dubovik et al. (2002a): Cape Verde (left), representative of desert dust aerosols, and African Savannah (right), representative of biomass burning aerosols. The horizontal dashed line in Figure 5.4 indicates the spectral reflectance obtained with the climatological model for an AOT value of 0.5. The spectral reflectance variations are obtained changing the size distribution parameters, the complex refractive index and the AOT one at a time, and leaving the other fixed by the climatological model, and the AOT set to 0.5.

Figure 5.5 shows the AOT derived from the GEO radiances as a function of the aerosol size distribution parameters and complex refractive index for the climatological aerosol models of Figure 5.4 (Cape Verde on the left, and African Savannah on the right). In this case, the horizontal dashed line indicates the reference AOT of 0.5, corresponding

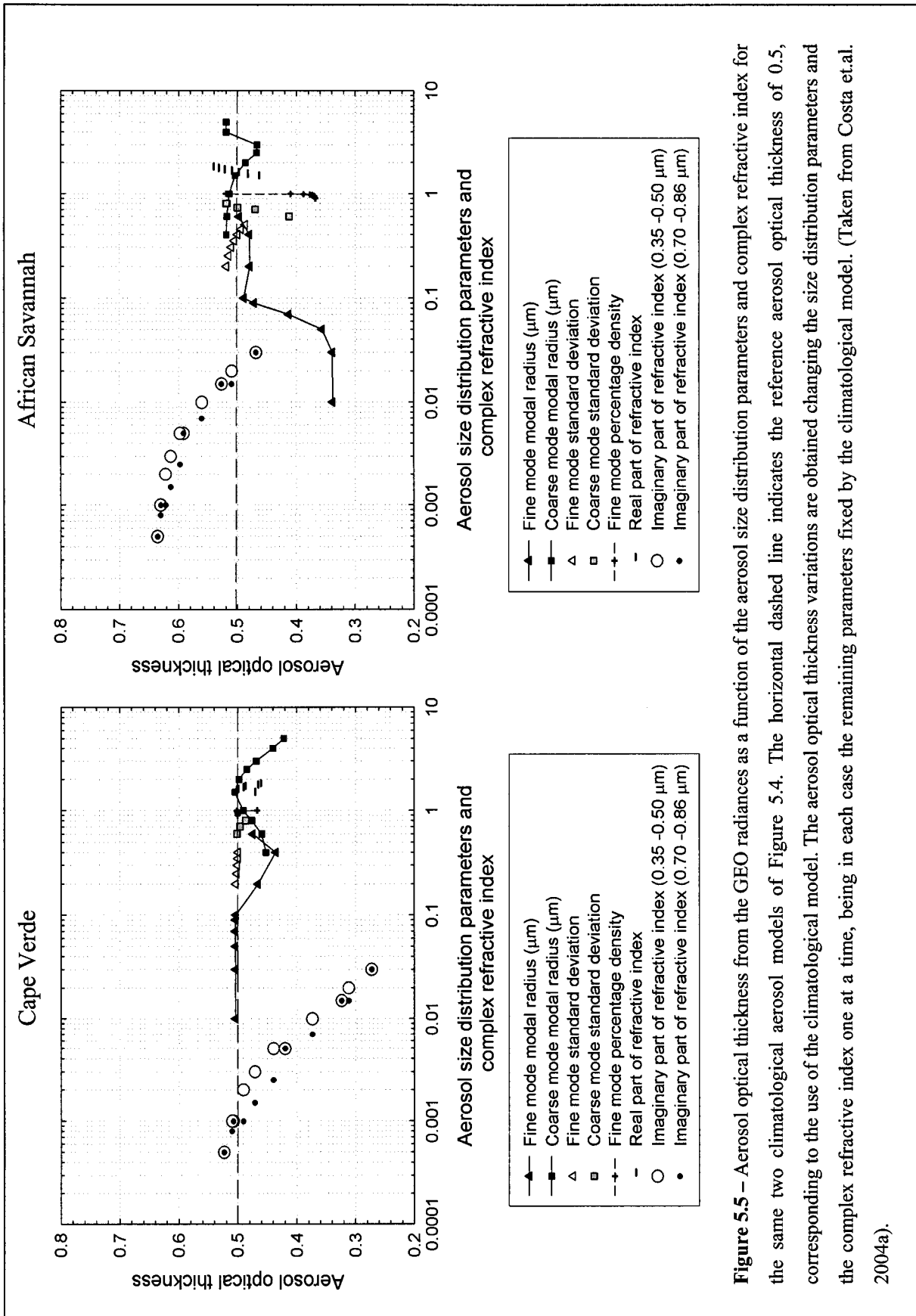
to the use of the climatological model. As for the previous quantity, the AOT variations result from changing the size distribution parameters and the complex refractive index one at a time, leaving in each case the remaining parameters fixed by the climatological model.

Figure 5.6 illustrates the TOA DSWARF as a function of the aerosol size distribution parameters, complex refractive index, and AOT, for the climatological aerosol models of Figure 5.4 (Cape Verde on the left, and African Savannah on the right). The horizontal dashed line indicates the TOA DSWARF obtained with the climatological model for an optical thickness value of 0.5. As before, the TOA DSWARF variations are obtained changing the size distribution parameters, complex refractive index and AOT one at a time, with the remaining parameters fixed by the climatological model and the AOT set to 0.5.

The analysis of the graphs in Figure 5.4, 5.5, and 5.6 shows that the fine and coarse mode standard deviations ( $\sigma_F$  and  $\sigma_C$ ) as well as the real part of the refractive index ( $m_r$ ) have a low effect on the variation of the spectral reflectance for any of the analysed wavelengths, on the AOT and on the TOA DSWARF. In most of the cases the sensitivity of the analysed quantities at the used wavelengths is greater to the fine mode modal radius ( $r_F$ ) than to that of the coarse mode ( $r_C$ ), especially in the cases where the fraction of smaller particles is greater (biomass burning case). The fine mode percentage particle density ( $Pd_F$ ) also originates high variations, especially of the spectral reflectances. The imaginary part of the refractive index ( $m_i$ ) in the two considered spectral regions, which is related to the aerosol absorption, is undoubtedly one of the most important parameters to be investigated, together with the AOT (Figure 5.4 and 5.6), which becomes increasingly important in the case of the spectral reflectance at longer wavelengths.



**Figure 5.4** – Spectral reflectance at four wavelengths as a function of the aerosol size distribution parameters (fine and coarse mode modal radius, fine and coarse mode standard deviation, and fine mode percentage density), complex refractive index, and aerosol optical thickness, for two climatological aerosol models described by Dubovik et al. (2002a): Cape Verde (left), representative of desert dust aerosols, and African Savannah (right), representative of biomass burning aerosols. The horizontal dashed line indicates the spectral reflectance obtained with the climatological model for an aerosol optical thickness of 0.5. The spectral reflectance variations are obtained changing the size distribution parameters, complex refractive index and optical thickness one at a time while the other parameters were fixed by the climatological model and the AOT set to 0.5. (Taken from Costa et al. 2004a).



**Figure 5.5** – Aerosol optical thickness from the GEO radiances as a function of the aerosol size distribution parameters and complex refractive index for the same two climatological aerosol models of Figure 5.4. The horizontal dashed line indicates the reference aerosol optical thickness of 0.5, corresponding to the use of the climatological model. The aerosol optical thickness variations are obtained changing the size distribution parameters and the complex refractive index one at a time, being in each case the remaining parameters fixed by the climatological model. (Taken from Costa et al. 2004a).

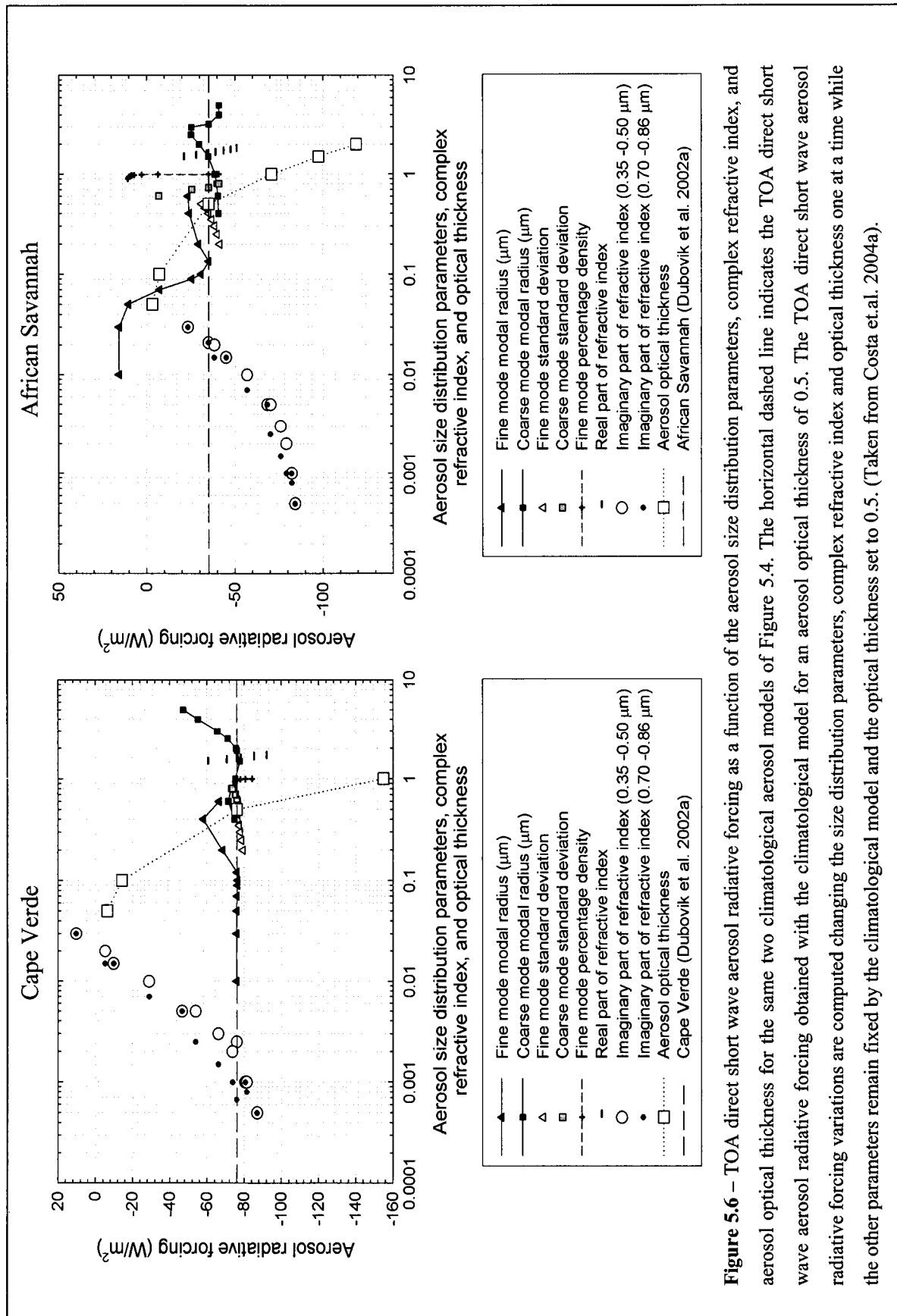


**Figure 5.6** – TOA direct short wave aerosol radiative forcing as a function of the aerosol size distribution parameters, complex refractive index, and aerosol optical thickness for the same two climatological aerosol models of Figure 5.4. The horizontal dashed line indicates the TOA direct short wave aerosol radiative forcing obtained with the climatological model for an aerosol optical thickness of 0.5. The TOA direct short wave aerosol radiative forcing variations are computed changing the size distribution parameters, complex refractive index and optical thickness one at a time while the other parameters remain fixed by the climatological model and the optical thickness set to 0.5. (Taken from Costa et al. 2004a).

This study allowed for the selection of the parameters that mostly influence the spectral reflectance (measured quantity), as well as the AOT and the TOA DSWARF (the key quantities to be derived). Therefore, the parameters fine mode modal radius ( $r_F$ ), fine mode percentage density of particles ( $Pd_F$ ), imaginary part of the refractive index in two spectral regions ( $m_i$ ), and AOT ( $\tau_{\lambda=0.55\mu m}^{aerosol}$ ) at the reference wavelength of 0.55  $\mu m$  are varied in the aerosol characterization used to simulate the spectral reflectance, which is subsequently compared to the GOME spectral reflectance measurements. The spectral regions considered for the imaginary refractive index are 0.35 – 0.50  $\mu m$  and 0.70 – 0.86  $\mu m$ .

The variation of the parameters is done via fixed combinations that depend on the aerosol event type, which is imposed *a priori* depending on the case under study (geographical location is an important indicator, combined with ancillary data such as trajectory analysis). The variation limits are indicated in Table 5.1 and 5.2. The parameters that originate smaller variations of the analysed quantities (coarse mode modal radius -  $r_C$ , fine and coarse mode standard deviations -  $\sigma_F$  and  $\sigma_C$ , and real part of the refractive index -  $m_r$ ) are fixed by the respective climatological model, which is established each time according to the case study. The percentage density of particles for each mode (see Section 4.2) are related as follows:

$$Pd_F = 100.0 - Pd_C \quad (5.1)$$

where  $Pd_C$  is the percentage density of particles of the coarse mode and  $Pd_F$  the percentage density of particles of the fine mode.

Aerosol type	Mode	Modal radius ( $\mu\text{m}$ )	Standard deviation of the modal radius ( $\mu\text{m}$ )	Percentage number density of particles
Biomass burning	Fine	$r_F$ : <b>0.05 – 0.6</b>	$\sigma_F$	<b>Pd<sub>F</sub>: 98.0 – 100.0</b>
	Coarse	$R_C$	$\sigma_C$	Pd <sub>C</sub> =100.0 – Pd <sub>F</sub>
Desert dust	Fine	$r_F$ : <b>0.09 – 0.6</b>	$\sigma_F$	<b>Pd<sub>F</sub>: 96.0 – 100.0</b>
	Coarse	$R_C$	$\sigma_C$	Pd <sub>C</sub> =100.0 – Pd <sub>F</sub>
Maritime	Fine	$r_F$ : <b>0.08 – 0.6</b>	$\sigma_F$	<b>Pd<sub>F</sub>: 97.0 – 100.0</b>
	Coarse	$R_C$	$\sigma_C$	Pd <sub>C</sub> =100.0 – Pd <sub>F</sub>

**Table 5.1** - Size distribution parameters. The lower and upper limits of the parameters allowed to vary are indicated in bold. The remaining parameter values are attributed a fixed value according to the test case under study.

Aerosol type	Spectral complex refractive index	Spectral regions ( $\mu\text{m}$ )	Aerosol optical thickness
Biomass burning	$m_r - \mathbf{(0.005 - 0.05)i}$	0.35 – 0.50	<b>0.4 – 2.0</b>
	$m_r - \mathbf{(0.005 - 0.05)i}$	0.70 – 0.86	
Desert dust	$m_r - \mathbf{(0.0008 - 0.008)i}$	0.35 – 0.50	<b>0.4 – 2.0</b>
	$m_r - \mathbf{(0.0006 - 0.006)i}$	0.70 – 0.86	
Maritime	$m_r - \mathbf{(0.0001 - 0.001)i}$	0.35 – 0.50	<b>0.0 – 0.4</b>
	$m_r - \mathbf{(0.0001 - 0.001)i}$	0.70 – 0.86	

**Table 5.2** - Complex refractive index and AOT parameters. The lower and upper limits of the parameters allowed to vary are indicated in bold. The real part ( $m_r$ ) is attributed a fixed value according to the test case under study.

The distinction between aerosol event and background aerosol conditions (considered to be described by a maritime aerosol model) is based on the GEO image

classification (described in Section 5.2.1) that allows for the selection of spatially homogeneous GOME pixels (Figure 5.3). If the classification indicates background aerosol contamination within the pixel, the maritime model is taken; on the contrary, if the classification suggests an aerosol event, the corresponding aerosol model is used according to the case under study.

Look-up Tables (LUTs) of spectral reflectances ( $\rho_{\lambda_i}^{model}$ ) are computed for a number of different geometric conditions and several fixed aerosol models. These models are built as explained before, fixing the parameters of the size distribution and complex refractive index and varying: the fine mode modal radius ( $r_F$ ), the fine mode percentage density of particles ( $Pd_F$ ), the imaginary part of the refractive index ( $m_i$ ) in two spectral regions (0.35 – 0.50  $\mu\text{m}$  and 0.70 – 0.86  $\mu\text{m}$ ), and the AOT ( $\tau_{\lambda=0.55\mu\text{m}}^{aerosol}$ ), in the ranges presented in Tables 5.1 and 5.2. The measured spectral reflectance corresponding to each selected GOME pixel is compared to the spectral reflectance from the LUTs. First, the solar and satellite geometry are identified and the corresponding LUT selected, and secondly a minimization method is applied to measurements and simulations until the best fit is achieved, leading to the retrieval of the aerosol quantities corresponding to that spectrum (pixel), which are given by the fixed combination of the aerosol parameters ( $A^{model}$ ) that generated the best fit. The chi-square function used for the minimization is:

$$\chi^2(A^{model}, \tau_{\lambda=0.55\mu\text{m}}^{aerosol}) = \sum_{i=1}^4 \left( \frac{\rho_{\lambda_i}^{GOME} - \rho_{\lambda_i}^{model}(A^{model}, \tau_{\lambda=0.55\mu\text{m}}^{aerosol})}{\sigma_{\lambda_i}} \right)^2 \quad (5.2)$$

It is assumed that the spectral reflectance measurements ( $\rho_{\lambda_i}^{GOME}$ ) are distributed independently and randomly as a normal distribution around the modelled GOME spectral reflectance values ( $\rho_{\lambda_i}^{model}$ ) considered as the “true” value, being  $\sigma_{\lambda_i}$  the standard deviation of the normal distribution associated with the GOME spectral measurements at the four selected wavelengths  $\lambda_i$  (0.361, 0.421, 0.753 and 0.783  $\mu\text{m}$ ). In equation 5.2,  $A^{model}$  are the aerosol models contained in the LUT, and  $\tau_{\lambda=0.55\mu\text{m}}^{aerosol}$  the aerosol optical thickness at the

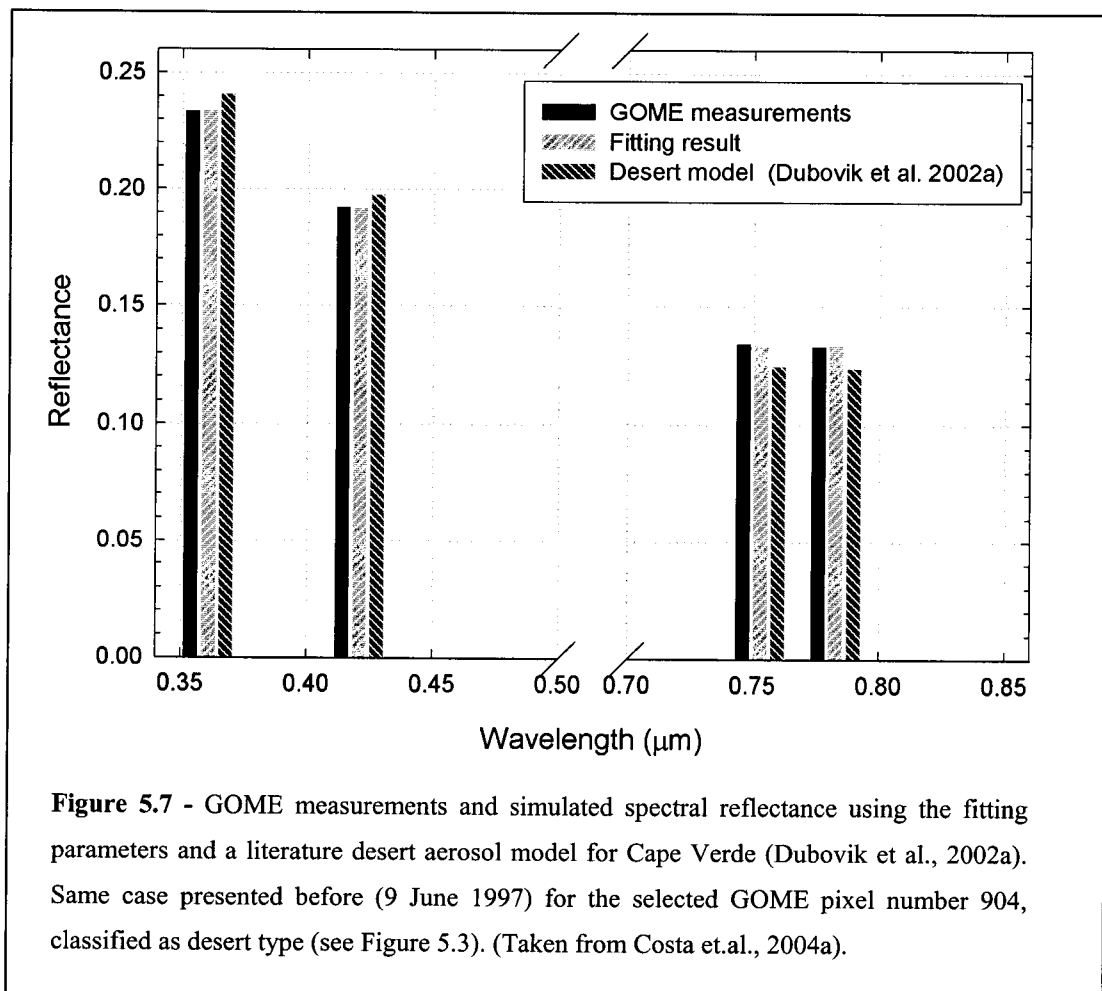


reference wavelength of  $0.55\mu\text{m}$ . The criterion to decide if the chi-square function can be considered minimised is expressed by the condition:

$$\chi^2(A^{\text{model}}, \tau_{\lambda=0.55\mu\text{m}}^{\text{aerosol}}) < 0.1 \quad (5.3)$$

The GOME modelled spectral reflectance ( $\rho_{\lambda}^{\text{model}}$ ) stored in the LUTs, is computed using the 6S code (see Section 4.2), taking into account the corresponding solar and satellite (GOME) geometry (zenith and azimuth angles). Simulations are done considering the ocean surface as a lambertian reflector, with a typical spectral reflectance of clear seawater (Viollier 1980) and a tropical atmospheric vertical profile (McClatchey et al. 1971).

The above-described fitting procedure is illustrated in Figure 5.7.



The graph refers to one of the selected pixels presented in Figure 5.3 (pixel number 904 from GOME orbit 115, 9 June 1997). The GOME spectral reflectance obtained using an aerosol class available in the literature describing desert dust conditions in Cape Verde (Dubovik et al. 2002a) is also plotted for comparison. Note that the use of the climatological aerosol model does not reproduce measurements as adequately as the derived parameters do.

The pseudo-inversion is performed over all selected GOME pixels, allowing for the retrieval of several size distributions, complex refractive indexes and optical thickness at GOME spatial scale ( $r_F$ ,  $Pd_F$  and  $m_i$ , since the remaining parameters are fixed according to the case under study) that characterize the mixture of aerosols present in the atmosphere for each space-time measurement. A subsequent spatial / temporal analysis of these inversion results is carried out, consisting of their separation in terms of the initial classification of each pixel – background aerosol or event (see Section 5.2.1). Results of the size distributions and complex refractive indexes for each of these classes are then used to derive the corresponding spectral aerosol optical quantities, namely the extinction, scattering and absorption coefficients ( $\beta_\lambda^e$ ,  $\beta_\lambda^s$  and  $\beta_\lambda^a$ ), phase function ( $P_\lambda(\Theta)$ ), and single scattering albedo ( $\varpi_\lambda$ ). The asymmetry parameter ( $g_\lambda$ ) is calculated from the aerosol phase function according to equation 2.42. These quantities are calculated assuming spherical aerosol particles, and using the GOME-derived size distributions and complex refractive indexes as input for Mie calculations (see Chapter 2, Section 2.3). The resulting aerosol optical quantities are then averaged, disregarding pixel results associated to variations larger than 30% with respect to the mean value. This permits the retrieval of effective aerosol optical quantities for a certain geographical area and period of time, which replace those out of literature models. The Ångström exponent  $\alpha$ , defined by the Ångström power law in equation 2.43, comes from the slope of the spectral extinction coefficient (from 0.40 to 0.86  $\mu\text{m}$ ). This parameter is related to particle size, decreasing as the particle size increases. In the present methodology the AOT is retrieved at one reference wavelength (0.55  $\mu\text{m}$ ) and the Ångström exponent can be used to extrapolate the AOT values to other wavelengths making use of equation 2.44.

### **5.2.3 Aerosol optical thickness retrieval from coupling GOME retrievals with GEO satellite measurements**

Aerosol optical quantities (single scattering albedo, phase function, and extinction coefficient) derived from GOME spectral measurements' fitting are then combined with data from GEO platforms to derive the AOT at the reference wavelength of 0.55  $\mu\text{m}$ . Note that the AOT was already retrieved from the minimization process at the GOME pixel scale. By coupling GOME retrievals with GEO data, the AOT is obtained at a considerably better spatial resolution, which is suitable for a monitoring strategy over large areas and longer time periods (the MVIRI image repeat cycle is half an hour – see Section 3.3.1) using the retrieved aerosol quantities instead of those from climatology. Note that the present method is aimed at the study of strong aerosol events, usually characterized by reasonably high AOT values, which lessens the difficulties associated with aerosol retrievals from satellite-based instruments since the signal due to the aerosols is much higher (Tanré et al. 1997; King et al. 1999).

The algorithm can be applied to any GEO satellite for a possible global coverage strategy. The foreseen use of data from Meteosat Second Generation (MSG) Spinning Enhanced Visible and InfraRed Imager (SEVIRI) would contribute to a further improvement with respect to the present MVIRI, since the sensor has a higher temporal as well as spatial resolution (see Section 3.3.1.3).

The GEO images used are classified using the automated neural network methodology trained with results from the statistical algorithm of Porcù and Levizzani (1992), described in Section 5.2.1, to select the cloud-free pixels over the ocean where the AOT will be retrieved, as well as to distinguish between aerosol event and background aerosol conditions. If the classification indicates background aerosol contamination on the pixel then the maritime model is taken. On the contrary, if the classification identifies an aerosol event, the corresponding aerosol model is once more used accordingly to the case under study.

Presently, GEO systems are equipped with a broadband VIS spectral channel (MVIRI: 0.3 – 1.1  $\mu\text{m}$ ; see also Section 3.3.1), which is used here for the AOT retrieval. For each mean aerosol class obtained from the inversion of GOME spectral reflectance over a certain geographical area and period, a LUT of the GEO VIS broadband radiance

( $I_{VIS}^{model}$ ) is derived considering all possible geometric conditions (Sun and GEO satellite) and seven AOT values (0.0, 0.1, 0.2, 0.5, 1.0, 1.5, 2.0). These seven AOT values chosen to integrate the LUTs are considered enough to calculate any AOT value between 0.0 and 2.0 by spline interpolation (Press et al. 1997). The GEO modelled VIS broadband radiance ( $I_{VIS}^{model}$ ) stems from radiative transfer calculations using the 6S code (see Section 4.2), considering the same surface and atmospheric characterization as those used for the GOME spectral reflectance simulations (see previous section). The LUT corresponding to each GEO cloud-free pixel is identified taking into account the observing geometry and the pixel classification (event or background aerosol type). Subsequently, the AOT at the reference wavelength of 0.55  $\mu\text{m}$  ( $\tau_{\lambda=0.55\mu\text{m}}^{aerosol}$ ), now at the spatial scale of the GEO pixel, corresponding to each of these GEO image pixels is computed by spline interpolation (Press et al. 1997) of the GEO radiances stored in the LUT ( $I_{VIS}^{model}$ ) using the GEO radiance measurement value ( $I_{VIS}^{GEO}$ ).

The procedure is applied to every single GEO cloud-free measurement (pixel) over the ocean, obtaining at last AOT maps suitable for space-time monitoring strategies of the aerosol loads over the ocean.

#### **5.2.4 Direct SW aerosol radiative forcing assessment from GEO satellite measurements**

The aerosol optical quantities derived from GOME spectral measurements' fitting and the AOT retrieved from GEO measurements are successively used to estimate the DSWARF at the TOA and at the surface, with the spatial resolution typical of GEO satellite-based instruments ( $5.0 \times 5.0 \text{ km}^2$ ; see also Section 3.3.1).

The 6S radiative transfer code computes the downward SW flux at the surface ( $F_{SW}^{-surf}$ ), the upward spectral reflectance at the TOA ( $\rho_{\lambda}^{TOA}$ ), and the upward spectral radiance at the TOA ( $I_{\lambda}^{+TOA}$ ). The extraterrestrial solar spectral irradiance  $F_{0\lambda}$  values used in the code are taken from Neckel and Labs (1984). Some changes were introduced in the original code, in order to permit also the calculation of the upward SW fluxes emerging

from the surface and at the TOA levels. The upward SW flux at the surface ( $F_{SW}^{+surf}$ ) is calculated considering that the surface reflectance in the SW spectral region ( $\rho_{SW}^{surf}$ ) is given by:

$$\rho_{SW}^{surf} = \frac{F_{SW}^{+surf}}{F_{SW}^{-surf}} \quad (5.4)$$

Equation 5.4 is a particular case of equation 2.71, written for the surface level and for the considered SW spectral interval (0.25 to 3.5  $\mu\text{m}$ ), instead of being referred to monochromatic calculations. The value used for the surface reflectance ( $\rho_{SW}^{surf}$ ) is attributed according to the case under study; nevertheless, the error associated is limited since the retrievals are restricted to regions over the ocean (see Section 2.6.1). As for the TOA upward flux ( $F_{SW}^{+TOA}$ ), it is obtained from the spatial integration of the TOA upward spectral radiance ( $I_{\lambda}(+\mu, \phi)$ ) computed over a grid of satellite (GEO) zenith ( $\mu$ ) and relative azimuth ( $\phi$ ) angles, applying equation 2.69, and then spectrally integrated from 0.25 to 4.0  $\mu\text{m}$  to yield the broadband (SW) flux, by means of equation 2.67.

The SW fluxes ( $F_{SW}^{-surf}$ ,  $F_{SW}^{+surf}$  and  $F_{SW}^{+TOA}$ ) are modelled using the 6S radiative transfer code (see Section 4.2) with the aforementioned modifications, considering the same surface and atmospheric characterization as those used for the GOME spectral reflectance and GEO VIS radiance simulations (see the two previous sections). The fluxes are calculated for a set of possible solar zenith angle (from  $0^{\circ}$  to  $85^{\circ}$  with a step of  $5^{\circ}$ ) and AOT values (0.0, 0.2, 0.5, 1.0, 1.5, 2.0) and LUTs are set up. The aerosol description is granted by the optical quantities derived from GOME spectral measurements ( $\beta_{\lambda}^e$ ,  $\beta_{\lambda}^s$ ,  $\beta_{\lambda}^a$ ,  $P_{\lambda}(\Theta)$ , and  $\varpi_{\lambda}$ ; see also Section 5.2.2), ensuring an aerosol characterization that describes the atmospheric conditions for the geographical area and period of the study. The LUT corresponding to each GEO cloud-free pixel is identified taking into account the observing geometry and the pixel classification (event or background aerosol type). Finally, the SW fluxes ( $F_{SW}^{-surf}$ ,  $F_{SW}^{+surf}$  and  $F_{SW}^{+TOA}$ ) are obtained by spline interpolation

(Press et al. 1997) of the LUT values, using the AOT at the reference wavelength of 0.55  $\mu\text{m}$  ( $\tau_{\lambda=0.55\mu\text{m}}^{\text{aerosol}}$ ) retrieved from GEO broadband measurements (see Section 5.2.3).

The net SW fluxes at the surface and TOA levels, respectively  $F_{SW}^{\text{net surf}}$  and  $F_{SW}^{\text{net TOA}}$ , are then calculated introducing the downward and upward SW fluxes, computed with the modified 6S code and obtained from the LUT interpolation, into equation 2.76. The DSWARF, i.e. the modification of the atmospheric radiation balance due to the presence of aerosols particles (through the scattering and sometimes absorption of radiation) at a certain atmospheric level, is in turn estimated from equation 2.79, at the TOA and surface levels ( $\Delta F_{SW}^{\text{TOA}}$  and  $\Delta F_{SW}^{\text{surf}}$ ). The DSWARF of the entire atmosphere ( $\Delta F_{SW}^{\text{atm}}$ ) is also estimated, following the definition given by Ramanathan et al. (2001):

$$\Delta F_{SW}^{\text{atm}} = \Delta F_{SW}^{\text{TOA}} - \Delta F_{SW}^{\text{surf}} \quad (5.5)$$

The  $\Delta F_{SW}^{\text{TOA}}$ ,  $\Delta F_{SW}^{\text{surf}}$  and  $\Delta F_{SW}^{\text{atm}}$  are calculated for every single GEO cloud-free pixel over the ocean, where the AOT was also previously retrieved, drawing in the end maps of the DSWARF at the TOA and surface levels and of the entire atmosphere, suitable for space-time monitoring strategies of the aerosol direct radiative impact over the ocean.

### 5.2.5 Validation of the aerosol methodology

The GOME-derived aerosol spectral optical quantities ( $\beta_{\lambda}^e$ ,  $\beta_{\lambda}^s$ ,  $\beta_{\lambda}^a$ ,  $P_{\lambda}(\Theta)$ , and  $\omega_{\lambda}$ ), as well as the AOT ( $\tau_{\lambda=0.55\mu\text{m}}^{\text{aerosol}}$ ) at the reference wavelength of 0.55  $\mu\text{m}$ , obtained from GEO data, the TOA, surface and atmospheric DSWARF ( $\Delta F_{SW}^{\text{TOA}}$ ,  $\Delta F_{SW}^{\text{surf}}$  and  $\Delta F_{SW}^{\text{atm}}$ ) values have to be compared with independent estimates of the same physical parameters in order to validate the present methodology.

The methodology described in the previous sections is applied to selected episodes of strong atmospheric aerosol loads that occurred over the ocean, specifically to three dust outbreaks originating in different desert Earth regions and to a vast biomass burning

transport event from fires in the southern part of the African continent. The validation is based on the comparisons between the results of the present methodology and completely independent measurements and/or results from internationally recognized algorithms, for restricted geographical areas during a certain period - case studies – selected during the occurrence of the episodes mentioned above. A complete description of the case studies, as well as of the data used for the comparisons is given in the next two sections.

### 5.2.5.1 Case studies

Four case studies of aerosol transport over the ocean were selected: 1) dust transport over the Atlantic Ocean, 2) dust transport over the Yellow Sea, 3) dust transport over the Indian Ocean (Arabian Sea), and 4) smoke transport event over the South Atlantic Ocean.

The first case study refers to a dust episode occurred in the first half of June 1997 over the Atlantic Ocean, where massive amounts of dust are frequently blown westward out of the Sahara desert especially during the northern hemisphere summer. This is due to the almost complete absence of rain out during this season, which prevents the

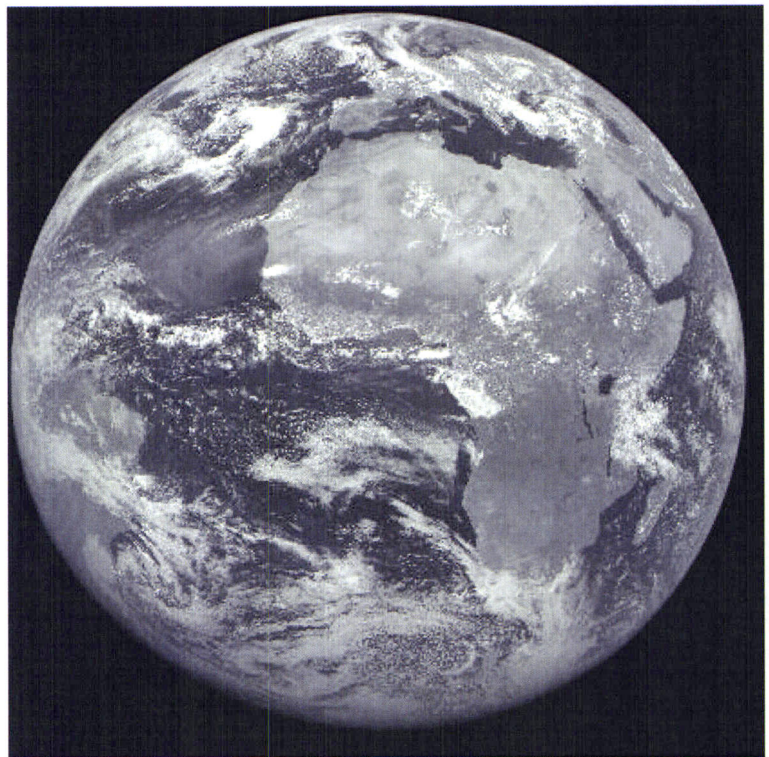


**Figure 5.8** - METEOSAT-6 full disk image from the VIS spectral channel on 8 June 1997 when the dust was blowing off the Sahara desert and crossing the Atlantic Ocean (© 2002 EUMETSAT).

deposition of dust particles and allows their long distance transport. The climatology of the African dust transport over the North Atlantic, mainly from the Sahara, was studied for a

period of about twelve years by Moulin et al. (1997a) and an average of more than 15 dust aerosol events was reported every year, an indication of their relative importance for the global aerosol load.

The Meteosat-6 full disk image corresponding to the VIS spectral channel (see Table 3.2) shown in Figure 5.8 demonstrates the extent and intensity of the dust event for one of the days (8 June 1997), as evident from the wide brighter region over the North Atlantic Ocean cloud free region. The aerosol absorption index map from the Total Ozone Mapping Spectrometer (TOMS) onboard the Earth Probe

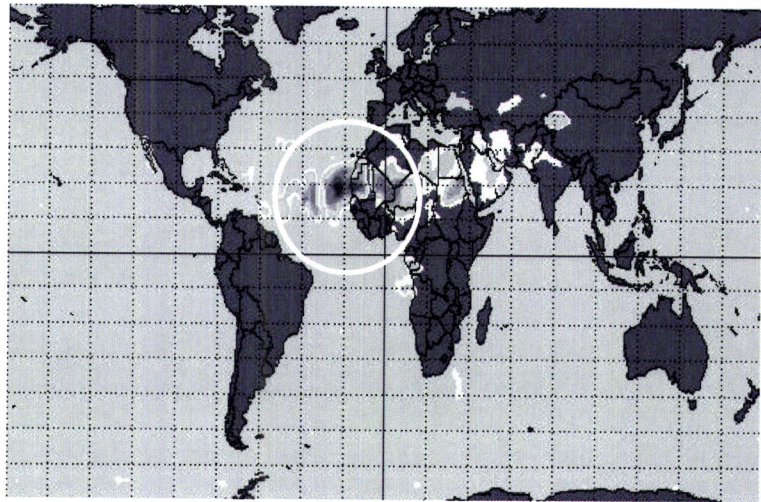


**Figure 5.9** - Absorbing aerosol particles detected by the Earth Probe TOMS on 8 June 1997. TOMS data distinguish between different types of aerosol particles (absorbing or non-absorbing) based on their absorbing properties in the UV. The greyish spots over land and over ocean represent strong aerosol absorption. The white circle indicates the location of the case study. Image available online at <http://toms.gsfc.nasa.gov/aerosols/aerosols.html>.

presented in Figure 5.9 corresponding to the same day unveils the presence of absorbing aerosol particles as dust and smoke, based on their absorption properties in the ultraviolet (UV) spectral region (Torres et al. 1998; see also Section 3.2). The TOMS aerosol index, however, does not prompt for a distinction among different types of absorbing aerosol particles so that in Figure 5.9 dust and biomass burning aerosols are not separated. The greyish spots over land and over ocean (that differ from the background colour) delimit the aerosol absorption areas and therefore the presence of absorbing particles and the white circle indicates the present case study. Although the main event took place in the first part of June and the aerosol optical quantities are derived from GOME measurements during this period, the entire month is then considered in the analysis of the aerosol optical thickness and DSWARF over the geographical oceanic area illustrated in Figure 5.14.



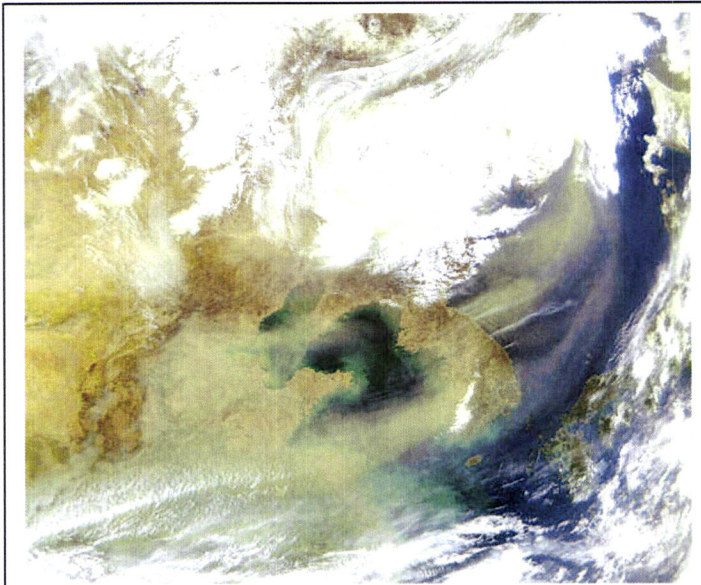


**Figure 5.10** - SeaWiFS image from 7 April 2000 showing a very large dust storm blowing eastward from China across Korea and Japan. At the same time, several fairly large fires on the Korean Peninsula were mingling their smoke with the dust over the Pacific Ocean. Image available online at <http://visibleearth.nasa.gov/>.

The second case study is an event of dust blowing off the Gobi desert eastward across China towards the Pacific Ocean, which is a common event in the Northern Hemisphere Spring. The dust is carried by the prevailing westerlies that blow in this period mostly from the Yellow River region and Gobi Desert in China. Occasionally, the dust load becomes heavy and moves as far as Korea as in the present case and then offshore over the Pacific. The frequency of these events seems to have increased in the past few years. One of the

reasons may be the progressive desertification of the regions neighbouring the Gobi Desert. On 7 April 2000 a strong dust storm originated in the Gobi desert and swept the Yellow Sea continuing towards the Pacific Ocean (Costa et al. 2002), over the oceanic geographical region shown in Figure 5.15. The SeaWiFS image in Figure 5.10 shows the extent and intensity of the dust event. Furthermore, the smoke from fires in Korea mixes with dust over the Pacific Ocean. However, the present

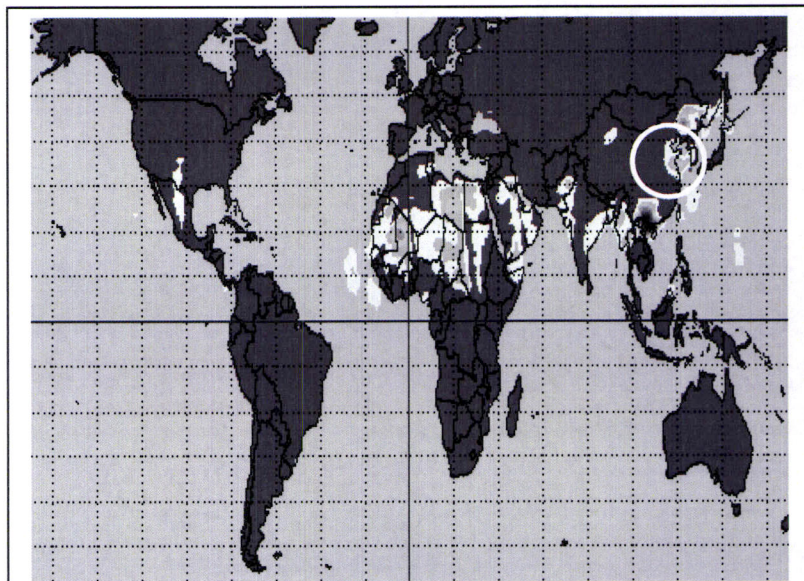


**Figure 5.11** – Same as in Figure 5.9 but for 7 April 2000.

study concentrates only on the dust transport event West of the Korean Peninsula over the Yellow Sea and not over the Pacific Ocean, therefore this mixture of different aerosol types is not considered in the study.

The TOMS aerosol absorption map in Figure 5.11 corresponding to the same day as the SeaWiFS image (Figure 5.10), shows the absorbing aerosol regions, circled in white (greyish spots over land and over ocean).



Figure 5.12 - Same as in Figure 5.9 but for 14 July 2000.

The third case study is a dust transport event that took place from 10 to 16 July 2000 over the Arabian Sea in the geographical area depicted in Figure 5.16. Figure 5.12 shows the absorption by aerosol particles detected by TOMS over the Middle East region,

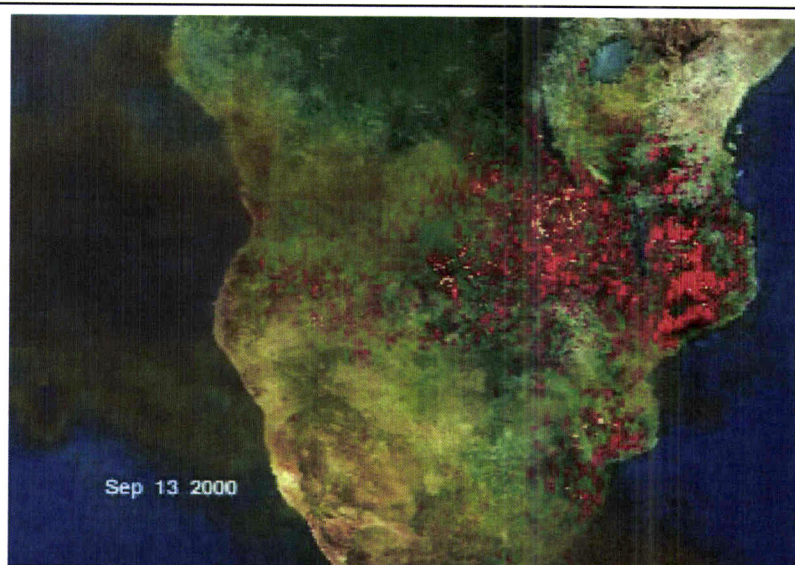


Figure 5.13 – Composite of TOMS and NOAA-14 AVHRR images from 13 September 2000 showing some of the fires that raged across southern Africa during August and September 2000, producing a thick "river of smoke" over the region. Image available online at <http://visibleearth.nasa.gov/>.

corresponding to the dust transport over the area in this period. The dust aerosols spill over the Persian Gulf and the Arabian Sea (areas distinguished with the brighter colour). The dust plume seems especially thick across Saudi Arabia, Yemen and Oman, but also covers Iraq and the United Arab Emirates, and over Africa can be

noted over Eritrea, Somalia and Ethiopia (brighter areas over land regions).

The fourth case study concerns a smoke transport event over the South Atlantic Ocean from the biomass fires that raged across southern Africa in early September 2000, when the fire season peaked. The region is subject to some of the highest levels of biomass burning in the world. The heaviest burning was in western Zambia, southern Angola, northern Namibia, and northern Botswana. Figure 5.13 obtained from TOMS in combination with NOAA-14 AVHRR (see Section 3.2) data for 13 September 2000 shows the multiple fires (indicated in red) burning across the region. The fires generated large amounts of heat-absorbing aerosols (the dark haze), which were observed with the TOMS instrument. The present case study is limited to the area illustrated in Figure 5.17 and the period from 6 to 13 September 2000.

Each one of the case studies corresponds entirely to a single aerosol type at a time, being excluded from the present study the situations where a mixture of different types could possibly occur (for example desert dust and biomass burning).

#### **5.2.5.2 Data**

Several GEO systems were used in the present work, depending on the case study location and date, specifically the operational Meteosat located at 0° longitude, the Meteosat system supporting the Indian Ocean Data Coverage (IODC), located at 63° E longitude and the Japanese GEO system – GMS – positioned at 140° E longitude (see Section 3.3). Table 5.3 reports the GEO satellite data used for each of the case studies, consisting of the VIS and IR broadband channel measurements.

For all cases, the GEO measurements are used together with the spectral reflectance data from the GOME orbits spatially and temporally closest to the corresponding GEO scan area (see Tables 3.2 and 3.3).

The validation datasets contain entirely independent measurements / results of the aerosol quantities and AOT obtained from ground-based measurements and satellite based algorithms and of the TOA upward solar fluxes derived from satellite measurements (see also Appendix A). One of the sources are the aerosol properties retrieved from the ground-based AERosol RObotic NETwork (AERONET) Sun and sky radiance measurements

available online at <http://aeronet.gsfc.nasa.gov/>. The AERONET program (Holben et al. 1998) imposes standardization of instruments, calibration and processing, providing globally distributed observations of spectral aerosol properties in geographically different aerosol regimes.

Case Study	Date	GEO instrument	Time range (UTC) and Frequency
Saharan dust over the Atlantic Ocean	1 – 30 June 1997	Meteosat-6	From 0800 to 1400 Hourly
Asian dust over the Yellow Sea	7 April 2000	GMS-5	From 0030 to 0930 Hourly
Dust over the Arabian Sea	10-16 July 2000	Meteosat-5	From 0430 to 0830 Hourly
Biomass burning over the southern Atlantic Ocean	6-13 September 2000	Meteosat-7	From 0800 to 1400 Hourly

**Table 5.3** – GEO satellite imagery used for each of the case studies.

Ground-based measurements of some of the aerosol quantities ( $\omega_\lambda$  and  $P_\lambda(\Theta)$ ), AOT ( $\tau_{\lambda=0.55\mu m}^{aerosol}$ ), Ångström exponent ( $\alpha$ ) and radiation fluxes taken at Anmyon-Do Island, just off the West Coast of South Korea, during an intensive measurement campaign are also used for comparison. The location of the ground-based stations used for the validation study, as well as the geographical areas of each of the case studies, are illustrated in the maps of Figures 5.14 through 5.17. In addition, comparisons are also made with the official aerosol products from the POLarization and Directionality of Earth Reflectances (POLDER) instrument (Goloub et al. 1999; Deuzé et al. 2000) onboard the ADEOS satellite (see Section 3.2) and the MODerate Resolution Imaging Spectroradiometer (MODIS) (Tanré et al. 1997) onboard the Terra spacecraft (see Sections 3.2 and 3.3). Finally, the TOA upward SW flux ( $F_{SW}^{+TOA}$ ) calculated as described in Section 5.2.4, is compared with the TOA flux product (dataset CERES Terra FM1 Edition1 ES8) of the Clouds and the Earth's Radiant Energy System (CERES) sensor (Wielicki et al. 1996), onboard Terra, with the purpose of controlling the flux modelling quality and indirectly the

estimated TOA DSWARF as suggested also by Christopher and Zhang (2002) and Chou et al. (2002).

Table 5.4 summarises the characteristics of the data used in the validation of the methodology.

Case Study	Validation data	Physical quantity compared	Location of the comparisons
Saharan dust over the Atlantic Ocean	AERONET	Single scattering albedo Phase function Ångström exponent Aerosol optical thickness	Cabo Verde (16.7°N,22.9°W) Dakar (14. 4°N, 16.9°W) Banizoumbou (13.5°N, 2.7°E)
	POLDER	Aerosol optical thickness	Area illustrated in Figure 5.14
Asian dust over the Yellow Sea	Intensive ground-based measurements campaign	Single scattering albedo Phase function Ångström exponent Aerosol optical thickness	Anmyon-Do (36.5°N, 126.3°E) South Korea
	CERES	TOA upward SW flux	Area illustrated in Figure 5.15
Dust over the Arabian Sea	AERONET	Single scattering albedo Phase function Ångström exponent Aerosol optical thickness	Bahrain (26.3°N, 50.5°E) Kaashidhoo (5.0°N, 73.5°E) Nes_Ziona (31.9°N, 34.8°E)
	MODIS	Aerosol optical thickness	Area illustrated in Figure 5.16
	CERES	TOA upward SW flux	Area illustrated in Figure 5.16
Biomass burning over the southern Atlantic Ocean	AERONET	Single scattering albedo Phase function Ångström exponent Aerosol optical thickness	Ascension Island (8.0°S, 14.4°W) Zambezi (13.5°S, 23.1°E) Etosha-Pan (19.2°S, 15.9°E) Swakopmund (22.6°S, 14.6°E)
	MODIS	Aerosol optical thickness	Area illustrated in Figure 5.17
	CERES	TOA upward SW flux	Area illustrated in Figure 5.17

Table 5.4 – Data used in the validation of the methodology.

The aerosol quantities retrieved ( $\omega_\lambda$ ,  $\alpha$  and  $P_\lambda(\Theta)$ ) at the GOME pixel spatial scale were compared with the AERONET official inversion product (Dubovik and King

2000) and with the aerosol properties derived from the ground-based radiation measurements taken in South Korea (Kim et al. 2002, 2004), assuming the aerosol plumes maintained their characteristics during the period considered for each of the case studies and that spatial homogeneity holds. The AERONET algorithm derives the aerosol size distribution ( $n(r)$ ), the spectral complex refractive index ( $m_{r,\lambda} - im_{i,\lambda}$ ) and the single scattering albedo ( $\omega_\lambda$ ) from measurements of sun and sky spectral radiances of the network's Sun-sky photometers. Level 1.0 data is used in this case since no level 2.0 inversion products were available for the present case studies. The AERONET size distribution and complex refractive index were used as input for Mie calculations (see Section 2.3) in order to determine the aerosol optical properties, such as the phase function ( $P_\lambda(\Theta)$ ), characteristic of the aerosol event under study according to the recommendations of Dubovik et al. (2000). The Ångström exponent ( $\alpha$ ) is also calculated from the AERONET spectral AOT values (from 0.44 to 0.87  $\mu\text{m}$ ) and compared to the value obtained from GOME.

The AOT ( $\tau_{\lambda=0.55\mu\text{m}}^{\text{aerosol}}$ ) retrieved at the GEO spatial and temporal scales was compared against measurements from several ground-based sites (AERONET and field campaign in Korea - see Table 5.4). The AERONET AOT values used in the comparisons are level 2.0 (Quality Assured) whose accuracy is around 0.02 (Holben et al. 1998). The GEO pixel AOT were enclosed in boxes ( $0.5^\circ \times 0.5^\circ$  for AERONET sites and  $0.25^\circ \times 0.25^\circ$  for the South Korean site) centred on the geographical location of the ground-based station, then spatially averaged, and the respective standard deviation computed, discarding all cloud and/or land contaminated pixels (Costa et al. 2001). AOT values from the ground-based stations were retained for about one hour before and one hour after the GEO scan time over the area. Values were time averaged and the standard deviation over the two-hour period computed. The ground-based averaged AOT was taken for comparisons only if the correspondent standard deviation was  $< 0.2$ . As regards to the spatially averaged AOT derived from GEO satellite measurements, values  $> 1.0$  are retained only if the correspondent standard deviation is  $< 0.5$ . The AOT ( $\tau_{\lambda=0.55\mu\text{m}}^{\text{aerosol}}$ ) retrieved at the GEO spatial and temporal scale was also compared with the corresponding POLDER and MODIS (version 004) aerosol products as referred before. For this purpose, the AOT values (from both sources: GOME-GEO based presented method and POLDER/MODIS product) lower

than 2.0 are averaged over coincident cells of  $0.5^\circ \times 0.5^\circ$  and compared within the best time coincidence, which is of maximum 15 minutes difference. The cell is retained for comparison if at least 40% of the pixels inside the cell have each an  $AOT < 2.0$

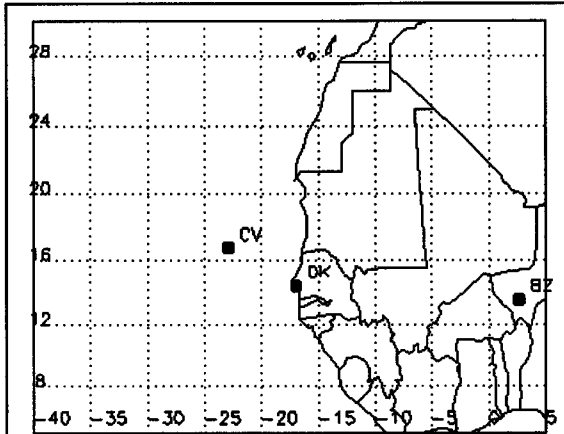


**Figure 5.14** - Map of the geographical area considered for the dust transport event over the North Atlantic Ocean. The black squares indicate the location of the AERONET stations used for comparison: CV – Cabo Verde; DK – Dakar; BZ – Banizoumbou.

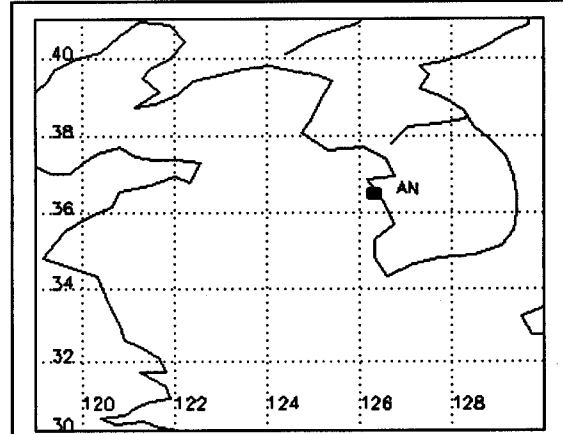


**Figure 5.15** – Same as in Figure 5.14 but for the Asian dust transport event over the Yellow Sea. The black squares indicate the location of the ground site used for comparison: AN – Anmyon-Do.

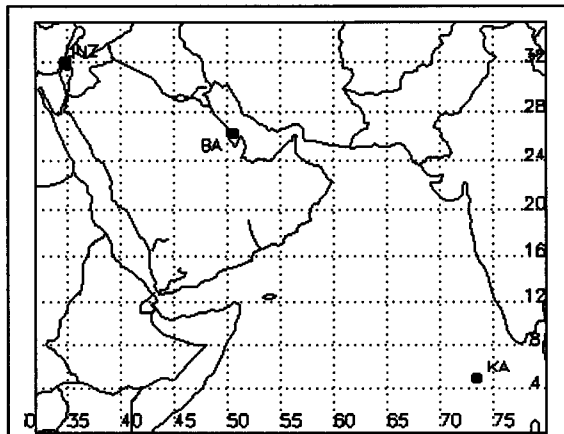


**Figure 5.16** - Same as in Figure 5.14 but for the dust transport event over the Arabian Sea. The black squares indicate the location of the AERONET stations used for comparison: BA – Bahrain; KA – Kaashidhoo; NZ – Nes\_Ziona.

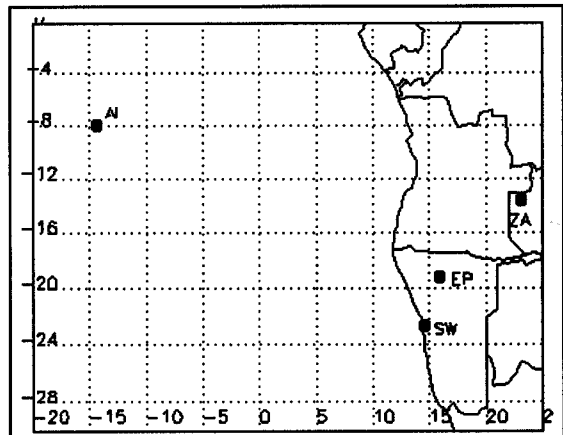


**Figure 5.17** - Same as in Figure 5.14 but for the biomass burning event over the South Atlantic Ocean. The black squares indicate the location of the AERONET stations used for comparison: AI - Ascension Island; EP - Etosha\_Pan; SW – Swakopmund; ZA – Zambezi.

The upward SW flux at the TOA ( $F_{SW}^{+TOA}$ ) modelled with the modified 6S code (at the GEO spatial scale) is compared to the CERES TOA SW flux product as a way of verifying the radiative transfer calculations. Coincident geographical areas of  $0.25^\circ \times 0.25^\circ$  are averaged over the study regions (Figures 5.15 through 5.17) taking only cloud and land free pixels.

The GOME derived aerosol quantities are weighed against literature aerosol models with the purpose of revealing the improvement in the aerosol characterization introduced by the present methodology. In addition, the AOT values retrieved at the GEO spatial and temporal scales are checked against results derived from the same GEO data considering aerosol models available in the literature as well. This serves the purpose not only to contribute for the validation of the new method, but also to show that there is a notable improvement when considering the aerosol quantities derived from GOME spectral measurements, instead of relying on a climatologically based characterization. The literature models used for the dust aerosol and biomass burning case studies are described by Dubovik et al. (2002a).

The results obtained from the methodology developed for the aerosol characterization and direct radiative forcing study as well as the respective validation and accuracy of the methodology are revealed in Chapter 6.

## 5.3 Cloud characterization

The methodology developed for the characterization of the cloud microphysical properties is based on satellite multi-spectral measurements in the VIS, near IR (NIR) and thermal IR spectral regions, used in combination with radiative transfer calculations. The radiative transfer calculations are done using the RSTAR code described in (Section 4.3) and part of the method relies on the CAPCOM code (Nakajima and Nakajima 1995), already described in Section 4.4.

The interest in studying cloud structure and the possible effects of the cloud-aerosol interaction has evolved significantly along the development of the present work, which was initially intended to focus mainly on the aerosol properties and their radiative effects. It is well known that clouds constitute the major regulating system of the Earth's climate.



The difficulty in drawing a separation line between aerosol and clouds, as for example in the classification method presented in Section 5.2.1, states the tight connection between them and the great complexity of the physical processes involved. Aerosols act as cloud condensation nuclei or may be incorporated by clouds, altering their properties and lifetime (see Chapter 1 for details). These reasons, along with the fact that this is a vast investigation field where uncertainties are still very high (IPCC 2001) constitute the main motivations in the present study to target not only aerosols but also clouds, even if the cloud analysis method presented is in an early stage of development relatively to the one developed and presented for the aerosol.

The methodology presented in this chapter intends to be a starting point for deeper investigation in the near future, not only on the improvement of methods for satellite remote sensing of cloud properties, but also on cloud radiative effects, taking into account their possible interaction with aerosol particles (Costa et al. 2004c).

Furthermore, the development of the present methodology is encouraged by the existence of a new generation of GEO satellite measurements such as those from the Spinning Enhanced Visible and Infrared Imager (SEVIRI) flying on the Meteosat Second Generation (MSG) (see Chapter 3, Section 3.3.1.3). This innovative sensor opens new perspectives with respect to past and present GEO systems since it provides the necessary additional spectral measurements, supplied until now exclusively by LEO satellite sensors and greatly improves the observational frequency, allowing for global monitoring of cloud properties (see Table 3.4) and eventually for advances in cloud-aerosol interaction studies. Data from MSG-1 SEVIRI was not yet available to the users at the moment the present study was carried out and consequently measurements from the MODIS sensor onboard Terra and Aqua satellites, which present comparable spectral channels in the VIS, NIR and IR (see Section 3.3.2.2), were used in view of the availability of SEVIRI multi-spectral measurements.

The MODIS Atmosphere Science Team makes available an operational cloud product through the Goddard Distributed Active Archive Center – DAAC. The product contains amongst other cloud properties cloud optical thickness, effective radius and top temperature, also retrieved from the present method. Results from MODIS cloud product are used in the comparisons of the retrieved cloud properties.

The full methodology is explained in the next sections and its block diagram presented in Appendix B.

### 5.3.1 Cloud properties retrieval

The first step of the method consists of cloud detection over the area and particle thermodynamic phase determination (liquid water or ice), assuming that clouds are constituted exclusively by either liquid water or ice particles, hence no mixed phase clouds are accounted for. It is assumed that there must be some variation of the satellite-sensed radiation between the cloudy and cloud free areas and in addition that this variation is also associated to the presence of water clouds or ice clouds. The principle of the technique is analogous to the bi-spectral GEO image classification (Porcù and Levizzani 1992) presented in Section 5.2.1 since it also relies on satellite measurements in the VIS and IR spectral regions. Clouds strongly reflect/scatter the visible radiation, therefore they can easily be distinguished from less reflecting surfaces as water and most of the times land surfaces. The radiation emitted in the IR spectral region is directly related with the temperature of the emitting media and, as a result, it is possible to distinguish between water or land surfaces (warmer) and clouds (colder) as well and many times also between water and ice clouds. In this case, satellite measurements are initially classified in terms of the underlying surface (land or water) using the corresponding land sea mask. Subsequently, the frequency histograms of the VIS radiance measurements (MODIS channel 1: 0.62 - 0.67  $\mu\text{m}$ ; spatial resolution:  $1 \times 1 \text{ km}^2$ ) and brightness temperature values obtained from the IR measurements (MODIS channel 31: 10.78 - 11.28  $\mu\text{m}$ ; spatial resolution:  $1 \times 1 \text{ km}^2$ ) are analysed for the case under study. The frequency histograms are a very useful tool to analyse the occurrence of a certain event and its relative importance with respect to the whole scenario under analysis. In this case, the frequency histograms of the VIS radiance and IR brightness temperature are used to determine threshold values that define the limits between clear sky, water clouds and ice clouds. Since the VIS radiance over land is extremely variable and reaches rather high values that could be wrongly attributed to the presence of clouds, over land the classification technique relies simply on the brightness temperature values.

The image in Figure 5.18 taken from MODIS onboard Terra over the South Atlantic Ocean and South African Continent regions on 16 September 2000 shows the presence of several clouds over land and over the ocean. Figure 5.19 shows an example of the histograms analysed for the image in Figure 5.18 and the corresponding thresholds determined for the pixels over the ocean and over land. In Figure 5.19a), where only the scene over the ocean is considered, the frequency

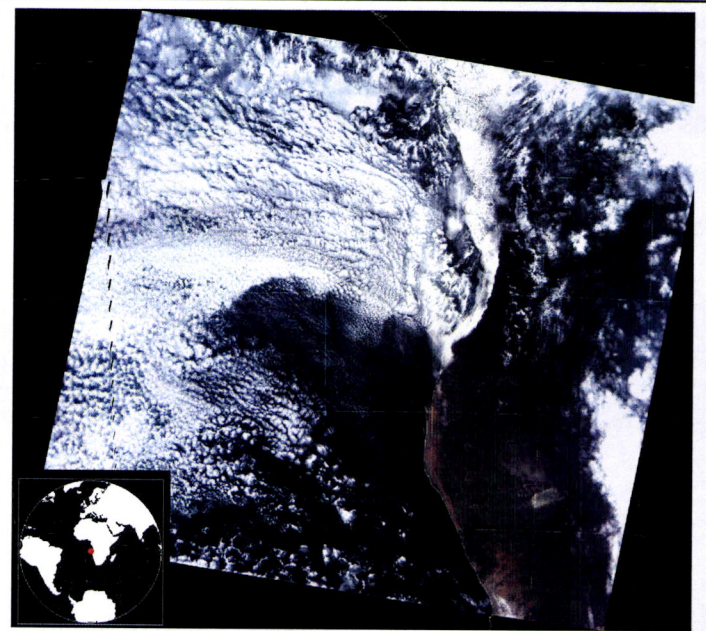


**Figure 5.18** – MODIS-Terra image on 16 September 2000 over the South Atlantic Ocean and South African Continent. The clouds over land and over the ocean enter the histogram analysis and classification in terms of their thermodynamic phase (liquid water or ice). Image available online at <http://modis-atmos.gsfc.nasa.gov>.

histogram of the VIS radiance shows a high radiance peak lower than  $30 \text{ Wm}^{-2} \text{ sr}^{-1} \mu\text{m}^{-1}$  (value highlighted by the dotted grey line). This is followed by an abrupt decrease at higher radiance values characterized by regular frequency values with a slight increase around  $200 \text{ Wm}^{-2} \text{ sr}^{-1} \mu\text{m}^{-1}$ . The sudden decrease of the frequency values for the value of  $30 \text{ Wm}^{-2} \text{ sr}^{-1} \mu\text{m}^{-1}$  suggests a discontinuity of the atmospheric scene under study, which is interpreted here as the change between clear sky and clouds. On the other hand, the frequency histogram of the IR brightness temperature shows the same kind of decrease, even though not so marked, at 285 K (highlighted by the dotted grey line): this is taken as the temperature threshold for distinguishing between clear sky and clouds. Moreover, this frequency histogram shows that the lowest temperature corresponding to clouds is 275 K, which is considered too high of a value to correspond to ice clouds, hence only water clouds are considered in this situation.

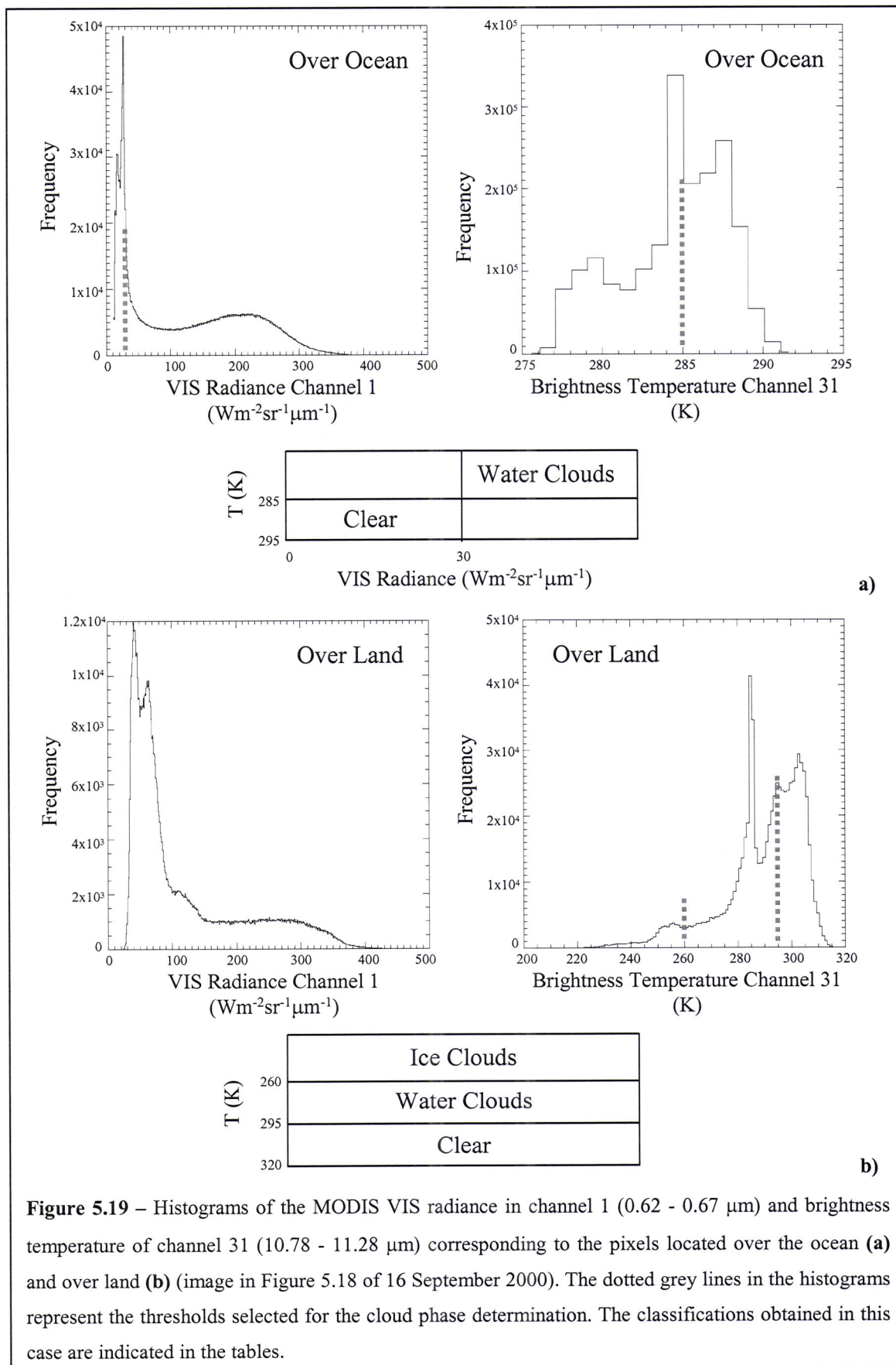


**Figure 5.19** – Histograms of the MODIS VIS radiance in channel 1 (0.62 - 0.67  $\mu m$ ) and brightness temperature of channel 31 (10.78 - 11.28  $\mu m$ ) corresponding to the pixels located over the ocean (**a**) and over land (**b**) (image in Figure 5.18 of 16 September 2000). The dotted grey lines in the histograms represent the thresholds selected for the cloud phase determination. The classifications obtained in this case are indicated in the tables.

Figure 5.19 b) corresponds to the scene analysis over land. The VIS radiance frequency histogram shows two high peaks for radiance values lower than  $80 \text{ Wm}^{-2} \text{ sr}^{-1} \mu\text{m}^{-1}$  approximately: this could be considered the limit between clear sky and cloud presence, but it could well be due to land surfaces characterized by high reflectance values. Therefore, as already mentioned, only the IR brightness temperature histogram is employed in this analysis. This frequency histogram shows a frequency peak for temperature values greater than 295 K, which is considered the distinction between clear sky and cloud presence. The histogram shows in addition that for temperatures lower than 295 K there are two other peaks, one around 280 K (probably corresponding to water clouds) and another for temperature values lower than 260 K, attributed here to ice clouds.

Such threshold classification is done at the pixel level and when the pixel is classified as cloudy, four possible cases are distinguished: water clouds over the ocean, ice clouds over the ocean, water clouds over land and ice clouds over land. The VIS, NIR and IR radiance measurements corresponding to the pixels classified in the four categories are inputs to the CAPCOM code for the retrieval of the cloud properties (see Section 4.4). The four categories are treated separately because relevant differences in cloud and surface characterization between the classes must be taken into account as described next. The MODIS channels used in the methodology are bands 1 (0.62 - 0.67  $\mu\text{m}$ ), 20 (3.66 - 3.84  $\mu\text{m}$ ) and 31 (10.78 - 11.28  $\mu\text{m}$ ), in the VIS, NIR and IR spectral regions, respectively. Although the spatial resolution in band 1 is  $250 \times 250 \text{ m}^2$ , the DAAC also provides the same band at the spatial resolution of  $1 \times 1 \text{ km}^2$  obtained as explained by Nishihama et al. (1997), which is used here to match those of bands 20 and 31 (see also Table 3.6).

The code relies on the comparison between the modelled cloud radiances in the three spectral bands and the corresponding satellite radiance measurements corrected to yield the cloud signal, as fully described in Section 4.4. The modelled radiances, as well as the corrections applied to the satellite radiance measurements are obtained from radiative transfer calculations, using the radiative transfer code RSTAR, described Section 4.3. The radiative transfer code is used to pre-compute Look-Up Tables (LUTs), which are computationally fast while maintaining the accuracy of the radiative transfer calculations. The LUTs contain the radiative quantities necessary for the cloud properties retrieval (see full description in Section 4.4), namely the cloud reflected radiances and spherical albedo in the VIS and NIR spectral bands, the atmospheric and cloud transmission in the VIS,

NIR and IR spectral bands, and the reflection and atmospheric emitted radiation in the NIR and IR spectral bands. The radiative transfer calculations are done taking into account the MODIS spectral response functions for each of the spectral channels indicated before (MODIS bands 1, 20 and 31), shown in the graphs of Figure 3.5.

Grid parameter	Number of values in the grid	Cloud Phase	
		Liquid water	Ice
Cloud optical thickness $\tau^c$	10	1, 2, 4, 6, 9, 14, 20, 30, 50, 70	0.1, 0.5, 1, 2, 4, 8, 16, 32, 48, 64
Cloud effective radius $r_{eff}$ ( $\mu\text{m}$ )	11	2, 4, 6, 9, 12, 15, 20, 25, 30, 35, 40	5, 10, 20, 40, 60, 80, 100, 120, 140, 160, 180
Cloud top temperature $T^c$ (K)	6	250, 260, 270, 280, 290, 300	220, 230, 240, 250, 260, 270
Equivalent water vapour above the cloud $ew^a$ ( $\text{g}/\text{m}^2$ )	7	50, 5000, 10000, 20000, 30000, 40000, 50000	
Equivalent water vapour of the cloud layer $ew^c$ ( $\text{g}/\text{m}^2$ )	7	50, 5000, 10000, 20000, 30000, 40000, 50000	
Solar zenith angle $\theta_0$ ( $^\circ$ )	13	0, 5, 10, 20, 30, 35, 40, 45, 50, 55, 60, 65, 70	
Satellite zenith angle $\theta$ ( $^\circ$ )	11	0, 5, 10, 20, 30, 35, 40, 45, 50, 55, 60	
Relative azimuth angle $\phi - \phi_0$ ( $^\circ$ )	19	0, 10, 20, 30, 40, 50, 60, 70, 80, 90, 100, 110, 120, 130, 140, 150, 160, 170, 180	

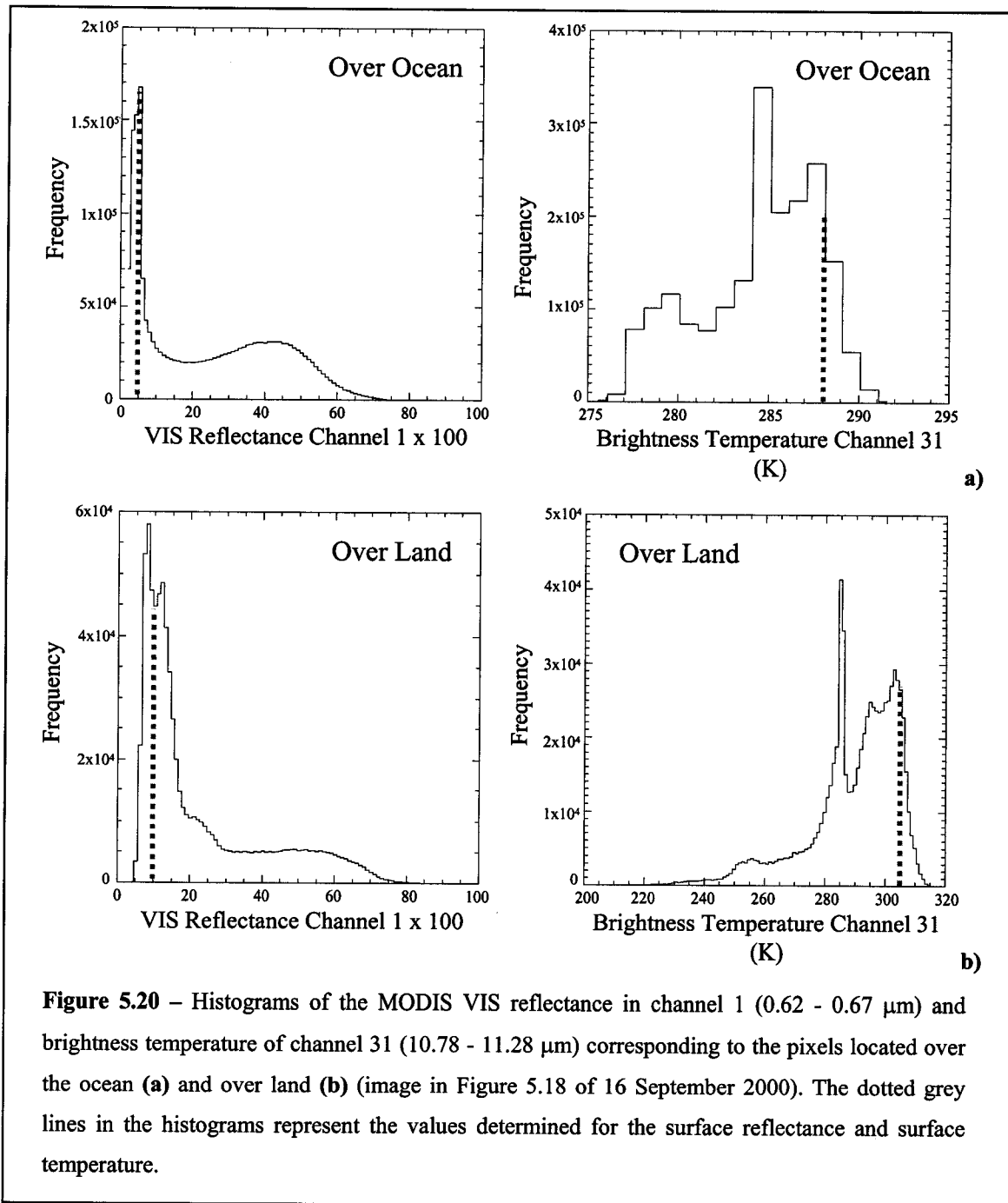
**Table 5.5** – Grid of parameter values used to build the Look-up Tables.

The LUTs were built for a grid of selected values of the cloud optical thickness ( $\tau^c$ ), cloud effective radius ( $r_{eff}$ ), cloud top temperature ( $T^c$ ), equivalent water vapour above the cloud ( $ew^a$ ), equivalent water vapour of the cloud layer ( $ew^c$ ), solar zenith ( $\theta_0$ ), satellite zenith ( $\theta$ ) and relative azimuth ( $\phi - \phi_0$ ) angles, shown in Table 5.5. These values are chosen to gradually range between the physically acceptable values for any of the quantities and therefore all physically possible solutions are considered. The cloud was

characterized by a log-normal size distribution (equation 2.31). Three sets of LUTs were built differing in the standard atmospheric vertical profiles considered: Tropical, Mid-Latitude Summer and Mid-Latitude Winter, all taken from McClatchey et al. (1971).

The CAPCOM code makes use of ancillary data, that is the atmospheric vertical profiles of pressure, temperature and water vapour taken from McClatchey et al. (1971), as well as the mean values of surface temperature and reflectance, all provided accordingly to the case under study.

The CAPCOM code used for this work was not in its original form, but modified as described next. Originally, the code was ready to work with AVHRR measurements and it was necessary to arrange it in order to allow functioning with MODIS and SEVIRI satellite data, taking into account the slightly different spectral channels and the new spectral response functions. Besides, changes were introduced in the way the vertical atmospheric profiles are input to the code, making it possible to use the same profile for the whole image or to change it according to the geographic location. On the other hand, the surface reflectance in the spectral bands and the surface temperature are now directly supplied to the code, according to the values obtained from a histogram analysis similar to the one described before and illustrated now in Figure 5.20. The frequency histograms of the VIS reflectance and IR brightness temperature are analysed separately over ocean and over land surfaces. The example in Figure 5.20 refers once again to the image in Figure 5.18 of 16 September 2000. In this case, the analysis over the ocean resulted in a mean VIS surface reflectance of 0.05 because the frequency peak corresponding to this value presents a maximum, which matches the expected low value, typical for ocean surfaces. The ocean surface temperature is 288K, representing a typical mean value of the clear sky scenes ( $T > 285\text{K}$  – see Figure 5.19a). As for the VIS land surface reflectance, a value of 0.1 is selected corresponding to a mean value of the higher peaks found for the lower reflectance values, assuming that the higher reflectance values in the frequency histogram correspond to clouds reflection. As for the mean land surface temperature, a value of 305K is considered from the analysis of the clear sky part in the frequency histogram of Figure 5.20b (when  $T > 295\text{K}$  – see Figure 5.19b).



Finally, the CAPCOM code was also modified in order to yield as an additional output the cloud type. In the original version of the code, the cloud type or the cloud geometrical thickness ( $D$ ) had to be initially defined as explained in Section 4.4. This forced the user to seek for a prior knowledge on clouds in the areas of study, which are many times remotely located with no observations available from platforms (ground-based or airborne) other than the satellite. In alternative, assumptions can be made, which can



introduce unknown uncertainties in the cloud properties determined. Conversely, in the modified version of the code used in the present work, the cloud type is established from the cloud optical thickness and cloud top pressure values determined from the code, using the ISCCP cloud classification as defined by Rossow and Schiffer (1999) and illustrated in Figure 5.21. Such classification separates not only the clouds in terms of the atmospheric level – *Low, Middle or High* – but also specifically into: *Cumulus* or *Stratocumulus*, *Stratus*, *Altostratus* or *Altostratus*, *Nimbostratus*, *Cirrocumulus* or *Cirrostratus* or *Cirrus*, *Cumulonimbus*. This code modification meets the need of having *a priori* information about cloud type or geometrical thickness.

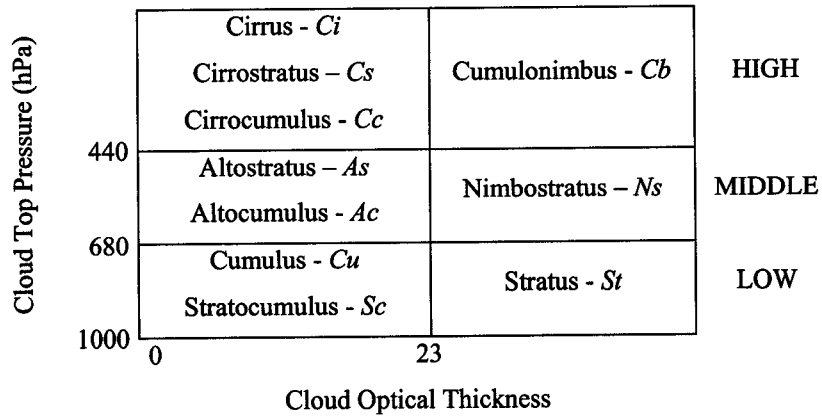


**Figure 5.21** – ISCCP cloud classification thresholds as defined by Rossow and Schiffer (1999).

The LUT grid values of the cloud optical thickness ( $\tau^c$ ), effective radius ( $r_{eff}$ ) and top temperature ( $T^c$ ) (see Table 5.5) are taken as first-guess to start the code procedure that uses the Newton-Raphson iterative method (see Section 4.4). The cloud top height ( $Z^c$ ) and pressure ( $P^c$ ) are directly calculated from linear interpolation of the selected atmospheric vertical profile, using the cloud top temperature value ( $T^c$ ). The cloud type is then determined in this modified version, as described above, from the current values of the cloud optical thickness and cloud top pressure via an iterative process until convergence (expressed by equations 4.24 and 4.25). When the convergence condition is fulfilled, the cloud optical thickness, cloud effective radius and cloud top temperature are considered retrieved and the cloud type determined, which in turn determines the cloud

liquid water content ( $w$ ), since these values are tabulated inside the code for each cloud type, as proposed by Liou (1976). On the other hand, the cloud liquid water path ( $W$ ) is retrieved directly from the cloud optical thickness ( $\tau^c$ ) and effective radius ( $r_{eff}$ ) using the following equation:

$$W = \frac{2}{3} \tau^c \cdot r_{eff} \cdot \rho \quad (5.6)$$

where  $\rho$  is the liquid water/ice density. The cloud geometrical thickness ( $D$ ) is finally obtained from equation 4.23. In case the convergence condition is never fulfilled, the code exits with a flag indicating that the retrieval was not successful and continues to the next pixel.

The cloud properties retrieved from the present methodology are intended to be used in future work to estimate the local and regional cloud radiative forcing over the areas under study, in a similar way the aerosol radiative forcing is already assessed (see Section 5.2.4).

### 5.3.2 Validation of the cloud methodology

The cloud microphysical properties, namely cloud optical thickness ( $\tau^c$ ), cloud droplet effective radius ( $r_{eff}$ ) and cloud top temperature ( $T^c$ ) derived from the multi-spectral methodology, as well as those obtained indirectly from these latter - cloud top height ( $Z^c$ ), cloud top pressure ( $P^c$ ), cloud liquid water path ( $W$ ), cloud liquid water content ( $w$ ) and cloud geometrical thickness ( $D$ ), - have to be checked using independent retrievals.

The methodology described in the previous section is applied to selected episodes where clouds are observed in the presence of strong aerosol events, specifically of two intense biomass burning transport events, one in the southern hemisphere and the other in the northern hemisphere. The validation is based on the comparisons between the results from the present methodology and completely independent *in situ* measurements and/or

results from internationally recognized algorithms, for restricted geographical areas during a certain period - case studies – selected during the occurrence of the episodes mentioned above. A complete description of the selected case studies, as well as of the data used for the comparisons is given in the next two sections.

### 5.3.2.1 Case studies

The two case studies selected for the study of the cloud microphysical / optical properties in the presence of aerosols are: 1) smoke transport event from fires in the southern part of the African continent, 2) smoke transport from fires in continental

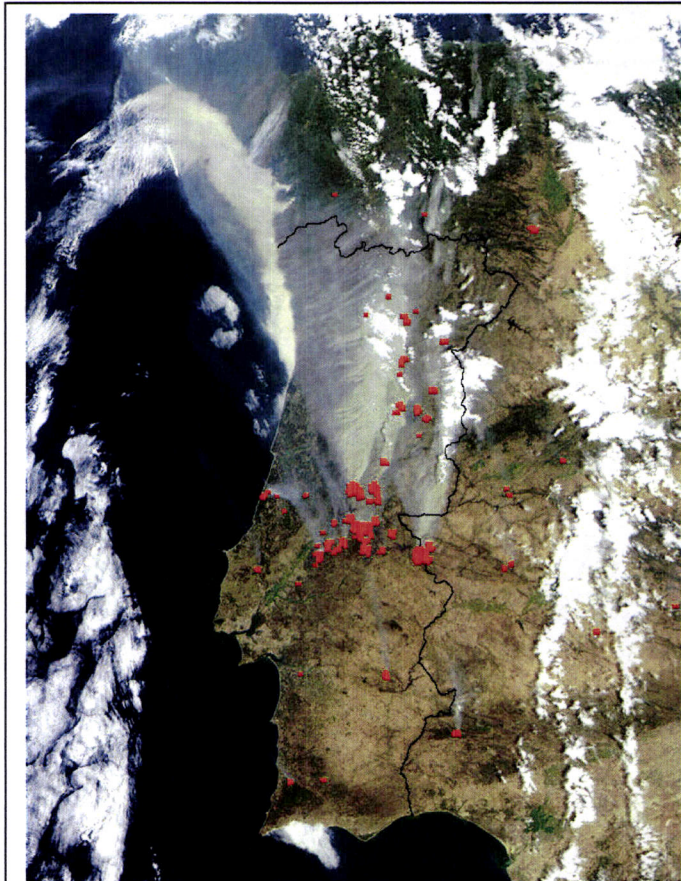


**Figure 5.22** – MODIS-Aqua image showing numerous wildfires burning across continental Portugal and Spain on 3 August 2003 and a thick smoke cloud obscuring most of the central and northern parts of Portugal. Image available online at <http://visibleearth.nasa.gov/>.

Portugal and Spain (Costa et al. 2003).

The first case concerns the smoke transport event already described in Section 5.2.5.1, selected also for the aerosol characterization. In this case the attention is focused on the cloudy areas over the ocean, as well as over land. The present case study refers to the first 25 days of September 2000, whenever MODIS-Terra imagery was available over cloudy regions (southern Africa and surrounding areas subject to the smoke plumes-see Figure 5.23). Table 5.6 shows the data used in the present case.

The second case study focuses on the smoke transport event originated from the

numerous uncontrolled fires burning across continental Portugal during August 2003, which turned out to be the worst fire season that Portugal faced in the last 23 years if not ever. The MODIS-Aqua image in Figure 5.22 evidences several fires burning across the Iberian Peninsula on 3 August 2003, as well as an impressive smoke plume. The fires continued to spread during several days taking advantage of the hot, windy and extremely dry conditions all over the country, destroying Portugal's landscape and killing at least 22 people. It is estimated that an area of about 360000 ha burnt until the 20 August, among which were near 301200 ha of forests, i.e. about 5.6% of the entire Portuguese forest area (Barbosa et al. 2003). The remaining burnt area corresponds to cultivated fields (~44000 ha), barren land (~9000 ha) and urban areas (1700 ha). These numbers do not include the fires occurring after 20 August, which continued at least until mid September, contributing to aggravate the dramatic scenario. This case study takes the first days of August 2003, whenever MODIS-Terra and/or MODIS-Aqua imagery was available over cloudy regions (Iberian Peninsula and surrounding areas subject to the smoke plumes – see Figure 5.24). Table 5.6 shows the data used in the present case study.

### 5.3.2.2 Data

Data from the LEO sensor MODIS flying onboard Terra and Aqua satellites (see Section 3.3.2.2) used in the present study was obtained from the NASA Distributed Active Archive Center (DAAC) (see online at <http://daac.gsfc.nasa.gov>). Table 5.6 summarises the data version (related with the DAAC data delivery), dates and acquisition times of the imagery– granules - each one representing 5 minutes of Terra or Aqua satellite viewing.

The validation datasets are constituted also in this case by completely independent results of the cloud microphysical / optical properties, obtained from aircraft *in situ* measurements and satellite based algorithms (see Appendix B).

Case Study	Satellite	Date	MODIS Granule Acquisition Time (UTC)	Version
Biomass burning over the southern African continent	Terra	02-09-2000	From 0945 to 0950	004
		02-09-2000	From 1120 to 1125	
		04-09-2000	From 0935 to 0940	
		05-09-2000	From 1015 to 1020	
		06-09-2000	From 0920 to 0925	
		07-09-2000	From 1005 to 1010	
		09-09-2000	From 0950 to 0955	
		10-09-2000	From 1035 to 1040	
		11-09-2000	From 0940 to 0945	
		12-09-2000	From 1020 to 1025	
		13-09-2000	From 0925 to 0930	
		14-09-2000	From 1010 to 1015	
		16-09-2000	From 0955 to 1000	
		17-09-2000	From 0900 to 0905	
		18-09-2000	From 0945 to 0950	
Biomass burning over the Iberian Peninsula	Terra	03-08-2003	From 1045 to 1050	004
		03-08-2003	From 1225 to 1230	
		04-08-2003	From 1125 to 1130	
		04-08-2003	From 1130 to 1135	
		05-08-2003	From 1210 to 1215	
	Aqua	03-08-2003	From 1400 to 1405	003
		04-08-2003	From 1305 to 1310	
		05-08-2003	From 1350 to 1355	

Table 5.6 – MODIS granules used for each of the case studies.

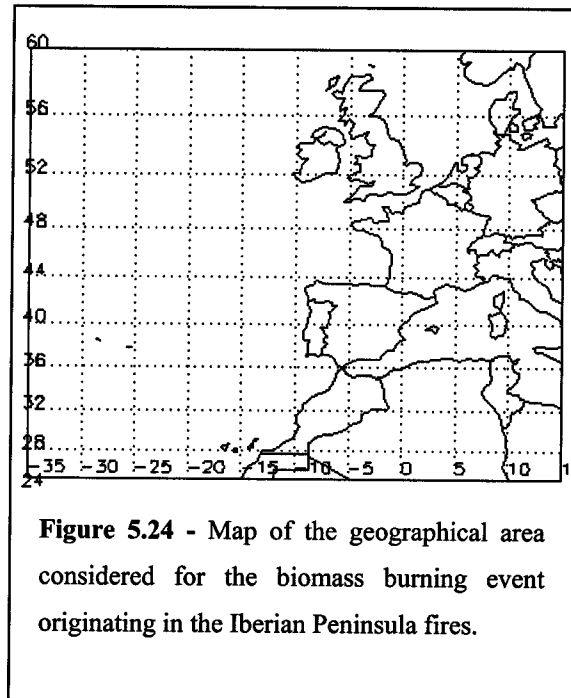
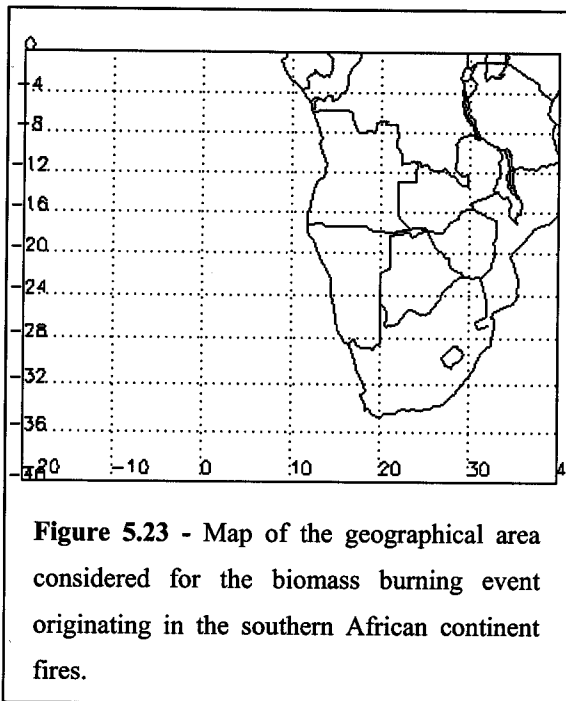
The available aircraft *in situ* measurements are used as a source of validation data only for the African case study, since these measurements were taken during the Southern African Fire-Atmosphere Research Initiative 2000 (SAFARI 2000) field campaign, which was an international regional science initiative (Swap et al. 2003). The campaign explored, studied and addressed the linkages between land-atmosphere processes, the relationship between biogenic, pyrogenic or anthropogenic emissions and the mechanisms of the biogeophysical and biogeochemical systems, and the consequences of deposition. The intensive SAFARI 2000 six-week field campaign was conducted from 13 August to 25 September and included satellite (Terra and Landsat-7) observations, numerous flights over AERONET sites, deployment of flux towers in South Africa, Botswana and Zambia, and *in situ* aircraft measurements. In addition, the cloud properties retrievals are also compared with the official cloud product from MODIS (King et al. 1998).

Table 5.7 summarises the data used in the validation of the methodology, as well as the cloud properties compared for each of the cases, and for the dates specified in Table 5.6. Note that the exact geographical areas of study cannot be defined since they vary accordingly to the location of the MODIS granule considered (indicated in Table 5.6). Nevertheless, the maps in Figures 5.23 and 5.24 delimit the regions where the MODIS granules used in each of the case studies were always picked up.

The SAFARI 2000 data sets used in this work (available online at <http://mercury.ornl.gov/SAFARI2K/SEARCH.HTM>) are constituted by the UK Met Office C-130 aircraft measurements (Keil and Haywood 2003) and by the cloud and aerosol measurements from the ER-2 Cloud Physics Lidar (CPL) (McGill et al. 2003). For comparison sake the SAFARI 2000 data are always attributed to the retrieved cloud parameters of the nearest MODIS pixel. Due to the availability of only one MODIS granule data per day over the regions of the case studies, the time coincidence between the aircraft measurements and the cloud retrieved parameters is not every time optimal, but always within a 2-3 hours time frame. Note again that data from a GEO satellite sensor like SEVIRI with a measurement frequency of 15 minutes would greatly improve the comparisons.

Case Study	Validation data	Cloud properties compared
Biomass burning over the southern African continent	SAFARI 2000: UK MetOffice C-130 aircraft	Effective radius ( $r_{eff}$ ) Liquid water content ( $w$ ) Top height ( $Z^c$ )
	SAFARI 2000: ER-2 Cloud Physics Lidar (CPL)	Top height ( $Z^c$ )
	MODIS cloud product	Thermodynamic phase Optical thickness ( $\tau^c$ ) Effective radius ( $r_{eff}$ ) Top temperature ( $T^c$ )
Biomass burning over the Iberian Peninsula	MODIS cloud product	Thermodynamic phase Optical thickness ( $\tau^c$ ) Effective radius ( $r_{eff}$ ) Top temperature ( $T^c$ )

Table 5.7 – Data used in the validation of the methodology developed.



Comparisons between the retrieval results and time-space collocated MODIS official product data sets of the cloud properties indicated in Table 5.7 (thermodynamic phase,  $\tau^c$ ,  $r_{eff}$ , and  $T^c$ ) were also carried out. The idea was to validate the present retrievals against a state of the art retrieval algorithm, in particular as regards to the set up of the algorithm and the threshold selection of cloudy pixels (see Section 5.3.1). The retrievals from the present methodology using MODIS radiance measurements has a spatial resolution of  $1 \times 1 \text{ km}^2$  so that it is possible to directly compare the values with MODIS official results of  $\tau^c$ , and  $r_{eff}$ . However, MODIS official results of the thermodynamic phase, and  $T^c$  have a spatial resolution of  $5 \times 5 \text{ km}^2$ , which is not suitable for directly check them against the results obtained here. Therefore, both results are arithmetically averaged in coincident boxes of  $0.05^\circ \times 0.05^\circ$  (areas around  $5.5 \times 5.5 \text{ km}^2$ ) and then compared.

The relative average difference (*Difr*) between the independent results ( $X^{indep}$ ) used in the comparisons and the results obtained from the present methodology ( $X^{derived}$ ) is defined as:



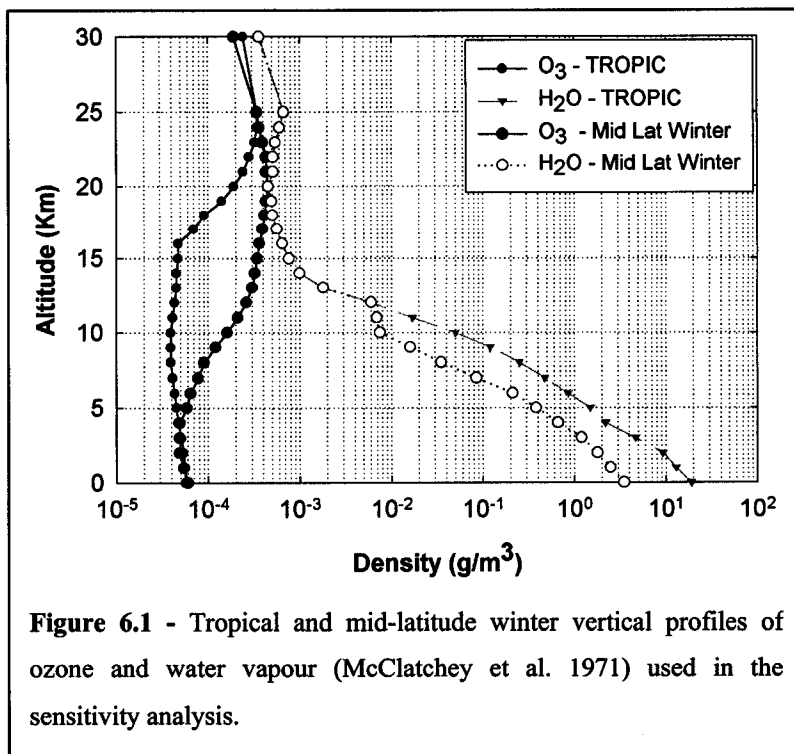
$$Difr = \frac{\sum_{i=1}^n \left| \frac{X^{indep} - X^{derived}}{X^{indep}} \right|}{n} \quad (5.7)$$

being  $n$  the number of comparisons performed. The error reported for MODIS cloud products such as the cloud optical thickness and effective radius ( $\tau^c$  and  $r_{eff}$ ) is  $\pm 25\%$  (King et al. 1998). Therefore, a threshold value of  $\pm 25\%$  is imposed for the *Difr* as the necessary condition to consider the validation accomplished and consequently the validity of the methodology.

Three-dimensional back trajectories are also used as an additional tool in order to trace the origin of the air masses under study, namely in the cases of cloudy scenarios where there are likely aerosol events of a certain type / origin. The trajectories were calculated using the NOAA HYbrid Single-Particle Lagrangian Integrated Trajectory Model (HYSPLIT4) (Draxler and Rolph 2003; Rolph 2003), over a duration of 72 hours and using the meteorological input fields from the 6-hourly FNL archive data generated by the National Centers for Environmental Prediction Global Data Assimilation System (NCEP GDAS). The data is subsequently processed by the NOAA's Air Resources Laboratory (ARL) to convert the  $1^\circ \times 1^\circ$  latitude-longitude grid to hemispheric  $129 \times 129$  polar stereographic grids. This meteorological dataset includes the u- and v-wind components, temperature and humidity at 13 vertical levels, from the surface up to 20 hPa. Further information on the FNL archive can be obtained online at <http://www.arl.noaa.gov/ss/transport/archives.html>. The back trajectories were calculated at different pressure levels, according to the case under study and to the cloud top pressure values retrieved ( $P^c$ ) and the vertical motion is determined using the vertical velocity fields from the meteorological data.



when applied to current satellite systems (Wang et al. 2003a). On one hand, satellite observations do not allow for an accurate determination of the particle shape and, on the other hand, even if these shapes were perfectly known, the necessary analytical tools for their description may not be available. In fact most of the satellite-based algorithms still rely on the use of Mie theory (Tanré et al. 1997; Veeffkind and de Leeuw 1998; Torres et al. 1998; Torricella et al. 1999; Wang et al. 2003b). Improvements in the retrievals were brought about by the use of ground-based measurements to take into account the effects of aerosol particle shape, but the issue is yet to be resolved (Dubovik et al. 2002b). The integration of non-spherical theories in the methodology at its present status of development would introduce further assumptions on particle shape and consequently further uncertainties: this is why the Mie theory is used. Nevertheless, planned future developments of the methodology will have to address the particle shape problem, making use of additional satellite and complementary ground-based measurements when necessary.



The vertical atmospheric profiles adopted for the analysis are the tropical and the mid-latitude winter (McClatchey et al. 1971). The ozone and water vapour profiles for both atmospheres are represented in Figure 6.1. These profiles aim at representing extreme conditions for the geographical areas where

the algorithm is to be applied (GEO satellite coverage), therefore the resulting differences represent the upper limit for real atmospheric conditions.

The results obtained with the assumption of a lambertian ocean surface, considering a typical spectral reflectance characteristic of clear seawater (Viollier 1980), are compared

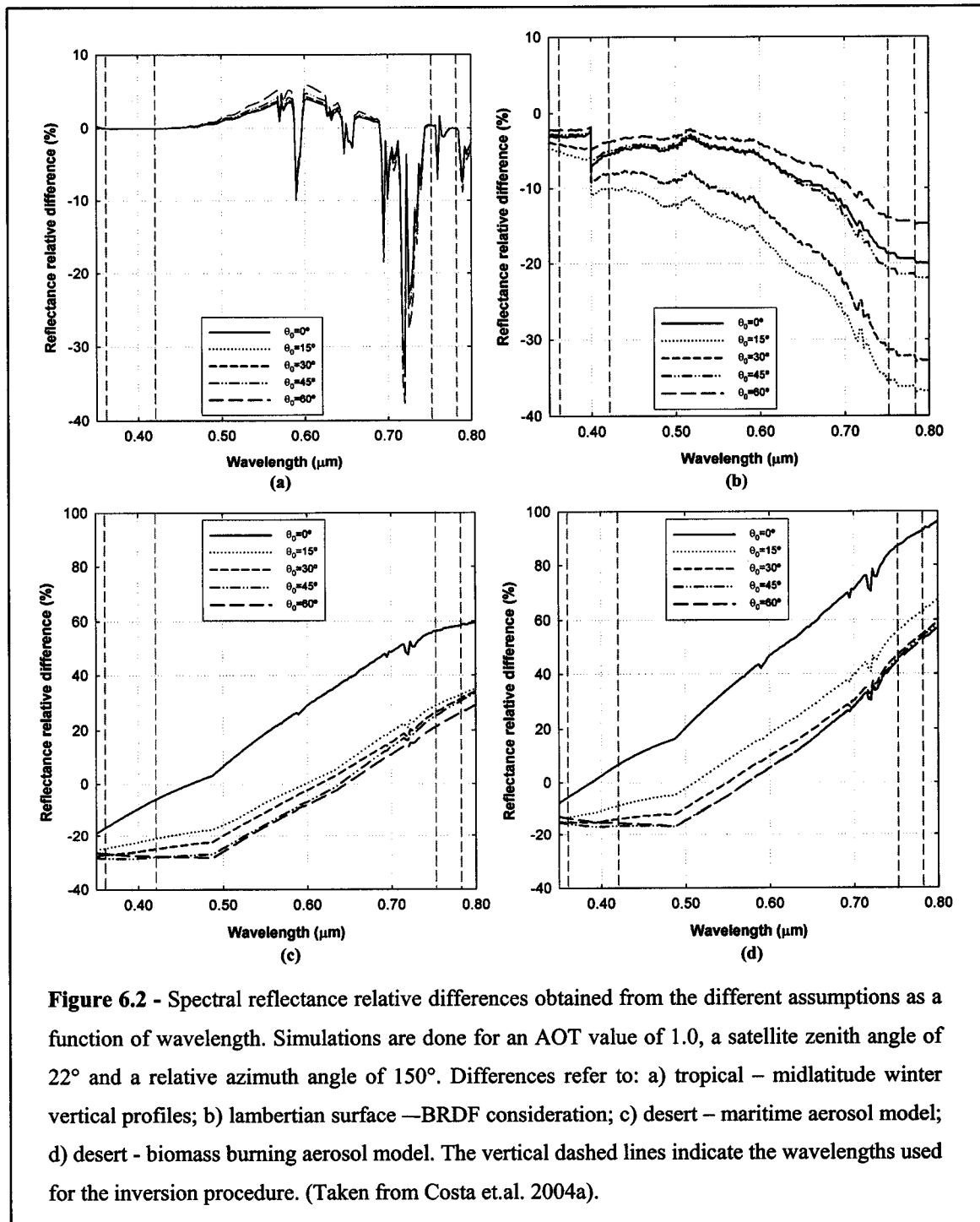
to those retrieved considering a Bi-directional Reflectance Distribution Function (BRDF) for the ocean surface, aiming at quantifying the differences between the two cases. The BRDF ocean model contained in 6S (Morel 1988) is used and takes into account wind speed and direction, ocean salinity, and pigment concentration. A wind speed value of  $6 \text{ m s}^{-1}$ , a wind direction of  $45^\circ$ , a salinity value of 35 ppt, and a pigment concentration of  $0.3 \text{ mg m}^{-3}$  were considered to represent mean values representative of the situations under study.

Three literature aerosol models were considered in the sensitivity analysis as indicated in Table 6.1 since they represent fairly different possible atmospheric aerosol scenarios: maritime, desert, and biomass burning defined by Dubovik et al. (2002a).

Aerosol Model	Reference
Maritime: Lanai	Dubovik et al. 2002a
Desert Dust: Cabo Verde	
Biomass Burning: African Savannah	

Table 6.1 – Literature aerosol models considered in the sensitivity analysis.

Figure 6.2 shows the graphs of the relative differences of the spectral reflectance obtained when changing the assumptions with respect to the vertical atmospheric profiles, surface type, and aerosol model. Results are shown as a function of the wavelength for different solar zenith angles, considering an AOT value of 1.0, a satellite zenith angle of  $22^\circ$ , and a relative azimuth angle of  $150^\circ$ . These angles are chosen because they correspond to a typical GOME geometry. The moderately high AOT value (1.0) is used to establish the maximum errors arising from the different assumptions. The grey vertical dashed lines in each graph of Figure 6.2 mark the position of the wavelengths considered in the inversion procedure.



Results in Figure 6.2a) refer to simulations of the spectral reflectance considering a lambertian ocean surface and the desert aerosol model. As for the vertical characterization, two situations are considered: a tropical and a midlatitude winter vertical profile. These results are subtracted and the respective difference converted in percentage with respect to the value obtained with the tropical profile. The analysis shows that the use of such

considerably different vertical atmospheric profiles of water vapour and ozone (see Figure 6.1) has a moderate impact on the modelled spectral reflectance, depending on the wavelength. The spectral reflectance relative differences are always  $< 1\%$  (absolute value) for all the wavelengths used (0.361, 0.421, 0.753, and 0.783  $\mu\text{m}$ ), as it would be reasonably expected since these wavelengths were chosen to avoid gas absorption regions as much as possible (see Section 5.2.1). The relative differences of the spectral reflectance presented in Figure 6.2b) result from considering first the surface as a lambertian reflector, and second its BRDF. In this case, the atmospheric tropical vertical profile and the desert aerosol model were considered. Relative differences were calculated with respect to values obtained with the lambertian surface. In this case, the results depend on the geometry (solar zenith angle), and in general the resulting differences, though higher than previously, are lower than 11% (absolute value) in the blue and 15 to 35% (absolute value) in the red spectral region. The spectral reflectance is also analysed with respect to the considered aerosol model. Figure 6.2c) and 6.2d) illustrate the results obtained when comparing the desert and maritime, and the desert and biomass burning aerosol models, respectively (see Table 6.1). In this case, the ocean surface is considered lambertian and the atmospheric profile is tropical. The spectral reflectance relative differences were calculated with respect to values obtained with the desert aerosol model. The graphs show slightly different behaviours for the two situations. The desert and maritime aerosol models present differences that range between 5 and 30% (absolute value) in the blue spectral region and are generally between 20% and 35% in the red, except for  $\theta_0=0^\circ$  that reaches 60%. When the biomass burning aerosol model is considered, the differences for smaller wavelengths are lower than the previous ones (between  $-5\%$  and  $-15\%$ ), whereas for the longer wavelengths they are higher, in general between 55% and 70%, and slightly higher for  $\theta_0=0^\circ$  as previously, reaching differences of 95%. The analysis of Figure 6.2 clearly shows that among the investigated assumptions the aerosol model is the factor that most influences the spectral reflectance. However, the surface characterization may also have an important role, depending on the geometric conditions, as illustrated in Figure 6.2b).

The AOT absolute differences as a function of the solar zenith angle (obtained from GEO data according to Section 5.2.3) are plotted in Figure 6.3 for different satellite zenith angles. An AOT reference value of 1.0 is considered, corresponding to the tropical atmospheric profile as an extreme high humidity case, the lambertian ocean surface, and

the desert model in all cases. The AOT differences are obtained subtracting the values obtained with the different assumptions from the reference AOT value of 1.0. An instrumental random error of  $\pm 15\%$  of the total GEO signal is considered in the analysis, which stems from the estimation of the Meteosat errors on calibration (10% [Govaerts 1999]) and spectral response (10% maximum, Govaerts personal communication).

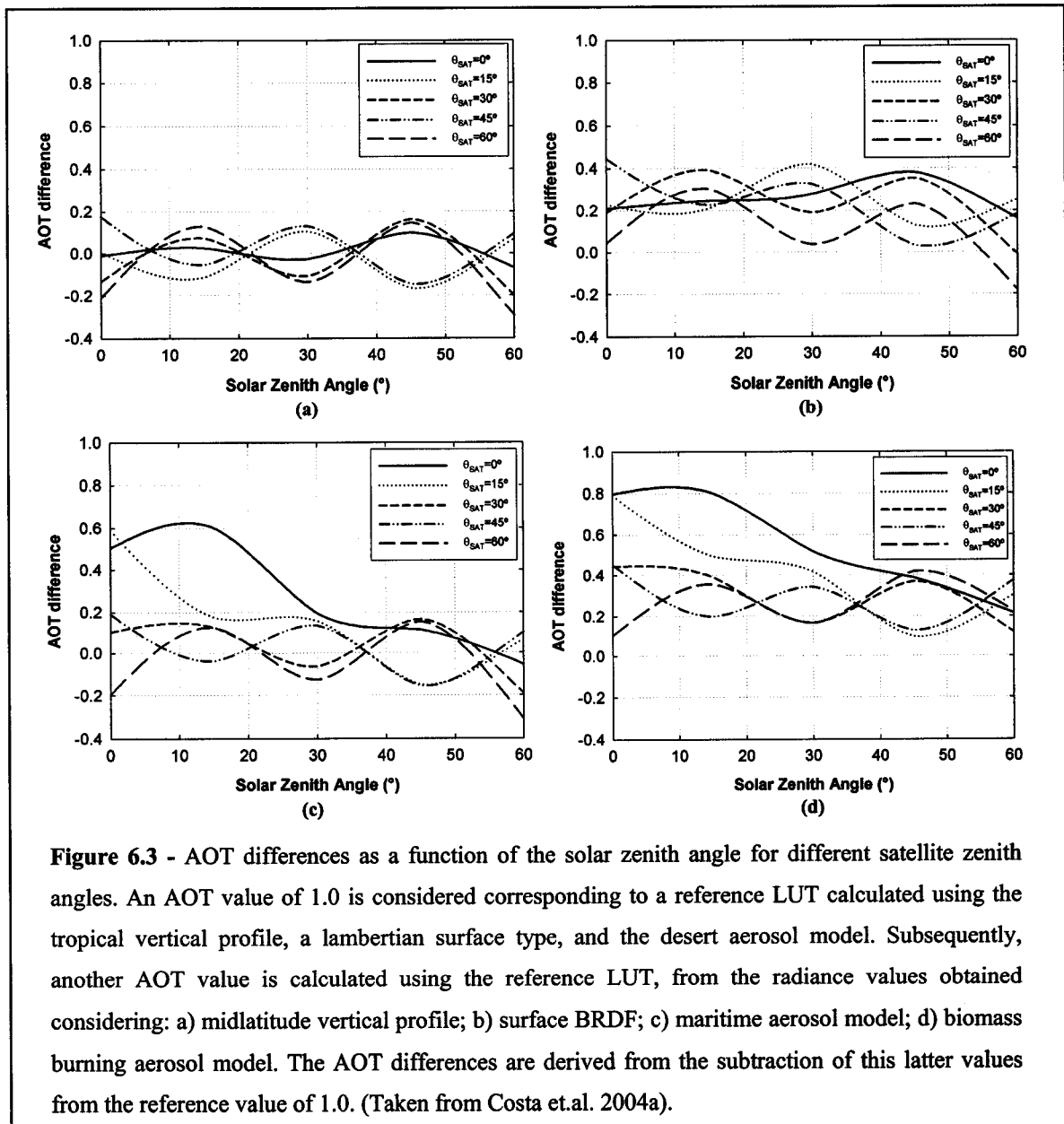


Figure 6.3a) shows the AOT differences while considering the midlatitude winter profile instead of the tropical profile used to estimate the reference value. The differences are in general within  $\pm 0.2$ , except for high solar and satellite zenith angles when the AOT deviates about  $-0.3$  from the AOT reference value of 1.0. The sinusoidal trend is related to

the random  $\pm 15\%$  error considered in the GEO simulated radiances. The graphs of Figure 6.3b) show the AOT absolute differences when the surface BRDF is considered, with respect to the reference values derived when considering the ocean surface as a lambertian reflector. Results exhibit maximum differences ranging from -0.2 (high solar and satellite zenith angles) up to 0.4, which constitute considerable deviations with respect to the AOT reference value of 1.0. The sinusoidal trend is once more introduced by the random  $\pm 15\%$  error considered. Figure 6.3c) illustrates the results stemming from the use of the maritime aerosol model as compared to the reference values with the desert aerosol model. A moderate dependence on the geometry is found. The highest AOT differences range from about -0.3 to 0.6. The plots of Figure 6.3d) show the AOT absolute differences when the biomass burning aerosol model is assumed, and then compared to the reference value (desert aerosol model). This case is also characterized by high differences in the AOT results with a maximum of 0.8; i.e. a deviation of 80% from the reference AOT, and a minimum of 0.1. The analysis of Figure 6.3 clearly shows that, among all the investigated possible influences, the aerosol model is the factor that most influences the AOT, including not only the aerosol size distribution parameters, but also the aerosol absorption through the imaginary part of the refractive index. Veefkind and de Leeuw (1998) show that an unrealistic aerosol size distribution may introduce substantial errors on the AOT retrievals from -40 to +60%, which is in agreement with the present results. The surface characterization has also a large impact on the AOT (not shown in the figure) that becomes increasingly important for low aerosol loads because the signal received by the satellite is dominated by the surface contribution. The sensitivity analysis of Tanré et al. (1997) has demonstrated that an additional surface contribution results in larger AOT values, and that this effect is more important the smaller the AOT values.

Figure 6.4 shows the graphs of the TOA DSWARF (Section 5.2.4) differences as originated with the different assumptions as a function of the AOT for different solar zenith angles, as already considered. Reference values of the TOA DSWARF are calculated considering the lambertian ocean surface, the tropical atmospheric profile, and the desert aerosol model. The vertical dashed grey lines represent the AOT variation limits resulting from the instrumental random error introduced in the GEO simulated radiances ( $\pm 15\%$ ) and from the different assumptions (see Figure 6.3). The aim is to quantify the



uncertainty in the TOA DSWARF from errors introduced in the AOT calculation from GEO data.

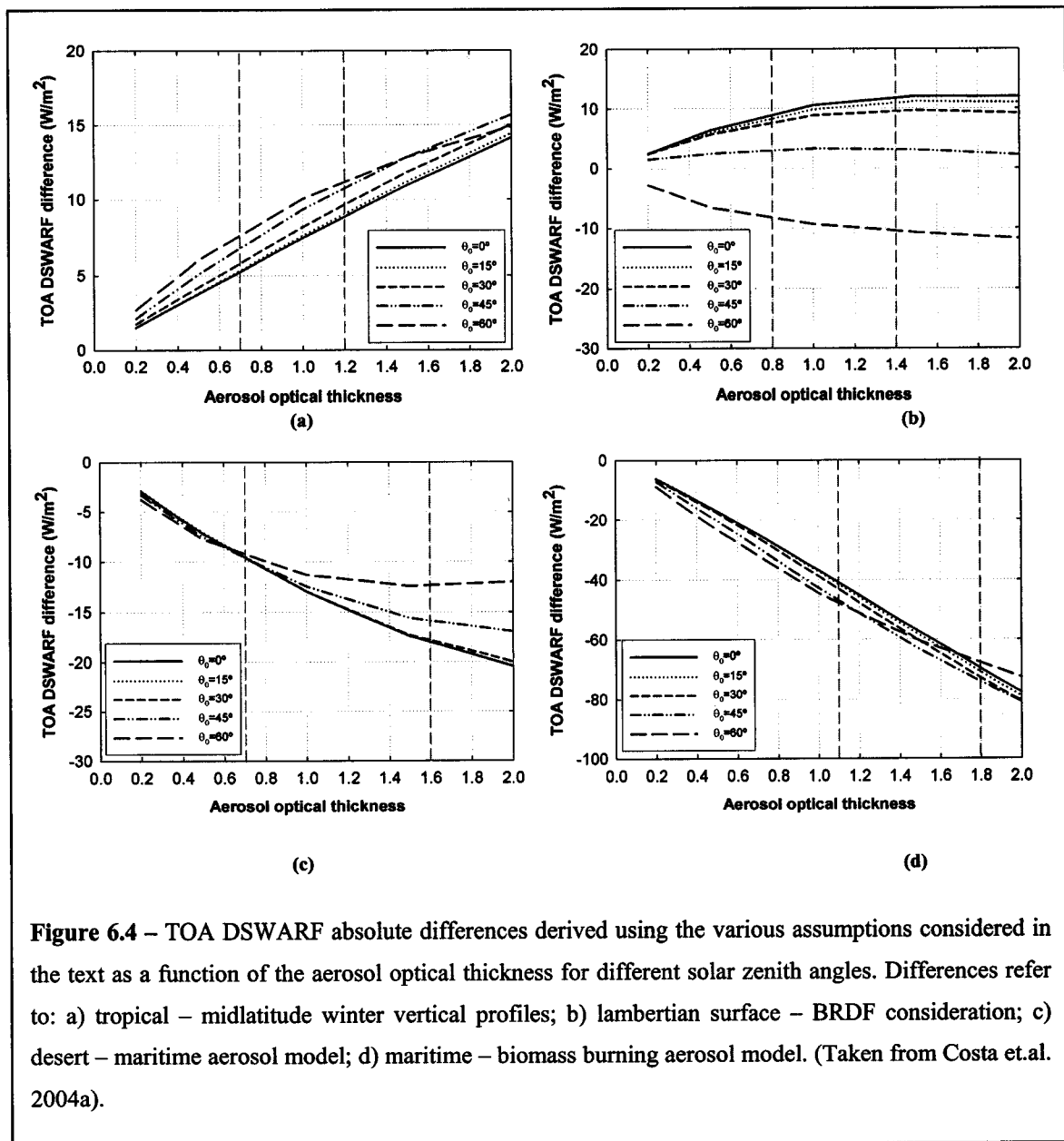


Figure 6.4a) illustrates the differences with respect to the reference values when calculations are done considering the midlatitude winter profile. Differences in this case are proportional to the AOT values and mostly independent of the solar zenith angle, reaching about 15 W m<sup>-2</sup> for AOT > 1.8. The AOT uncertainty of  $\Delta\tau^a = \pm 0.2$  introduced by the GEO instrumental error and the use of different atmospheric profiles (see Figure 6.3a) generates an uncertainty of about 4 W m<sup>-2</sup> in the TOA DSWARF difference. The impact of considering the surface BRDF instead of the Lambertian surface is displayed in Figure

6.4b) where the highest differences (about  $12 \text{ W m}^{-2}$  in absolute values) are observed for  $\text{AOT} > 1.4$  and  $\theta_0=0^\circ$  or  $\theta_0=60^\circ$ . For a solar zenith angle  $\theta_0=45^\circ$  the differences are generally lower than  $2.5 \text{ W m}^{-2}$ . In Figure 6.4b) one can see that the propagation of the AOT uncertainty (between  $-0.2$  and  $+0.4$ ) upon the TOA DSWARF difference is up to about  $2 \text{ W m}^{-2}$ , which is lower than the one introduced by the vertical profile. These results are inverted with respect to those presented in Figures 6.2 and 6.3, where the surface was a more important assumption than the gaseous profiles. This is connected to the fact that the TOA DSWARF results from flux calculations (see Sections 2.5 and 5.2.4), which are radiative quantities integrated over a broadband SW spectral region ( $0.25$  to  $4.0 \mu\text{m}$ ). In this broadband region important gas absorption bands are included, especially water vapour and ozone and consequently the assumption on the gaseous atmospheric constituents becomes more important. The differences arising from the use of the different aerosol models are reported in Figures 6.4c) and 6.4d). The first one refers to the use of a maritime aerosol model against the desert model used in the computation of the reference values. The differences are proportional to the AOT with maximum values around  $-20 \text{ W m}^{-2}$ . The second one corresponds to the comparison between the desert and the biomass burning aerosol models. In this case, the differences are also proportional to the AOT values although with a lower dependence on the solar zenith angle than the one found in the previous case (Figure 6.4c). Nevertheless, differences are much higher than in the previous case (Figure 6.4c), with the maximum value situated around  $-80 \text{ W m}^{-2}$ , whereas in Fig. 6.4c the maximum value reached down to  $-20 \text{ W m}^{-2}$ . In these cases the GEO AOT uncertainties delimited by the vertical dashed lines ( $-0.3$  to  $+0.6$  in Figure 6.4c and  $+0.1$  to  $+0.8$  in Figure 6.4d) generate greater TOA DSWARF difference uncertainties that may reach about  $11 \text{ W m}^{-2}$  in the first case (Figure 6.4c), and around  $30 \text{ W m}^{-2}$  in the second case (Figure 6.4d).

For all the situations investigated in the present study, the aerosol model is the factor that most influences any of the analysed radiative quantities: spectral reflectance (Figures 6.2c,d), AOT (Figures 6.3c,d), and TOA DSWARF (Figures 6.4c,d). The retrieval of the effective aerosol quantities is therefore extremely important in order to reduce the errors in the retrievals of the aerosol load and its direct radiative forcing, particularly for situations of aerosol events. The adoption of one or the other of atmospheric vertical profiles has a relatively small impact on the retrievals and this implies that the use of

latitudinal- and seasonal- dependent atmospheric profiles is a reasonable approximation to be adopted in the present algorithm. The different surface characterizations (Lambertian / BRDF) originate moderate differences in the results that become more significant for low aerosol loads, as reported by Mishchenko et al. (1999). Since the aim of the present algorithm is the study of aerosol events over the ocean generally distinguished by moderately high aerosol contents and low impact of the surface characterization on the TOA DSWARF, the Lambertian ocean surface may be considered a reasonable approximation. Nevertheless, it is planned to build LUTs considering the surface BRDF aiming at improving the accuracy of the methodology.

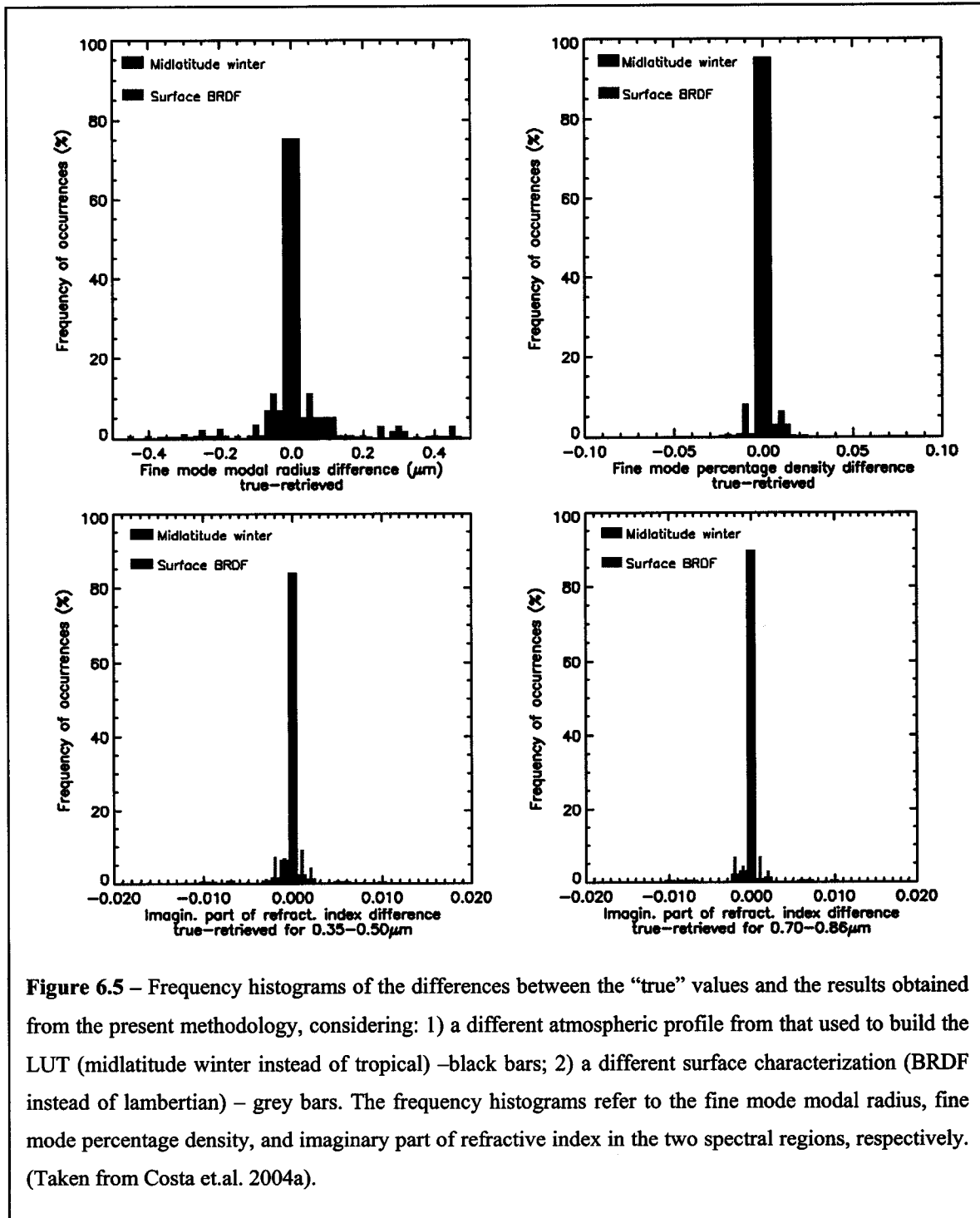
The methodology is tested using synthetic GOME measurements calculated via the 6S code. The synthetic GOME spectral reflectance values are obtained for 231 cases that comprehend different geometric conditions, aerosol models, and AOT values. The aerosol model parameters and AOT values used to calculate the synthetic GOME measurements are hereinafter referred to as “true” values. Firstly, these synthetic data were given as input to the algorithm without changing any assumption with respect to those considered in the LUTs and the spectral reflectances were measured error free in order to test the algorithm performance. In this case, the values of the fine mode modal radius ( $r_F$ ), the fine mode percentage density ( $Pd_F$ ), the imaginary part of refractive index ( $m_{i,\lambda}$ ) in the two spectral regions (0.35 – 0.50  $\mu\text{m}$  and 0.70 – 0.86  $\mu\text{m}$ ), and the AOT ( $\tau_{\lambda=0.55\mu\text{m}}^{\text{aerosol}}$ ) were perfectly retrieved with 100% of the differences peaking at zero (not shown). Successively, the synthetic data were tested for different assumptions of the surface characterization, and of the atmospheric vertical profiles of water vapour and ozone. In addition, values of the fine mode modal radius, the fine mode percentage density of particles, the imaginary part of the refractive index in the two spectral regions, and the AOT not included in the LUTs were also considered. Finally, the assumption that the aerosol is homogeneously distributed horizontally over the GOME pixel and the effect of using a single Sun/satellite geometry were also assessed through the investigation of the best time coincident GEO radiance values (maximum time difference of 15 minutes) enclosed by the geographical coordinates of the corners of each of the GOME pixels selected for inversion. The mean and standard deviation of the GEO radiance distribution inside each of the analysed GOME pixels was computed. The relative error was obtained from the ratio between the standard deviation and mean values for each of the pixels. More than 800 pixels selected for the case studies

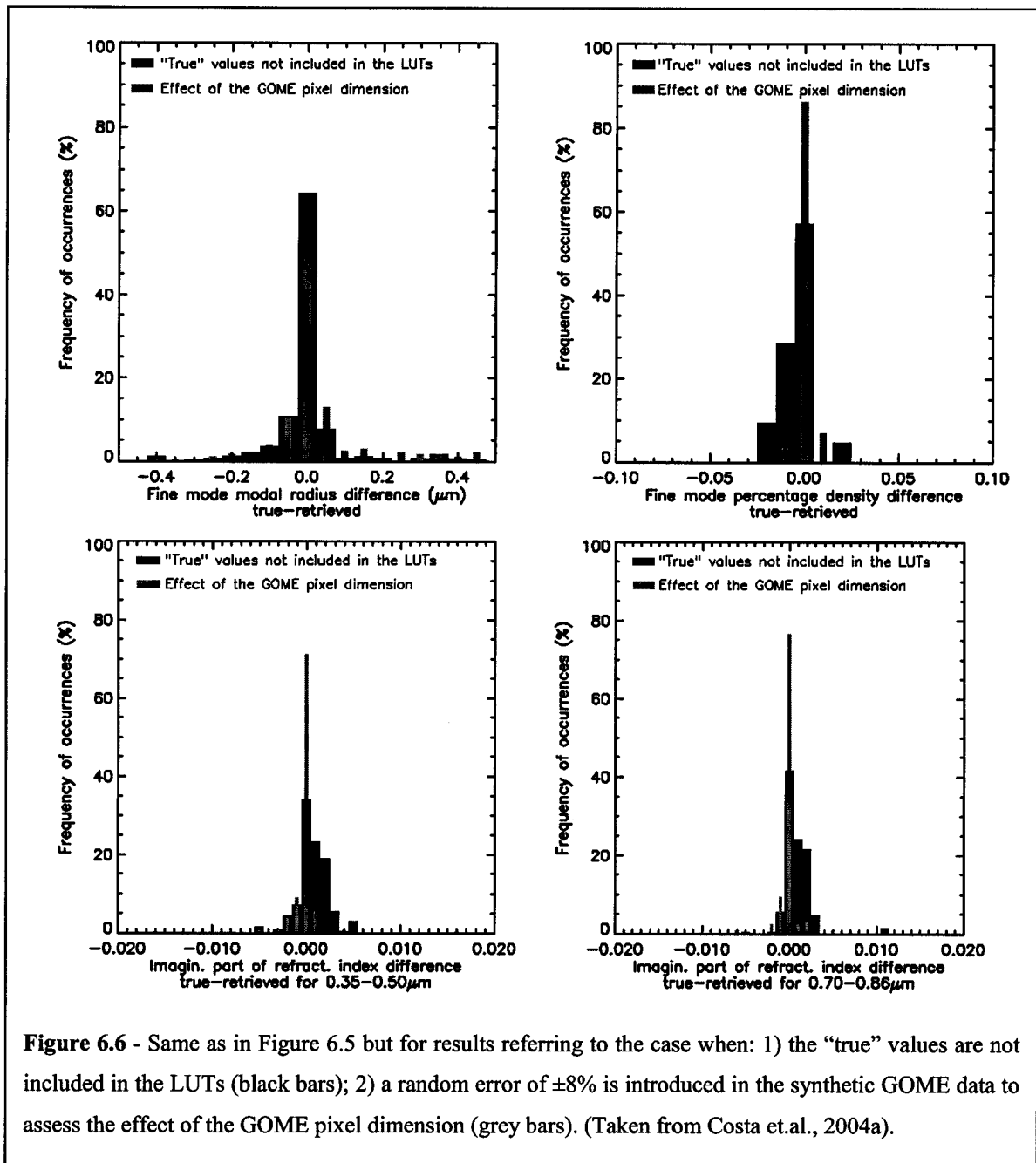
presented here (see Section 5.2.5.1) were analysed and the relative errors averaged, obtaining a mean relative error of 8%. It was assumed that this is the error affecting the GOME spectral reflectance therefore a random error of  $\pm 8\%$  was introduced in the synthetic GOME data. The instrumental radiometric calibration error is considered in all cases by introducing a random noise of  $\pm 1\%$  to the synthetic data, reflecting in the GOME relative radiometric accuracy less than 1% (Burrows et al. 1999).

The frequency histograms in Figure 6.5 show the differences between the “true” values and the results from the present methodology considering: 1) a different atmospheric profile from that used to build the LUT (midlatitude winter instead of tropical) – black bars; 2) a different surface characterization (BRDF instead of lambertian) – grey bars. The frequency histograms refer to the fine mode modal radius ( $r_F$ ), the fine mode percentage density ( $Pd_F$ ), and the imaginary part of refractive index ( $m_i$ ) in the two spectral regions, respectively. For the different vertical profile the differences are quite low: about 92% of the fine mode modal radius differences are within  $\pm 0.075 \mu\text{m}$ . As for the fine mode percentage density, more than 95% of the cases are very well retrieved, being the differences between the “true” and derived values within  $\pm 0.005$ . The differences obtained for the imaginary part of the refractive index are also quite low, i.e. about 93% of the values fall inside the interval  $\pm 0.0015$  for both spectral regions (0.35-0.50  $\mu\text{m}$  and 0.70-0.86  $\mu\text{m}$ ). When the surface BRDF is considered, the differences are in general higher as it would be expected also from the results in the graph of Figure 6.2b). The fine mode modal radius differences present 72% of the cases within  $\pm 0.075 \mu\text{m}$ . The fine mode percentage density is still well retrieved with about 84% of the differences within  $\pm 0.005$ . As for the imaginary part of the refractive index, differences are within  $\pm 0.0015$  for 78% of the cases in the first spectral region and 81% of the cases in the second spectral region.

The performance of the methodology was also tested for situations where the aerosol models and AOT values were not included in the LUTs calculation, which may often occur. On the other hand, the effect of the large GOME pixel on the assumption that the aerosol is homogeneously distributed horizontally over the GOME pixel and the effect of using a single Sun/satellite geometry were also assessed. The frequency histograms in Figure 6.6 illustrate the differences between the “true” values and the results obtained from the present methodology, when: 1) the “true” values are not included in the LUTs (black

bars); 2) a random error of  $\pm 8\%$  is introduced on the synthetic GOME data to assess the effect of the GOME pixel dimension (grey bars).





About 82% of the fine mode modal radius differences are within  $\pm 0.075 \mu\text{m}$ , when the "true" values are not included in the LUTs, whereas 75% of the values are within  $\pm 0.075 \mu\text{m}$  when the effect of the GOME pixel dimension is considered. The fine mode percentage density is well retrieved with 86% ("true" values not included in the LUTs - black bars) and 95% (effect of the GOME pixel dimension - grey bars) of the differences both within  $\pm 0.015$ . As to the imaginary part of the refractive index, the frequency histograms are slightly broader when the "true" values are not included in the LUTs,

translating into larger differences between “true” and retrieved values. Differences are within  $\pm 0.0015$  for 65% of the cases within the first spectral region. About 71% of the cases are within  $\pm 0.0015$  in the second spectral region. The effect of the GOME pixel shows differences within  $\pm 0.0015$  for 86% and 89% of the cases for the first and second spectral regions, respectively.

The graphs in Figure 6.7 illustrate the analysis of the AOT derived from GOME measurements together with the aforementioned aerosol quantities.

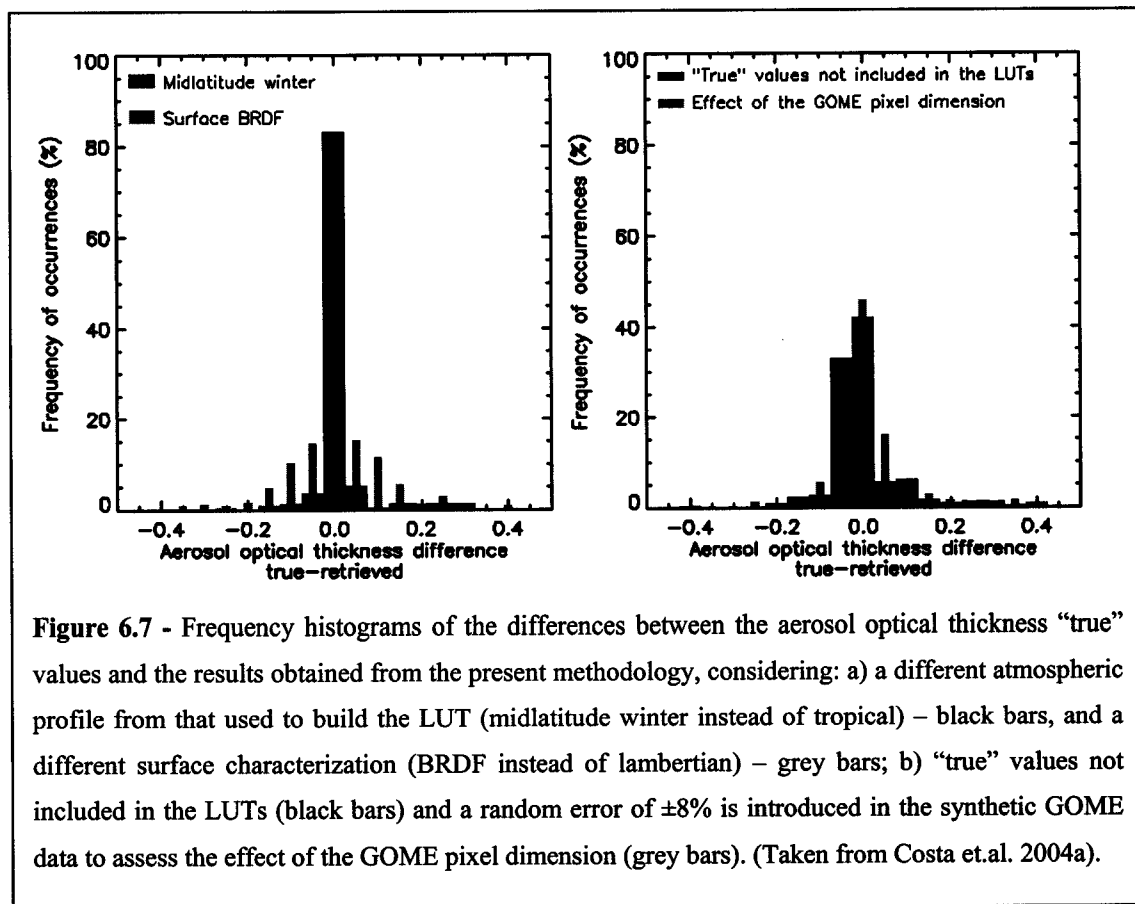


Figure 6.7a) refers to the different atmospheric and surface assumptions, and Figure 6.7b) is obtained when the “true” AOT values are not included in the LUTs and when the GOME pixel dimension is considered. Note that once again the AOT is well retrieved when the vertical profile is changed (black bars in Figure 6.7a) with more than 90% of the differences situated between  $\pm 0.075$ , whereas only about 56% of the differences are within this limit when the surface characterization is changed (grey bars in Figure 6.7a). Nevertheless, about 90% of the AOT differences are within  $\pm 0.175$ . As seen before, these differences are more significant for low aerosol loads (not shown in the graph). When the

“true” AOT values are not included in the LUTs (black bars in Figure 6.7b), about 81% of the differences are within  $\pm 0.075$ , while 78% of the cases are within this limit when the effect of the GOME pixel dimension is accounted for (grey bars in Figure 6.7b).

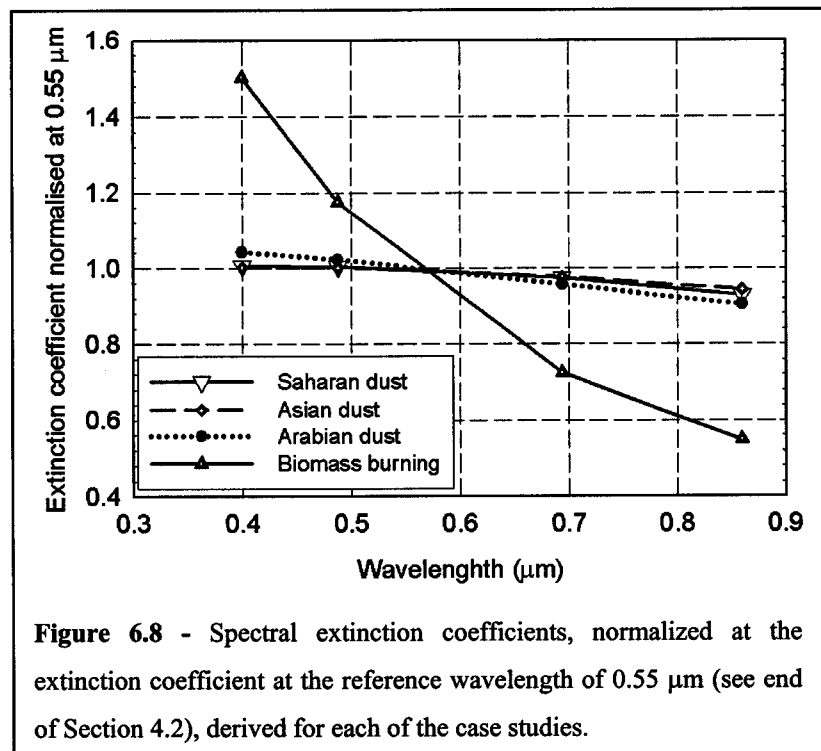
The above results reflect the differences between the aerosol models used to build the synthetic spectral reflectance and those contained in the LUTs that best fit the synthetic spectra. Note that no interpolation of the LUT values is done, since the aerosol models in the LUTs are fixed. Therefore, the resulting narrow histograms and the peaks near zero are an indication of the good performance of the algorithm search in the LUT for values closest to the “true” value.

## 6.2.2 Aerosol quantities derived from GOME

The fitting procedure described in the previous chapter (Section 5.2.2), performed over all selected GOME pixels for each of the four case studies considered (Section 5.2.5.1), resulted in the retrieval of several size distributions and complex refractive indexes at the GOME spatial scale, characterizing the mixture of aerosols present in the atmosphere for each space-time measurement. In fact only the fine mode modal radius ( $r_F$ ), the percentage density of particles for the fine mode ( $Pd_F$ ) and the imaginary part of the refractive index ( $m_i$ ) in the two considered spectral regions (0.35 – 0.50  $\mu\text{m}$  and 0.70 – 0.86  $\mu\text{m}$ ), are derived, since the remaining size distribution parameters and the real part of refractive index are fixed for each case study according to the values of the climatological aerosol model considered (taken from Dubovik et al. 2002a) or to the values obtained from ground-based measurements (Asian dust case study; Sohn personal communication), for each case study. Results of the size distributions and complex refractive indexes for each of the case studies are successively used to obtain the corresponding spectral aerosol optical quantities, namely the extinction, scattering and absorption coefficients ( $\beta_\lambda^e, \beta_\lambda^s$  and  $\beta_\lambda^a$ ), the aerosol phase function ( $P_\lambda(\Theta)$ ), and the spectral single scattering albedo ( $\varpi_\lambda$ ). These quantities are calculated assuming spherical aerosol particles, hence using the GOME-derived size distributions and complex refractive indexes as input for Mie calculations (see Section 2.3). The subsequent spatial and temporal analysis carried out for



the GOME-derived aerosol optical quantities result in mean effective aerosol models describing the actual atmospheric conditions for each of the case studies, replacing the



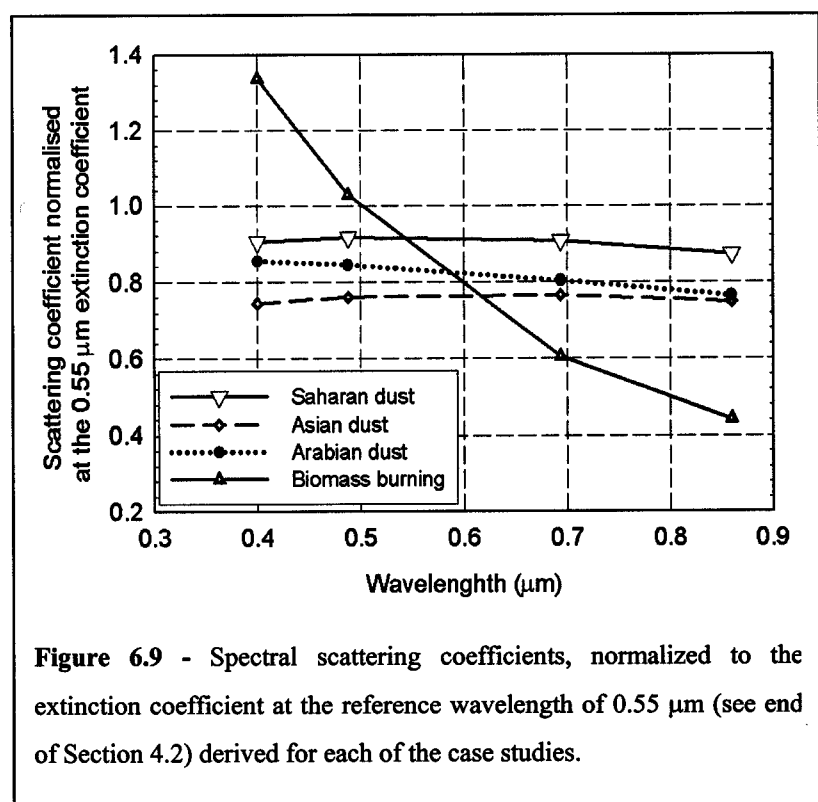
literature aerosol model.

The Ångström exponent  $\alpha$  is also calculated as explained in Section 5.2.2.

The results obtained for the extinction and scattering coefficients, normalized in the 6S code to the extinction coefficient at 0.55  $\mu\text{m}$  (see Section 4.2) are shown in Figure 6.8 and 6.9, respectively.

The normalized extinction coefficients shown in Figure 6.8 present a spectral behaviour

which is rather similar for the three dust cases, with a slight decrease of the values from the blue to the red spectral regions. However, the extinction coefficient corresponding to the biomass burning case presents at 0.4  $\mu\text{m}$  a higher value that decreases reaching much lower values at 0.86  $\mu\text{m}$  in comparison to the dust values. The GOME derived normalized



scattering coefficients (Figure 6.9) present a spectral behaviour comparable to the corresponding normalized extinction coefficients, as expected. The Saharan dust case presents slightly higher values of the scattering coefficients in comparison with the other two dust cases. The scattering coefficients derived for the biomass burning case present once more a strong decrease of the values between the blue and the red spectral regions. The normalized absorption coefficients are calculated from the extinction and scattering coefficients through the use of equation 2.17 (graph not shown).

The retrieved single scattering albedo ( $\omega_\lambda$ ), phase function ( $P_\lambda(\Theta)$ ) and Ångström exponent ( $\alpha$ ) values were compared with ground-based measurements from the official inversion product of the AErosol RObotic NETwork (AERONET) (Dubovik and King 2000) and with the aerosol properties derived from the ground-based radiation measurements taken in South Korea during Spring 2000 (Kim et al. 2002; Kim et al. 2004), assuming that the aerosol plumes kept moderately homogeneous during the period of the study. These comparisons are shown here in Figure 6.10, 6.11 and 6.12. A complete description of the datasets used in the comparisons can be found in Section 5.2.5.2 – Table 5.4.

### 6.2.2.1 Single scattering albedo

Figure 6.10 shows the values of the aerosol spectral single scattering albedo ( $\omega_\lambda$ ) for the four case studies together with those from literature aerosol models. The vertical error bars represent the standard deviation of the GOME derived single scattering albedo (around 0.04). AERONET single scattering albedo values have accuracy of the order of 0.03 for dust and for biomass burning events with AOT at  $0.44\mu\text{m} > 0.5$  (Dubovik et al. 2000). These error bars are not reported in the graphs of Figure 6.10 for clarity sake.

In Figure 6.10a the GOME derived values for the Sahara dust event are compared with AERONET's taken at the Dakar and Banizoumbou, sites that were over passed by dust plumes several times during this period; results from the AERONET inversion algorithm were not available from Cabo Verde and they are not shown. The single scattering albedo is in good agreement with the AERONET measurements, especially for the Dakar site in the red spectral region with differences lower than 0.01, whereas there is a

slight underestimation in the blue region reflecting in higher aerosol absorption than that reported by the AERONET Dakar measurements (differences of 0.016 at  $0.4\mu\text{m}$  and of 0.013 at  $0.488\mu\text{m}$ ). The climatological desert dust model derived from the AERONET data at Cabo Verde (Dubovik et al. 2002) presents considerably higher spectral single scattering albedo values outside the error bars associated with GOME derived results, with differences ranging between 0.05 at  $0.4\mu\text{m}$  and 0.07 at  $0.694\mu\text{m}$ . These differences may be related to the fact that on one hand the climatological model derived from AERONET data at Cabo Verde may reflect a mixture of “pure” desert dust blowing out from inland with the marine aerosol, a mist / haze frequently observed in this AERONET site. This means that the presence of marine aerosols within the desert dust plumes, contributes to higher single scattering albedo results (climatological aerosol model) due to the low absorption of the marine aerosols. On the other hand, the present method does not incorporate combined aerosol models, which have been shown previously to be key factors influencing spectral reflectances and the AOT. The fact that the AERONET single scattering albedo values in Banizoumbou are lower, particularly in the red spectral region (higher aerosol absorption) with differences that reach 0.035 at  $0.86\mu\text{m}$ , is probably connected with the site location well inland (see Figure 5.14), where the aerosol load might have been higher and the land surface properties are quite different from those of the ocean surface. The desert plume mixes over the ocean with marine aerosol particles characterized by very low absorption, which reflects in higher single scattering albedo results. Nevertheless, the values corresponding to the Banizoumbou AERONET site are still within the GOME derived error bars.

The spectral single scattering albedo values derived from GOME spectra for the case of the Asian dust over the Yellow Sea (Figure 6.10b) are in good agreement with the ground-based measurements taken at Anmyon-Do island, as well. There is a slight overestimation of GOME results in the blue spectral region and an underestimation in the red, but both results are very close and within the GOME derived error bars. As for the results from the literature desert model (Shettle 1984; no climatological model from Dubovik et al. (2002) was available for the area), they do not represent at all the measurements in this case, presenting much higher single scattering albedo values, representative of a much less absorbing aerosol type. In fact, the derived and measured single scattering albedo values in the Korean area are extremely low and found to be

smaller than those observed in source regions (0.9 at  $0.5\mu\text{m}$  according to Kim et al. (2004)). This may be an indication that industrial or urban aerosols (containing sulfates and nitrates) transported from China may affect the Asian dust aerosols found in Korean and Japanese areas, altering its properties through the mixing processes (Nakajima et al. 2003; Kim et al. 2004).

In the dust transport case over the Arabian Sea, illustrated in Figure 6.10c), the GOME derived spectral single scattering albedo values are in-between measurements taken at Bahrain and Kaashidhoo AERONET sites. Bahrain registers the lowest single scattering albedo values in this case, differing from the GOME results of 0.01 in the blue and of 0.02 to 0.03 in the red. Numbers referring to Kaashidhoo are higher, hinting to a less absorbing aerosol type, with differences from the GOME results between 0.04 (blue) and 0.02 to 0.01 (red). A possible explanation of this difference is that the Kaashidhoo site, situated on the extreme southwest part of the area (see Figure 5.16), was less affected by the dust plume than the other site and the single scattering albedo values characterize in reality a mixture of dust and marine particles. Once again the literature climatological model representative of desert dust over Bahrain (Dubovik et al. 2002) induces higher single scattering albedo values (less absorbing aerosol), with differences from the GOME derived values around 0.08.

A comparison between the single scattering albedo for the dust aerosol in the three cases indicates that the Asian desert dust originating from the Gobi desert and neighbouring regions is the most absorbing of all, presenting single scattering albedo values lower than 0.8 in the investigated spectral region (Figure 6.10b). The Middle East desert dust aerosol (Figure 6.10c), although less absorbing than the Asian, absorbs more than that originated from the Sahara desert (Figure 6.10a), which is found to be the less absorbing of the three types studied. Nevertheless, a similar spectral behaviour of the single scattering albedo was found for the three desert dust types, with an increase of the values from the blue to the red. The comparisons with the literature desert aerosol models represented in Figure 6.10 reveals the improvement brought to the aerosol characterization by the present methodology.

The results for the biomass burning episode over the southern Atlantic Ocean are reported in Figure 6.10d). Note that the aerosol properties from the Swakopmund AERONET site do not correspond to the period of study (6 – 13 September 2000) but to a

few days later (15 – 24 September 2000) due to problems with data availability: the comparison was therefore done assuming the smoke plume maintained its characteristics during the second period, which is not necessarily true. GOME derived values are in good agreement with AERONET measurements in Ascension Island, differing by 0.005 in the blue and by 0.017 to 0.01 in the red. Yet, AERONET results for Zambezi and Swakopmund are a little lower, with greater differences for the lower wavelengths (always less than 0.03). Again, these sites are located inland and closer to the fires (see Figure 5.17), especially Swakopmund. Moreover, the two ground and satellite datasets are close in time but not coincident. The biomass burning case displays an optimal agreement with the AERONET values reported for the African Savannah (Dubovik et al. 2002), with differences lower than 0.004, except at 0.86 $\mu$ m where a difference of 0.02 is observed. Note that this difference is lower than the accuracy limit of AERONET retrievals and of GOME derived standard deviations and therefore these results are considered quite good.

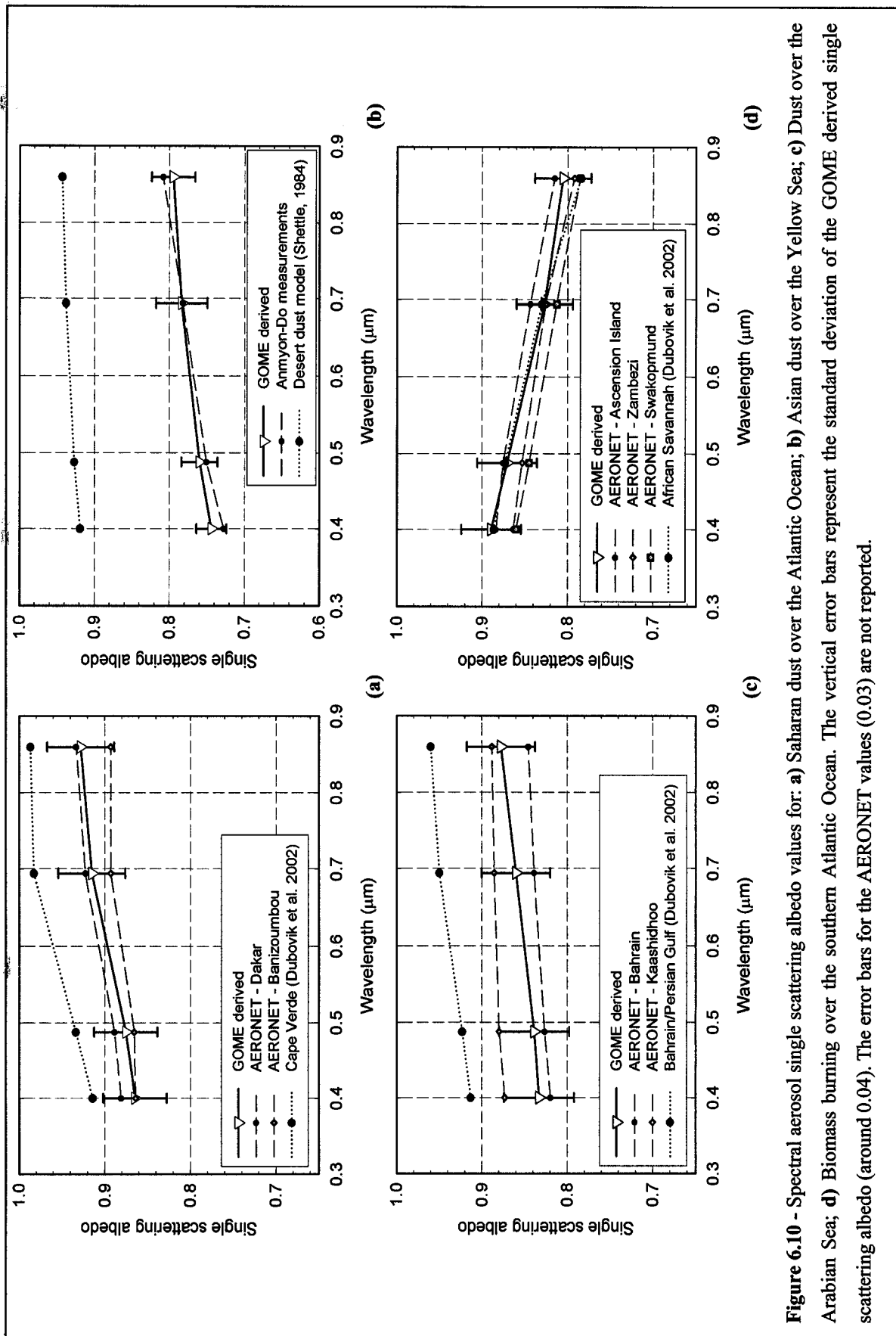


**Figure 6.10** - Spectral aerosol single scattering albedo values for: **a)** Saharan dust over the Atlantic Ocean; **b)** Asian dust over the Yellow Sea; **c)** Dust over the Arabian Sea; **d)** Biomass burning over the southern Atlantic Ocean. The vertical error bars represent the standard deviation of the GOME derived single scattering albedo (around 0.04). The error bars for the AERONET values (0.03) are not reported.

### 6.2.2.2 Phase function

Figure 6.11 shows the GOME derived phase function ( $P_{\lambda}(\Theta)$ ) at the wavelength of  $0.4 \mu\text{m}$  for three of the case studies, which are directly compared with AERONET measurements: Saharan dust over the Atlantic Ocean (Figure 6.11a)), dust over the Arabian Sea (Figure 6.11c)) and biomass burning over the southern Atlantic Ocean (Figure 6.11d)). The phase function corresponding to the Asian dust over the Yellow Sea is represented for two close wavelengths. The GOME derived phase function refers to the  $0.515 \mu\text{m}$  wavelength since the corresponding campaign measurements are available at the wavelength of  $0.5 \mu\text{m}$  (Figure 6.11d)). The values from literature models (Dubovik et al. 2002a; Shettle 1984) are once more represented in the graphs as well, for comparison purposes.

GOME based retrievals are generally in better agreement with AERONET values than the corresponding literature model. Figure 6.11a) corresponding to the Saharan dust transport shows that the phase function obtained from GOME is lower than AERONET values for scattering angles between  $80^{\circ}$  and  $150^{\circ}$ , and the same tendency is found for the Cabo Verde literature model. As for the Asian dust, the comparison between results and ground-based measurements stated by Figure 6.11b) reveals a fine agreement, except for the small differences found for scattering angles greater than  $160^{\circ}$ . The desert dust literature model tends in general to overestimate the values with respect to the measurements also in this case. In the Arabian dust case the underestimation of the GOME derived phase function, as well as of the Bahrain literature phase function values, is still appreciable although less marked. This could be connected with artifacts arising from considering in both aerosol models (this one and Dubovik's) spherical aerosol shapes for desert dust particles. As pointed out by Dubovik et al. (2002), the non-spherical shape for desert dust particles is responsible for deviations of the phase function at scattering angles  $\geq 90^{\circ}$ . On the contrary, the biomass burning case shows a good agreement between GOME derived values and AERONET aerosol phase function retrievals for the Zambezi and Swakopmund sites, where the spherical aerosol shape is suitable. The African Savannah literature model is also in good agreement, especially for scattering angles  $< 150^{\circ}$ .

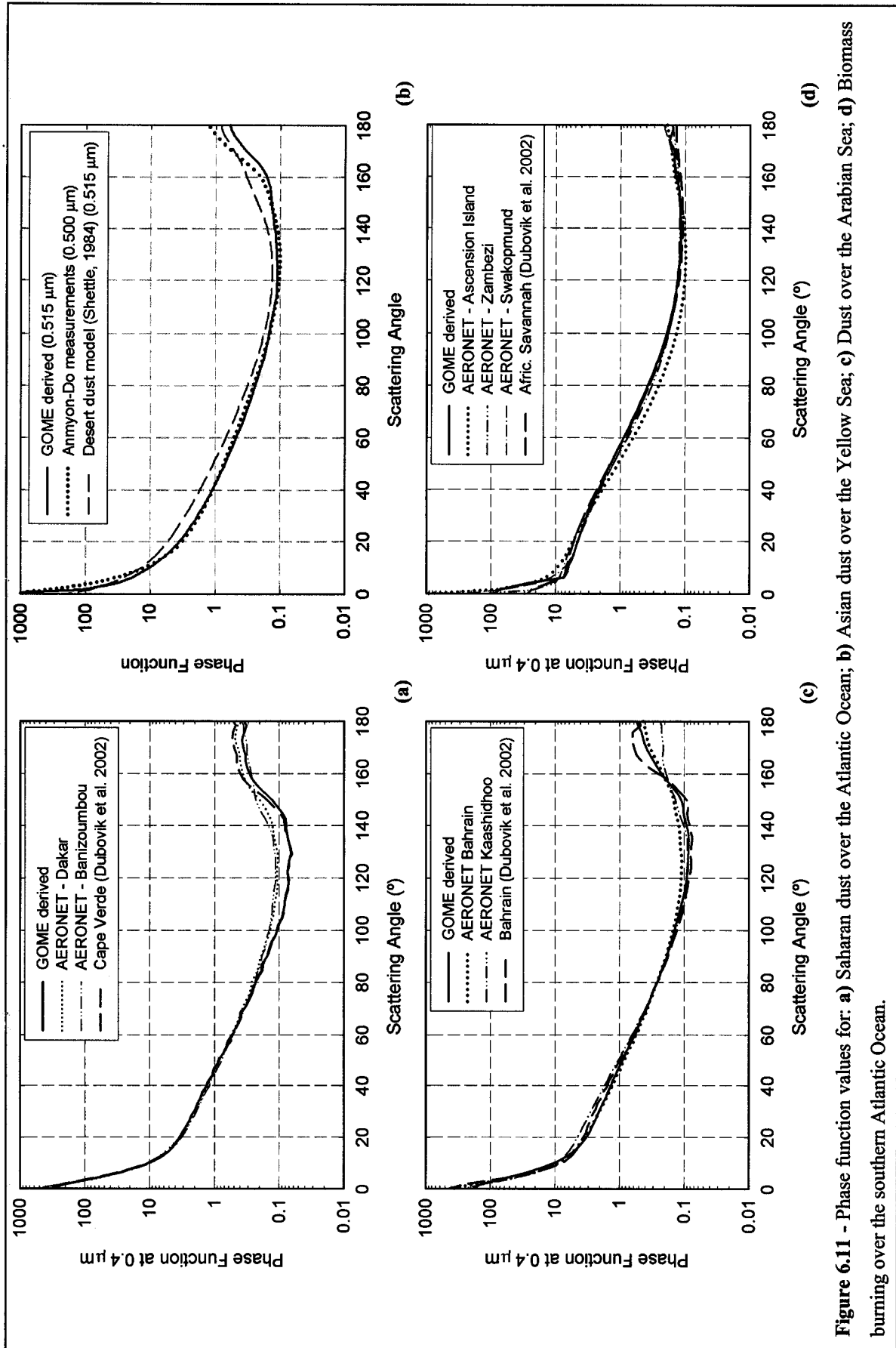


**Figure 6.11** - Phase function values for: **a)** Saharan dust over the Atlantic Ocean; **b)** Asian dust over the Yellow Sea; **c)** Dust over the Arabian Sea; **d)** Biomass burning over the southern Atlantic Ocean.



### 6.2.2.3 Ångström exponent

The Ångström exponent ( $\alpha$ ) defined by the Ångström power law in equation 2.43 and related to particle size (see Section 2.3) is also considered in the comparisons. The graphs in Figure 6.12 represent the Ångström exponent values derived from GOME measurements (Section 5.2.2) as well as those obtained from the AOT ground-based measurements (Section 5.2.5.2). The values obtained from the satellite-based algorithm (GOME measurements) are constant, since they are function of the derived aerosol model, which does not fluctuate as a function of time and remains unchanged for the case under study.

The Ångström exponent values in the first case (Figure 6.12a) – Saharan dust event) are generally very low throughout the month of June 1997, especially in the first half, which is typical of dust aerosol particles presenting a dominant larger, unlike biomass burning aerosols where the Ångström exponent values are larger. The GOME derived value was 0.04 for the Saharan desert dust situation, which is generally in good agreement with results from Cabo Verde, Dakar and Banizoumbou. The results obtained from ground measurements for the Asian dust event (Figure 6.12b)) show negative values for the first part of the day, then a slight increase to positive values and after 0630 UTC the Ångström exponent values increase again. The analysis of the aerosol optical thickness hourly variation (see Section 6.2.3.2, Figure 6.18) indicates that after 0230 UTC the dust plume starts moving south from Anmyon-Do Island, therefore the higher Ångström exponent values later in the day are probably not characterizing dust, but other types of aerosol. Nevertheless the agreement with the GOME derived value (0.08) is quite good. Also for the Arabian dust, although values are slightly higher (0.20), the accordance with AERONET values taken at Bahrain and Kaashidoo sites is quite acceptable (Figure 6.12c)). In the biomass burning case (Figure 6.12d)) the Ångström exponent values show a substantial increase in comparisons with the previous three cases, as it would be expected for aerosol of such origin characterized by much smaller particle sizes than dust aerosol. Also in this case the GOME derived value of 1.55 matches the increase of AERONET results, standing in-between results of Ascension Island (situated in the Atlantic Ocean - Figure 5.14) and Zambezi and Etosha\_Pan sites, both located inland and closer to the fires as already mentioned.

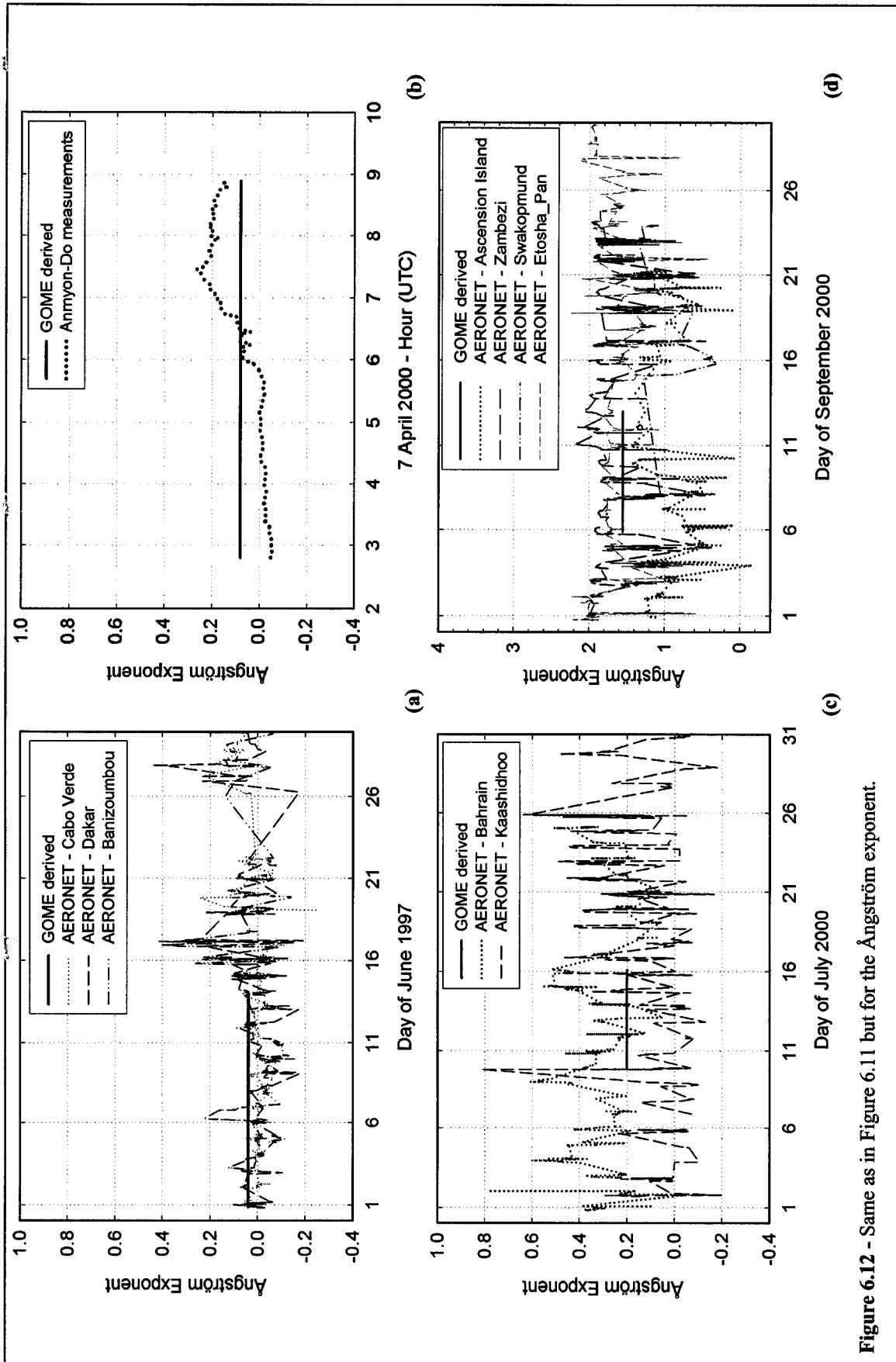


Figure 6.12 - Same as in Figure 6.11 but for the Ångström exponent.

## **Chapter 6**

# **Results and discussion**

### **6.1 Introduction**

This chapter presents the results of the application of the new methodologies developed to characterize the aerosol and cloud properties presented in Chapter 5. The chapter is divided into two major sections, the first one on the aerosol studies and the second one dealing with the cloud methodology outcomes. The comparisons carried out between the results obtained from the present methods and independent measurements / retrievals, which lead to the validation of the methodologies developed, are also presented in this chapter.

### **6.2 Aerosols**

The methodologies developed for the aerosol characterization and direct radiative forcing assessment, as well as the case studies and the independent measurements and/or results from other state-of-the-art algorithms used for the comparisons were all presented before in Section 5.2. In this section the results are presented and, in addition, an initial sub-section (6.2.1) presents the results of the sensitivity analysis performed to understand the effects of the atmospheric vertical profile, surface type and aerosol model assumptions on the spectral reflectance, aerosol optical thickness and top of the atmosphere (TOA) short wave (SW) net flux. The second sub-section regards the aerosol optical properties retrieved from GOME spectral measurements, the third one the aerosol optical thickness retrieved from GEO satellite measurements and the fourth one is dedicated to the presentation of the direct SW aerosol radiative forcing estimates.

### 6.2.1 Sensitivity analysis

The physical assumptions made in the radiative transfer calculations with respect to the vertical atmospheric profiles, surface and aerosol description, were tested through a sensitivity analysis (Costa et al. 2000a). For this purpose and in order to identify the main uncertainty affecting the radiative quantities entering the present method, the spectral reflectance, the AOT derived from GEO radiances (see computation procedure in Section 5.2.3 and the TOA DSWARF (see computation procedure in Section 5.2.4) are analysed for a set of possible geometric conditions. The results of these analyses are presented in terms of the differences resulting from adopting different literature aerosol models (indicated in Table 6.1), two different surface optical characterization (Lambertian vs Bidirectional Reflectance Distribution Function, BRDF), and two different vertical profiles of water vapour and ozone (tropical vs midlatitude winter). In addition, the efficiency of the algorithm in deriving the fine mode modal radius, the fine mode percentage particle density, the imaginary part of the refractive index in two spectral regions (0.35 – 0.50  $\mu\text{m}$  and 0.70 – 0.86  $\mu\text{m}$ ), and the AOT (at GOME spatial scale) is tested using synthetic GOME measurements, obtained from calculation with the 6S code.

The location of the aerosol layer in the atmosphere, although not entering the present methodology, is also an important factor affecting the radiative quantities for wavelengths below 0.4  $\mu\text{m}$  (spectral reflectance at 0.361  $\mu\text{m}$ ) especially for absorbing aerosols such as desert dust or biomass burning types. Torres et al. (1998) investigated the radiance change relative to the Rayleigh scattering limit at the wavelength of 0.380  $\mu\text{m}$  due to the aerosol layer height for several aerosol models. Their values relative to the aerosol model that presents the strongest altitude dependence range from about -15% (at 1.4 km height) to -30% (at 5.8 km) for a surface reflectance of 0.05. However, in order to include the aerosol vertical distribution among the variable parameters, LIDAR data (backscattering coefficient) and/or measurements from intensive airborne campaigns would be needed, which are not always available.

Throughout the present work the aerosol particles are assumed spherical. However, the aerosol particle shape may be an issue, especially for desert dust (Dubovik et al. 2002a) and also for marine aerosol in low humidity atmospheric conditions (Silva et al., 2002). The application of non-spherical theories to satellite based retrieval algorithms is a difficult

## 6.2.3 Aerosol optical thickness derived from GEO satellite measurements

### 6.2.3.1 Saharan dust over the Atlantic Ocean

The AOT was retrieved from Meteosat broadband VIS (0.3 – 1.05  $\mu\text{m}$ ) measurements using the GOME derived aerosol properties presented in the previous section. The desert dust model by Dubovik et al. (2002a) from AERONET measurements

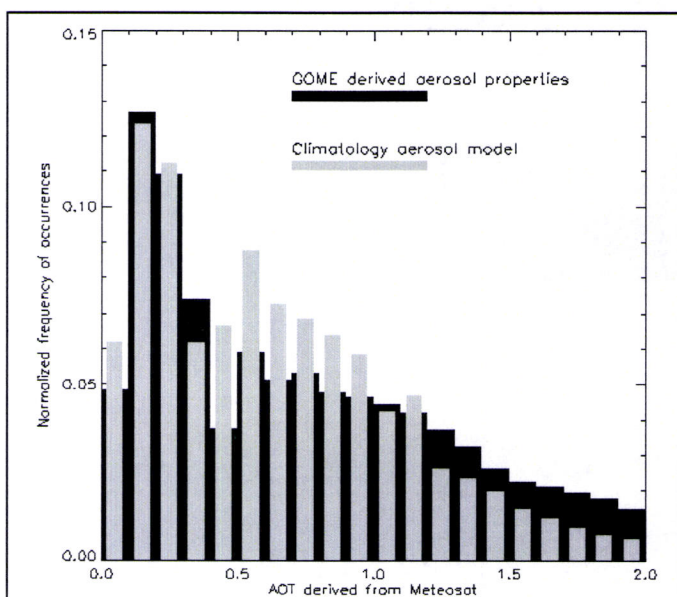


**Figure 6.13** - Frequency histogram of the AOT derived from METEOSAT imagery (period: 1 to 14 June 1997; frequency: hourly from 0800 to 1400 UTC), using the GOME derived aerosol properties and the aerosol model derived from AERONET data for Cabo Verde (Dubovik et al. 2002). (Taken from Costa et.al. 2004b).

in Cabo Verde provides the “climatological” AOT values, which are compared with the AOT derived from Meteosat measurements to verify the impact of the aerosol model on the AOT retrievals. Figure 6.13 shows the frequency histogram of the AOT values and encompasses about 5 million Meteosat pixels processed during the event in the first part of June 1997 (hourly frequency from 0800 to 1400 UTC) over the area shown in Figure 5.14. For both aerosol models a bimodal distribution of the AOT can be distinguished, which corresponds to

a background marine situation and to the Saharan dust transport event. While the modalities correspondent to the background marine particles (low AOT values) are very similar, substantial differences can be noted for optical thickness values of the dust event (larger AOT values). This shows how significant is the impact that the choice of the adequate aerosol properties (aerosol model) can have on the AOT in the presence of high aerosol loads in the atmosphere. The sensitivity studies shown in Section 6.2.1 revealed the same trend.

Figure 6.14 shows the AOT maps derived from Meteosat-6 slot 25 (acquisition time between 1200 and 1230 UTC), from 5 to 10 June 1997 over the Atlantic Ocean.

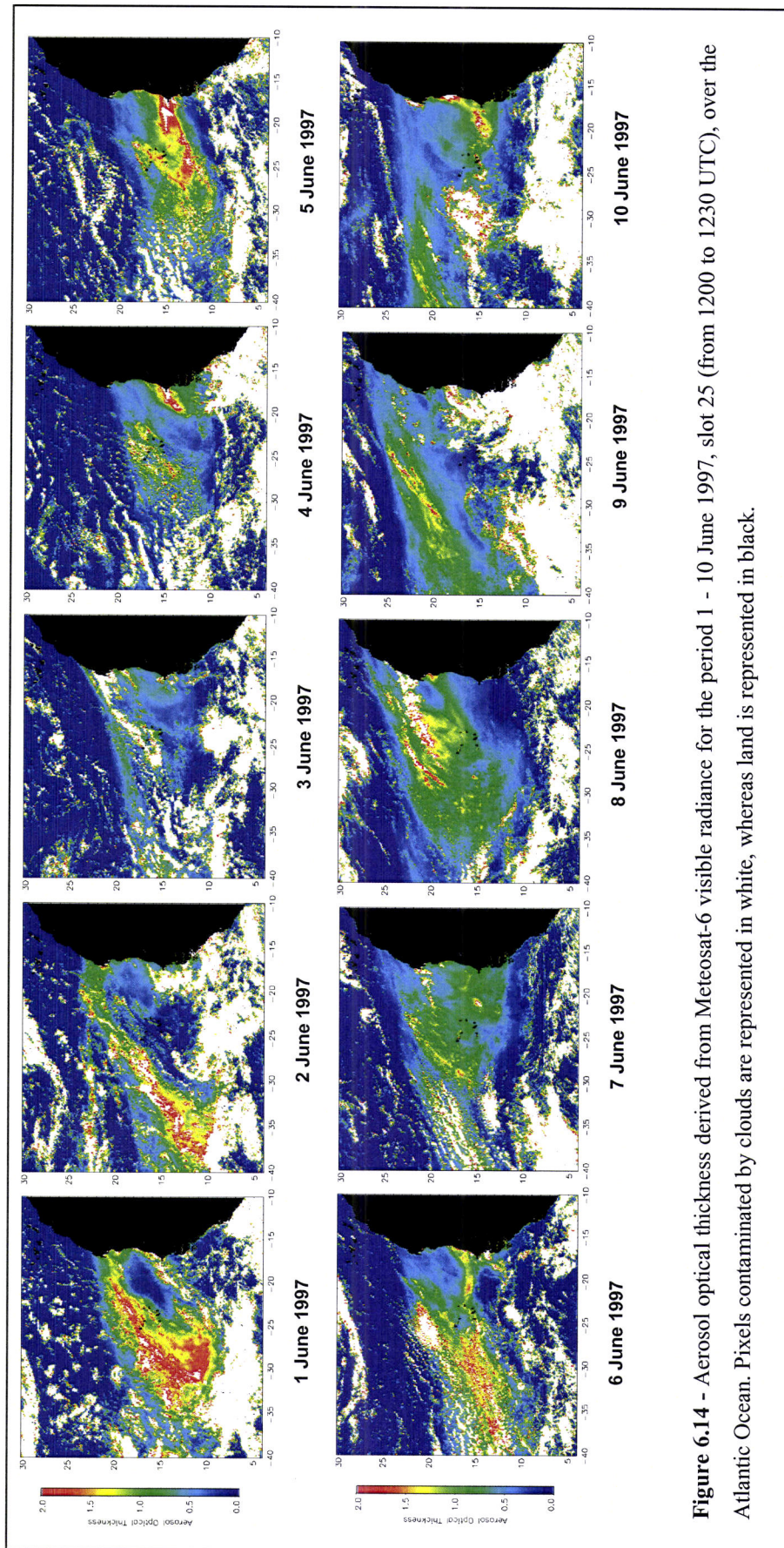
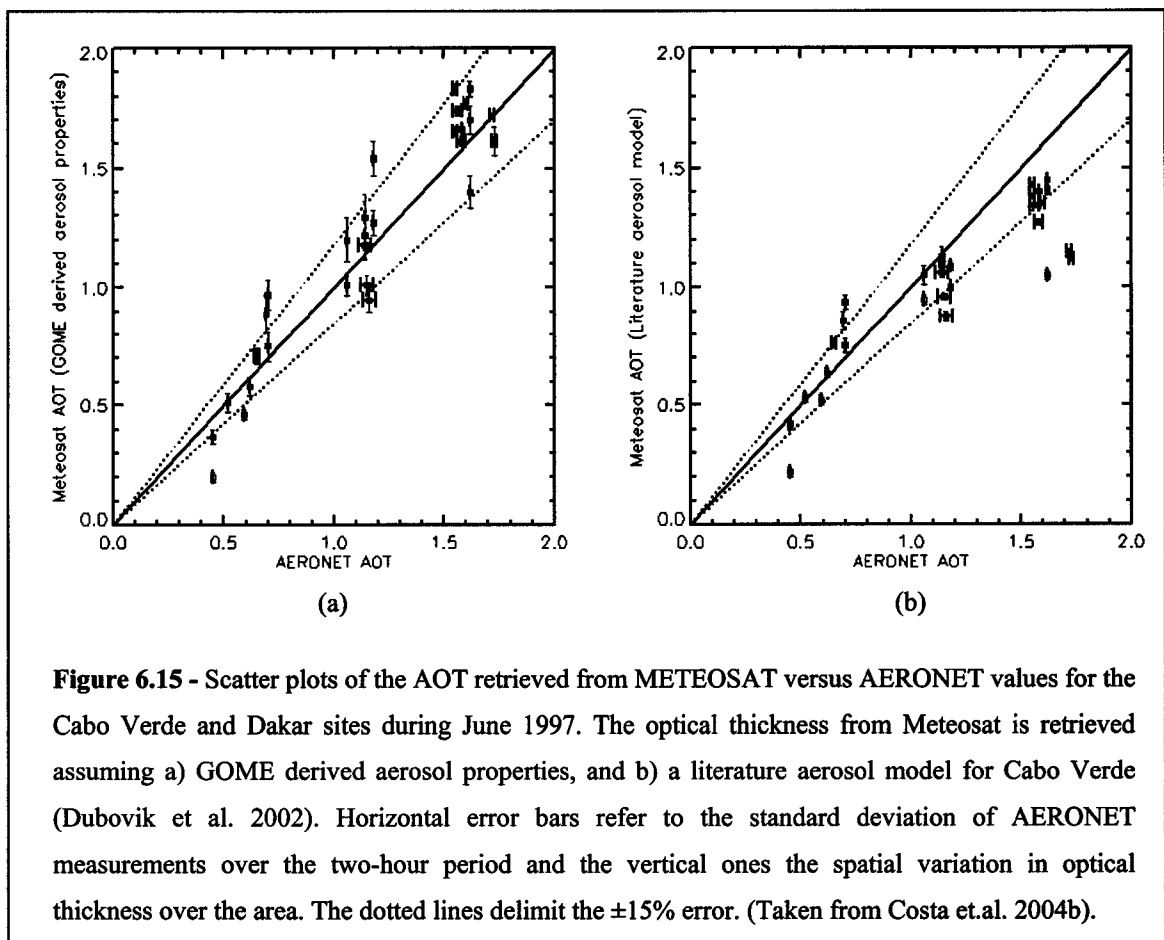


**Figure 6.14** - Aerosol optical thickness derived from Meteosat-6 visible radiance for the period 1 - 10 June 1997, slot 25 (from 1200 to 1230 UTC), over the Atlantic Ocean. Pixels contaminated by clouds are represented in white, whereas land is represented in black.

The dust aerosol transport is clearly evidenced in the areas of higher AOT values. Figure 6.14 illustrates the daily monitoring of the AOT from GEO data; whereas the AOT hourly monitoring is shown in Figure 6.19.

The AOT derived from the Meteosat data was compared with measurements from the selected AERONET sites as described before in Section 5.2.5.2. Figure 6.15 shows the scatter plots of the optical thickness derived from Meteosat using GOME derived aerosol properties (a) and the Cabo Verde dust literature aerosol model (b), versus the AERONET measurements taken in Cabo Verde and Dakar, for the first half of June 1997, after the data screening. The horizontal error bars represent the standard deviation of AERONET measurements over the two-hour period, whereas the vertical ones document the spatial variation in optical thickness over the chosen area. The dotted lines delimit the  $\pm 15\%$  error, representative of the Meteosat instrumental error (see Section 6.2.1).



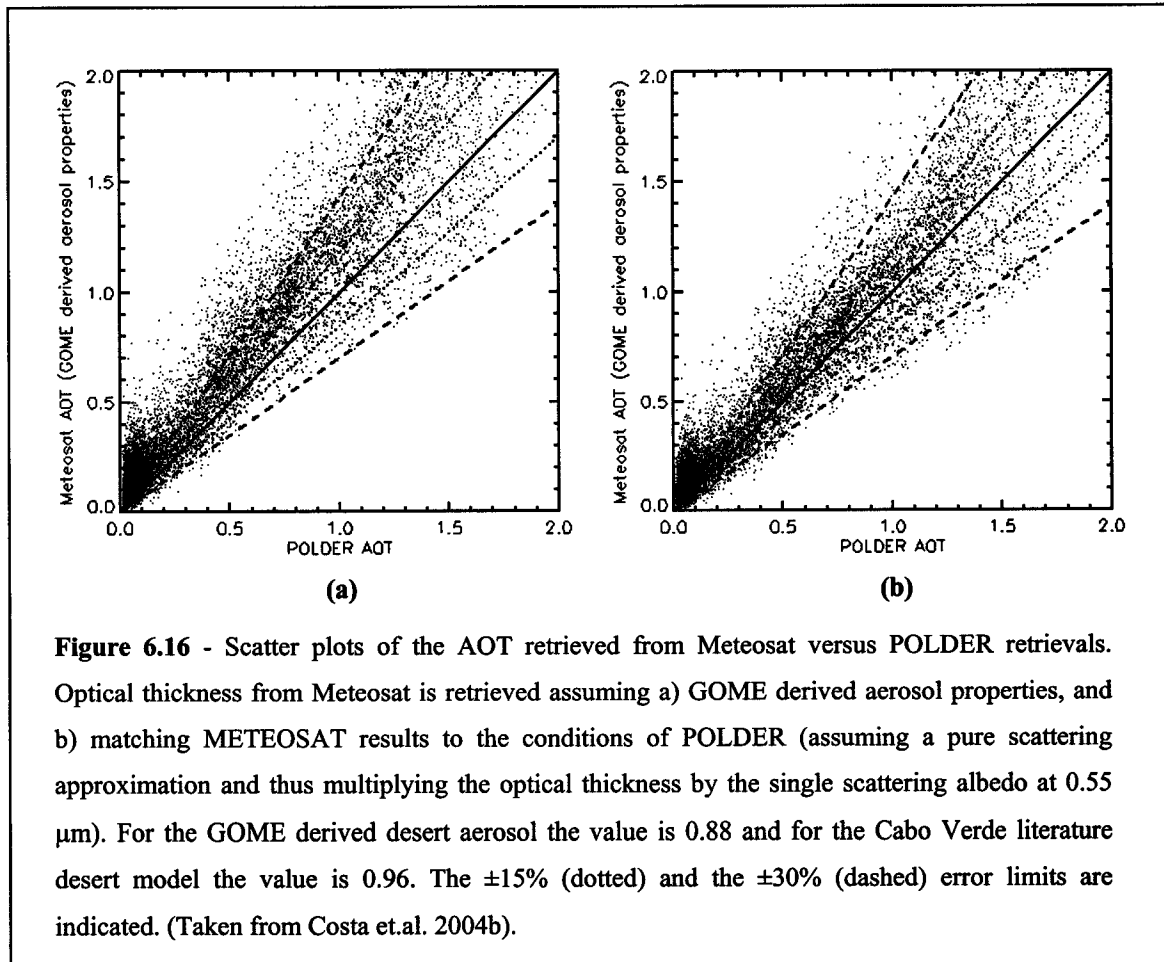
In general, there is quite a good agreement between the AOT values retrieved from Meteosat using GOME derived aerosol properties and the ones measured by the

AERONET sites (Figure 6.15a). Differences can be attributed to the scatter of Meteosat retrieved values within the averaged area. Nevertheless, the accordance is better than in the case of the literature aerosol models (Figure 6.15b), which seem to show a tendency to underestimate the AOT values. In fact, 74% of the AOT values retrieved from Meteosat using GOME derived aerosol properties have an agreement better than 15% with AERONET AOT measurements, whereas for the AOT derived using the Cabo Verde desert dust model (Dubovik et al. 2002a) only 62% of the values fall within this error limit. This fact proves that, although Meteosat has only a broadband channel in the VIS spectral region, its data can be used for aerosol studies when associated with the GOME derived aerosol properties. The retrieval accuracy improves significantly over the one that can be achieved by using literature aerosol models, as stated by the comparisons with AERONET measurements.

The AOT retrieved from Meteosat-6 is also compared to the corresponding POLDER product (Goloub et al. 1999). The scatter plots of Meteosat versus POLDER AOT for the aerosol characterization with the GOME derived aerosol properties are displayed in Figure 6.16a) for the whole June 1997. Error limits are  $\pm 15\%$  (dotted) and  $\pm 30\%$  (dashed). Data are somehow scattered and this may be due to differences in the algorithms. If all AOT values are compared, 23% of the values lay within the  $\pm 15\%$  limit and 44% within  $\pm 30\%$ . If only values of  $AOT > 0.4$  are considered (aerosol event situation), percentages increase to 36% ( $\pm 15\%$  error limit) and 70% ( $\pm 30\%$  error). When the Cabo Verde literature dust model is considered, a higher number of cases stay within the same limits: 29% and 53% for the  $\pm 15\%$  and  $\pm 30\%$  error limits, respectively, when all values are considered; 45% and 80% for the  $\pm 15\%$  and  $\pm 30\%$  error limits, respectively, if only  $AOT > 0.4$  values are retained. Note that the Look-Up Tables (LUT) built for the retrieval of the optical thickness from POLDER have 0.6 as the largest AOT value (Goloub et al. 1999), whereas in the present method the range of AOT is between 0.0 and 2.0. This means that in POLDER algorithm higher AOT values come from a linear extrapolation, possibly leading to an under or overestimation. The highest value considered acceptable for the validation and shown in the figure is 2.0, since it may be considered representative of a typical desert aerosol dust load for these events (Tanré et al. 1997). On the other hand, aerosol absorption is taken into account in the present method, but not considered in the POLDER algorithm, and this may be the cause of the systematic differences observed in

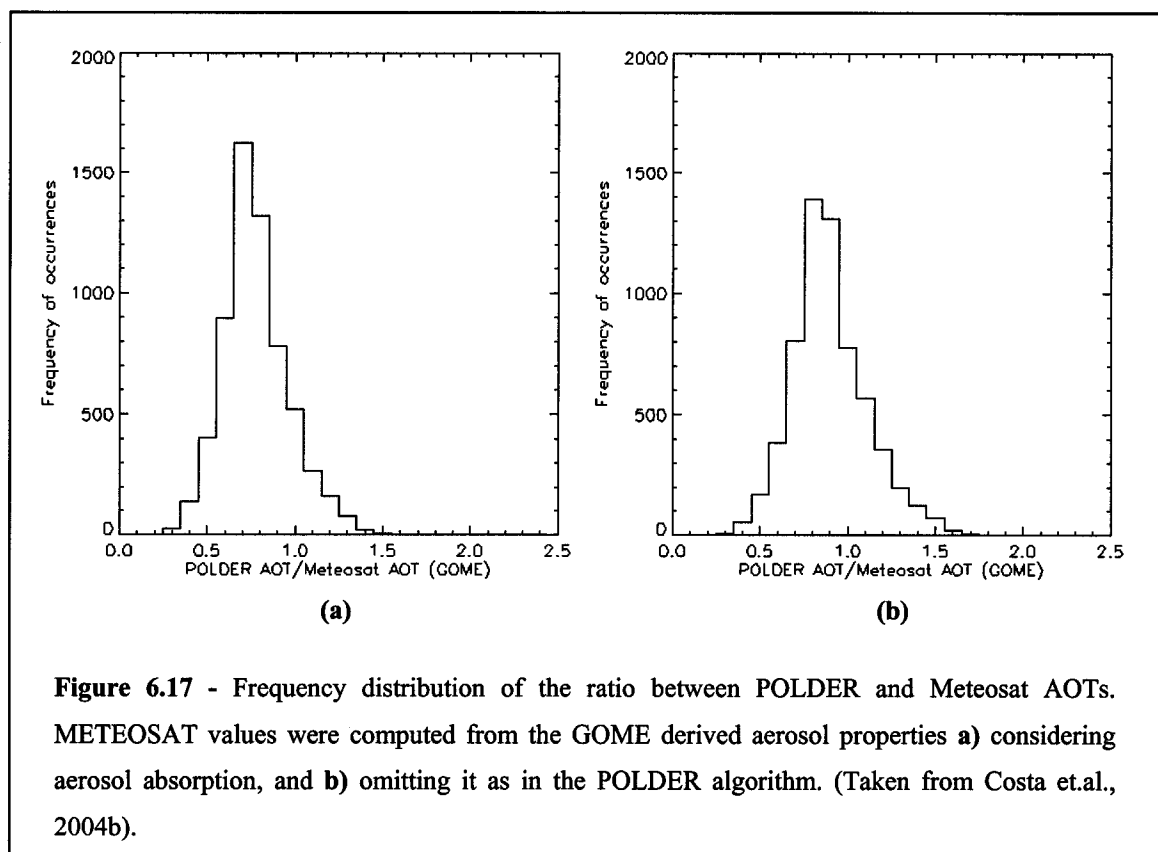


the plots. In order to compare results on the same ground, i.e. the POLDER situation, the values of the present method were re-processed assuming a pure scattering approximation. In this case, the optical thickness was multiplied by the single scattering albedo at  $0.55 \mu\text{m}$ . The value obtained from Mie calculations of the single scattering albedo from the GOME retrieval is 0.88 while that from the literature desert class is 0.96. The new results are now illustrated in the scatter plot of Figure 6.16b).



After matching the retrieval conditions of the GEO retrieved AOT values to those of POLDER, the two sets of AOT values come closer to each other when using the GOME derived aerosol properties (see Figure 6.16b). 34% of the values in the scatter plot agree within  $\pm 15\%$  and when only AOT > 0.4 values are taken, the percentage increases up to 55%. As for the  $\pm 30\%$  limit (dashed lines in the graphs of Figure 6.16), 55% and 86% are obtained, respectively, when all the AOT values are considered and only AOT > 0.4 are taken. When using the desert dust literature model the agreement between Meteosat and

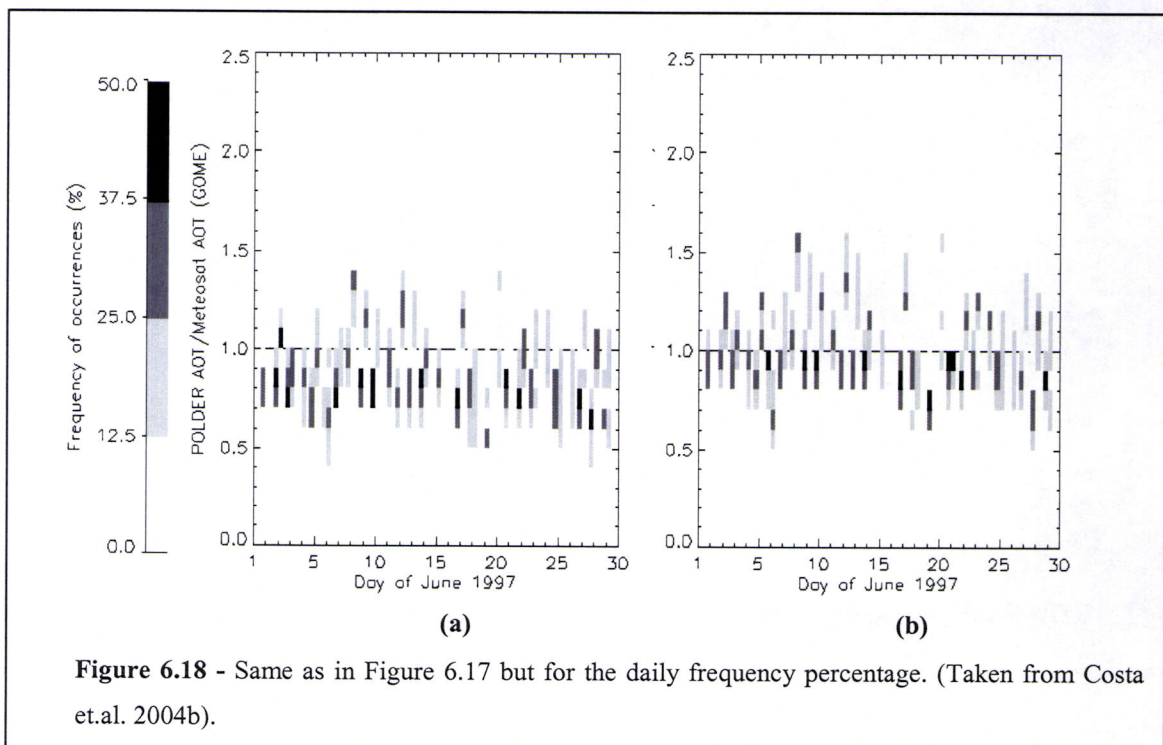
POLDER AOT is now worse with an underestimation trend of the optical thickness: 26% and 52% for the  $\pm 15\%$  and  $\pm 30\%$  error limits, respectively, when all values are considered; 38% and 77% for the  $\pm 15\%$  and  $\pm 30\%$  error limits, respectively, if only AOT > 0.4 values are considered. This exercise of removing the absorption in order to be in the same conditions as the POLDER algorithm has proved that the present method improved the AOT retrievals.



The frequency distributions of the ratio between the AOT obtained from POLDER and that from Meteosat displayed in Figure 6.17 summarize the results for June 1997. The left column refers to the optical thickness derived from Meteosat using the GOME aerosol properties plotted **(a)** considering aerosol absorption and **(b)** matching its values to the conditions of POLDER that is multiplying them by the single scattering albedo. In case **(a)** it seems that there is a systematic overestimation tendency of Meteosat. This difference is minimized in case **(b)** when the results are matched to POLDER conditions, which means considering non-absorbing aerosols and using GOME derived properties as illustrated in Figure 6.17b).

The graphs in Figure 6.18 show the frequency percentage of the ratio between POLDER and Meteosat AOT during June 1997. Even though the desert dust properties are

derived from GOME data gathered in the first half of June, the results refer to the whole month. The aim is to detect significant differences and set a temporal limit to the validity of the aerosol optical properties retrieved from GOME spectral reflectance fitting. The inspection of the graphs, which show once more Meteosat results with and without aerosol absorption (Figures 6.18a and b, respectively), suggests that the agreement between Meteosat and POLDER retrievals is slightly worse for the last week of June than for the rest of the month. This may be an indication that retrieved aerosol classes at that time were not anymore representative of the aerosol atmospheric situation and should have been updated.



### 6.2.3.2 Asian dust over the Yellow Sea

The maps in Figure 6.19 show the evolution of the aerosol optical thickness values over the area shown in Figure 5.15. These values are derived from GMS-5 visible reflectance measurements (see Section 3.3.1.2) using the aerosol properties obtained from GOME spectral inversions. The region considered for the comparisons of the AOT with the ground-based measurements is delimited on the maps by the square. It corresponds to an area of  $0.25^\circ \times 0.25^\circ$  in latitude and longitude, centred on the geographical coordinates of Anmyon-Do, the site where measurements were taken.

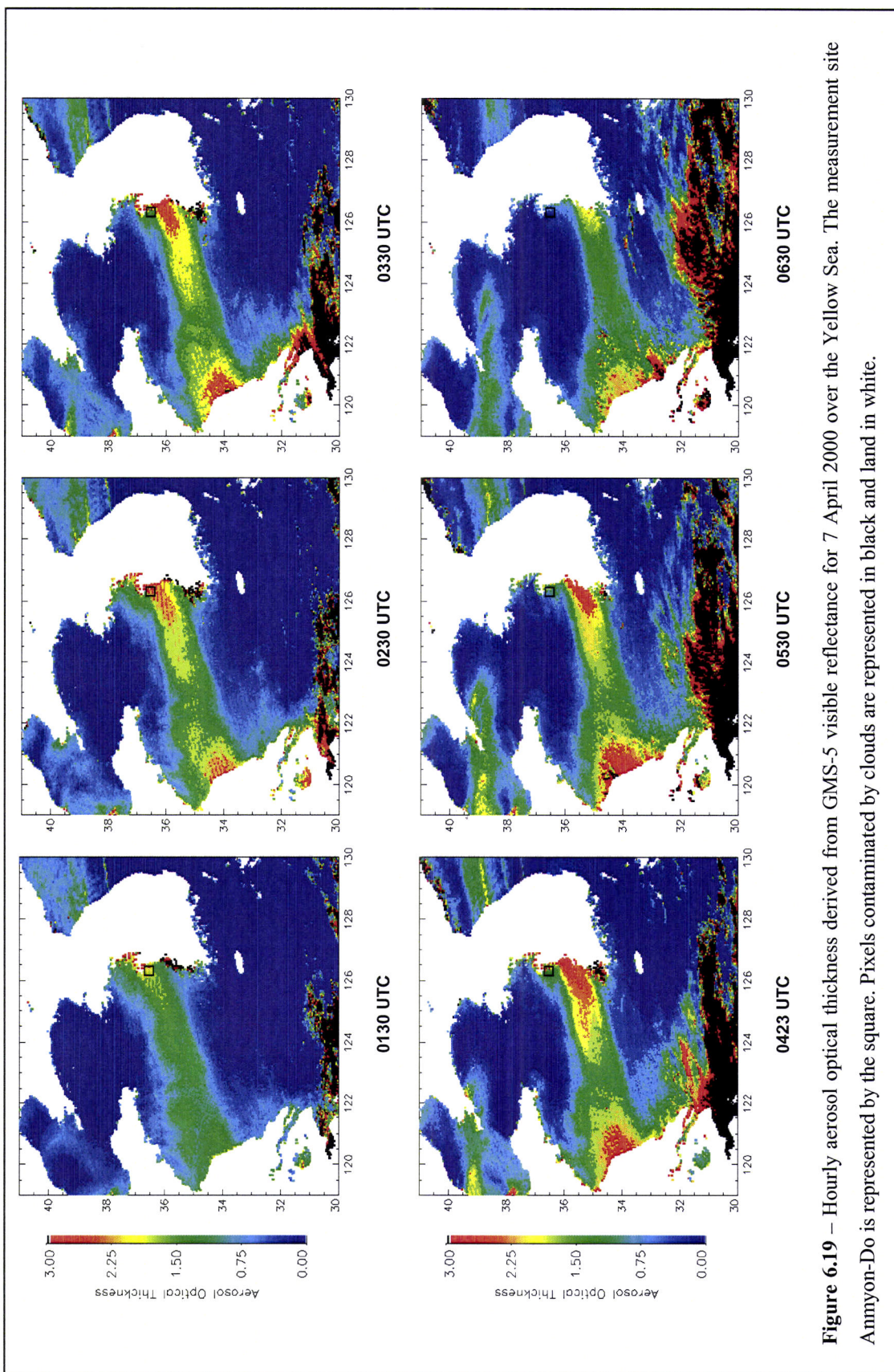
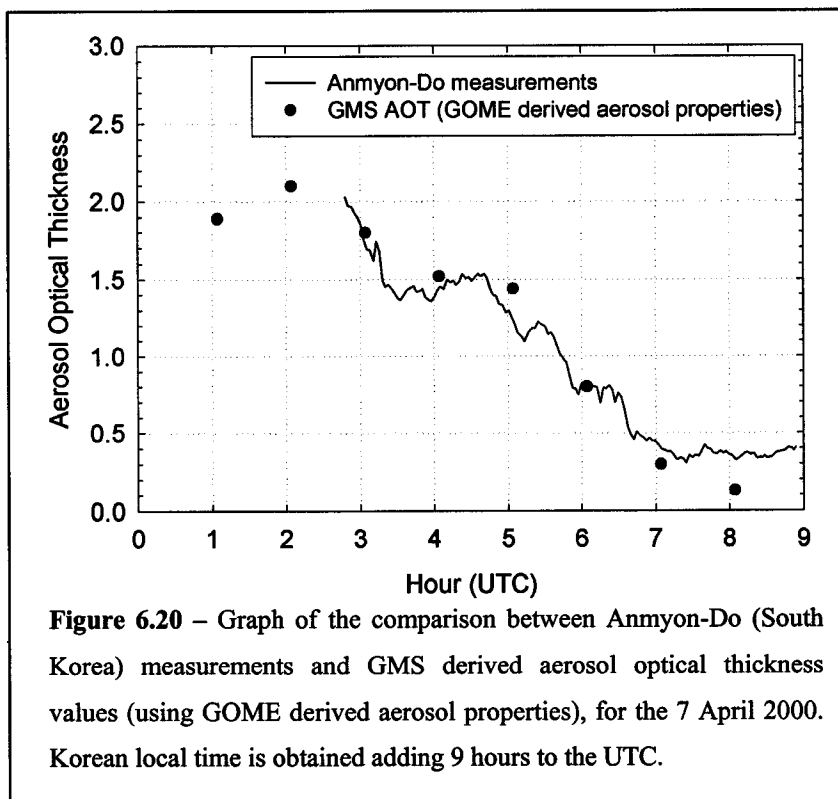


**Figure 6.19** – Hourly aerosol optical thickness derived from GMS-5 visible reflectance for 7 April 2000 over the Yellow Sea. The measurement site Amnyon-Do is represented by the square. Pixels contaminated by clouds are represented in black and land in white.

The maps in Figure 6.19 illustrate the hourly monitoring of the AOT using the present methodology. The variation of the AOT values, as well as of the geographical position of the aerosol plume itself along the day, demonstrate the importance of developing monitoring capabilities from available satellite sensors. Such information would be completely lost by methods based exclusively on LEO sensors, which would be scanning the area only once in this period, depending on the time of the satellite overpass.

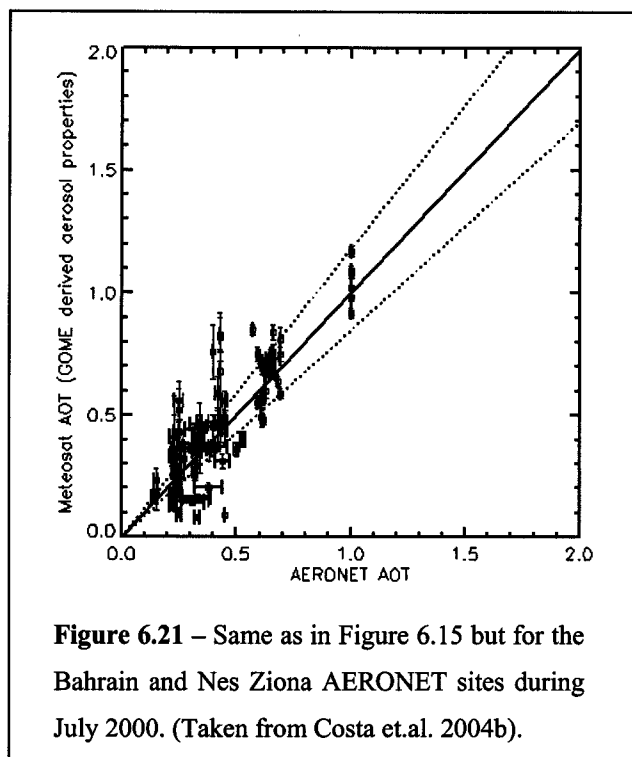
The AOT inside the area defined by the square are arithmetically averaged



(excluding cloud and land contaminated pixels) and compared to ground measurements of the aerosol optical thickness taken at Anmyon-Do. The comparison is not presented in the same way as for the previous case study (see Figure 6.15), since only a few measurements are available during the

day of the study. The graph in Figure 6.20 shows the AOT comparison for the 7 April 2000, as a function of UTC time. Korean local time is 9 hours ahead of UTC. Measurements and results show a very good agreement, with absolute differences always lower than 0.2. Moreover, the satellite retrieval closely reproduces the trend of ground-based measurements during the day.

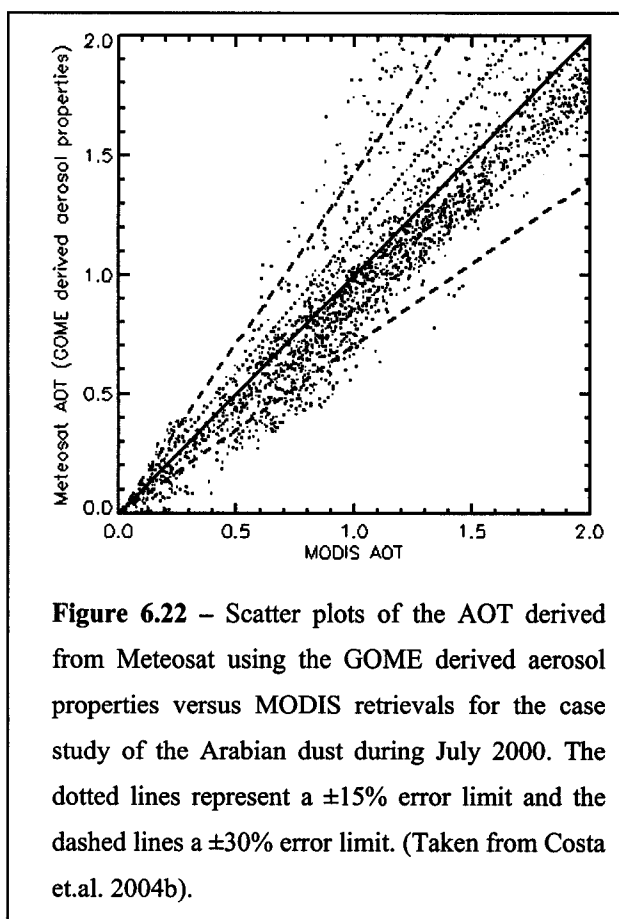
### 6.2.3.3 Dust over the Arabian Sea



The AOT derived from Meteosat-5 pixel radiances in July 2000 over the area in Figure 5.16 over the Arabian Sea are compared with AERONET measurements taken at Bahrain and Nes\_Ziona. Results are reported in the scatter plot of Figure 6.21. The conditions imposed for the comparisons are those applied to the Sahara dust event (Section 6.2.3.1). In general, the agreement between ground-based measurements and satellite retrievals using the aerosol properties derived from GOME spectral

measurements is good, with 40% of the values within the  $\pm 15\%$  (dotted lines in Figure 6.21) and 54% of the cases within the same limit if only AOT > 0.4 values are considered. Furthermore, the agreement is better than that resulting from the application of the literature aerosol model (not shown), which once again discloses a tendency to underestimate the AOT values. In fact only 32% of the AOT values derived using the literature aerosol model are within the agreement limit of  $\pm 15\%$ , and rise up to 45% if only AOT > 0.4 are considered.

The retrieved AOT values are also compared to the corresponding values out of the MODIS official aerosol product (version 004). Coincident areas



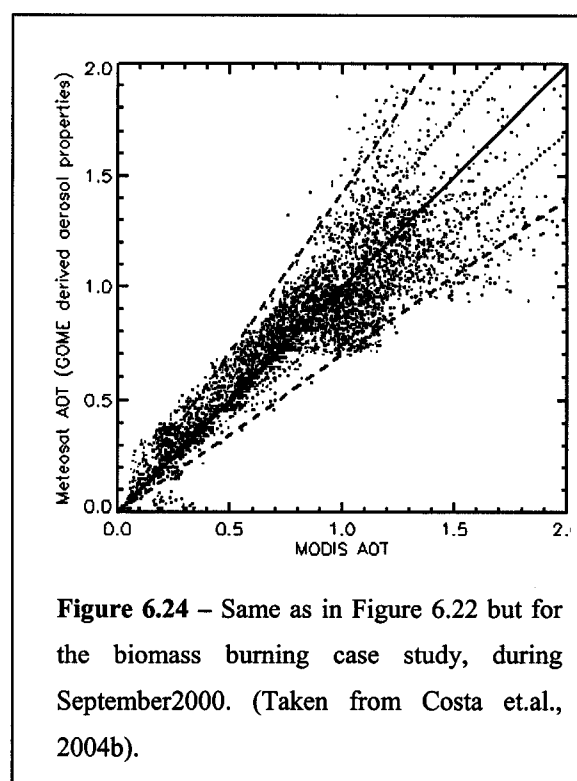
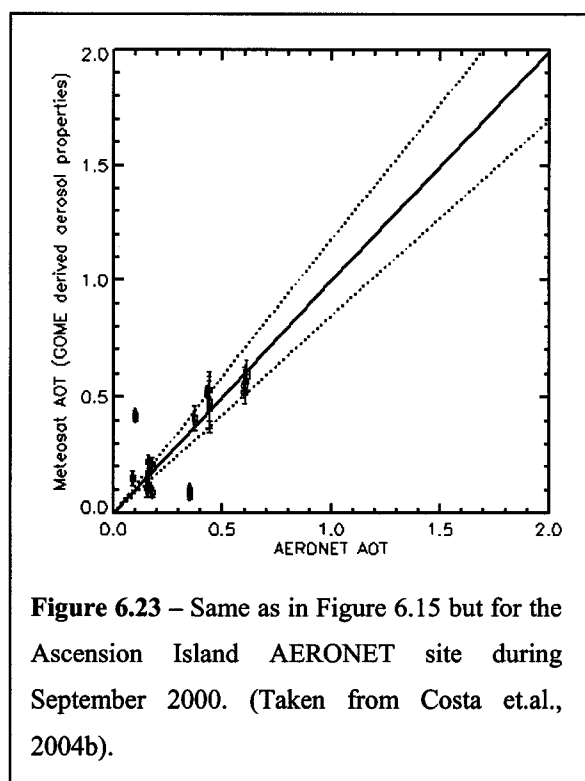
of  $0.5^\circ \times 0.5^\circ$  are averaged and compared keeping the best time coincidence (maximum 15 minute difference). Figure 6.22 shows the scatter plots of Meteosat versus MODIS AOT for the case of aerosol characterization with GOME derived aerosol properties. Results refer to the period from 10 to 16 July 2000. There is again a better agreement between the results from both algorithms when the aerosol properties obtained from GOME spectral measurements' inversion are used in the Meteosat retrievals: 55% of data agree within  $\pm 15\%$ , whereas the agreement drops down to only 45% when the Bahrain desert dust model is used. If the limit is relaxed to  $\pm 30\%$ , then the numbers are 75% and 70% for the GOME derived properties and the literature model, respectively. If only values with  $AOT > 0.4$  are considered, 70% and 90% of the cases are within  $\pm 15\%$  and  $\pm 30\%$ , respectively, when the GOME derived properties are considered. Under the same conditions the Bahrain desert models results in 62% of the cases within  $\pm 15\%$  and 90% of the cases within  $\pm 30\%$ . Note that the greatest differences stemming from the use of the different aerosol models (GOME derived and literature) are obtained for the lowest error limit ( $\pm 15\%$ ). This indicates that the use of the GOME derived aerosol properties improves the accuracy of the retrieved AOT values.

#### 6.2.3.4 Biomass burning over the southern Atlantic Ocean

AERONET measurements from Swakopmund were not available during the period of the event, and Etosha\_Pan and Zambezi are located inland. Therefore, there were no coincident Meteosat AOT results since presently the method is limited to retrievals only over the ocean. The only AERONET site used for AOT comparisons is Ascension Island (see Figure 5.17) and results are shown in Figure 6.23. Only a limited number of coincident data points are available for AERONET values  $< 0.7$ . If only  $AOT > 0.4$  values are considered, 78% of them is within  $\pm 15\%$ , against a 54% resulting from the use of the African Savannah literature model. If all values are retained, 34% are confined within the  $\pm 15\%$  limit for the GOME derived properties and 27% for the literature aerosol model.

AOT values computed from Meteosat VIS radiances are compared also with the official MODIS AOT product during the period of the event (6 – 13 September 2000). Once again, coincident areas of  $0.5^\circ \times 0.5^\circ$  are averaged and compared, thus ensuring the

best temporal match between MODIS and Meteosat image acquisitions. Figure 6.24 shows these comparisons for the case of aerosol characterization with GOME derived properties. When using the GOME derived properties, 48% and 60% of the cases are respectively within the  $\pm 15\%$  and  $\pm 30\%$  error limits, when all values are considered. If only values with  $AOT > 0.4$  are considered, 70% and 96% of the cases are within the  $\pm 15\%$  and  $\pm 30\%$  error limits, respectively. As for the African Savannah literature model, 32% (within  $\pm 15\%$ ) and 57% (within  $\pm 30\%$ ) are the figures when all the AOT values are considered, and 40% (within  $\pm 15\%$ ) and 87% (within  $\pm 30\%$ ), if only  $AOT > 0.4$  results are taken.



### 6.2.3.5 Discussion

A first estimate of the accuracy of the GOME / Meteosat derived AOT at  $0.55\mu\text{m}$  inferred from AERONET comparisons leads to  $\Delta\tau^a = \pm 0.02 \pm 0.22 \tau^a$  when all AOT values are examined. For aerosol event situations where  $\tau_{\lambda=0.55\mu\text{m}}^{aerosol} > 0.4$  the estimate of the AOT accuracy is  $\Delta\tau^a = \pm 0.02 \pm 0.16 \tau^a$ . The accuracy is not as good as the one published for MODIS AOT ( $\Delta\tau^a = \pm 0.03 \pm 0.05 \tau^a$ , dust excluded) by Tanré et al. (1997) and this is



probably due to inherent problems of the satellite data used (GOME pixel dimension, Meteosat calibration; see Section 6.2.1). Nevertheless, the proposed methodology is not merely suited for AOT monitoring (Figures 6.14 and 6.19), but also for deriving the TOA direct SW aerosol radiative forcing at the GEO temporal scale (see next section). Other methods based exclusively on LEO satellite data lack this feature that is relevant for climate applications. On the other hand, if the methodology is applied to better calibrated and high space/time resolution MSG SEVIRI data, it is conceivable that the AOT accuracy of the present method will significantly improve.

#### **6.2.4 DSWARF assessment from GEO satellite measurements**

The TOA SW flux modelled with the radiative transfer code 6S (Second Simulation of the Satellite Signal in the Solar Spectrum; Vermote et al. 1997a) is compared to the CERES TOA SW flux product as a way of verifying the radiative transfer calculations and checking the validity of the calculated LUTs (see details in Section 5.2.4). The fluxes are modelled considering a tropical vertical atmospheric profile, except for the Asian dust case where a midlatitude summer profile is used, all taken from McClatchey et al. (1971), a lambertian ocean surface, and the GOME derived aerosol properties. The comparison was carried out only for the aerosol events occurred during the year 2000 that is, the dust event over the Yellow Sea, Arabian Sea and the biomass burning episode since for the 1997 dust event there was no CERES data available. Results are shown in Figure 6.25. The data points correspond to averages over  $0.25^\circ \times 0.25^\circ$ -wide areas over the study regions (Figures 5.15 to 5.17) for cloud and land free pixels. A slight tendency of the model to underestimate with respect to CERES results is observed. Nevertheless, the agreement between measurements and correspondent modelled data is in general quite good. In the case of Asian dust (Figure 6.25a), 98% of the modelled values agree with CERES data within a 15% error (dotted lines in the plots). In the second case (Arabian dust event – Figure 6.25b), 96% of the modelled values show an agreement with CERES data better than  $\pm 15\%$  (dotted lines in the plots), whereas in the third case (biomass burning episode – Figure 6.25c) 93% of the values are within the same level of agreement.

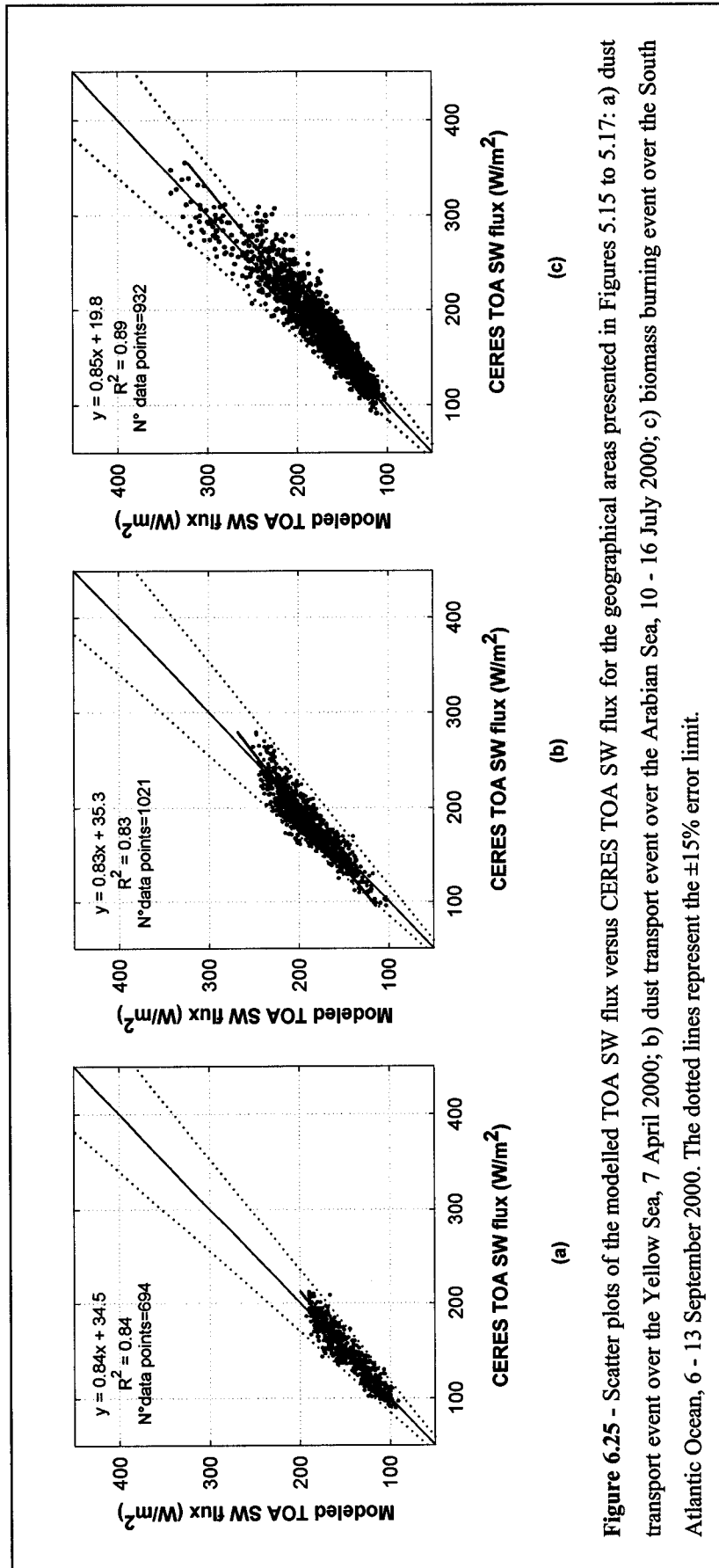


**Figure 6.25** - Scatter plots of the modelled TOA SW flux versus CERES TOA SW flux for the geographical areas presented in Figures 5.15 to 5.17: a) dust transport event over the Yellow Sea, 7 April 2000; b) dust transport event over the Arabian Sea, 10 - 16 July 2000; c) biomass burning event over the South Atlantic Ocean, 6 - 13 September 2000. The dotted lines represent the  $\pm 15\%$  error limit.

The TOA DSWARF is then retrieved over the study areas, using the AOT values previously estimated from GEO VIS measurements and LUTs calculated using the aerosol properties retrieved from GOME (Section 5.2.4). Figure 6.26 shows the variation of the DSWARF at the TOA and at the surface with the AOT at the reference wavelength of 0.55  $\mu\text{m}$  calculated from GEO VIS radiances considering the GOME derived aerosol properties for each of the four aerosol events. The points in the graphs correspond to pixels in the imagery and what varies is time during the event and the geometry of the illumination. Note how the points fall along well-defined curves that correspond basically to different solar zenith angles. The graphs show that the TOA DSWARF per unit AOT is greater for the Saharan dust event than in the other cases. On the other hand the surface DSWARF per unit AOT is the lowest for Saharan dust. This is probably connected to the fact that the spectral single scattering albedo values are higher in this case (particularly when compared with the Asian and Arabian desert dust), thus leading to more radiation reflected at the TOA. The Asian and Arabian dust events, as well as the biomass burning case, present the lower single scattering albedo values that reflect in higher aerosol absorption, reducing the downward solar fluxes arriving at the surface, and the reflected solar fluxes at the TOA, possibly leading to atmospheric heating. In these last three cases the surface and atmospheric radiative forcing become more relevant for climate studies than the TOA forcing (Satheesh and Ramanathan 2000; see also Figure 6.26 b, c, and d). Thus in these cases, the aerosol particles may exert a significant cooling effect at the surface level, but a warming effect at the TOA level, due to the increased absorption of solar energy within the atmosphere (Kim et al. 2004).

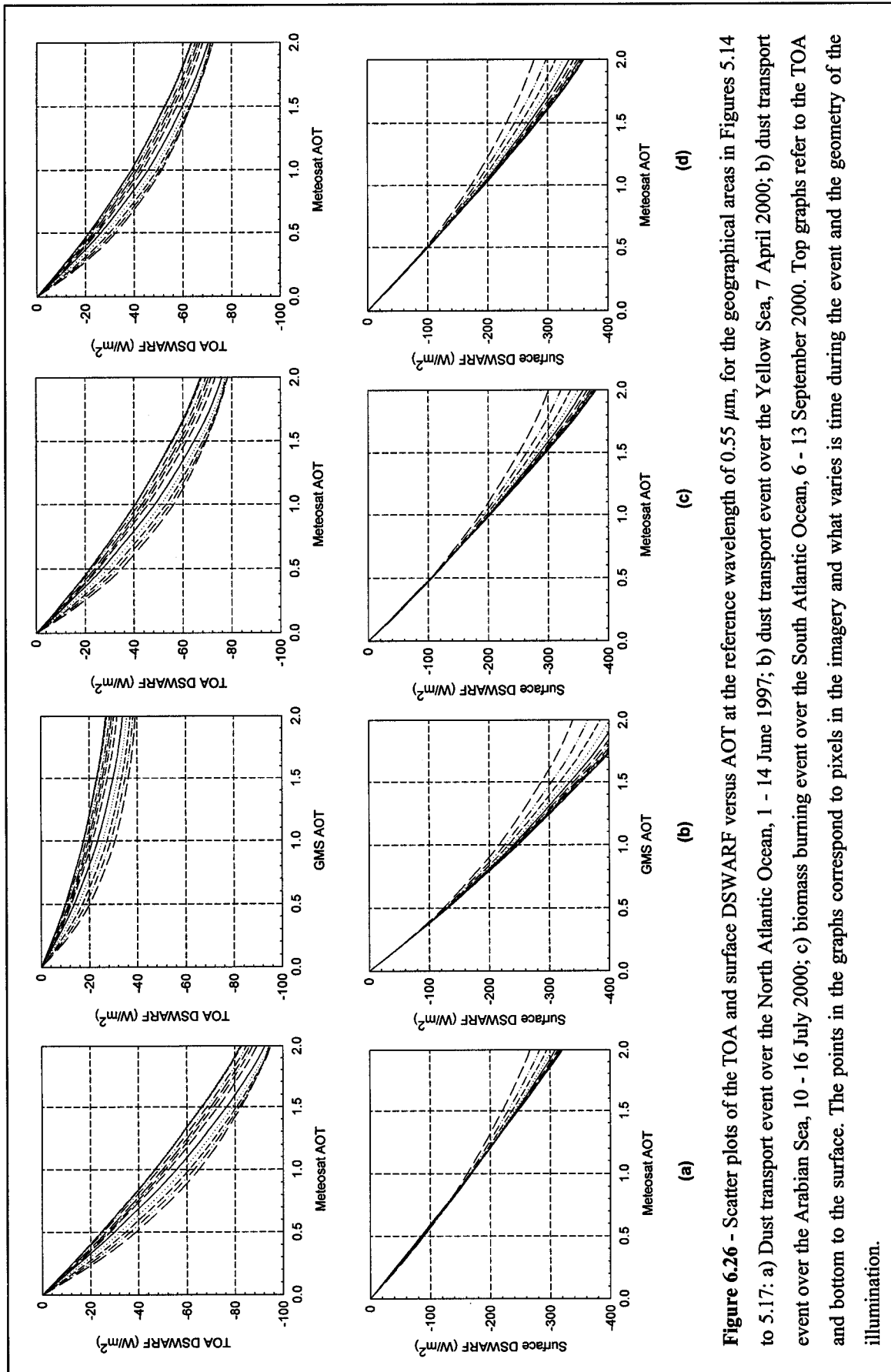


**Figure 6.26** - Scatter plots of the TOA and surface DSWARF versus AOT at the reference wavelength of  $0.55 \mu m$ , for the geographical areas in Figures 5.14 to 5.17: a) Dust transport event over the North Atlantic Ocean, 1 - 14 June 1997; b) dust transport event over the Yellow Sea, 7 April 2000; c) dust transport event over the Arabian Sea, 10 - 16 July 2000; d) biomass burning event over the South Atlantic Ocean, 6 - 13 September 2000. Top graphs refer to the TOA and bottom to the surface. The points in the graphs correspond to pixels in the imagery and what varies is time during the event and the geometry of the illumination.

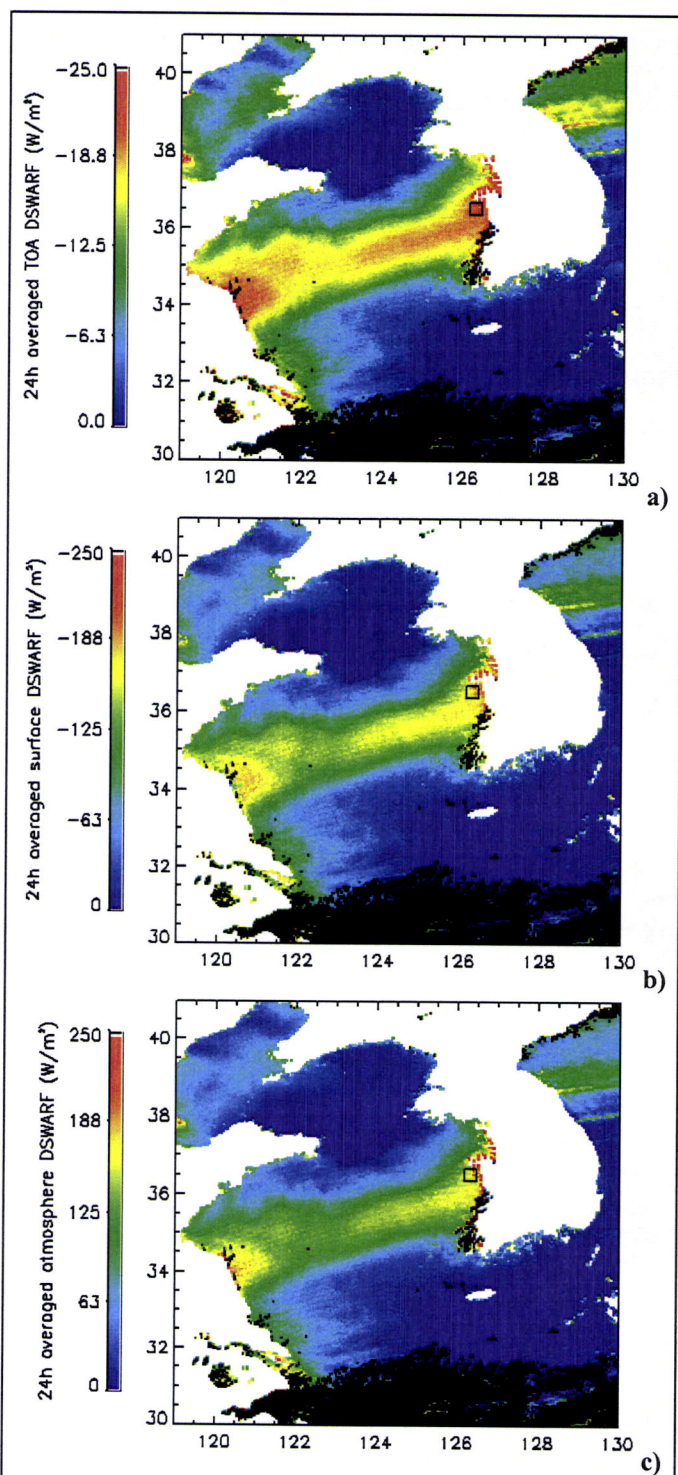
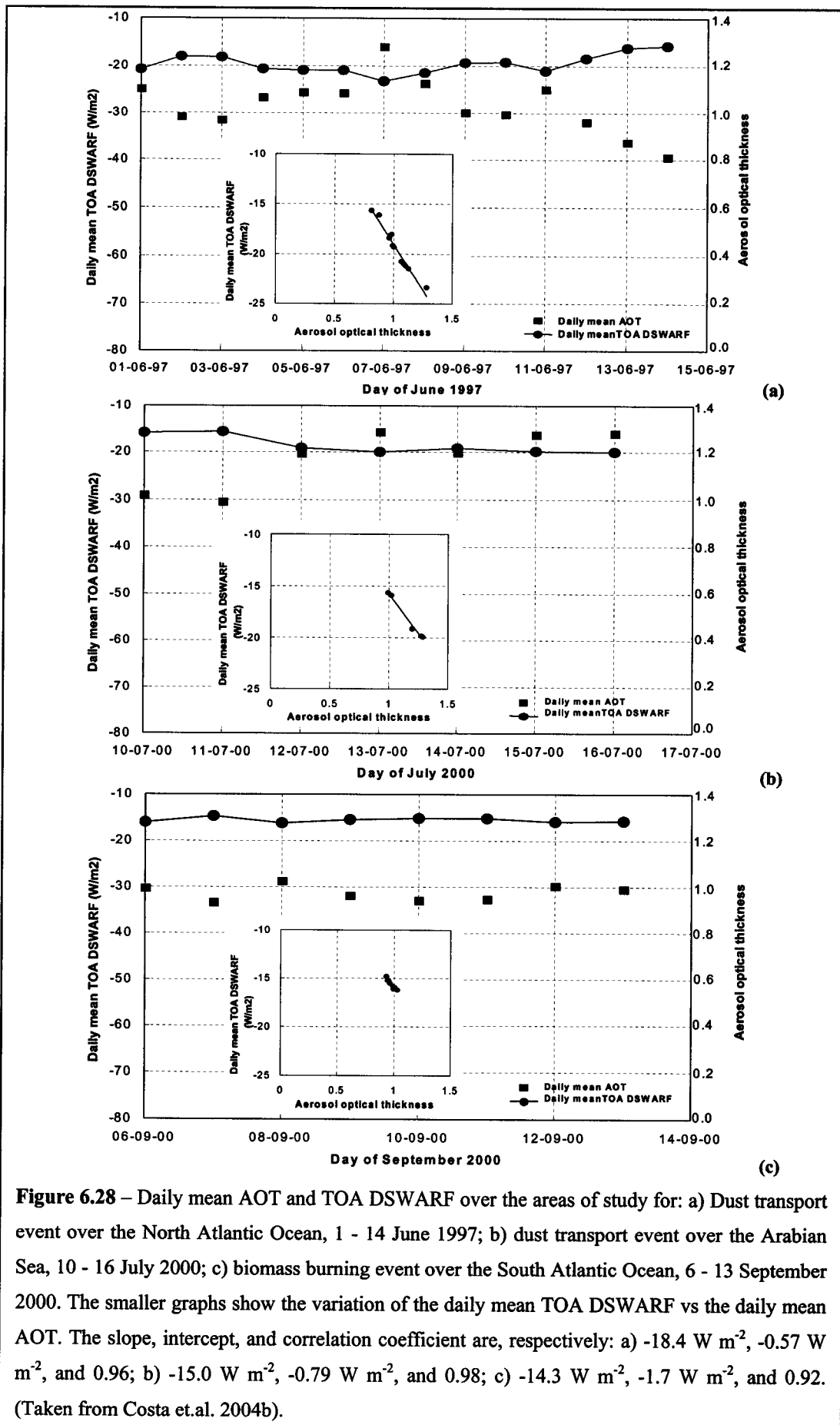


**Figure 6.27** – 24 hour averaged DSWARF at the TOA (a) surface (b), and of the entire atmosphere (c) for the 7 April 2000. The measurement site Anmyon-Do is represented by the square. Pixels contaminated by clouds at any time of the day are represented in black.

The instantaneous DSWARF values obtained from Meteosat and GMS-5 data (see Section 5.2.4) were averaged for the 24-hour period, over the case study regions (Figures 5.14 through 5.17), assuming that the instantaneous satellite retrievals can be considered hourly values, to obtain the mean daily DSWARF variation at the surface and TOA levels, as well as the DSWARF of the entire atmosphere, during the aerosol events studied. The maps in Figure 6.27 show the estimated values for the 24 hour averaged DSWARF at the TOA and surface levels, as well as of the atmosphere, for the dust transport event over the Yellow Sea, on 7 April 2000. Clouds occurring at any time of the day are identified in black. The region considered for the comparisons with the ground-based measurements is represented on the maps by the square, which corresponds to an area of  $0.25^\circ \times 0.25^\circ$  in latitude and longitude, centred on the geographical coordinates of Anmyon-Do. The mean value of the TOA DSWARF obtained for the area considered around Anmyon-Do (square box in

Fig.6.27) is of  $-21.5 \text{ W m}^{-2}$ , and the TOA DSWARF per unit optical thickness is found to be of  $-15.3 \text{ W m}^{-2}$ . Results from ground-based measurements at Anmyon-Do site report a TOA DSWARF of  $-20.7 \text{ W m}^{-2}$  and a forcing per unit optical thickness of  $-13.5 \text{ W m}^{-2}$ . As for the surface DSWARF, results obtained in the area around Anmyon-Do are of  $-164.5 \text{ W m}^{-2}$  and the forcing per unit optical thickness is of  $-116.9 \text{ W m}^{-2}$ , whereas the values obtained from ground-based measurements are  $-174.0 \text{ W m}^{-2}$  and  $-113.3 \text{ W m}^{-2}$ , respectively. The DSWARF of the atmosphere (equation 5.5) for the area considered around Anmyon-Do is of  $143.0 \text{ W m}^{-2}$ , whereas the ground measurements indicate a value of  $153.3 \text{ W m}^{-2}$ . The DSWARF of the atmosphere per unit optical thickness derived from the methodology is  $101.6 \text{ W m}^{-2}$ , and the one measured is  $99.8 \text{ W m}^{-2}$ . Considering that the satellite retrieval is based in instantaneous measurements assumed as hourly, the above results are in very good agreement with measurements, given that differences are always lower than 10%. The analysis of Figure 6.27 shows that the Asian dust has in this case a great cooling effect at the surface (Figure 6.27b), whereas not much radiation is reflected at the TOA (Figure 6.27a), translating in the heating of the atmosphere (Figure 6.27c).

Results referring to the Saharan and Arabian dust transport events, as well as to the biomass burning case are shown together with the daily mean variation of the AOT derived from Meteosat pixel radiances considering GOME aerosol optical properties, in Figures 6.28 (TOA DSWARF), 6.29 (surface DSWARF), and 6.30 (atmosphere DSWARF). The variation of the daily mean TOA DSWARF with the daily mean AOT is also shown in the smaller graphs of Figure 6.28. Note again that larger negative TOA DSWARF values were derived over the Atlantic Ocean for the Saharan dust, meaning that in this case the Earth-atmosphere system “looses” more energy that results in cooling of the system. In particular, note that the maximum TOA DSWARF is found on 7 June 1997 when also the AOT value is the highest (Figure 6.28a). For an AOT = 1.0 the computed daily mean TOA DSWARF is of  $-19.0 \text{ W m}^{-2}$ , which is quite close to the value of  $-20.7 \text{ W m}^{-2}$  published by Liu et al. (2003) for Saharan dust aerosols. In the other two events (Arabian dust and biomass burning), lower daily mean TOA DSWARF values are observed and therefore the cooling is not so pronounced. The Arabian dust event is associated to a daily mean TOA DSWARF of  $-15.8 \text{ W m}^{-2}$  for an AOT = 1.0 and the biomass burning case shows a value of  $-16.0 \text{ W m}^{-2}$  for the same AOT.



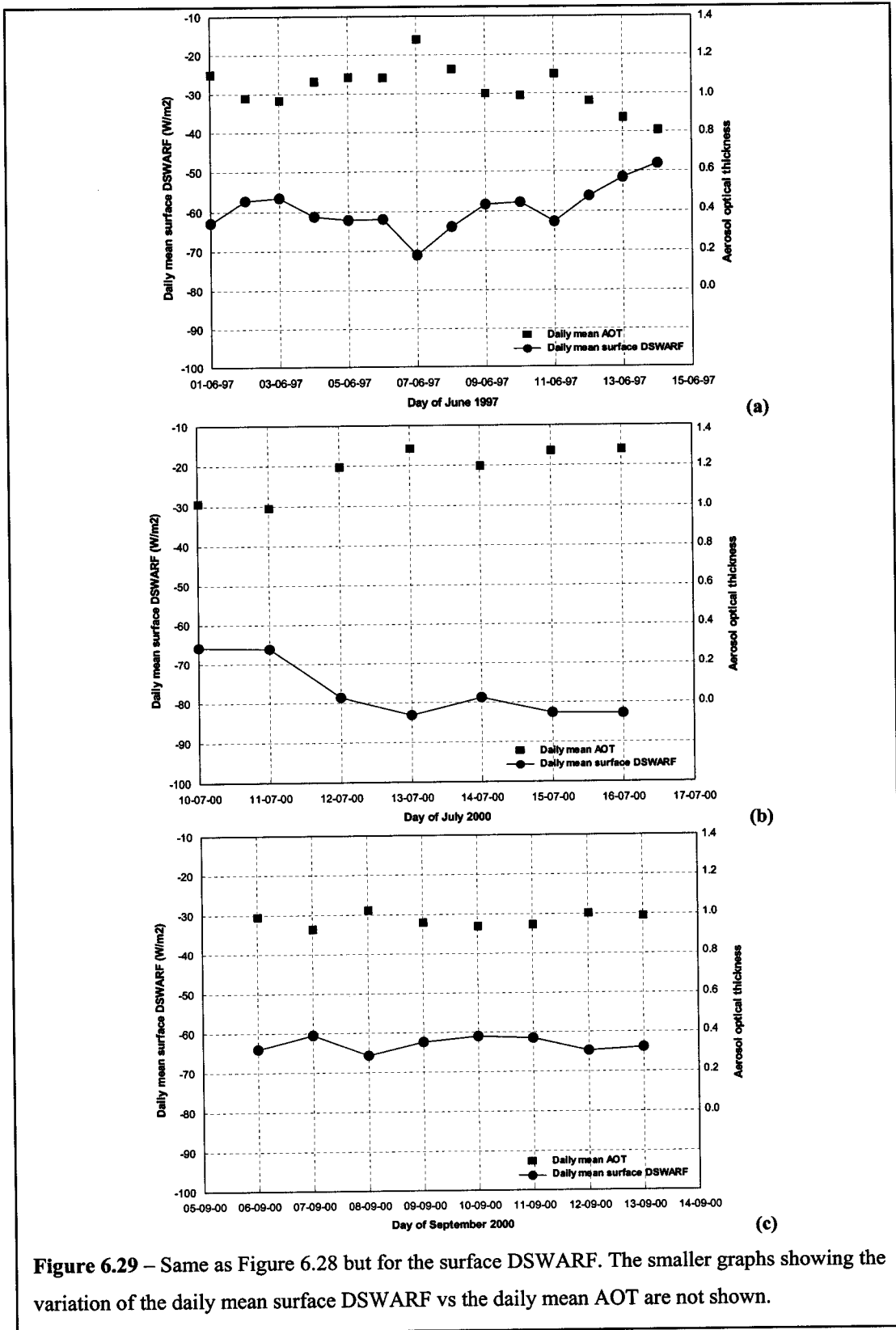


Figure 6.29 – Same as Figure 6.28 but for the surface DSWARF. The smaller graphs showing the variation of the daily mean surface DSWARF vs the daily mean AOT are not shown.



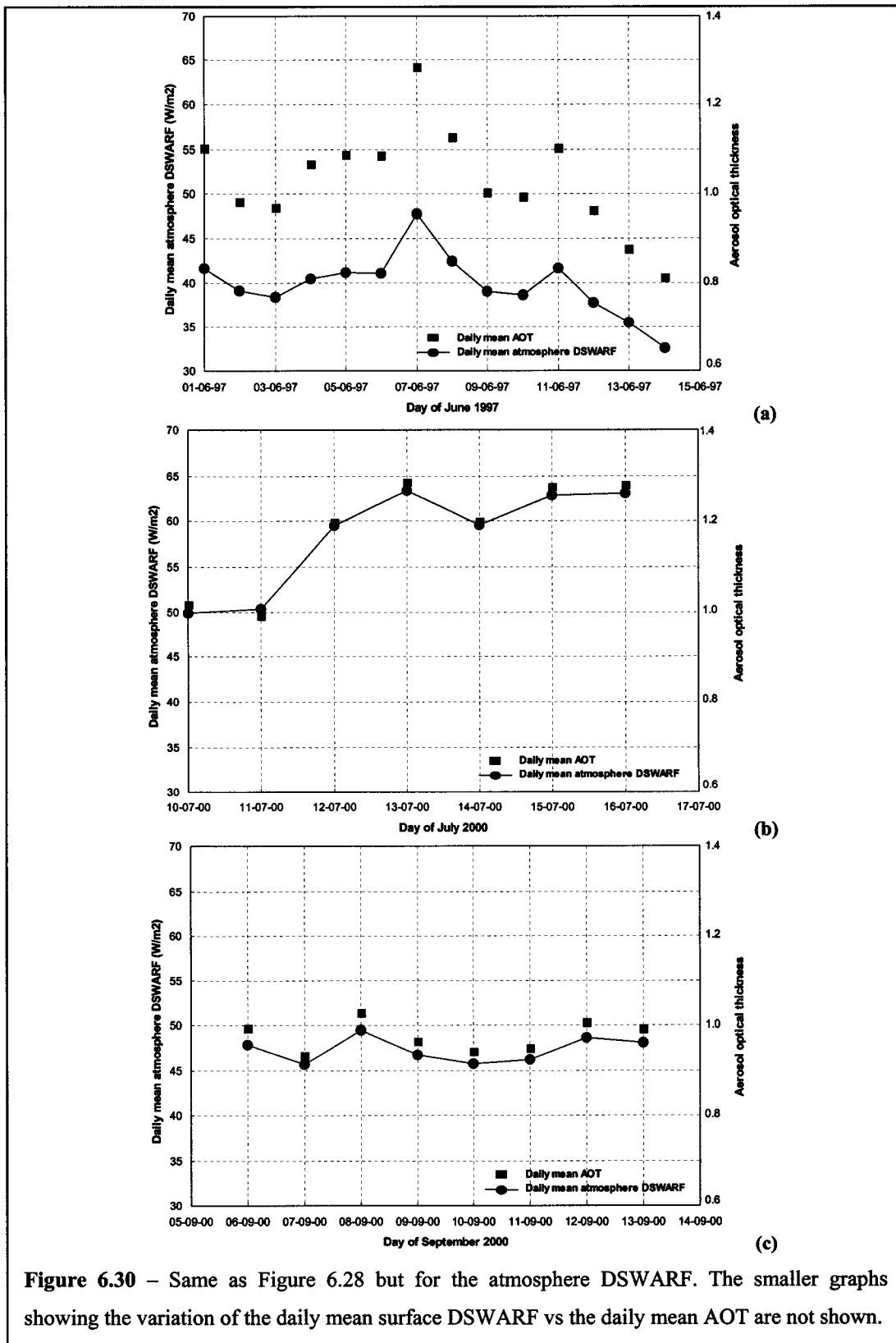


Figure 6.30 – Same as Figure 6.28 but for the atmosphere DSWARF. The smaller graphs showing the variation of the daily mean surface DSWARF vs the daily mean AOT are not shown.

The surface DSWARF shown in Figure 6.29 in each of the case studies shows, similar trends as those observed in the graphs of Figure 6.28 (TOA DSWARF). Yet, the surface DSWARF values are considerably higher (more negative). For an AOT of 1.0 the computed daily mean surface DSWARF is found to be  $-57.4 \text{ W m}^{-2}$  due to Saharan dust aerosols. In the other two events (Arabian dust and biomass burning), higher daily mean surface DSWARF values are observed and therefore the cooling is more pronounced. The Arabian dust event is associated to a daily mean surface DSWARF of  $-65.4 \text{ W m}^{-2}$  for an AOT = 1.0 and the biomass burning case shows a value of  $-64.3 \text{ W m}^{-2}$  for the same AOT. The DSWARF of the atmosphere presented in Figure 6.30 shows that the highest values are observed for the Arabian dust case study (Figure 6.30b), translating in a greater warming of the atmosphere. The lowest atmosphere DSWARF values are observed for the Saharan dust case as expected (Figure 6.30a).

## 6.3 Clouds

The methodology developed for the cloud characterization, as well as the case studies considered and the independent measurements and/or results from other state-of-the-art algorithms used for the comparisons were all presented in Section 5.3. This section reports the results obtained for the cloud parameters such as: optical thickness ( $\tau^c$ ), effective radius ( $r_{eff}$ ), top temperature ( $T^c$ ), top height ( $Z^c$ ), top pressure ( $P^c$ ), type, liquid water path ( $W$ ), and geometrical thickness ( $D$ ). A comparison with MODIS cloud product and *in situ* measurements is also included.

### 6.3.1 Results

The thresholds determined from the bi-spectral analysis in terms of the IR brightness temperature ( $T_b$ ) and of the VIS radiance ( $I_{VIS}$ ), described in Section 5.3.1, are summarised in Table 6.2. In Table 6.3, the vertical profiles taken from McClatchey et al. (1971), as well as the used surface reflectance and temperature values, are indicated.

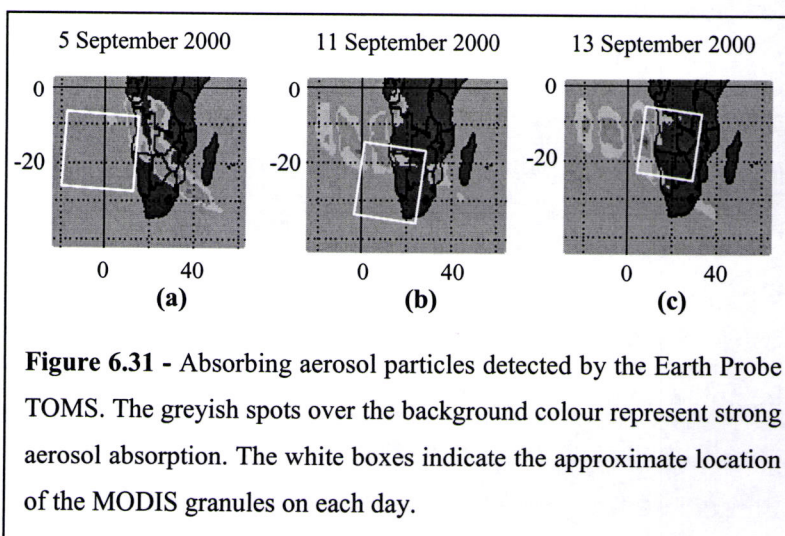
Case Study	Water Clouds		Ice Clouds
	Over Ocean	Over Land	
African fires September 2000	$260K < T_B < 285K$ and $I_{VIS} > 40Wm^{-2}sr^{-1}\mu m^{-1}$	$260K < T_B < 290K$	$T_B \leq 260K$
Iberian Peninsula fires August 2003	$260K < T_B < 290K$ and $I_{VIS} > 40Wm^{-2}sr^{-1}\mu m^{-1}$	$260K < T_B < 295K$	$T_B \leq 260K$

**Table 6.2** – Threshold values obtained from the bi-spectral cloud classification for each of the case studies.

Case study	Vertical profile	Ocean		Land	
		VIS Reflectance	Surface Temperature	VIS Reflectance	Surface Temperature
African fires	Tropical	0.05	288K	0.10	305K
Iberian Peninsula fires	Midlatitude summer	0.05	285K	0.12	305K

**Table 6.3** – Vertical profile, surface reflectance and temperature values used in the work.

The aerosol absorption maps from TOMS presented in Figure 6.31 corresponding to 5, 11 and 13 September 2000 reveal absorbing aerosol particles (smoke), based on their absorption properties in the UV spectral region (see Section 3.2 and Section 5.2.5.1). The greyish spots over the dominating background colour delimit the aerosol absorption areas and therefore the presence of absorbing particles. The white boxes delimit the



approximate location of the MODIS-Terra granules used in each of the days. 5 September 2000 is representative of background conditions since the aerosol event can be barely noted on the upper right part of the white box, which corresponds to a cloud-free area. On 11 September aerosol and background conditions co-exist since the aerosol event does not concern the lower part of the granule, but only the upper part, where clouds are also detected. A vast aerosol mass extends over the ocean in a cloudy area on 13 September.

The TOMS images in Figure 6.32 illustrate the regions with absorbing aerosol particles, presumably coming from the fires burning across Portugal and Spain (second case study).

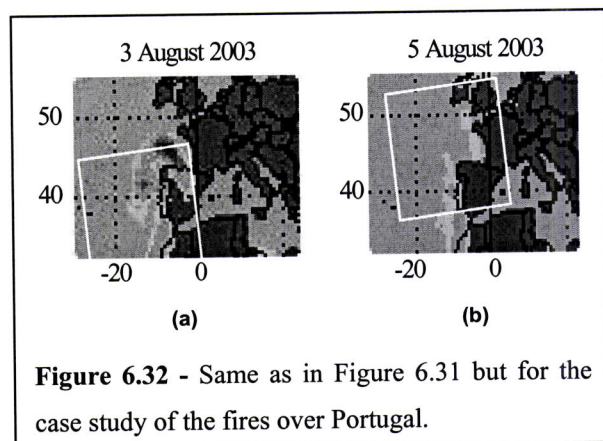


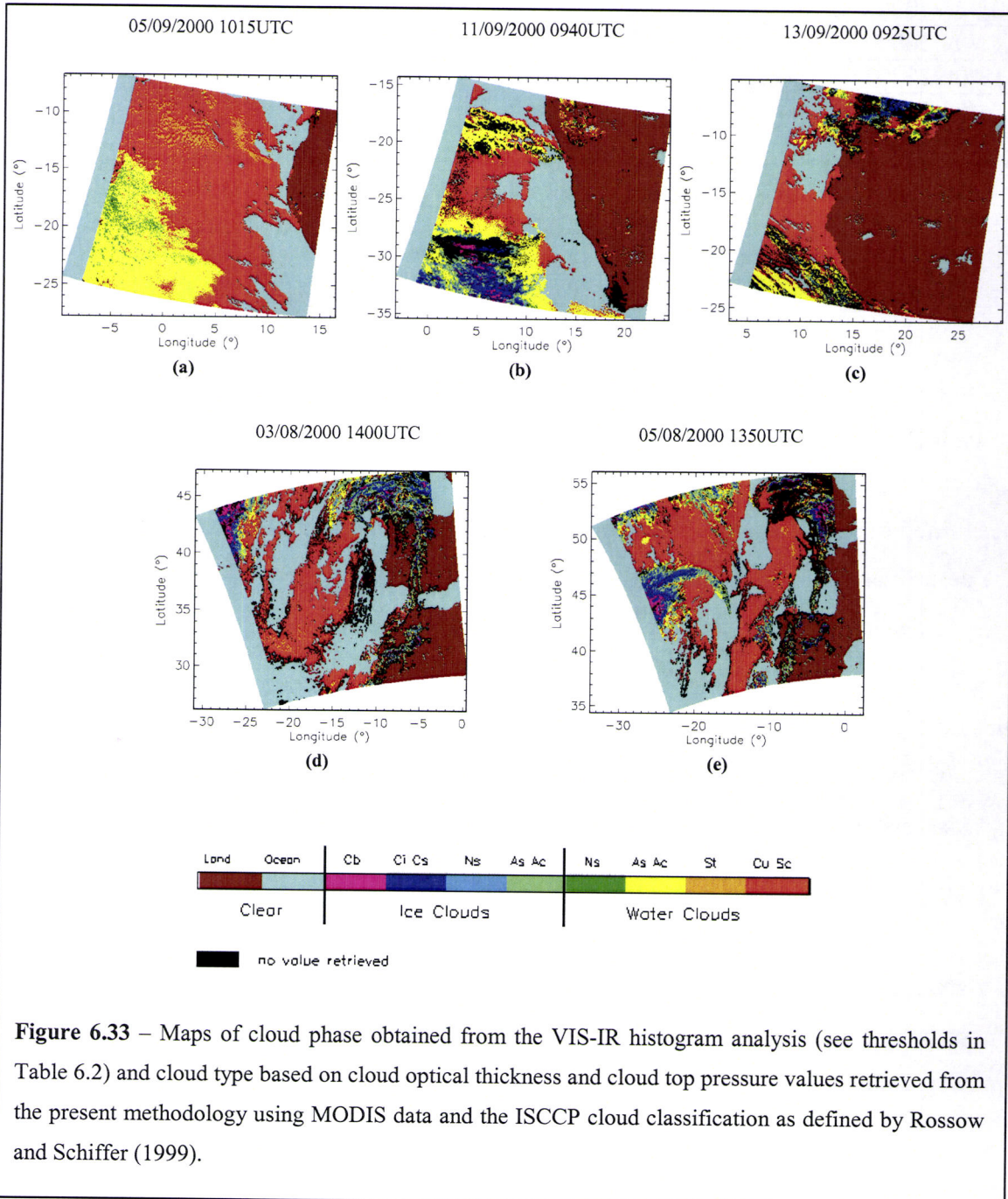
**Figure 6.32** - Same as in Figure 6.31 but for the case study of the fires over Portugal.

Clouds are detected on the three days in the areas affected by the absorbing aerosol plumes. The white boxes indicate the geographical location of the MODIS-Aqua (3 and 5 August) granules used for the retrieval.

The maps in Figure 6.33 show the cloud type using the present methodology. Three selected images are presented for

each of the two case studies. The results for 5 September 2000 show that the classification distinguished merely water clouds located mainly over the ocean, but not in the area where the absorbing aerosols are detected (Figure 6.31a). Therefore, we are probably seeing clouds in the absence of any absorbing aerosol from the biomass fires. The classification results for 11 and 13 September 2000 not only show water clouds over the ocean but also a few ice clouds, with minor broken clouds of both types over land. The attention was focused on the analysis of the properties of water clouds, for which the influence of the aerosol particles is more immediate. In the 11 September case, the comparison of the absorbing aerosol detected by TOMS (Figure 6.31b) with the classified MODIS image (Figure 6.33b) shows that, although water clouds cover most of the oceanic area of the granule, only the upper part of the granule unveils the presence of the absorbing aerosols. On 13 September 2000 the presence of absorbing aerosol particles (see Figure 6.31c) can be noted all over the oceanic area covered by the MODIS granule where also water clouds are distinguished by the pixel classification technique (Figure 6.33c). In the case of the Portuguese fires, mainly water clouds are distinguished by the classification in the MODIS granules (Figures 6.33d, and e). Note from the TOMS maps in Figure 6.32 that the absorbing aerosol particles are present on the two days (3, and 5 August 2003) even though they do not cover the whole area swept by the granules. Table 6.4 summarizes the mean and standard deviation values of the retrieved cloud properties ( $\tau^c$ ,  $r_{eff}$ , and  $T^c$ ) for the water clouds over the ocean in Figure 6.33. The pixels retained for these calculations had

to obey the conditions  $\tau^c \geq 2$  and  $r_{eff} \geq 2$ , representing minimum boundary values for which the errors in the retrieval are still acceptable (Nakajima and Nakajima 1995).



Date	Time (UTC)	Mean values retrieved		
		$\tau^c \pm \sigma$	$r_{eff} \pm \sigma$ ( $\mu\text{m}$ )	$T^c \pm \sigma$ (K)
05/09/2000	1015	$12.4 \pm 7.2$	$11.1 \pm 2.4$	$283.6 \pm 3.3$
11/09/2000	0940	$5.3 \pm 3.8$	$12.7 \pm 6.1$	$274.9 \pm 8.4$
13/09/2000	0925	$6.8 \pm 3.9$	$14.4 \pm 7.0$	$279.5 \pm 7.4$
03/08/2003	1400	$7.8 \pm 3.1$	$8.4 \pm 5.1$	$286.2 \pm 7.7$
05/08/2003	1350	$9.2 \pm 5.6$	$11.8 \pm 6.7$	$284.8 \pm 7.2$

**Table 6.4** – Mean values of cloud optical thickness, cloud particle radius, cloud top temperature, and the respective standard deviations for the water clouds over the ocean in the analysed areas (see cloud type maps in Figure 6.33), considering only the cases where  $\tau^c \geq 2$  and  $r_{eff} \geq 2$ .

One of the apparent effects out of the cloud-aerosol interaction is the reduction of the cloud particle size due to the increase of cloud condensation nuclei that induce a redistribution of the cloud water content (Twomey 1974). The analysis was therefore concentrated on the retrieved effective radius values to detect any cloud modification due to the aerosol effect.

5 September 2000, when no absorbing aerosol particles were detected over cloudy areas, presents a frequency histogram (Figure 6.34a) with a low spread of the values resulting in small variations of the particle effective radius with a mean value of  $11.1 \mu\text{m}$ . The values of the mean effective radius on 11 and 13 September 2000 are higher along with a larger spread. Figure 6.34 shows the frequency histograms of  $r_{eff}$  (for the water clouds over the ocean) corresponding to these three days. The histogram of the 11 September shows a bimodal distribution with a peak of the effective radius towards  $14 \mu\text{m}$  and a smaller peak around  $6 \mu\text{m}$ . This second peak may be connected to the presence of biomass burning aerosol on the upper part of the granule, where the pixels with lower particle sizes were located. The mean  $r_{eff}$  value and the respective standard deviation were calculated only for the area where, according to TOMS information, the absorbing aerosol particles were present obtaining  $r_{eff} = 7.7 \pm 3.2 \mu\text{m}$  and the cloud top height located at  $5.2 \pm 0.9 \text{ km}$ . This effective radius value is clearly lower than the one considering the whole granule ( $r_{eff} = 12.7 \pm 6.1 \mu\text{m}$ ) and with a lower standard deviation. Additional information from vertically resolved measurements indicate that the smoke plume in the surrounding

cloud-free area (approximate location: 22.5°S and 12.2°E) was detected between 2 and 5 km (Kaufman et al. 2003). Since the retrieved average cloud top height is quite close to these measurements, it could well be that the cloud suffered the influence of the aerosol particles, reflecting in lower values of the particle radius. However, the retrieved cloud top height values may have been overestimated due to the vertically separated cloud and aerosol layers, which are currently not taken into account by the method. The  $r_{eff}$  values for 13 September 2000 are spread over a larger interval and peak around 11  $\mu\text{m}$ . As it appears from the TOMS map (Figure 6.31c), the absorbing aerosol is located over the ocean and spatially coexists with the clouds in the area (Figure 6.33c). However, no trend could be distinguished in this case.

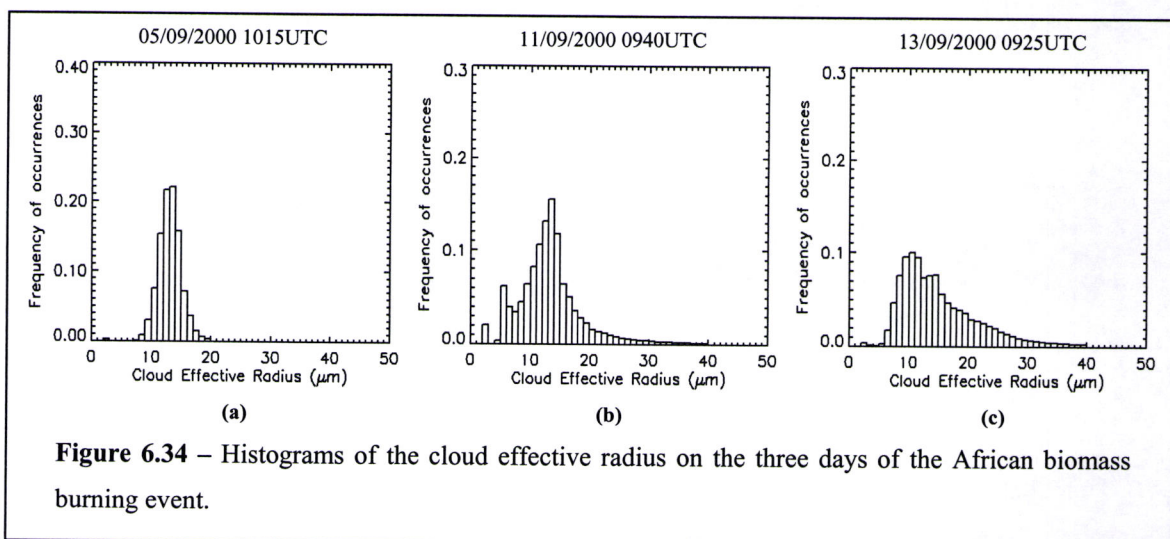
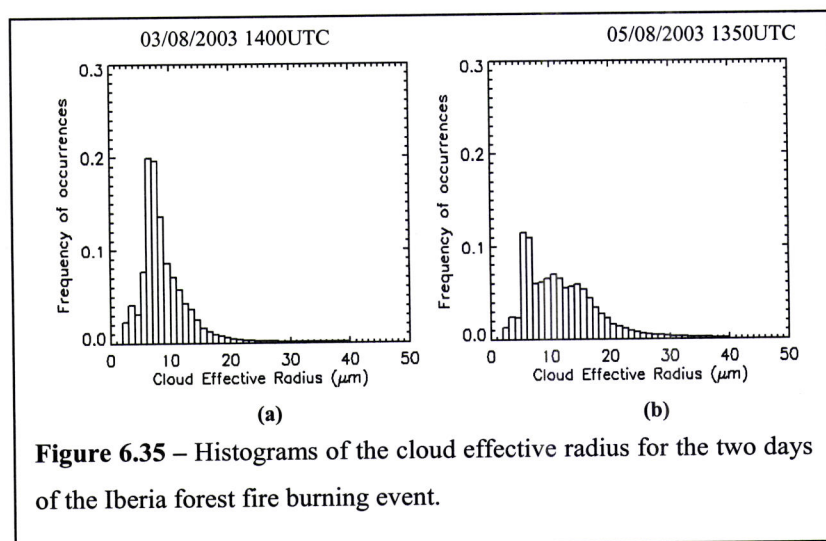


Figure 6.35 shows the frequency histograms of the effective radius (for the water clouds over the ocean) corresponding to the Portuguese case study. The analysis of the effective radius results for 3 August 2003 during the Iberian Peninsula fires revealed a relatively low dispersion of the values (Figure 6.35a), with a mean  $r_{eff} = 8.4 \pm 5.1 \mu\text{m}$ . On 5 August, the average  $r_{eff}$  and the standard deviation are higher as evident from the broad form of the histogram in Figure 6.35b) that shows two higher peaks at lower  $r_{eff}$  values well differentiated from the rest of the distribution. In this case, two water cloud systems were identified by the classification (Figure 6.33e). In particular, these cloudy pixels, characterized by lower effective radius values, refer to the cloud system located near the Portuguese coast, where the absorbing aerosol was detected (Figure 6.32b). The mean  $r_{eff}$  value and standard deviation calculated for the area where TOMS indicated the presence of

the absorbing aerosol, result in lower mean  $r_{eff}$  values and associated standard deviation ( $r_{eff} = 7.9 \pm 3.1 \mu\text{m}$ ) with respect to that obtained considering all cloudy pixels of the granule ( $r_{eff} = 11.8 \pm 6.7 \mu\text{m}$ ). The exceptionally low effective radius values found in the water clouds near the Portuguese coast could be connected to the interaction of clouds with the smoke from the fires burning across the country. On the other hand, once more it can simply be the result of aerosol and cloud layers at different atmospheric levels not taken into account by the radiative transfer calculations. Additional information to understand the cause of the low  $r_{eff}$  values could be derived from atmospheric profiles of the regions, which unfortunately are not available.

The origin of the cloudy systems in Figure 6.33d), and f) near the Portuguese west coast, which supposedly contain biomass burning aerosol particles, is traced back for 72



**Figure 6.35** – Histograms of the cloud effective radius for the two days of the Iberia forest fire burning event.

hours using three-dimensional back trajectories calculated via the NOAA HYbrid Single-Particle Lagrangian Integrated Trajectory Model (HYSPLIT4) (Draxler and Rolph 2003; Rolph 2003), (see Section 5.3.2.2). The back

trajectories were calculated considering a start location at latitude of  $38.0^{\circ}\text{N}$  and longitude of  $12.5^{\circ}\text{W}$ , and a start height of 1km, corresponding to the approximate mean cloud top height in the two cases (Figure 6.33d), and f)). The back trajectories are shown in Figure 6.36. In both cases, the air masses under study originate in Continental Portugal, where the forest fires are burning. Therefore, it is reasonable to assume that the investigated cloud systems were contaminated by the aerosol particles originating from the fires.

The maps in the figures of the next two pages present the results obtained of the retrieved cloud parameters: optical thickness ( $\tau^c$ ), effective radius ( $r_{eff}$ ), top temperature



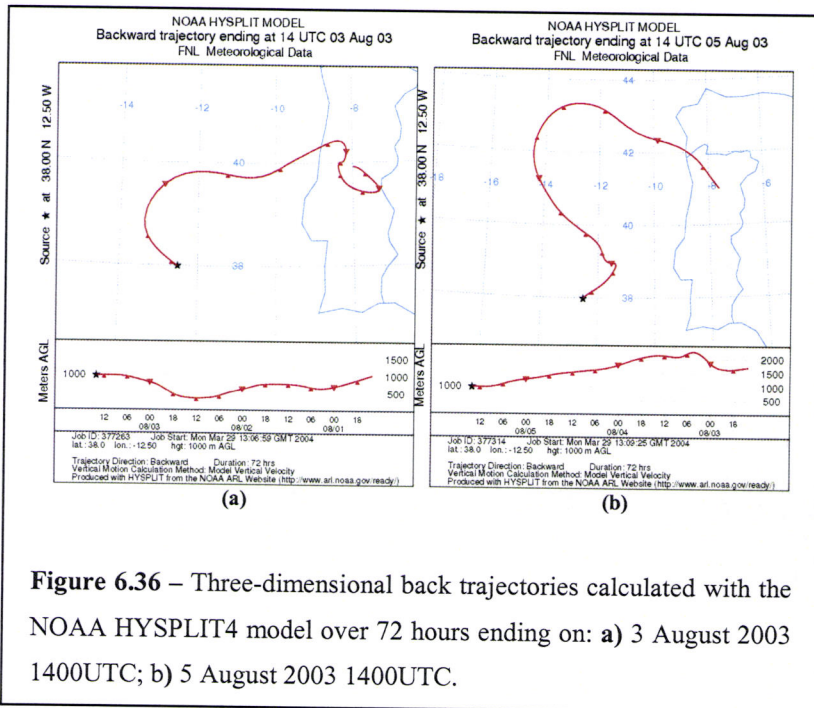


**Figure 6.36** – Three-dimensional back trajectories calculated with the NOAA HYSPLIT4 model over 72 hours ending on: **a)** 3 August 2003 1400UTC; **b)** 5 August 2003 1400UTC.

( $T^c$ ), top height ( $Z^c$ ), top pressure ( $P^c$ ), type, liquid water path ( $W$ ), and geometrical thickness ( $D$ ). The results shown in the plates refer to two of the analysed MODIS granules. The first one corresponds to the MODIS – Terra granule of 13 September 2000 at 0925UTC (Figure 6.37)

and the second one to the MODIS – Aqua granule of 5 August 2003 at 1350UTC (Figure 6.38). The cloud type has already been presented in Figure 6.33 and it is shown again for completeness.

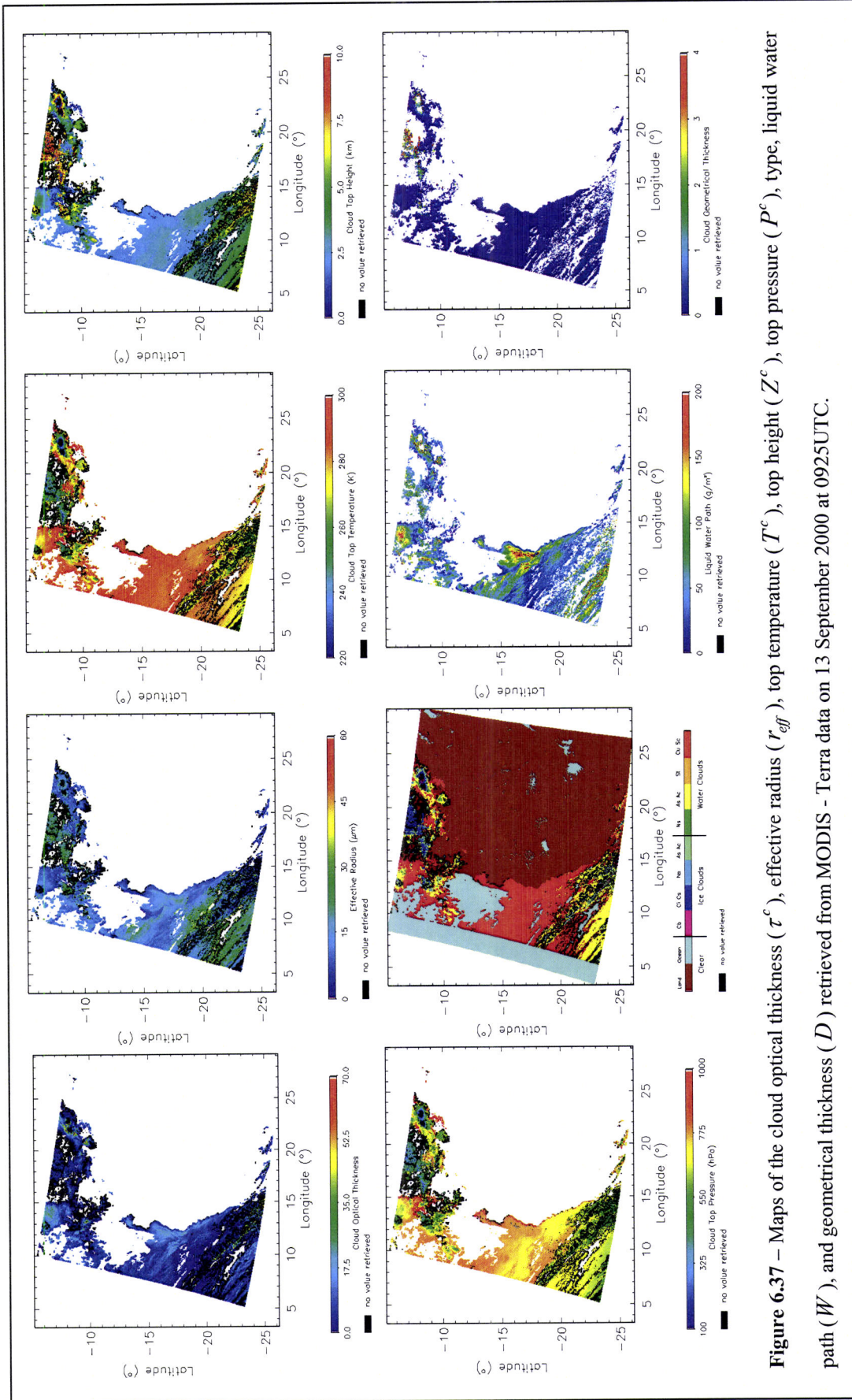


**Figure 6.37** – Maps of the cloud optical thickness ( $\tau^c$ ), effective radius ( $r_{eff}$ ), top temperature ( $T^c$ ), top height ( $Z^c$ ), top pressure ( $P^c$ ), type, liquid water path ( $W$ ), and geometrical thickness ( $D$ ) retrieved from MODIS - Terra data on 13 September 2000 at 0925UTC.

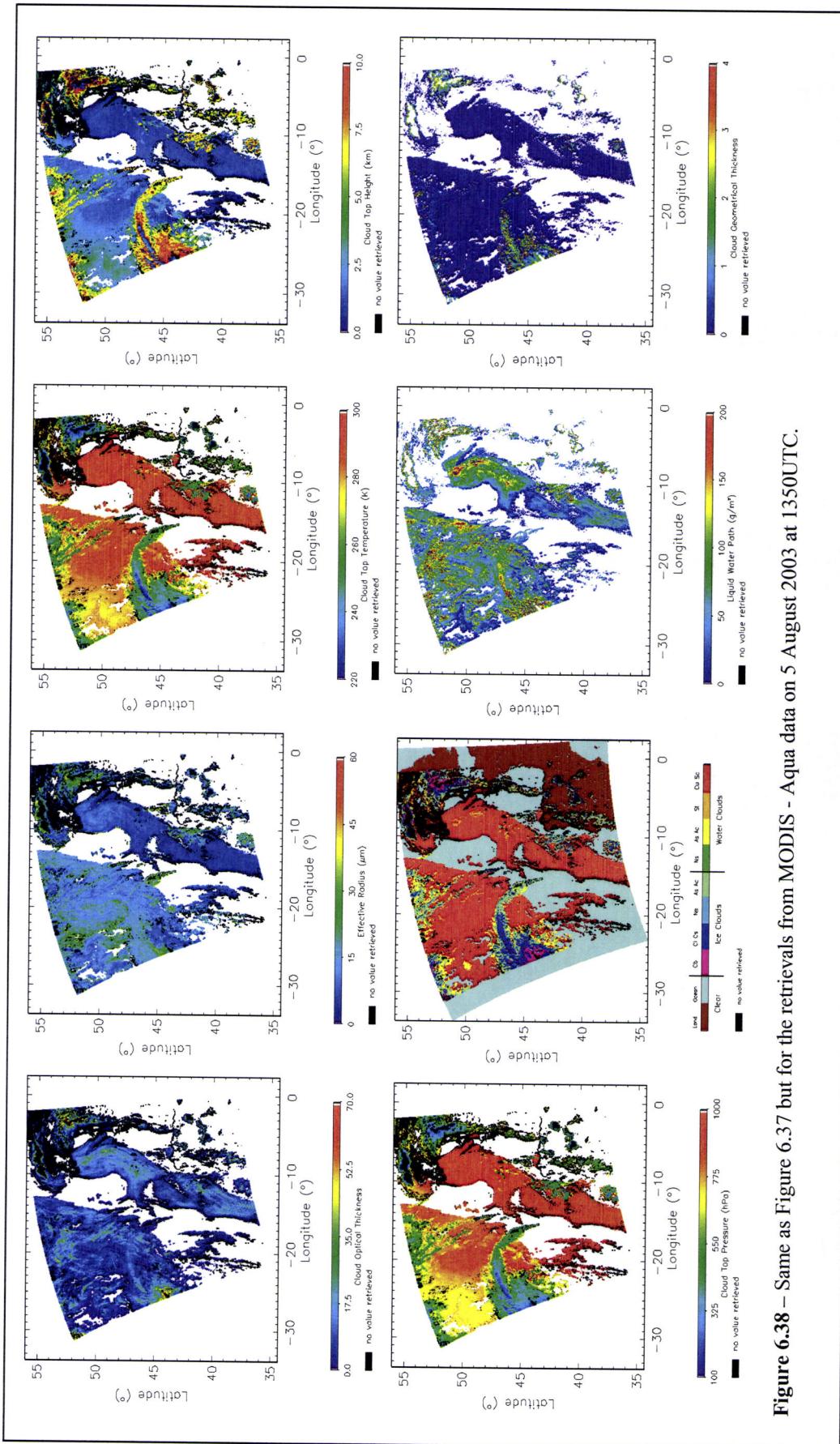
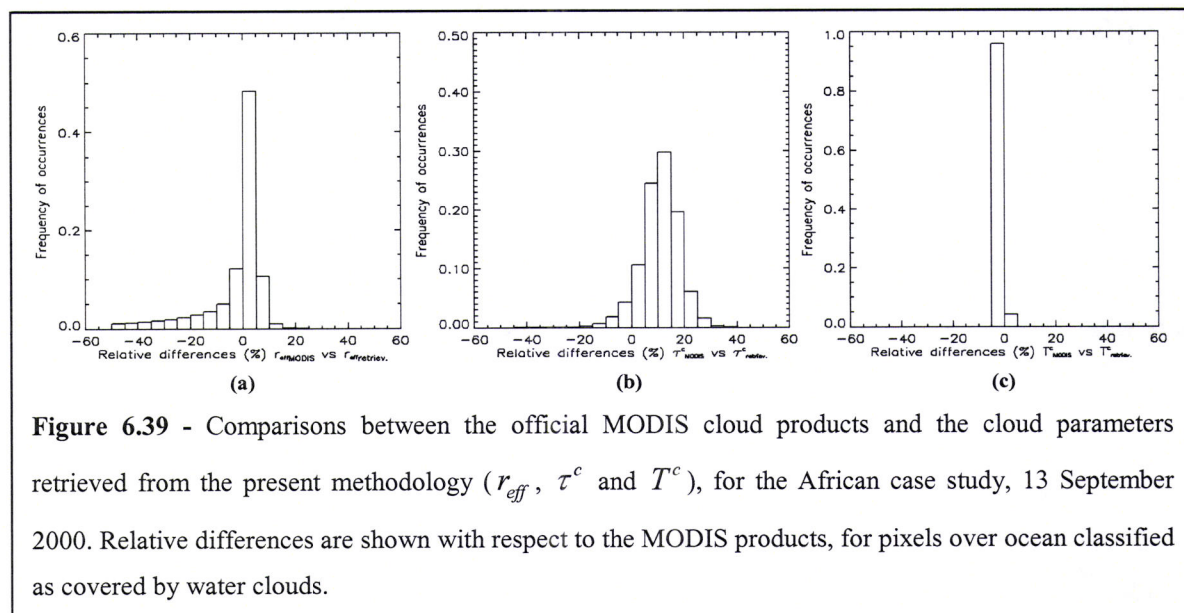


Figure 6.38 – Same as Figure 6.37 but for the retrievals from MODIS - Aqua data on 5 August 2003 at 1350UTC.

### 6.3.2 Comparisons with MODIS cloud products and *in situ* measurements

The results of the retrieval ( $\tau^c$ ,  $r_{eff}$ , and  $T^c$ ), as well as the cloud type, are compared with the corresponding MODIS cloud products for both case studies (see Table 5.7). The histograms of the results of the comparisons for the African case study are shown in Figure 6.39. The frequency of occurrence is plotted as a function of the relative differences between the cloud parameters of the MODIS official products and our retrieved cloud parameters. 13 September 2000 was selected as representative of a typical scenario containing biomass burning aerosols and clouds, but similar results are obtained for the other days (not shown). The results reported in these graphs are relative to the MODIS pixels over ocean classified as covered by water clouds. The agreement between the MODIS official product parameters and the ones retrieved according to the present methodology is encouraging since for all three cloud parameters the frequency of occurrence distributions are sharp and peaked near zero.



**Figure 6.39** - Comparisons between the official MODIS cloud products and the cloud parameters retrieved from the present methodology ( $r_{eff}$ ,  $\tau^c$  and  $T^c$ ), for the African case study, 13 September 2000. Relative differences are shown with respect to the MODIS products, for pixels over ocean classified as covered by water clouds.

Only the cloud optical thickness ( $\tau^c$ ) histogram is peaked near the 15 % relative difference, pointing out a slight underestimation of  $\tau^c$  by the present retrieval method. However, more than 50% of cases show relative differences lower than 15%. The same analysis was conducted for the case study over Portugal, whose results are reported in Figure 6.40 for 5 August 2003, confirming once again an agreement between the two retrieval procedures. In this case, the histogram of  $r_{eff}$  differences is the broadest, but 50% of the examined cases show differences lower than 10%. It is conceivable that a better agreement can be obtained by refining the selection technique of the cloud covered pixels and the cloud thermodynamic phase determination.

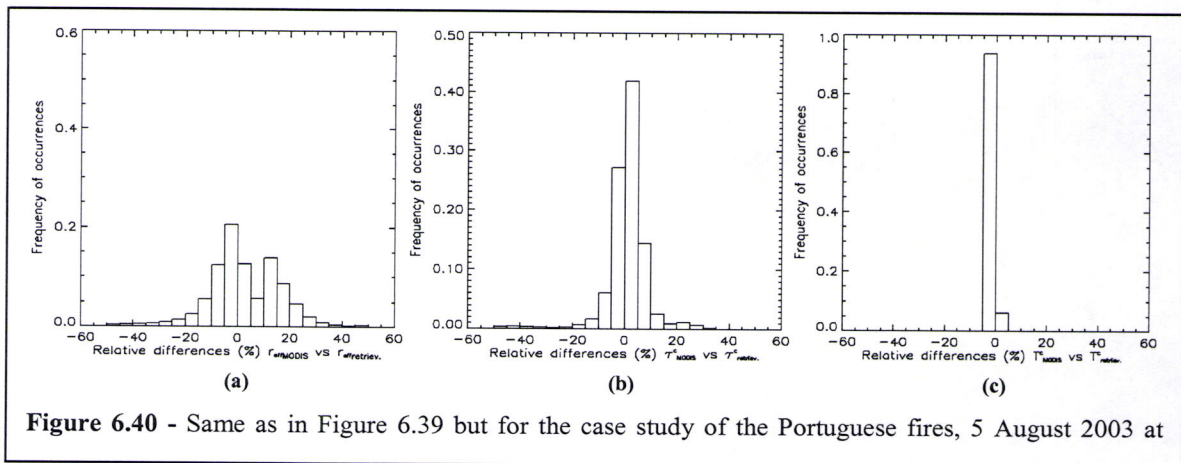
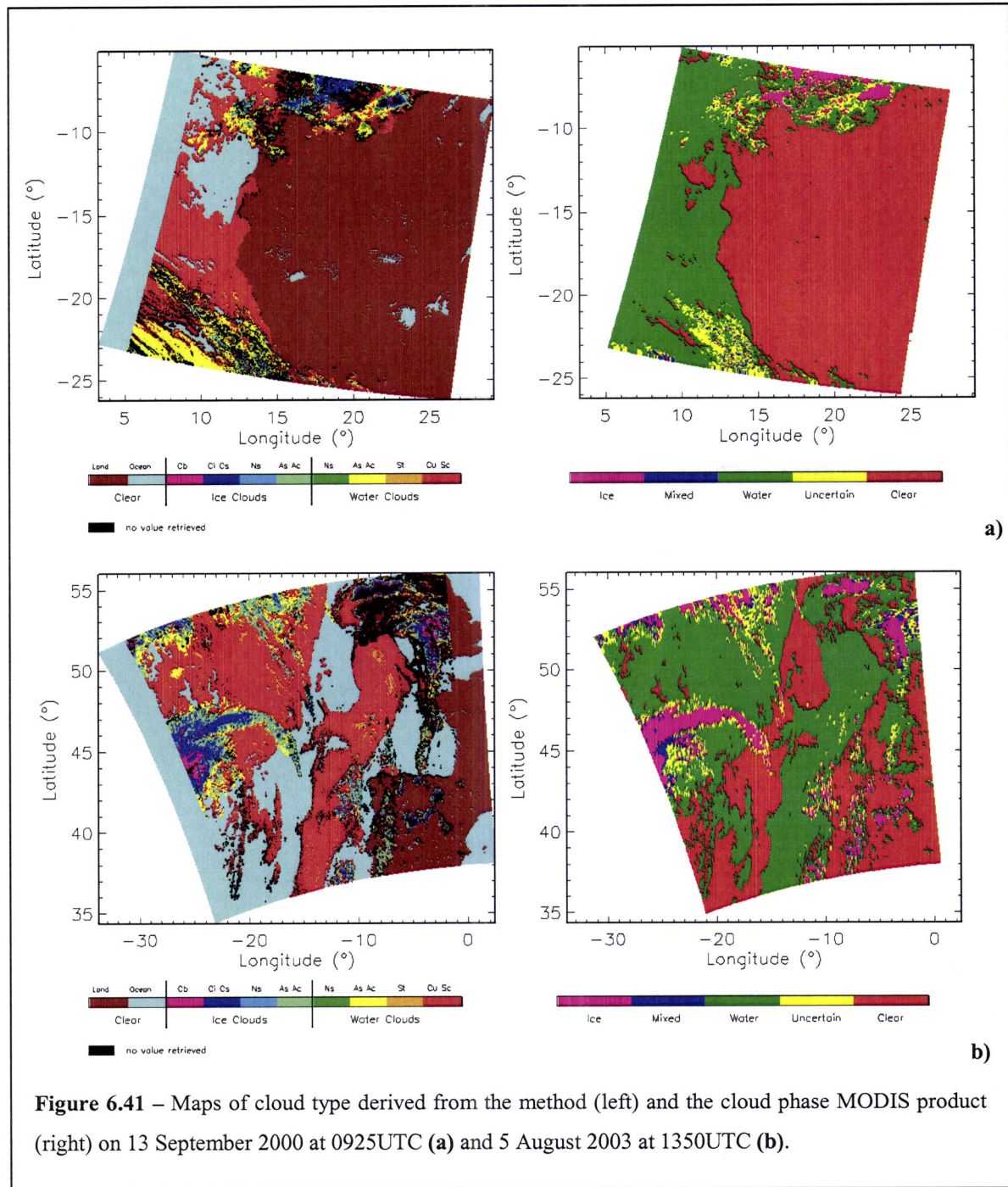


Figure 6.40 - Same as in Figure 6.39 but for the case study of the Portuguese fires, 5 August 2003 at

Figure 6.41 shows the cloud type derived from the present methodology, as well the MODIS product cloud phase presented for comparison, which considers five different classes: clear sky, uncertain, water clouds, mixed phase clouds, and ice clouds. Results are of 13 September 2000 at 0925UTC and 5 August 2003 at 1350UTC. The comparison between the derived cloud type and the one obtained from MODIS shows a good agreement. In fact, the pixels assigned water or ice in the MODIS product correspond to the same class derived here. Some problems may arise on the edges of water or ice clouds, or when pixels are partially filled with clouds, leading to an erroneous class. Nevertheless, the class is very well derived in all cases (maps only shown for two cases in Figure 6.41). The cases where no retrieval is achieved (black on the maps of Figure 6.41) may also be connected with the existence of an aerosol layer, not classified as cloud but also not classified as clear.

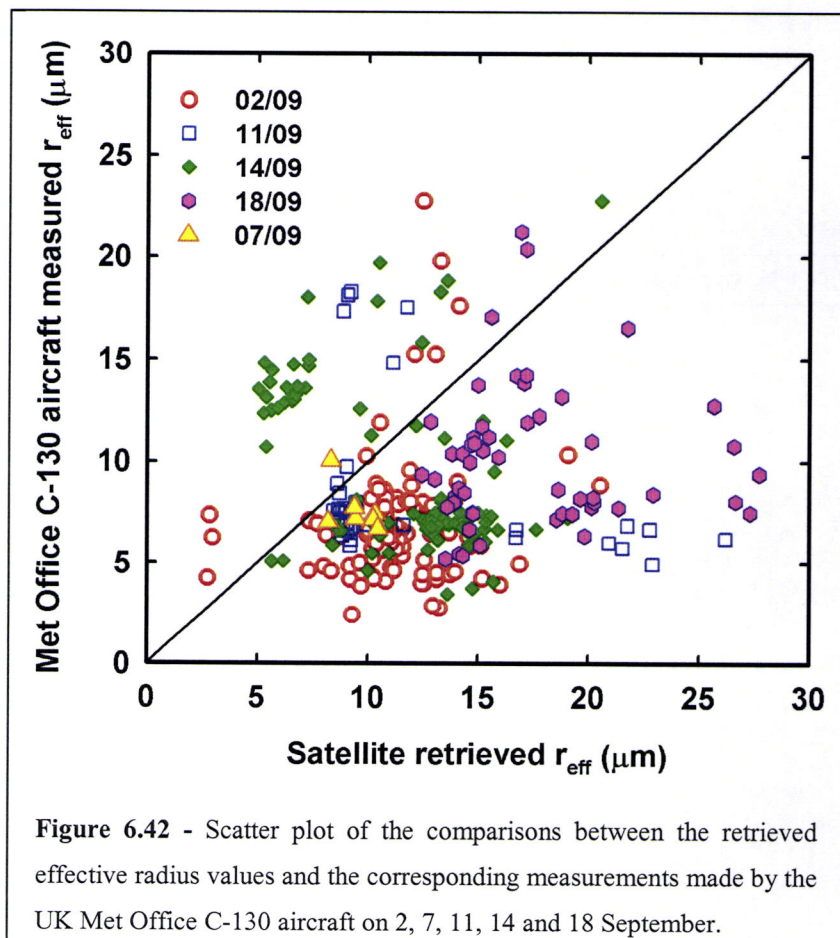


Further comparisons were carried out using data sets of the SAFARI 2000 measurements campaign, for the Southern Africa case study (see Table 5.7). Results of the comparisons between the retrieved effective radius values and the corresponding measurements made by the Met Office C-130 aircraft for 2, 7, 11, 14 and 18 September are displayed in Figure 6.42 (different symbols and colours refer to the different days). Spatial

average values of the aircraft-measured  $r_{eff}$  are plotted against the satellite-retrieved  $r_{eff}$ . Due to the different spatial resolution of the data each aircraft measurement was referred to the nearest MODIS pixel and then, considering all the aircraft measurements attributed to the same satellite pixel, the average value of the aircraft effective radius was computed; the maximum time difference between the aircraft measurements and the satellite overpass is of 3 hours. The satellite-retrieved  $r_{eff}$  values are in general larger than the ones measured

by the C-130, even if the differences are moderate. For example, on 2 September most of the retrieved  $r_{eff}$  values fall within the range of 10-15  $\mu\text{m}$  and the measured ones are in the range 5-10  $\mu\text{m}$ . A good agreement between the two data sets is found on 7 September although very few coincident satellite-aircraft data were available on this day. The reasons for these findings could be

twofold: on one hand, aircraft measurements may refer to different altitudes into the cloud from bottom to top, whereas the satellite retrieved  $r_{eff}$  belong only to the uppermost cloud layers (see Figure 6.44). On the other hand, the typical scenario observed during these days showed an elevated biomass aerosol layer and low-level stratiform clouds located below it (Keil and Haywood 2003; Haywood et al. 2003). The present retrieval algorithm does not consider the presence of an aerosol layer in the atmosphere. These two reasons could partially justify the differences between measured and retrieved  $r_{eff}$  in Figure 6.42. This



remains to be verified since it constitutes ongoing research work, by means of radiative transfer simulations of the near infrared radiance data (usually employed for the  $r_{eff}$  retrieval, as in the present work), where aerosol load is properly described with respect to the scattering properties. On 18 September the aerosol load was greatly diminished off coast of Namibia and Angola, so the  $r_{eff}$  values retrieved during this day can be considered characteristic of clouds, which didn't suffer the aerosol influence. Note from the scatter plot in Figure 6.41 that this day was characterized by the largest  $r_{eff}$  for both the data sets with respect to the previous days, e.g. 2 or 7 September. This can probably be considered as a signal of the aerosol influence on cloud microphysical properties in the other days (2, 7, 11 and 14 September), when the  $r_{eff}$  presented lower values.

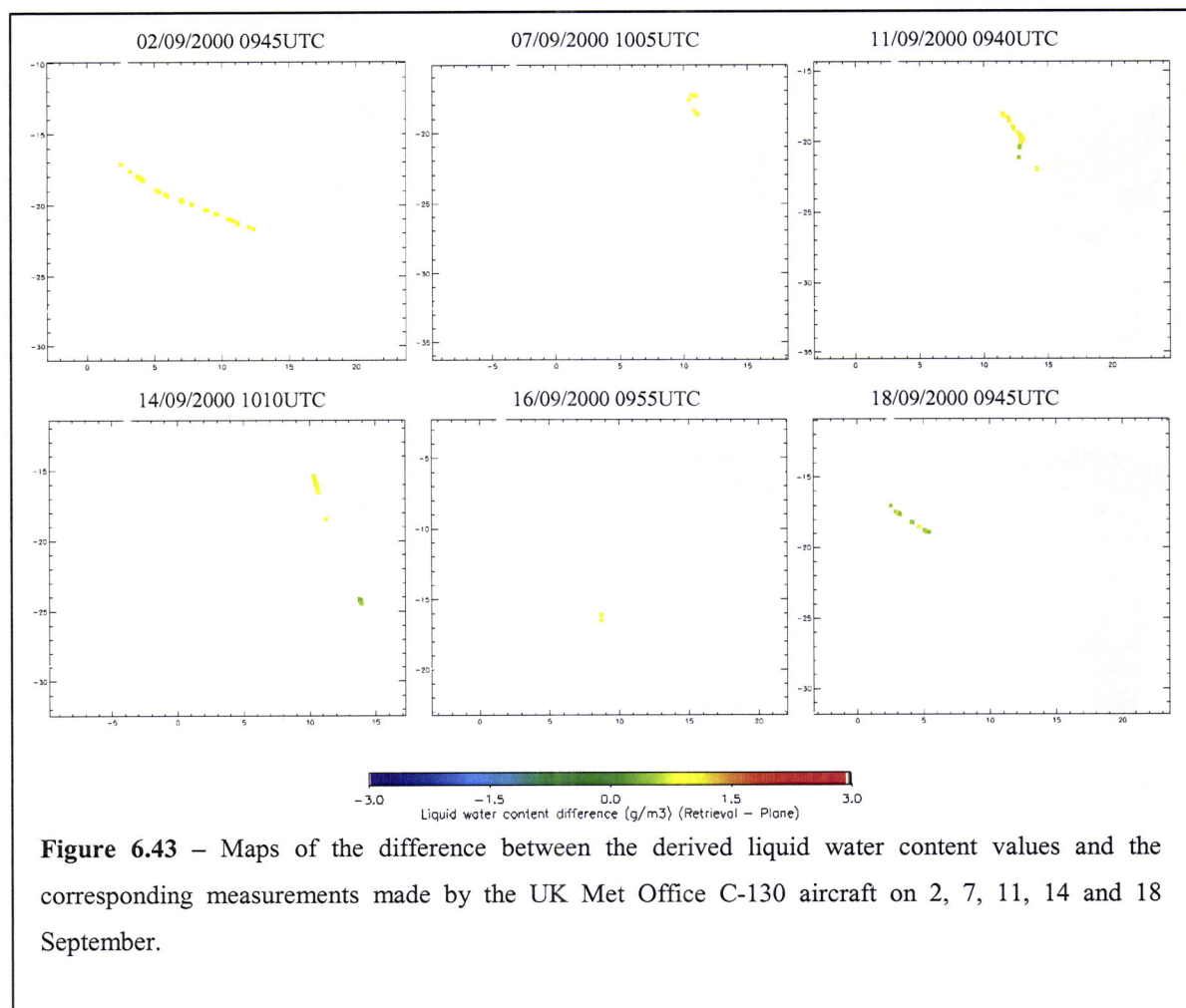
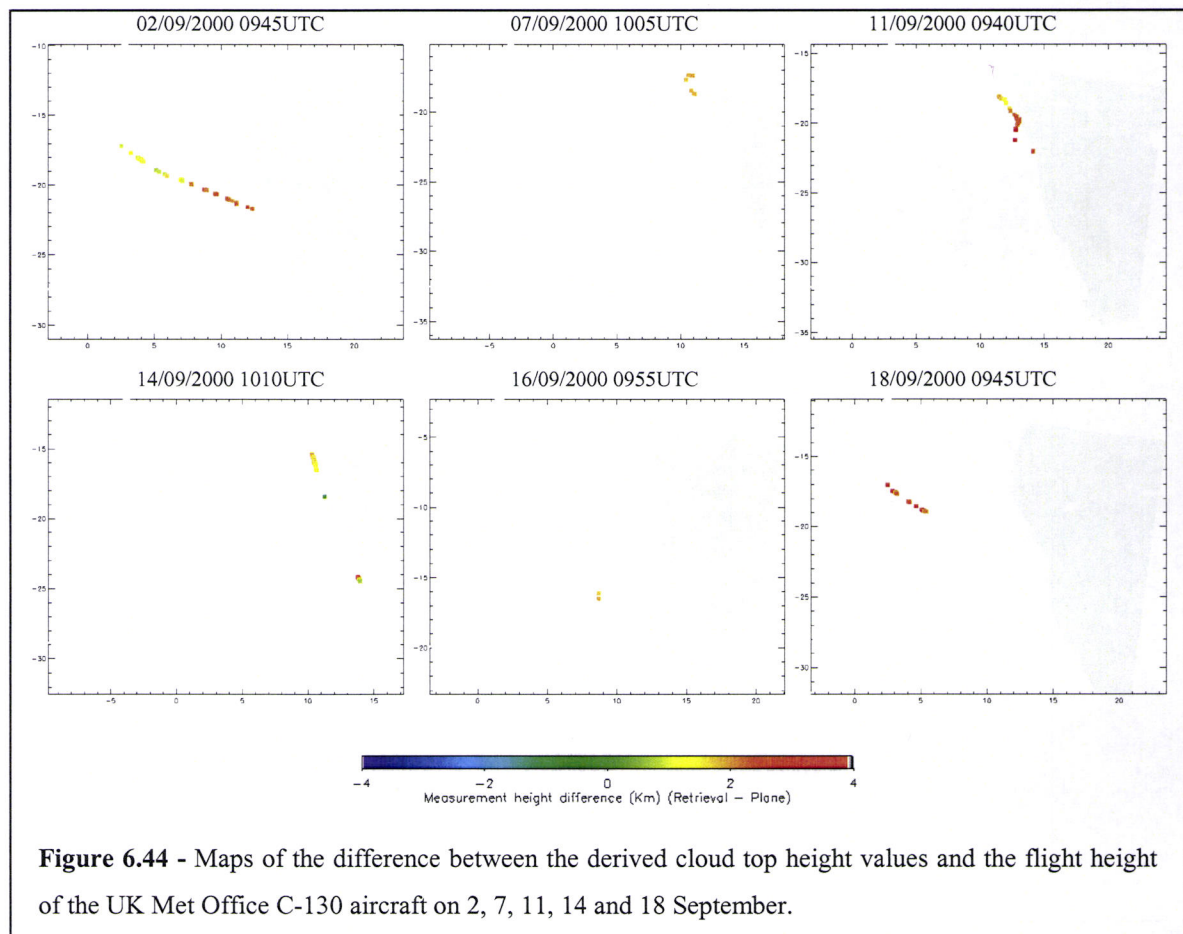


**Figure 6.43** – Maps of the difference between the derived liquid water content values and the corresponding measurements made by the UK Met Office C-130 aircraft on 2, 7, 11, 14 and 18 September.



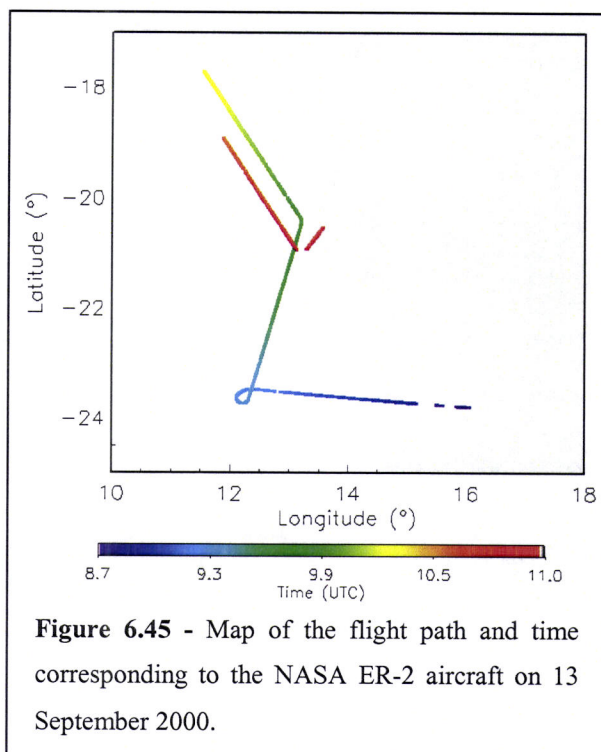
Figure 6.43 shows the differences between the derived liquid water content ( $w$ ) and the corresponding UK Met Office C-130 aircraft measurements. In general, the retrieved values are higher than those measured, which may be connected to the fact that the two sets of values are taken at different heights (see Figure 6.44). On 18 September, aircraft measurements and results from the present methodology come closer, which may also be connected with the fact that clouds were not exposed to interactions with biomass burning aerosol on this day. This may hint at a better performance of the methodology for “clean” clouds, since at the present stage of development the methodology does not take into account a separate atmospheric aerosol layer.

Figure 6.44 shows the differences between the derived cloud top height and the height at which the measurements were taken. Note that the retrieved cloud top height is always higher than the aircraft cruising height, which means that the aircraft probably flew inside the clouds measuring the cloud properties ( $r_{eff}$  and  $w$ ) at these levels. On the contrary, the satellite retrievals respect the uppermost layers of the clouds and this



probably explains the higher  $r_{eff}$  and  $w$  values derived with respect to the ones measured onboard the aircraft.

For 13 September one more comparison was done between the satellite retrieved cloud top height ( $Z^c$ ) and the one measured by the Cloud Physics Lidar (CPL) onboard the NASA ER-2 aircraft. Figure 6.45 shows the flight path and time on 13 September 2000. The CPL data are always attributed to the retrieved  $Z^c$  of the nearest MODIS pixel. Due to the availability of only one MODIS granule data per day for this case



**Figure 6.45** - Map of the flight path and time corresponding to the NASA ER-2 aircraft on 13 September 2000.

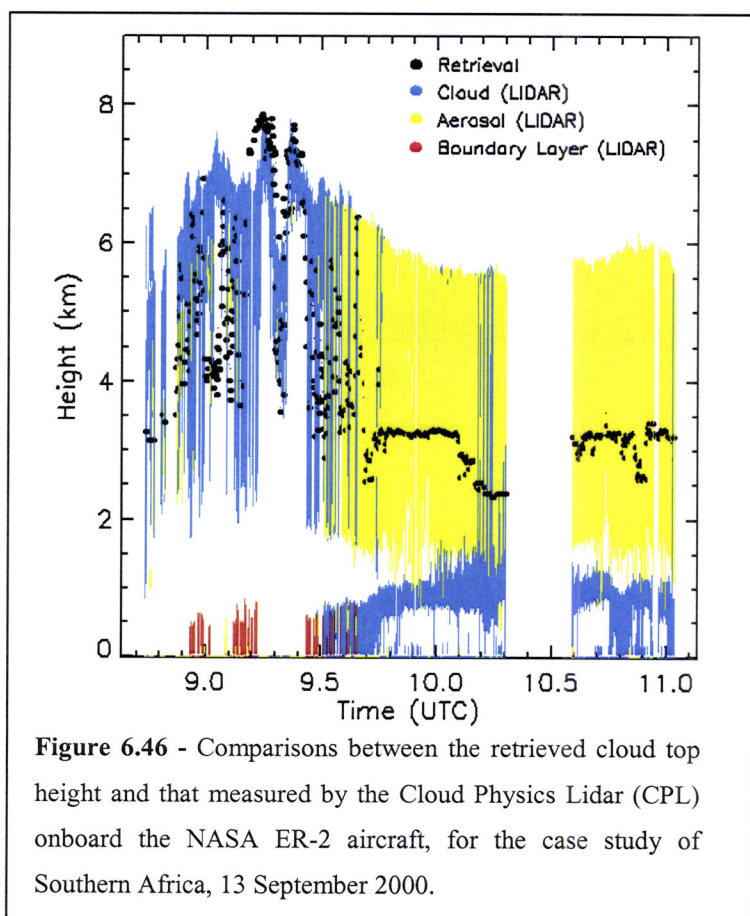


**Figure 6.46** - Comparisons between the retrieved cloud top height and that measured by the Cloud Physics Lidar (CPL) onboard the NASA ER-2 aircraft, for the case study of Southern Africa, 13 September 2000.

study, the time coincidence between the aircraft measurements and the retrieval is not every time optimal, but always within the 2-3 hours time frame. Data from a GEO satellite sensor like SEVIRI with a frequency of 15 minutes would greatly improve the comparisons and this is a goal for the future. In Figure 6.46 the vertical lines identify the bottom and top heights of the various layers retrieved by the CPL as a function of flight time. The cloud top height retrieved from the present

algorithm is also plotted. Note that a large portion of the flight was characterized by the

presence of a thick aerosol layer located above the cloud top. The agreement between the CPL and MODIS cloud top height is good enough when the aerosol layer is absent, whereas there is a clear overestimation of the cloud top height computed by the retrieval algorithm in the other case. The same trend was already observed in the comparisons with measurements from the Met Office C-130 aircraft (Figure 6.42). Again, this confirms that the presence of an absorbing aerosol layer above the cloud damages the quality of the cloud top parameter retrieval from satellite sensors with the present methodology, as already anticipated from the previous comparisons. The incorporation of the aerosol layer in this methodology is still being investigated.

The relative difference ( $Difr$ ) between the independent results obtained from MODIS cloud product used in the comparisons and the results from the present methodology, was defined by equation 5.7. The relative difference was computed for the droplet effective radius ( $r_{eff}$ ), cloud optical thickness ( $\tau^c$ ), and cloud top temperature ( $T^c$ ) and results are illustrated in Figure 6.47, for the African biomass burning case study (a) and for the Portuguese forest fire case study (b). Note that in the first case study (Figure 6.47a) the three analysed quantities present relative differences much lower than the imposed limit of  $\pm 25\%$  (see Section 5.3.2.2). Especially the cloud top temperature can be distinguished for the excellent agreement between the MODIS product and the retrieved values, with relative differences close to zero. As for the second case study (Figure 6.47b), the cloud top temperature still present very low relative differences. The cloud optical thickness and effective radius relative differences seem now characterized by different trends indicating that the retrieved  $\tau^c$  is larger than the one from the MODIS cloud product and on the contrary, that the retrieved  $r_{eff}$  is lower than the corresponding MODIS cloud product. Nevertheless, the relative difference values are still confined between the  $\pm 25\%$  limits.

The results shown in Figure 6.47 allow for considering that the present methodology is a valid one, since the relative differences computed to compare the retrievals with a state-of-the-art algorithm (MODIS cloud product) revealed to be within the error reported for the MODIS cloud product (King et al. 1998).

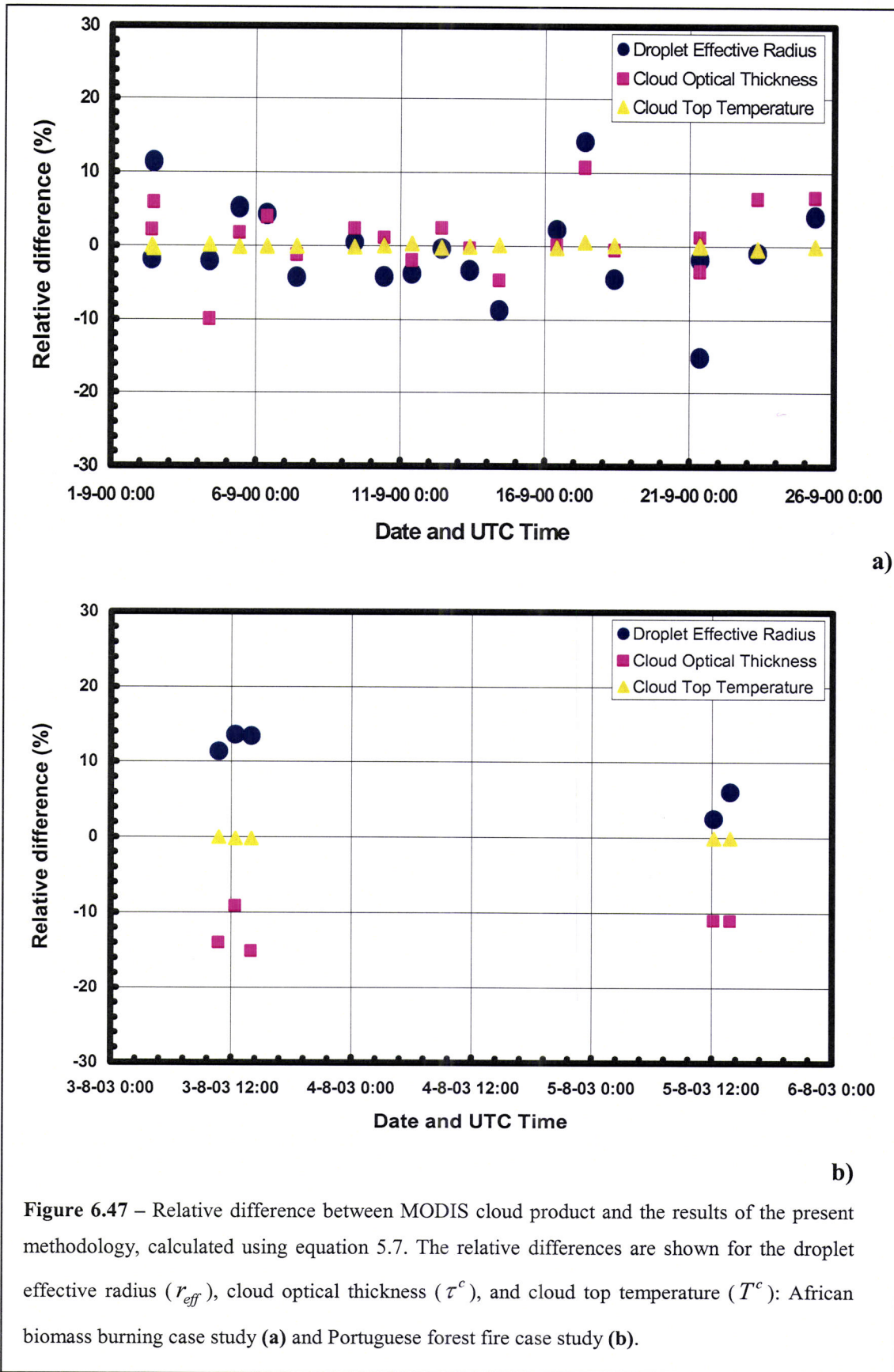


**Figure 6.47** – Relative difference between MODIS cloud product and the results of the present methodology, calculated using equation 5.7. The relative differences are shown for the droplet effective radius ( $r_{eff}$ ), cloud optical thickness ( $\tau^c$ ), and cloud top temperature ( $T^c$ ): African biomass burning case study (a) and Portuguese forest fire case study (b).

## Chapter 7

### Conclusions and final remarks

The aim of this thesis was to determine how satellite remote sensing can provide information on aerosol properties, particularly during strong aerosol events over the ocean, combining data from sensors onboard satellites with different orbits (LEO and GEO) having different spectral, spatial and temporal resolutions. The ultimate purpose was the estimation of the direct aerosol radiative forcing, which remains highly uncertain depending on the aerosol type (IPCC 2001). This investigation was focused on the study of aerosol events, characterized by “heavy” particle loads in the atmosphere in specific dates and geographical locations, which may alter the atmospheric composition and enter delicate mechanisms such as the water cycle (Haywood and Boucher 2000; Ramanathan et al. 2001; Kaufman et al. 2002; see also Chapter 1). Due to the close link between aerosols and clouds, the research further aimed to retrieve cloud properties and information on the possible modification of cloud properties through the interaction with atmospheric aerosol particles, as this may lead to important changes of the Earth’s climate (Twomey 1974; Albrecht 1989; Bréon et al. 2002; Kawamoto and Nakajima 2003; see also Chapter 1).

#### 7.1 First objective

The first goal was achieved by developing a method based on the synergistic use of LEO and GEO satellite measurements for aerosol type characterization, aerosol optical thickness retrieval, and TOA direct SW aerosol radiative forcing assessment over the ocean. The method is a tool for monitoring aerosol events at the GEO time and space scales, while maintaining the accuracy achieved with LEO instruments.

Aerosol optical properties were derived from GOME high spectral resolution measurements and used to estimate the aerosol optical thickness and the direct SW aerosol radiative forcing from GEO VIS measurements (Meteosat and GMS) over selected areas and during significant aerosol transport episodes. It is demonstrated that the proposed

method is a valid tool for aerosol characterization and optical thickness monitoring over the ocean, especially for strong aerosol events, provided that a GEO satellite covers the area of interest. This potential is illustrated using data from the Meteosat operational service (positioned at  $0^\circ$ ,  $0^\circ$ ), from the Indian Ocean Meteosat 5 coverage service (positioned at  $0^\circ$ ,  $63^\circ\text{E}$ ), and from the Japanese GMS-5 (positioned at  $0^\circ$ ,  $140^\circ\text{E}$ ).

The sensitivity analysis performed investigating the possible impact of the instrumental errors as well as of some of the physical assumptions of the method reveals that the radiative quantities are mostly influenced by the assumed aerosol characterization (aerosol model). It is therefore crucial that the aerosol properties introduced in the method reflect as much as possible the real atmospheric aerosol properties. This is the main advantage of the present method when compared to others that make use of literature aerosol models not necessarily adherent to the observed conditions, particularly during strong aerosol events. In addition, the algorithm was tested using synthetic data and its good performance demonstrated, even when the values used to compute the simulated measurements were not included in the LUTs and when the effects of GOME pixel dimension and instrumental errors were taken into account (Section 6.2.1).

The aerosol layer height and the non-sphericity of aerosol particles such as desert dust are not presently considered by the methodology, although they may introduce important errors in the retrievals. Further work is planned to include these issues on the retrievals.

Differences arising from considering the ocean BRDF with respect to the reference values (lambertian ocean surface) are mostly important for background and clean aerosol situations, where the aerosol load is negligible as well as the atmospheric radiance when compared with the surface signal. For higher aerosol loads, a lambertian ocean was found to be a reasonable approximation to the real ocean surface. Nevertheless, there is ongoing work to introduce a more accurate surface characterization on the methodology. Note that the sensitivity analysis reports differences corresponding to limit situations and the actual results are often confined in the lowest difference value range. As regards to the different vertical atmospheric profiles of water vapour and ozone that were considered, a relatively small impact on the retrievals is found. The use of latitudinal- and seasonal- dependent atmospheric profiles, if co-located data are not available, can be adopted as a reasonable approximation.

Comparisons of model derived aerosol properties, such as single scattering albedo, phase function (two key aerosol quantities for the estimation of the direct aerosol radiative forcing), and Ångström exponent with independent retrievals from several AERONET sites show that the agreement is generally quite good. The single scattering albedo values from AERONET are in fact always within the error bars associated to GOME retrievals, resulting in differences always lower than 0.04. In addition, the spectral behaviour of the single scattering albedo is well reproduced by GOME retrievals for all case studies.

The comparison of the aerosol optical thickness retrieved from Meteosat-5, 6, and 7 and GMS-5 with independent measurements from AERONET and a field campaign show a good agreement as well when GOME derived aerosol properties representative of the actual aerosol population are used. A first estimate of the derived AOT accuracy ( $\Delta\tau^a$ ) for all values leads to  $\Delta\tau^a = \pm 0.02 \pm 0.22\tau^a$  and to  $\Delta\tau^a = \pm 0.02 \pm 0.16\tau^a$  for aerosol events when  $\tau_{\lambda=0.55\mu\text{m}}^{\text{aerosol}} > 0.4$ . A reasonable agreement is also found from comparisons with the AOT products obtained from POLDER and MODIS data. Comparisons with POLDER show that 34% of the AOT values agree with POLDER within a  $\pm 15\%$  limit, whereas with MODIS the agreement increases up to 55%. When only  $\tau_{\lambda=0.55\mu\text{m}}^{\text{aerosol}} > 0.4$  are considered the agreement is even better, with 55% of the values within the  $\pm 15\%$  limit for POLDER, and 70% of the values within the same limit for MODIS. Results demonstrate that the choice of the aerosol model is crucial for accurate retrievals and consequently the atmospheric characterization should as much as possible be representative of the actual situation. This implies that the atmospheric characterization should be regularly updated while conducting long time retrievals. On the other hand, the great potential of the method for the study of strong aerosol transport events is also demonstrated.

The TOA SW fluxes retrieved from GEO data and the CERES product compare well, with more than 90% of the values differing from CERES fluxes for less than  $\pm 15\%$ . The direct short wave aerosol radiative forcing (DSWARF) estimates for the four aerosol events show that the effect at the TOA is higher for the Saharan dust in June 1997. As expected, the stronger absorption of aerosol particles in the Asian and Arabian regions, and over south Atlantic results in a lower negative TOA DSWARF probably increasing the radiative forcing at the surface. In addition, the daily means of the TOA DSWARF per unit optical thickness were estimated for the four aerosol events leading to:  $-19 \text{ W m}^{-2}$  for the

Saharan dust event (in agreement with Liu et al. 2003 whose value was  $-20.7 \text{ W m}^{-2}$ ),  $-15 \text{ W m}^{-2}$  for the Asian dust,  $-16 \text{ W m}^{-2}$  for the Arabian dust event, as well as  $-16 \text{ W m}^{-2}$  for the biomass burning episode.

As for the surface DSWARF, for an AOT of 1.0 the computed daily mean surface DSWARF is found to be  $-57 \text{ W m}^{-2}$  due to Saharan dust aerosols. However, both in the Arabian dust and biomass burning events higher (more negative) daily mean surface DSWARF values are observed being therefore the cooling more pronounced than in the Saharan case. The Arabian dust event is associated to a daily mean surface DSWARF of  $-65 \text{ W m}^{-2}$  for an AOT = 1.0 and the biomass burning case shows a value of  $-64 \text{ W m}^{-2}$  for the same AOT. The result obtained in the area around Anmyon-Do (Asian dust) of the forcing per unit optical thickness is  $-117 \text{ W m}^{-2}$ , whereas the value obtained from ground-based measurements is  $-113.3 \text{ W m}^{-2}$ . The more pronounced DSWARF is the one obtained in the area of Anmyon-do for the Asian dust event. The DSWARF of the atmosphere showed that the lowest atmosphere DSWARF values are observed for the Saharan dust case, whereas the highest were obtained for the Asian dust, translating in a greater warming of the atmosphere. The DSWARF of the atmosphere per unit optical thickness obtained for the area considered around Anmyon-Do is of  $101.6 \text{ W m}^{-2}$ , where the ground measurements indicate a value of  $99.8 \text{ W m}^{-2}$ .

## 7.2 Second objective

The second goal of this research work was achieved, developing a methodology to retrieve the cloud properties, specifically cloud optical thickness, droplet effective radius (near cloud top) and cloud top temperature. A fundamental part of the method relies on a well-known algorithm (Nakajima and Nakajima 1995; Kawamoto et al. 2001). The methodology was adapted to the retrieval of cloud properties from MODIS data and to the near future application to MSG-SEVIRI measurements. Foreseen future applications could be the monitoring (GEO temporal and spatial scales) of cloud top microphysical / optical properties. The modification of cloud properties through the interaction with aerosols was also partially achieved.



The case studies revealed in some conditions a substantial decrease of the droplet effective radius when aerosol particles were present over the same area. However, it is not totally clear from the present results whether this effect is due to cloud-aerosol interactions or to the existence of an atmospheric aerosol layer separated from the cloud layer. This latter case can induce considerable errors while performing the satellite retrievals if not adequately modelled. Vertical profiling of the atmosphere can be very useful in these studies.

The results obtained from the present methodology were compared against retrievals of the official MODIS cloud products (King et al. 1998) and datasets of effective radius, liquid water content and cloud top height from aircraft measurements taken during the SAFARI 2000 campaign, in order to evaluate the performances of the present methodology and the possible effects of the aerosol-cloud interactions. The comparisons have pointed out a good agreement with MODIS cloud parameters. The relative difference between the independent results obtained from the MODIS cloud product used in the comparisons and the results obtained from the present methodology, was computed for the droplet effective radius, cloud optical thickness, and cloud top temperature, for both case studies (African biomass burning and Portuguese forest fires). The results demonstrated the validity of the methodology, since the relative differences computed to compare the retrievals with a state-of-the-art algorithm (MODIS cloud product) revealed to be within the  $\pm 25\%$  error reported for the MODIS cloud product (King et al. 1998). However, the interpretation of the comparisons with the SAFARI 2000 data is more complicated. It will be necessary to undertake an investigation of other case studies similar to those examined in this work together with a sensitivity analysis of the variations of the microphysical cloud properties in presence of biomass burning aerosol layers. These are necessary steps towards a better understanding of the aerosol-cloud interactions. Moreover, similar studies using MSG-SEVIRI data are planned, taking advantage of the high image frequency and considering the atmospheric aerosol layer.

## 7.3 Future work

As the research progressed, several points that worth further investigation emerged:

- **Improvement of the aerosol methodology:**
  - Use of more accurate sea surface reflectance characterization. The sensitivity analysis showed that an accurate surface characterization is more important for clean and background aerosol situations than for aerosol events (Section 6.2.1). A more exact surface characterization will contribute to improve the performance of the method for low atmospheric aerosol loads.
  - Use of atmospheric vertical profiles from radio soundings or from other sources when available. The sensitivity analysis showed that the atmospheric vertical profiles are more important for flux calculations (Section 6.2.1). Consequently, an improvement of the profile quality would improve the accuracy of the radiative forcing estimates.
  - Use of data from newer sensors with respect to GOME, such as the three nadir viewing spectrometers onboard ENVISAT-1 (AATSR, MERIS and SCIAMACHY; see Section 3.3.2.3). The synergistic use of the three sensors will enlarge the present spectral coverage and provide a better spatial resolution with respect to GOME's, contributing to improve the detection and characterization of atmospheric aerosols (Torricella et al. 2001; Costa et al. 2000b). The introduction of such combined measurements in the present algorithm will certainly have positive effects in reducing uncertainties in the inversion method, since the additional spectral information is important for aerosol absorption and size distribution characterization; this information is also very useful for simultaneous cloud detection. The improvement in spatial resolution in turns will increase the number of selectable cloud free homogeneous pixels, thus improving the confidence on the retrieved mean aerosol model.
  - Extension of the methodology to regions over land. The main problem is the accurate characterization of the land surface spectral reflectance, which may

be extremely variable. The synergistic use of data from different satellite sensors still to be defined, for example with additional angular measuring capabilities, may represent a possibility for aerosol studies over land surfaces.

- Take into account the role of the atmospheric layer height, which is an important factor affecting the radiative quantities for wavelengths below 0.4  $\mu\text{m}$ , especially for absorbing aerosols such as desert dust or biomass burning types (Torres et al. 1998).
  - Take into account the non-sphericity of aerosol particles. The aerosol particle shape may be an issue, especially for desert dust (Dubovik et al. 2002a) and for marine aerosol in low humidity atmospheric conditions (Silva et al. 2002). Future developments of the methodology will have to address the particle shape problem, making use of additional satellite data still to be defined, and complementary ground-based measurements when necessary.
  - Use of data from the GOME-2 instrument, which will fly on the first European Meteorological Operational polar satellite (METOP), planned to be ready for launch by mid 2005. This instrument maintains GOME's spectral characteristics, but greatly increases the spatial resolution to  $40 \times 40 \text{ km}^2$ , which would surely increase the number of selectable cloud free homogeneous pixels and improving the confidence on the retrieved mean aerosol model.
- **Improvement of the cloud methodology:**
    - Study the possibility of including an aerosol layer that can be of different types (dust, biomass burning, industrial and urban polluted, etc), at different levels with respect to the cloud. The comparisons with measurements taken during the SAFARI 2000 campaign showed that satellite results may be affected by the existence of such a separated aerosol level if not taken into account (Section 6.3.2).
    - Use of atmospheric vertical profiles from radio soundings when available or from other sources. The accuracy of the atmospheric vertical profile is

extremely important, since cloud properties such as the cloud top height, pressure, and type directly depend on them.

- Use of MSG-1 SEVIRI measurements in order to retrieve the same information derived here from MODIS data, however with a repeat cycle of 15 minutes. These improved observational capabilities are ideal to enhance the understanding of cloud microphysics through cloud top retrievals of hydrometeor radiative properties, opening unprecedented scenarios to analyse the temporal evolution of cloud systems, and eventually the interaction with aerosols. Such a study is in addition very useful to support satellite rainfall studies (Rosenfeld and Gutman 1994; Rosenfeld 2004; Cattani et al. 2004).
- Estimate cloud radiative forcing, especially in situation when there are interaction between clouds and aerosol particles of different types. Since the present knowledge of the radiative forcing due to this effect is considered very low according to the IPCC (2001).

---

## References

- Ackerman, A. S., O. B. Toom, D. E. Stevens, A. J. Heymsfield, V. Ramanathan, and E. J. Welton, 2000: Reduction of tropical cloudiness by soot. *Science*, **288**, 1042-1047.
- Alados, I., F. J. Olmo, I. Foyo-Moreno, and L. Alados-Arboledas, 2000: Estimation of photosynthetically active radiation under cloudy conditions. *Agricultural and Forest Meteor.*, **102**, 39-50.
- Albrecht, A. A., 1989: Aerosols, cloud microphysics, and fractional cloudiness. *Science*, **245**, 1227-1230.
- Arking, A., and J. D. Childs, 1985: Retrieval of cloud cover parameters from multispectral satellite images. *J. Climate Appl. Meteor.*, **24**, 322-333.
- Barbosa, P., G. Libertà, and G. Schmuck, 2003: The European Forest Fires Information System (EFFIS) results on the 2003 fire season in Portugal by the 20th of August. European Commission, Directorate General Joint Research Centre, Institute For Environment And Sustainability, Land Management Unit.
- Barnes, W. L., T. S. Pagano, and V. V. Salomonson, 1998: Prelaunch characteristics of the MODerate Resolution Imaging Spectroradiometer (MODIS) on EOS-AM1. *IEEE Trans. Geosci. Remote Sens.*, **36**, 1088-1100.
- Bartoloni, A., P. Colandrea, R. Loizzo, M. Mochi, F. Pascuali, N. Santantonio, E. Zappitelli, and M. Cervino, 2000: SYSGOME: Processing chain for aerosol optical thickness product generation at I-PAF. *Proc 2000 EUMETSAT Meteorological Satellite Data Users' Conf.*, Bologna, Italy, 29 May -2 June, 460-467.
- Bergman, J. W., and H. H. Hendon, 2000: Cloud radiative forcing of the low-latitude tropospheric circulation: linear calculations. *J. Atmos. Sci.*, **57**, 2225-2245.
- Bortoli, D., M. J. Costa, and M. Nardino, 2002: Influence of clouds on the surface radiative balance for two Mediterranean sites. *CD-ROM Proc. 27th General Assembly of the European Geophysical Society*, 21-26 April, Nice, France.
- Bovensmann, H., J. P. Burrows, M. Buchwitz, J. Frerick, S. Noël, V. V. Rozanov, K. V. Chance, and A. P. H. Goede, 1999: SCIAMACHY: Mission objectives and measurement modes. *J. Atmos. Sci.* **56**, pp. 127-150.
- Bréon, F.-M., D. Tanré, and S. Generoso, 2002: Aerosol effect on cloud droplet size monitored from satellite. *Science*, **295**, pp 834-838.

- Burrows, J. P., M. Weber, M. Buchwitz, V. Rozanov, A. Ladstätter-Weißmeyer, A. Richter, R. DeBeek, R. Hoogen, K. Bramstedt, K.-U. Eichmann, and M. Eisinger, 1999: The Global Ozone Monitoring Experiment (GOME): Mission concept and first scientific results. *J. Atmos. Sci.*, **56**, 151-175.
- Cattani, E., S. Melani, V. Levizzani, and M. J. Costa, 2004: Cloud studies in support of satellite rainfall measurements: The retrieval of cloud top properties using VIS-IR channels. In: *Measuring precipitation from space: EURAINSAT and the future*, V. Levizzani, P. Bauer, and F. J. Turk Eds., Kluwer Acad. Publ., Dordrecht (The Netherlands), submitted.
- Cervino, M, V. Levizzani, C. Serafini, A. Bartoloni, M. Mochi, P. Colandrea, and B. Greco, 2000: Cloud fraction within GOME footprint using a refined cloud clearing algorithm. *Adv. Space Res.*, **25**, 993-996.
- Cess, R., G. L. Potter, J. P. Blanchet, G. J. Boer, S. J. Ghan, J. T. Kiehl, H. Le Treut, Z. X. Li, X. Z. Liang, J. F. B. Mitchell, J. J. Morcrette, D. A. Randall, M. R. Riches, E. Roeckner, U. Schlese, A. Slingo, K. E. Taylor, W. M. Washington, R. T. Wetherald, and I. Yagai, 1989: Interpretation of cloud-climate feed-back as produced by 14 atmospheric general circulation models. *Science*, **245**, 513-516.
- Chandrasekhar, S., 1960: *Radiative transfer*. Dover Publications, New York, 393 pp.
- Chen, T., W. B. Rossow, and Y. Zhang, 2000: Radiative effects of cloud-type variations. *J. Climate*, **13**, 264-286.
- Chou, M.-D., P.-K. Chan, and M. Wang, 2002: Aerosol radiative Forcing Derived from SeaWiFS-retrieved aerosol optical properties. *J. Atmos. Sci.*, **59**, 748-757.
- Christopher, A. S., and J. Zhang, 2002: Daytime variation of shortwave direct radiative forcing of biomass burning aerosols from GOES-8 imager. *J. Atmos. Sci.*, **59**, 681-691.
- Costa, M. J., M. Cervino, E. Cattani, F. Torricella, V. Levizzani, and A. M. Silva, 1999: Aerosol optical thickness and classification: use of METEOSAT, GOME, and modelled data. Proc. SPIE, *Satellite Remote Sensing of Clouds and the Atmosphere IV*, J. E. Russell Ed., **3867**, 268-279.
- Costa, M. J, M. Cervino, E. Cattani, F. Torricella, V. Levizzani, and A. M. Silva, 2000a: An update of a GOME-METEOSAT method for aerosol optical thickness determination and classification. *Proc 2000 EUMETSAT Meteorological Satellite Data Users' Conf.*, Bologna, Italy, 29 May -2 June, 420-427.

- 
- Costa, M. J., M. Cervino, E. Cattani, F. Torricella, V. Levizzani, and A. M. Silva, 2000b: Tropospheric aerosol characterisation: from GOME towards an ENVISAT perspective. *Proc. CD-ROM ERS-ENVISAT Symp.*, ESA, Göteborg, Sweden, 16-20 Oct.
- Costa, M. J., M. Cervino, E. Cattani, F. Torricella, V. Levizzani, and A. M. Silva, 2001: Lessons learnt from synergistic use of polar and geostationary satellite sensors for the retrieval of aerosol characteristics. *Proc. SPIE, Optical Spectroscopic Techniques, Remote Sensing, and Instrumentation for Atmospheric and Space Research IV*, Allen M. Larar, Martin G. Mlynczac Ed., **4485**, 17-27.
- Costa, M. J., B. J. Sohn, V. Levizzani, and A. M. Silva, 2002: Aerosol characterisation from polar and geostationary satellite data: a case study over the yellow sea (South Korea). *Proc. 2002 EUMETSAT Meteorological Satellite Data Users' Conf.*, Dublin, Ireland, 2-6 Sept., 682-689.
- Costa, M. J., M. Cervino, E. Cattani, F. Torricella, V. Levizzani, A. M. Silva, and S. Melani, 2002: Aerosol characterization and optical thickness retrievals using GOME and METEOSAT satellite data. *Meteorol. Atmos. Phys.*, **81**, 289-298.
- Costa, M. J., E. Cattani, F. Torricella, A. M. Silva, and V. Levizzani, 2003: Cloud microphysical properties retrieval in the presence of strong aerosol events. *Proc. 2003 EUMETSAT Meteorological Satellite Data Users Conf.*, Weimar, Germany, 29 Sept.-3 Oct., 671-677.
- Costa, M. J., A. M. Silva, and V. Levizzani, 2004a: Aerosol characterization and direct radiative forcing assessment over the ocean. Part I: Methodology and sensitivity analysis. *J. Appl. Meteor.*, in press.
- Costa, M. J., V. Levizzani, and A. M. Silva, 2004b: Aerosol characterization and direct radiative forcing assessment over the ocean. Part II: Application to test cases and validation. *J. Appl. Meteor.*, in press.
- Costa, M. J., E. Cattani, V. Levizzani, and A. M. Silva, 2004c: Cloud microphysical properties retrieval during intense biomass burning events over Africa and Portugal. In: *Measuring precipitation from space: EURAINSAT and the future*, V. Levizzani, P. Bauer, and F. J. Turk Eds., Kluwer Acad. Publ., Dordrecht (The Netherlands), in press.
- Curran, R. J., and M. L. C. Wu, 1982: Skylab near-infrared observations of clouds indicated supercooled liquid water droplets. *J. Atmos. Sci.*, **39**, 635-647.
-

- D'Almeida, G. A., P. Koepke, and E. P. Shettle, 1991: *Atmospheric aerosols. Global climatology and radiative characteristics*. A. Deepak Publishing.
- Deirmendjian, D., 1964: Scattering and Polarization properties of water clouds and hazes in the visible and infrared. *Appl. Opt.*, **3**, 187-196.
- DeMott, P. J., K. Sassen, M. Poellot, D. Baumgardner, D. C. Rogers, S. Brooks, A. J. Prenni, and S. M. Kreidenweis, 2003: African dust aerosols as atmospheric ice nuclei. *Geophys. Res. Lett.*, **30**, No. 14, 1732, doi:10.1029/2003GL017410.
- Deschamps, P. Y., F. M. Breon, M. Leroy, A. Podaire, A. Bricaud, J. C. Buriez, and G. Seze, 1994: The POLDER mission: Instrument characteristics and scientific objectives. *IEEE Trans. Geosci. Remote Sensing*, **32**, 598-615.
- Deuzé, J.-L., P. Goloub, M. Herman, A. Marchand, G. Perry, S. Susana, and D. Tanré, 2000: Estimate of the aerosol properties over the ocean with POLDER. *J. Geophys. Res.*, **105**, 15329-15346.
- Draxler, R. R., and G. D. Rolph, (2003): HYSPLIT (HYbrid Single-Particle Lagrangian Integrated Trajectory) Model access via NOAA ARL READY Website (<http://www.arl.noaa.gov/ready/hysplit4.html>). NOAA Air Resources Laboratory, Silver Spring, MD.
- Dubovik, O., A. Smirnov, B. Holben, M. King, Y. Kaufman, T. Eck, and I. Slutsker, 2000: Accuracy assessments of aerosol optical properties retrieved from Aerosol Robotic Network (AERONET) Sun and sky radiance measurements. *J. Geophys. Res.*, **105**, 9791-9806.
- Dubovik, O., and M. King, 2000: A flexible inversion algorithm for retrieval of aerosol optical properties from sun and sky radiance measurements. *J. Geophys. Res.*, **105**, 20673-20696.
- Dubovik, O., B. N. Holben, T. F. Eck, A. Smirnov, Y. J. Kaufman, M. D. King, D. Tanré, and I. Slutsker, 2002a: Variability of absorption and optical properties of key aerosol types observed in worldwide locations. *J. Atmos. Sci.*, **59**, 590-608.
- Dubovik, O., B. N. Holben, T. Lapyonok, A. Sinyuk, M. I. Mishchenko, P. Yang, and I. Slutsker, 2002b: Non-spherical aerosol retrieval method employing light scattering by spheroids. *Geophys. Res. Lett.*, **29**, 1415, doi:10.1029/2001GL014506.



- Dulac, F, D. Tanré, G. Bergametti, P. Buat-Ménard, M. Desbois, and D. Sutton, 1992: Assessment of African airborne dust mass over the western Mediterranean Sea using Meteosat data. *J. Geophys. Res.*, **97**, 2489-2506.
- EUMETSAT, 2000: The Meteosat system. EUM TD 05, 66 pp.
- EUMETSAT, 2001: Meteosat Second Generation - MSG System Overview. EUM TD 07, 44 pp.
- Goloub, P., D. Tanré, J.L. Deuzé, M. Herman, A. Marchand, and F-M. Bréon, 1999: Validation of the first algorithm for deriving the aerosol properties over the ocean using the POLDER/ADEOS measurements, *IEEE Trans. Geosci. Remote Sensing*, **37**, 1586-1596.
- Goody, R.M., 1964: Atmospheric Radiation 1, Theoretical Basis, *Oxford University Press*, 436 pp.
- Goody, R., J. Anderson, T. Karl, R. B. Miller, G. North, J. Simpson, G. Stephens, and W. Washington, 2002: Why monitor the climate? *Bull. Am. Meteorol. Soc.*, **83**, 873-878.
- Govaerts Y 1999: Correction of the Meteosat-5 and -6 radiometer solar channel spectral response with the Meteosat-7 sensor spectral characteristics. *Int J Remote Sensing*, **20**, 3677-3682.
- Govaerts, Y., A. Arriaga, and J. Schmetz, 2001: Operational vicarious calibration of the MSG/SEVIRI solar channels, *Advances in Space Research*, **28**, 21-30.
- Griggs, M., 1979: Satellite observations of atmospheric aerosols during the EOMET cruise, *J. Atmos. Sci.*, **36**, 695-698.
- Hansen, J., and J.B. Pollack, 1970: Near-infrared light scattering by terrestrial clouds. *J. Atmos. Sci.*, **27**, 265-281.
- Haywood, J., and O. Boucher, 2000: estimates of the direct and indirect radiative forcing due to tropospheric aerosols; a review. *Rev. Geophys.*, **38**, 513-543.
- Holben B.N., T.F.Eck, I.Slutsker, D.Tanre, J.P.Buis, A.Setzer, E.Vermote, J.A.Reagan, Y.Kaufman, T.Nakajima, F.Lavenu, I.Jankowiak, and A.Smirnov, 1998: AERONET - A federated instrument network and data archive for aerosol characterization, *Rem. Sens. Environ.*, **66**, 1-16.
- Hsu, N. C., J. R. Herman, J. F. Gleason, O. Torres, and C. J. Seftor, 1999: Satellite detection of smoke aerosols over a snow/ice surface by TOMS, *Geophys. Res. Lett.*, **26**, 1165-1168.

- IPCC, 2001: Climate Change 2001: The Scientific Basis. Contribution of Working Group I to the Third Assessment Report of the Intergovernmental Panel on Climate Change, J. T. Houghton, Y. Ding, D. J. Griggs, M. Noguer, P. J. v. d. Linden, X. Dai, K. Maskell, and C. A. Johnson, Eds., Cambridge University Press, 881 pp.
- Junge, C.E., 1952: Gesetzmäßigkeiten in der Droßenverteilung atmosphärischer Aerosole über dem Kontinent. *Ber d. Deirsch Wetterdienst U.S.-Zone*, **35**, 261-277.
- Karyampudi VM, Palm SP, Reagen JA, Fang H, Grant WB, Hoff RF, Moulin C, Pierce HF, Torres O, Browell EW, Melfi SH, 1999: Validation of the Saharan Dust Plume Conceptual Model Using Lidar, Meteosat, and ECMWF Data. *Bull Am Meteor Soc*, **80**, 1045-1075.
- Kaufman Y, Tanré D, Gordon HR, Nakajima T, Lenoble J, Frouin R, Grassl H, Herman BM, King MD, Teillet PM, 1997: Passive remote sensing of tropospheric aerosol and atmospheric correction for the aerosol effect. *J Geophys Res*, **102**, 16815-16830.
- Kaufman, Y. J., D. Tanré and O. Boucher, 2002: A satellite view of aerosols in the climate system, *Nature*, **419**, 215-223.
- Kaufman, Y. J., J. M. Haywood, P. V. Hobbs, W. Hart, R. Kleidman, and B. Schmid, 2003: Remote sensing of vertical distributions of smoke aerosol off the coast of Africa, *Geophys. Res. Lett.*, **30**, 1831-1834.
- Kawamoto, K., T. Nakajima, and T. Y. Nakajima, 2001: A global determination of cloud microphysics with AVHRR remote sensing, *J. Climate*, **14**, 2054-2068.
- Kawamoto, K., and T. Nakajima, 2003: Seasonal variation of cloud particle size from AVHRR remote sensing. *Geophys. Res. Lett.*, **30**, 1810-1813.
- Keil, A., and J.M., Haywood, 2003: Solar radiative forcing by biomass burning aerosol particles during SAFARI 2000: A case study based on measured aerosol and cloud properties. *J. Geophys. Res.*, **108**, doi: 10.1029/2002JD002315.
- Kim, D, H, B. J. Sohn, T. Nakajima, I. Okada, and T. Takamura, 2002: Aerosol radiative forcing estimated from ground-based radiation measurements at GAME/AAN sites. Atmospheric Radiation Conference, American Meteorological Society, June 3-8, 2002, Ogden, Utah, Proceeding in press.
- Kim, D.-H., B.-J. Sohn, T. Nakajima, T. Takamura, T. Takamura, B.-C. Choi, and S.-C. Yoon 2004: Aerosol optical properties over east Asia determined from ground-based sky radiation measurements, *J. Geophys. Res.*, **109**, D02209, doi:10.1029/2003JD003387.

- King, M., Harshvardhan, and A. Arking, 1984: A model of the Radiative Properties of the El Chichon Stratospheric Aerosol Layer, *J. Climate and Appl. Meteor.*, **23**, 1121-1137.
- King, M. 1987: Determination of scaled optical thickness of clouds from reflected solar radiation measurements. *J. Atmos Sci.* **44**, 29-144.
- King, M., S.-C., Tsay, S. Platnick, M. Wang, and K.N., Liou, 1998: Cloud retrieval algorithms for MODIS: optical thickness, effective particle radius, and thermodynamic phase. ATBD Reference Number: ATBD-MOD-05.
- King, M., Y. Kaufman, D. Tanré, and T. Nakajima, 1999: Remote sensing of tropospheric aerosols from space: Past, present, and future, *Bull. Am. Meteorol. Soc.*, **80**, 2229-2259.
- Kneizys, F.X., E.P. Shettle, L.W. Abreu, J.H. Chetwynd, G.P. Anderson, W.O. Gallery, J.E. Selby, and S.A. Clough, 1988: User's Guide to LOWTRAN7 AFGL-TR-88-01 77, *Environmental Research Papers*, No. 1010, Air Force Geophysics Laboratory, Hanscom AFB, Bedford, MA, 137 pp.
- Kondratyev K. Ya 1969: Radiation in the atmosphere, *Academic Press*, N.Y., U.S.A.
- Lenoble, J., 1985: Radiative transfer in scattering and absorbing atmospheres: standard computational procedures, A. Deepak Publishing, USA, 300 pp.
- Lenoble, J., 1993: Atmospheric radiative transfer. A. Deepak Publishing, USA, 532 pp.
- Leroy, M., J. Deuzé, F. Bréon, O. Hautecoeur, M. Herman, J. Buriez, D. Tanré, S. Bouffières, P. Chazette and J.L. Roujean, 1997: Retrieval of atmospheric properties and surface bidirectional reflectances over land from POLDER/ADEOS, *J. Geophys. Res.*, **102**, 17,023-17,037.
- Levizzani, V., and M.Setvák, 1996: Multispectral, high-resolution satellite observations of plumes on top of convective storms. *J.Atmos.Sci.*, **53**, 361-369.
- Levizzani, V., 2000: I satelliti meteorologici tra passato e futuro. *Ricerca & Futuro*, **17**, 45-47.
- Levizzani,V., J.Schmetz, H.J.Lutz, J.Kerkmann, P.P.Alberoni, and M.Cervino, 2001: Precipitation estimations from geostationary orbit and prospects for METEOSAT Second Generation. *Meteor.Appl.*, **8**, 23-41.
- Levizzani, V., 2004a: Satellite observation of clouds. In: *McGraw-Hill Yearbook of Science and Technology*, McGraw-Hill, New York, 303-306.

- Levizzani, V., 2004b: Satellite sensing of water in the atmosphere. In: *Encyclopedia of Water Sciences*. Marcel Dekker, Inc., doi:10.1081/E-EWS120020401. (<http://www.dekker.com>).
- Levoni, C., E.Cattani, M.Cervino, R.Guzzi, W.Di Nicolantonio, F.Torricella, 2001: Effectiveness of the MS-method for computation of the intensity field reflected by a multi-layer plane-parallel atmosphere, *J. Quant. Spectrosc. Radiat. Transfer*, **69**, pp. 635-650.
- Liou, K. N., 1976: On the absorption, reflection and transmission of solar radiation in cloudy atmospheres, *J. Atmos. Sci.*, **33**, 798–805.
- Liou, K. N., 1980: An introduction to atmospheric radiation, Academic Press, USA, 392 pp.
- Liou, K. N., 1992: Radiation and cloud processes in the atmosphere, Oxford University Press, 487 pp.
- Liu, X., J. Wang, and S. A. Christopher, 2003: Shortwave direct radiative forcing of Saharan dust aerosols over the Atlantic Ocean. *Int. J. Rem. Sensing*, **24**, 5147-5160.
- Malkmus, W., 1967: Random Lorentz Band Model with Exponential- Tailed S-1 Line-intensity Distribution Function, *J. Opt. Soc. Am.* **57**, 323-329.
- Manual of Remote Sensing, 1983, Falls Church, Virginia, American Society of Photogrammetry.
- McClatchey, R.A., W. Fenn, J.E.A. Selby, F.E. Volz, and J.S. Garing, 1971: Optical properties of the Atmosphere, AFCRL-TR- 71-0279, *Enviro. Research papers*, No 354, Air Force Cambridge Research Laboratories, Hanscom AFB, Bedford, MA, 85 pp.
- McGill, M.J., Hlavka, D.L., Hart, W.D., Welton, E.J., and Campbell, J.R., (2003): Airborne lidar measurements of aerosol optical properties during SAFARI 2000, *J. Geophys. Res.*, doi: 10.1029/2002JD002370.
- Melani, S., E.Cattani, V.Levizzani, M.Cervino, F.Torricella, and M.J. Costa, 2003: Radiative effects of simulated cirrus clouds on top of a deep convective storm in METEOSAT Second Generation SEVIRI channels. *Meteor.Atmos.Phys.*, **83**, 109-122.
- Menzel, P., 2001: Applications with meteorological satellites. University of Wisconsin.
- Mishchenko, M., Geogdzhayev, I., Cairns, B., Rossow, W. and Lacis, A., 1999: Aerosol retrievals over the ocean by use of channels 1 and 2 AVHRR data: sensitivity analysis and preliminary results, *Appl. Opt.*, **38**, 7325-7341.

- 
- Morel, A., 1988: Optical modelling of the upper ocean in relation to its biogenous matter content (Case I Waters), *J. Geophys. Res.*, **93**, 10,479-10,768.
- Moulin C, F. Guillard, F. Dulac, C. E. Lambert, 1997a: Long-term daily monitoring of Saharan dust load over ocean using METEOSAT ISCCP-B2 data: 1. Methodology and preliminary results for 1983-1994 in the Mediterranean. *J Geophys Res*, **102**, 16947-16958.
- Moulin C, F. Dulac, C. E. Lambert, P. Chazette, I. Jankowiak, B. Chatenet, F. Lavenu, 1997b: Long-term daily monitoring of Saharan dust load over ocean using METEOSAT ISCCP-B2 data: 2. Accuracy of the method and validation using Sun photometer measurement. *J Geophys Res*, **102**, 16959-16969.
- Nakajima, T., and M. Tanaka, 1983: Effect of wind-generated waves on the transfer of solar radiation in the atmosphere-ocean system. *J. Quant. Spectrosc. Radiant. Transfer*, **29**, 521–537.
- Nakajima, T., and M. Tanaka, 1986: Matrix formulation for the transfer of solar radiation in a plane-parallel scattering atmosphere, *J. Quant. Spectrosc. Radiat. Transfer*, **35**, 13-21.
- Nakajima, T., and M. Tanaka, 1988: Algorithms for radiative intensity calculations in moderately thick atmospheres using a truncation approximation, *J. Quant. Spectrosc. Radiat. Transfer*, **40**, 51-69.
- Nakajima, T., and M. D. King, 1990: Determination of the optical thickness and effective particle radius of clouds from reflected solar radiation measurements. Part I: Theory. *J. Atmos. Sci.*, **47**, 1878–1893.
- Nakajima, T. Y., and T. Nakajima, 1995: Wide-area determination of cloud microphysical properties from NOAA AVHRR measurements for FIRE and ASTEX regions. *J. Atmos. Sci.*, **52**, 4043-4059.
- Nakajima, T., M. Sekiguchi, T. Takemura, I. Uno, A. Higurashi, D. Kim, B. J. Sohn, S.-N. Oh, T. Y. Nakajima, S. Ohta, I. Okada, T. Takamura, and K. Kawamoto, 2003: Significance of direct and indirect radiative forcings of aerosols in the East China Sea region, *J. Geophys. Res.*, **108**, 8658, doi:10.1029/2002JD003261.
- NASA GISS National Aeronautics and Space Administration – Goddard Institute for Space Studies, 1997: How can we use satellite data, global models and analysis to

- advance our understanding of aerosol (direct and indirect) climate effects?, *Aerosol Workshop Proc.*, New York, 2-3 June.
- Neckel, H. and D. Labs, 1984: The solar radiation between 3300 and 12500 *Solar Physics*, **90**, 205-258.
- Nishihama M., R. Wolfe, D. Solomon, F. Patt, J. Blanchette, A. Fleig, E. Masuoka (1997): MODIS Level 1A Earth Location: Algorithm Theoretical Basis Document Version 3.0. SDST-092.
- Paltridge, G.W., and C.M.R. Platt, 1976: Radiative Processes in Meteorology and Climatology, *Development in Atmospheric Science*, **5**, Elsevier Scientific Publishing Company, 300-314.
- Porcù F, Levizzani V 1992: Cloud classification using METEOSAT VIS-IR imagery. *Int J Remote Sensing*, **13**, 893-909.
- Press, W. H., S. A. Teukolsky, W. T. Vetterling, and B. P. Flannery, 1997: Numerical Recipes in Fortran 77, 2<sup>nd</sup> ed., vol. 1. Cambridge University Press, 436-448.
- Ramanathan V., 1987: The role of Earth radiation budget studies in climate and general circulation research. *J. Geophys. Res.*, **92**, 4075-4095.
- Ramanathan, V., P. J. Crutzen, J. T. Kiehl and D. Rosenfeld, 2001: Aerosols, climate and the hydrological cycle, *Science*, **294**, 2119-2124.
- Remer, L. A., Y. J. Kaufman, and B. N. Holben, 1996: The size distribution of ambient aerosol particles: Smoke vs. urban/industrial aerosol. Biomass Burning and Global Change, J. S. Levine, Ed., MIT Press, 519-530.
- Ramon, D., R. Ramanaherisoa, R. Santer, M. Chami, J. Fischer, E. Dilligeard, and T. Heinneman, 1999: Characterisation of aerosols over land from space sensors. *Final Report of a study for the CEO*.
- Reynolds, D., W., and T. H. Vonder Haar 1977: A bispectral method for cloud parameter determination. *Mon. Wea. Rev.*, **105**, 446-457.
- Rolph, G.D., 2003: Real-time Environmental Applications and Display sYstem (READY) Website (<http://www.arl.noaa.gov/ready/hysplit4.html>). NOAA Air Resources Laboratory, Silver Spring, MD.
- Rosenfeld, D., and G. Gutman, 1994: Retrieving microphysical properties near the top of potential rain clouds by multispectral analysis of AVHRR data. *Atmos. Res.*, **34**, 259-283.

- Rosenfeld, D., 1999: TRMM observed first direct evidence of smoke from forest fires inhibiting rainfall, *Geophys. Res. Lett.*, **26**, 3105-3108.
- Rosenfeld, D., 2000: Suppression of rain and snow by urban and industrial air pollution, *Science*, **287**, 1793-1796.
- Rosenfeld, D., 2004: Cloud top microphysics as a tool for precipitation measurements. In: *Measuring precipitation from space – EURAINSAT and the future*. V. Levizzani, P. Bauer, and F. J. Turk Eds, Kluwer Acad. Publ., in press.
- Rossow, W. B. and R. A. Schiffer, 1991: ISCCP cloud data products, *Bull. Amer. Meteor. Soc.*, **72**, 2-20.
- Rossow, W. B. and R. A. Schiffer, 1999: Advances in understanding clouds from ISCCP, *Bull. Amer. Meteor. Soc.*, **80**, 2261-2287.
- Rothman, L. S., R.R. Gamache, A. Barbe, A. Goldman, J.R. Gillis, L.R. Brown, R.A. Toth, J.M. Flaud, and C. Camy-Peyret, 1983: AFGL Atmospheric Absorption Line Parameters Compilation: 1982 Edition, *Applied. Optics*, **22**, 2247-2256.
- Sassen, K., 2002: Indirect climate forcing over the western US from Asian dust storms. *Geophys. Res. Lett.*, doi:10.1029/2001GL014034.
- Sassen, K., P. DeMott, J. Prospero, and M. Poellot, 2003: Saharan dust storms and indirect aerosol effects on clouds: CRYSTAL-FACE results. *Geophys. Res. Lett.*, doi:10.1029/2003GL017371.
- Satheesh, S. K., and V. Ramanathan, 2000: Large differences in tropical aerosol forcing at the top of the atmosphere and Earth's surface, *Nature*, **405**, 60-63.
- Schmetz, J., P. Pili, S. Tjemkes, D. Just, J. Kerkmann, S. Rota, and A. Ratier, 2002: An introduction to METEOSAT Second Generation (MSG) , *Bull. Am. Meteorol. Soc.*, **83**, 977-992.
- Shettle, E. P., 1984: Optical and radiative properties of a desert aerosol model, *International Radiation Symposium (IRS): Current problems in atmospheric radiation*, G. Fiocco Ed., 74-77, A. Deepak, Hampton, Va.
- Silva, A. M., M. L. Bugalho, M. J. Costa, W. von Hoyningen-Huene, T. Schmidt, J. Heintzenberg, and S. Henning, 2002: Aerosol optical properties from columnar data during the second Aerosol Characterization Experiment on the south coast of Portugal, *J. Geophys. Res.*, **107**, 4642, doi:10.1029/2002JD002196.

- Staetter, R., and M. Schroeder, 1978: Spectral characteristics of natural surfaces, *Proceeding of ten Int. Conf. on Earth Obs. from Space*, (ESA-SP, 134).
- Stephens, G. L., D. G. Vane, R. Boain, G. Mace, K.Sassen, Z. Wang, A. Illingworth, E. O'Connor, W. Rossow, S.L. Durden, S. Miller, R. Austin, A. Benedetti, C. Mitrescu, and the CloudSat Science Team, 2002: The CloudSat Mission and the A-Train: A new dimension of space-based observations of clouds and precipitation. *Bull. Amer. Meteor. Soc.*, **83**, 1771-1790.
- Swap, R.J., Annegarn, H.J., Suttles, J.T., King, M.D., Platnick, S., Privette, J.L., and Scholes, R.J., 2003: Africa burning: A thematic analysis of the Southern African Regional Science Initiative (SAFARI 2000), *J. Geophys. Res.*, **108**, doi: 10.1029/2003JD003747.
- Tanré, D., Y. Kaufman, M. Herman and S. Mattoo, 1997: Remote sensing of aerosol properties over oceans using the MODIS/EOS spectral radiances, *J. Geophys. Res.*, **102**, 16,971-16,988.
- The GMS User's Guide, 1997, Third Edition, Meteorological Satellite Center, Japan Meteorological Agency, Tokyo, Japan, 190 pp.
- Tokuno, M., 1997: The Present and Future Calibration of Meteorological Satellite Sensors in Japan. *Proc. The 1997 EUMETSAT Meteorological Satellite Data Users' Conf.*, 615-622.
- Torres, O., P. K. Bhartia, J. R. Herman, Z. Ahmad, and J. Gleason, 1998: Derivation of aerosol properties from satellite measurements of backscattered ultraviolet radiation: theoretical basis, *J. Geophys. Res.*, **103**, 17099-17110.
- Torres, O., P. K. Bhartia, J. R. Herman, A. Sinyuk, P. Ginoux, and B. Holben, 2002: A Long-Term Record of Aerosol Optical Depth from TOMS Observations and Comparison to AERONET Measurements, *J. Atmos. Sci.*, **59**, 398-413.
- Torricella F, Cattani E, Cervino M, Guzzi R, Levoni C (1999) Retrieval of aerosol properties over the ocean using GOME measurements: Method and applications to test cases. *J Geophys Res*, **104**, 12085-12098.
- Torricella,F., E.Cattani, M.Cervino, V.Levizzani, and M.J.Costa, 2001: Simulations of time-coincident, co-located measurements from ENVISAT-1 instruments for the characterization of tropospheric aerosol: a sensitivity study including cloud

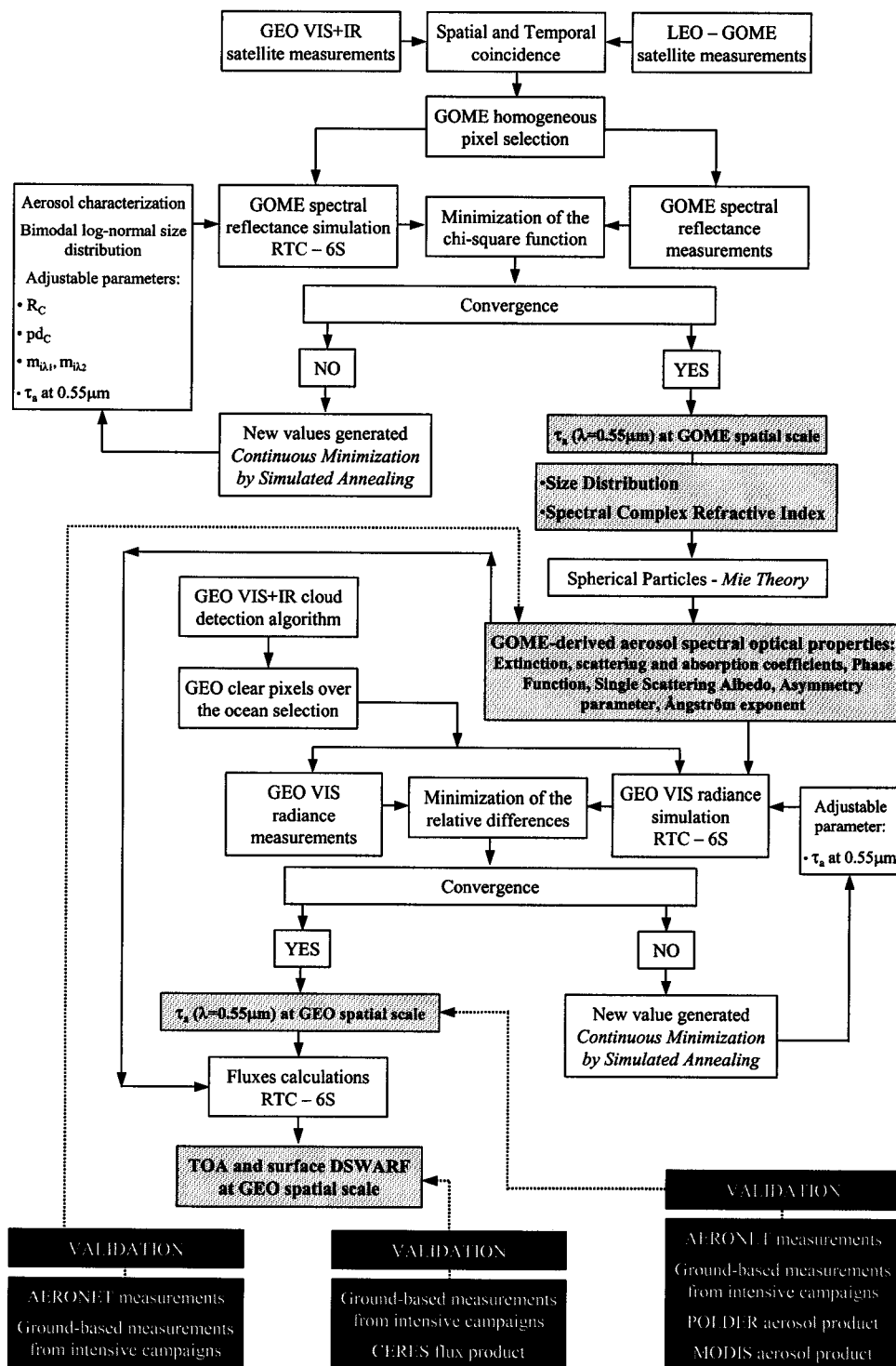


- contamination effects. *Atmos.Sci.Lett.*, 1, doi:10.1006/asle.2000.0021, <http://www.academicpress.com/asl>.
- Twomey, S., 1974: Pollution and the planetary albedo. *Atmos. Res.*, **8**, 1251-1256.
- Twomey, S., T. Cocks, 1982: Spectral Reflectance of Clouds in the Near-Infrared: Comparison of Measurements and Calculations, *J. Meteorol. Soc. Jap.*, **60**, 583-592.
- Veefkind, J., and G. de Leeuw, 1998: A new algorithm to determine the spectral aerosol optical depth from satellite radiometer measurements, *J. Aerosol Sci.*, **29**, 1237-1248.
- Vermote, E. F. and D. Tanré 1992: Analytical Expressions for Radiative Properties of Planar Rayleigh Scattering Media Including Polarization Contribution. *Journal Of Quantitative Spectroscopy and Radiative Transfer*, **47**, 4, 305-314.
- Vermote E. F., Tanré D, Deuze J-L, Herman M, Morcrette J-J 1997a: Second simulation of the satellite signal in the solar spectrum: An overview. *IEEE Trans Geosci Remote Sensing*, **35**, 675-686.
- Vermote, E., Tanré, D., Deuzé, J.L., Herman, M. and Morcrette, J.J. 1997b: Second simulation of the satellite signal in the solar spectrum (6S): User Guide Version 2, 218 pp.
- Viollier, M., 1980: Télédétection des concentrations de seston et pigments chlorophylliens contenus dans l'Océan, *Thèse de Doctorat d'Etat*, **503**.
- Wang, J., X. Liu, S. Christopher, J. Reid, E. Reid, and H. Maring, 2003a: The effects of non-sphericity on geostationary satellite retrievals of dust aerosols. *Geophys. Res. Lett.*, **30**, 2293, doi:10.1029/2003GL018697.
- Wang, J., S.A. Christopher, J.S. Reid, H. Maring, D. Savoie, B.H. Holben, J.M. Livingston, P.B. Russell, and S.K. Yang, 2003b: GOES-8 retrieval of dust aerosol optical thickness over the Atlantic Ocean during PRIDE, *J. Geophys. Res.*, **108**, doi:10.1029/2002JD002494.
- Wielicki, B. A., B. R. Barkstrom, E. F. Harrison, R. B. Lee III, G. L. Smith, and J. E. Cooper, 1996: Clouds and the Earth's Radiant Energy System (CERES): An Earth Observing System Experiment, *Bull. Am. Meteorol. Soc.*, **77**, 853-868.
- Wilks DS (1995) Statistical methods in the atmospheric sciences. Academic Press, 467 pp.
- Wiscombe, W. J., 1977: The delta-M method: rapid yet accurate radiative flux calculations for strongly asymmetric phase functions, *J. Atmos. Sci.*, **34**, 1408-1422.

World Meteorological Organization (CAS) 1983: Radiation Commission of IAMAP Meeting of experts on aerosols and their climatic effects, WCP 55, Williamsburg, Virginia, U.S.A., 28-30.

# Appendix A

## Block diagram of the aerosol method

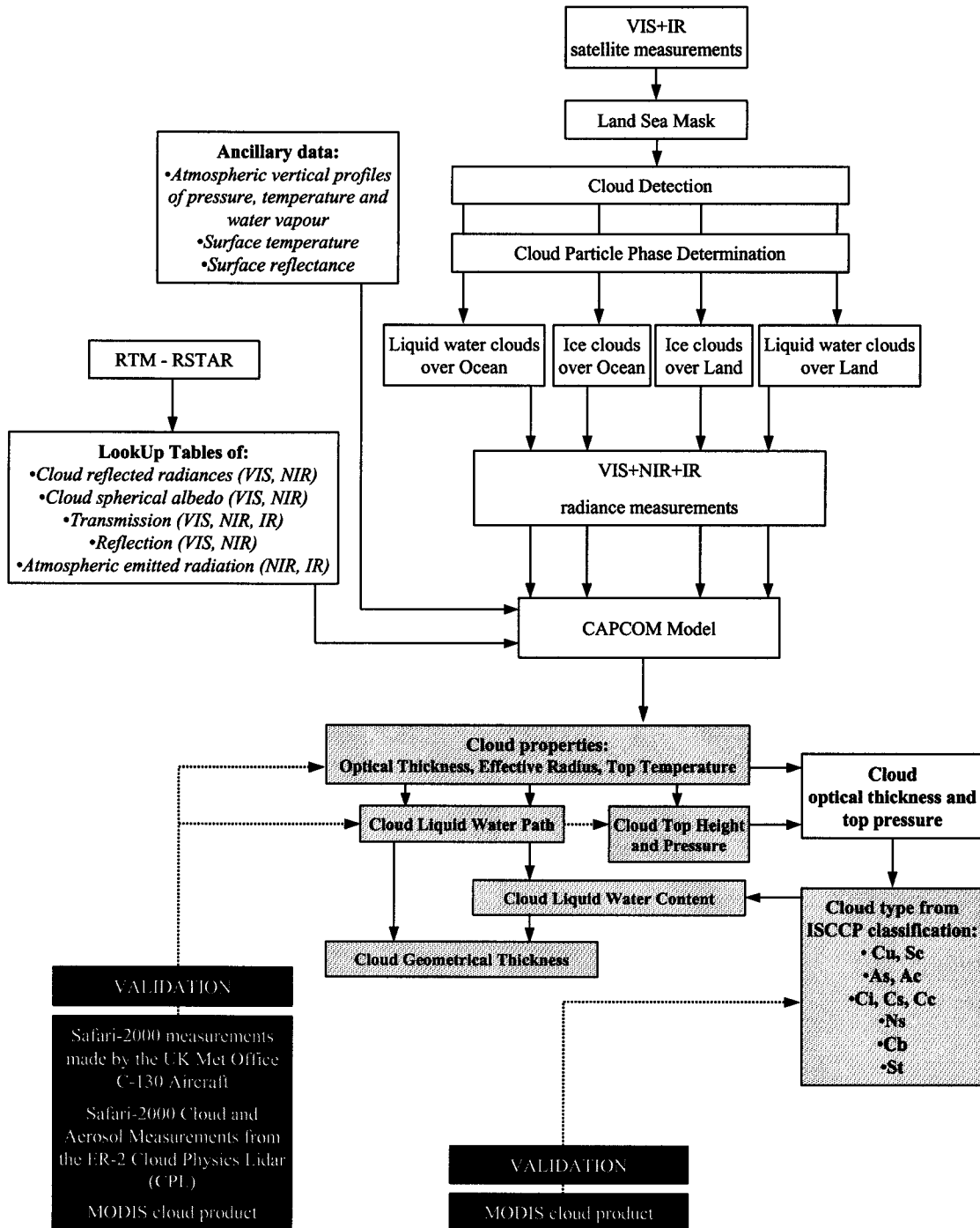


Grey boxes represent the results and black boxes the validation data sets (taken from Costa et.al. 2004a).



# Appendix B

## Block diagram of the cloud method



Grey boxes represent the results and black boxes the validation data sets.

